A multifaceted investigation of the resolved properties of galaxy mergers

by

Mallory D. Thorp
B.Sc., University of Washington, 2017
M.Sc., University of Victoria, 2019

A Dissertation Submitted in Partial Fulfillment of the
Requirements for the Degree of

DOCTOR OF PHILOSOPHY

in the Department of Physics and Astronomy

© Mallory D. Thorp, 2022
University of Victoria

All rights reserved. This Dissertation may not be reproduced in whole or in part, by photocopying or other means, without the permission of the author.

A multifaceted investigation of the resolved properties of galaxy mergers

by

Mallory D. Thorp
B.Sc., University of Washington, 2017
M.Sc., University of Victoria, 2019

Supervisory Committee

Dr. Sara Ellison, Supervisor
(Department of Physics and Astronomy, University of Victoria)

Dr. Luc Simard, Departmental Member
(Department of Physics and Astronomy, University of Victoria)

Dr. Rana El-Sabaawi, Outside Member
(Department of Biology, University of Victoria)

ABSTRACT

One promising mechanism to understand the impressive diversity of galaxies observed today, and how galaxies may transition between different populations, is galactic mergers. Interactions between galaxies of comparable masses can dramatically alter the morphology, chemical composition, star formation activity, and central black-hole accretion of their constituents. Although the impacts of galaxy interactions can be seen at relatively early stages of an encounter, the entire process from first approach to coalescence takes hundreds of millions of years. Consequently, observations of galaxies at different stages of an interaction are required to reconstruct the complete merging process. Such an investigation requires large spectroscopic galaxy surveys to probe a variety of merger stages, which until recently were limited to global properties. The advent of large integral field spectroscopy (IFS) surveys has provided the novel opportunity to examine changes induced by a merger on a kpc-scale.

This thesis presents the largest IFS analysis of galaxy mergers to date using the Mapping Nearby Galaxies at Apache Point Observatory (MaNGA) survey. From 10,000 MaNGA galaxies I visually classify 400 post-merger galaxies, and with the aid of spectroscopic pair catalogues identify 1523 interacting pairs. The global and resolved star formation rate (SFR) properties of the merger sample have significant overlap with the non-interacting galaxies, though post-mergers tend to have slightly higher star formation rate and stellar mass surface densities. Enhancements and deficits in star formation ($\Delta\Sigma_{\rm SFR}$) and metallicity (Δ O/H) are determined for every spatial pixel containing a spectrum (spaxel) based on well established scaling relationships with stellar mass surface density; these are subsequently compressed into 2-dimensional radial profiles to investigate how the impact of an interaction varies with radius. Radial profiles reveal how a centralized starburst in mergers depends on interaction stage, global SFR enhancement, and the ratio of interacting galaxy masses. Though average trends arise, such as post-mergers and galaxies with larger or comparable mass companions having the strongest central starburst and metallicity dilution, I uncover considerable variation in $\Delta\Sigma_{\rm SFR}$ and Δ O/H profiles in mergers.

In an effort to expose spatially resolved changes concealed in azimuthally averaged radial profiles, I propose adopting non-parametric morphology metrics asymmetry and concentration for IFS data products as an alternative analysis tool. In this thesis I utilize galaxies from the IllustrisTNG simulation to assess the applicability of concentration and asymmetry indicators to the stellar mass distribution in galaxies.

Specifically, I test whether the intrinsic values of concentration and asymmetry (measured directly from the simulation stellar mass particle maps) are recovered after the application of measurement uncertainty and varying resolution. I find random noise has a non-negligible systematic effect on asymmetry that scales inversely with signal-to-noise, to a degree that would make its application on IFS data highly problematic. I evaluate different methods to correct for the noise contribution to asymmetry at very low signal-to-noise, where previous studies have been unable to explore due to systematics, and present new algebraic corrections for noise and resolution to recover the intrinsic morphology measurements. I confirm these fit corrections can be applied to simulations with different physical models using the Illustris simulation, and provide estimations for the uncertainty on different correction methods at varying signal-to-noise and resolution regimes.

This thesis also investigates how resolved molecular gas properties may impact the variety of $\Delta\Sigma_{\rm SFR}$ behaviour in mergers. Spatially resolved measurements of CO emission are acquired using the Atacama Large Millimetre Array (ALMA) for 20 merging galaxies (either pairs or post-mergers) selected from the MaNGA survey. Eleven additional merging galaxies are selected from the ALMA MaNGA QUEnching and STar formation (ALMaQUEST) survey, resulting in a set of 31 mergers at various stages of interaction and covering a broad range of SFR. Combining resolved measurements of CO luminosity (from which molecular gas is derived) with MaNGA star formation rate maps provides insights on what drives merger-induced enhancements in star formation: an excess of molecular gas to fuel star formation, or a heightened efficiency in the rate at which gas is converted into stars. Using this data set I investigate galaxy-to-galaxy variations in key resolved scaling relations between star formation rate surface density, molecular gas surface density, and stellar mass surface density, revealing substantial diversity amongst mergers. Offsets in each resolved relation are quantified to determine if star formation rate, molecular gas fraction, and/or star formation efficiency (SFE) is enhanced in different regions of an individual galaxy. By comparing offsets in all three parameters I can discern whether gas fraction or SFE powers local enhancements in star formation rate. From this analysis I find merger-induced star formation can be driven by a variety of mechanisms, both within a galaxy and between different mergers, regardless of interaction stage. In closing remarks I highlight some exciting follow-up studies to this work: such as determining what causes mergers to have suppressed star formation, or how a merger-triggered active galactic nucleus might impact local star formation and gas properties.

Contents

Supervisory Committee ii

Abstract iii

Table of Contents v

List of Tables viii

List of Figures x

List of Abbreviations xxxix

Author Contribution Statement xli

Acknowledgements xlii

Dedication xliii

1 Introduction 1

1.1 Galaxy types and evolution . . . 3
1.2 Star formation in galaxies . . . 5
1.2.1 Gas - phase metallicity . . . 8
1.2.2 Resolved scaling relations . . . 10
1.3 Galaxy mergers as a keystone for cosmic evolution . . . 13
1.3.1 What happens when galaxies collide? . . . 14
1.4 Statistical observational studies of merging galaxies . . . 18
1.4.1 Integrated Studies . . . 18
1.4.2 Resolved spectroscopic studies . . . 22
1.5 Thesis outline . . . 28

2 Star formation and metallicity of mergers in MaNGA 30

2.1 MaNGA survey . . . 31
2.1.1 Spectral reduction and PIPE3D . . . 34
2.1.2 Extended data products . . . 35
2.1.3 Star-forming criteria . . . 37
2.2 Merger classification algorithm and sample characteristics . . . 39
2.2.1 Review and evaluation of merger classification methods . . . 39
2.2.2 MaNGA sample selection and characteristics . . . 42
2.3 Results: resolved properties of mergers . . . 44
2.3.1 Resolved scaling relations for merging galaxies . . . 46
2.3.2 Post-merger radial profiles . . . 53
2.3.3 Pair radial profiles . . . 60
2.4 Summary & future work . . . 67

3 Robust determinations of non-parametric morphologies in marginal astronomical data 72
3.1 Morphology and non-parametric indices . . . 73
3.2 TNG simulation and sample selection . . . 76
3.2.1 Adding observational effects to simulated galaxies . . . 77
3.3 Concentration and asymmetry calculations . . . 80
3.4 Correcting non-parametric morphologies for noise and resolution . . . 84
3.4.1 Noise . . . 84
3.4.2 Spatial resolution . . . 94
3.5 Comparison to unseen data . . . 104
3.6 Implications for merger studies . . . 112
3.6.1 Example of effects of noise on merger asymmetries . . . 114
3.7 Summary . . . 117

4 Resolved molecular gas and star formation properties of mergers with ALMaQUEST 119
4.1 Observing molecular gas in other galaxies . . . 120
4.2 ALMaQUEST merger set . . . 122
4.2.1 Sample selection . . . 122
4.2.2 ALMA observations . . . 126
4.2.3 Additional MaNGA dataproducts . . . 131
4.3 Results: resolved scaling relations . . . 133

4.3.1 Spaxel offsets from resolved relations . . . 140
4.3.2 What drives enhanced star formation? . . . 141
4.4 Impact of varying techniques to compute Σ_{H_2} and Σ_{SFR} . . . 156
4.4.1 Metallicity dependent α_{CO} . . . 156
4.4.2 Estimating Σ_{SFR} with D4000 . . . 159
4.5 Summary . . . 163

5 Conclusions **165**
5.1 Diversity of resolved star formation and metallicity properties of mergers 165
5.2 Recovering accurate asymmetry and concentration measurements for observations of varying quality . . . 168
5.3 What powers merger-induced star formation? . . . 169
5.4 Future work . . . 171

Bibliography **175**

A Additional Information **205**
A.1 MaNGA DR17 merger sample . . . 205
A.2 ALMaQUEST - merger dataproducts . . . 227
A.3 ALMaQUEST control spaxels - including D4000-Σ_{SFR} . . . 233
A.4 Offset maps for entire ALMaQUEST merger sample . . . 238

List of Tables

Table 3.1 Summary of the validity of different asymmetry noise correction methods in various S/N regimes. For each method (no noise correction ("No corr"), subtract $A_{\rm noise}$ from the observed asymmetry ("Noise Sub"), subtract $A_{\rm noise}/1.2$ from the observed values ("$A_{\rm noise}/1.2$"), and corrected based on Equation 3.8 ("LM Fit")) we provide the mean difference and scatter in difference between the intrinsic asymmetry and the measured asymmetry. From this one can approximate the bias in asymmetry measurement for data with differing S/N regimes. The signal to noise must be measured as laid out in this analysis, using the median within an aperture of $1R_{\rm half}$ (an alternative radius with comparable size to $R_{\rm half}$ could be used as well). 113

Table 4.1 Summary of global properties of post-merger and pair galaxies observed with ALMA, with post-mergers first (no r_p values), followed by pairs ordered by r_p. Key global properties derived from the MaNGA VAC are included ($M_\star$, SFR, ΔSFR, z), as well as merger properties such as r_p, Δv, and mass ratio (the mass of the galaxy divided by that of its companion). Post-mergers have empty columns for merger properties, which require information about a companion galaxy. Pair galaxies that were visually identified only have r_p values, since spectroscopic information is not available for the companion. 124

Table 4.2 Spaxel counts for each galaxy merger that meet the various star-forming and CO S/N cuts, along with the overlap between these regions. Galaxies with less than 10 spaxels of CO+SF(Hα+D4000) overlap are excluded for plots of individual galaxies. 128

Table 4.3 The fraction of $\Delta\Sigma_{\rm SFR}>0$ spaxels in the fuel-driven regime (i.e., $\Delta f_{\rm H_2}>\Delta$SFE) for each merger with more than 20 $\Delta\Sigma_{\rm SFR}>0$ spaxels. The fraction of fuel-driven spaxels is computed using the combined Hα+D4000 $\Sigma_{\rm SFR}$, as well as just the Hα star formation rates (with appropriate cuts). Note some galaxies do not have fractions computed for Hα, because they do not have more than 20 spaxels that meet my star-forming cuts. Fractions greater than 0.6, what I consider a fuel-driven merger, are coloured blue. Fractions less than 0.4, what I consider an efficiency-driven merger, are coloured red. Those between 0.4 and 0.6 are left black, since both mechanisms contribute relatively equally. 147

List of Figures

Figure 1.1 Hubble's classification scheme, summarized with both cartoons depicting basic galaxy structure and examples of real galaxy images. Es denote elliptical galaxies, with higher numbers corresponding to degree of elongation. Spiral galaxies are denoted with S, with S0 representing a disk galaxy with no spiral arm structure (lenticulars). Spirals are further separated into those with and without a bar (B), with additional subclasses (a,b,c) denoting the tightness of the spiral arms. Image Credit: NASA & ESA. 2

Figure 1.2 The u-r colour-mass diagram for galaxies in the Sloan Digital Sky Survey. All galaxies are shown in the top left panel, where two populations emerge: a tight red sequence (red being larger u-r values), and a more diffuse blue cloud (low u-r values). The green valley is sectioned off as the intermediate space between both populations. The top right and bottom right panel separate galaxies into early- and late-type, respectively. The early type galaxies (also called ellipticals) make up the majority of the red population, where as late-type (spiral) galaxies make up the blue cloud. Source: Schawinski et al. (2014). 4

Figure 1.3 The SFR - $M_\star$ relation for SDSS galaxies between $0.02<z<0.085$. The third dimension represents the number of galaxies in each bin, demonstrating the peaks that represent the star-forming and passive population of galaxies. Source: Renzini & Peng (2015). 7

Figure 1.4 A 3D distribution of $\Sigma_{\star}$, Σ_{H_2}, and Σ_{SFR} for star-forming regions in main-sequence galaxies. Each individual scaling relation is shown on a 2D plane: red for the rSFMS, blue for the rKS (called Schmidt-Kennicutt, or SK, here), and orange for the rMGMS. Contours show levels corresponding to 20%, 40%, 60%, 80%, and 90% of the density peaks. Fits for each scaling relation are calculated, shown as a solid dashed line, with parameters (a,b) and associated scatter (σ) shown in the legend. Through a 3D representation it becomes clear that all three scaling relations are merely one component of a more complex relationship between gas and stars. Source: Lin et al. (2019). 12

Figure 1.5 *Left:* Image of NGC 4676, two interacting galaxies also known as the Mice, taken with The Advanced Camera for Surveys (ACS) on the Hubble Space Telescope. The Mice are a textbook example of both bridge features (between the two nuclei), and tidal tails (streaming to the left and right of each). Image credit: NASA, H. Ford (JHU), G. Illingworth (UCSC/LO), M.Clampin (STScI), G. Hartig (STScI), the ACS Science Team, and ESA. *Right:* Image of NGC 474, taken with the MegaCam camera on the Canada-France-Hawaii Telescope (CFHT). The CFHT observation picks up faint galactic features, and fantastically captures both stellar shells and streams that are often less obvious than tidal tails. Image credit: CFHT, Coelum, MegaCam, J.C. Cuillandre (CFHT) & G. A. Anselmi (Coelum). 15

Figure 1.6 Enhancements in SFR compared to a control sample (ΔSFR) for star-forming galaxies in close pairs, shown as a function of projected separation between pairs. Enhancements for a post-merger sample are shown in the grey shaded box. Note how as galaxy pairs get closer the star formation enhancement increases, with the greatest enhancement at the moment of coalescence. Filled circles show the fibre SFR, whereas empty circles show the SFR outside the fibre. Source: Ellison et al. (2013b). 20

Figure 1.7 An illustration of the data cube produced by integral field spectroscopy, made specifically for the Multi-Unit Spectroscopic Explorer (MUSE) instrument. The data cube is split into different wavelengths of light, such that every wavelength interval has a complete image of NGC 4650A (an Hα emission map is shown here). Image Credit: ESO/MUSE consortium/R. Bacon/L. Calçada 22

Figure 1.8 Radial profiles of the enhancement in sSFR compared to a control population (Δ logsSFR) for merging galaxies, separated into different interaction stages. The shaded area around each line represents the standard error of the mean. Stage 1 (red) are well separated galaxies with no morphology distortion, indicating they are likely incoming galaxy pairs. Stage 2 (yellow) are close pairs with strong morphological signs of an interaction, such as tails or bridges, assumed to be close to first pericentric passage. Stage 3 (blue) are well separated pairs with weak morphology distortions, implying that first passage has already occurred and galaxies are either approaching or just passing apocentre. Stage 4 represents galaxies near coalescence, with either two highly distorted components overlapping (green) or a single galaxy with obvious tidal features (purple). Source: Pan et al. (2019). . . . 25

Figure 1.9 Radial profiles of the enhancement in $\Sigma_{\rm SFR}$ ($\Delta\Sigma_{\rm SFR}$) for a sample of 48 post-merger galaxies, each colour-coded by the global offset from the star-forming main sequence. Note that although strong central enhancements in star formation are most common, there is a wide range of changes in resolved star formation. Three profiles with similar central starbursts are highlighted, to demonstrate how much they differ at larger radii. Source: Thorp et al. (2019). 26

Figure 2.1 Infographic describing the MaNGA IFU, and how it is used to collect data, provided by the SDSS official website. A picture of an IFU, ready to be plugged into an SDSS plate, is shown at left. To the right a zoom-in is provided to show the structure of fibres within the IFU, and how they cover an example galaxy. The infographic demonstrates how each fibre outputs a separate spectrum for different points on the galaxy. The SDSS telescope is shown in the top left. Image Credit: Dana Berry/SkyWorks Digital Inc., David Law, and the SDSS collaboration. Available on the SDSS official website: https://www.sdss.org/surveys/manga/ 32

Figure 2.2 MaNGA footprint for the 17th data release, with possible MaNGA sky plates shown in grey and observed sky plates shown in blue. Image available on the SDSS official website: https://www.sdss.org/dr17/manga/manga-survey-strategy/footprint/ 33

Figure 2.3 A BPT diagnostic diagram for global galaxy emission using emission line data from MaNGA data release 13, published in Belfiore et al. (2016). The Kauffmann et al. (2003) line is shown in solid black, and the Kewley et al. (2001) line is dashed. Within each diagram each axis is divided into 100 bins to create 2D histogram, the first column is colour coded by the log density of these bins. The second and third column are colour-coded by the 4000 Å break index (D4000) and Hδ_A equivalent width (EW); bins with more than 20 galaxies take the average of the bin, those with less show a point for each galaxy. Both D4000 and Hδ_A scale with stellar population age, demonstrating how younger stellar populations lie to the left of the Kauffmann et al. (2003) demarcation. 38

Figure 2.4 *Left:* The distribution of projected separation in kpc between a target galaxy and its companion, separated into visual pairs (orange) and spectroscopic pairs (green). The r_p distribution for the full sample is shown as a shaded grey histogram. The median of each distribution is shown as a vertical dashed line. Note that the visual pair sample is heavily biased to close pairs, which are undersampled by the spectroscopic pairs. *Middle:* The distribution of change in line of sight velocity for the spectroscopic pairs (visual pairs do not have Δv or μ information) in km/s. *Right:* The distribution of mass ratio for the spectroscopic pairs. Log $\mu = 0$ means that the two galaxies interacting galaxies are the same size, log $\mu < 0$ means the target MaNGA galaxy is the smaller of the two, and log $\mu > 0$ means the target is the larger of the two. 43

Figure 2.5 *Top:* Total star formation rate versus total stellar mass for the entire MaNGA survey (grey), with the post-merger (circles) and pair (triangle) galaxies select for this work over plot. Pair galaxies are colour-coded by the projected separation between the target and its companion (in kpc). Note that both the pre- and post-coalescence sample cover a broad range of SFRs and $M_\star$s. *Bottom:* Distribution of global ΔSFR values for non-interacting MaNGA galaxies (grey), post-mergers (orange), and pair galaxies (blue). The median ΔSFR of each sample are -0.49, 0.02, and -1.17 dex respectively (represented as dashed vertical lines). The pair sample is likely biased towards lower ΔSFR than the rest of MaNGA because it oversamples dense environments where star formation is overall lower. The post-merger sample is offset to larger ΔSFR, confirming that merger events on average boost star formation (at least in the timescale for which mergers can be visually identified). 45

Figure 2.6 *Left:* $\Sigma_{\rm SFR}$ vs. $\Sigma_\star$ for all star-forming spaxels in the MaNGA survey (grey hexbin representing density of spaxels in each bin, with the distribution of the post-merger (orange) and pair (blue) sample overplot. Histograms for each variable are provided on the x and y axis, with a vertical line indicating the mean of the distribution. *Right:* The same as the left diagram, but with metallicity plot on the y-axis to show the mass-metallicity relation. Note that post-mergers seems to be biased towards larger $\Sigma_\star$ and $\Sigma_{\rm SFR}$ values, but not lower metallicities. For the rMZR, this bias for larger $\Sigma_\star$ not corresponding to a bias towards higher metallicities implies that post-mergers have lower metallicities than is expected given the average relation established by the rMZR. 47

Figure 2.7 $\Sigma_\star$ distribution of spaxels from control galaxies (grey), pair galaxies (blue), and post-mergers (orange). Spaxel distributions are separated into two groups: those belonging to galaxies roughly on or above the SFMS (left, Δ SFR> -0.6 dex), and those belonging to galaxies below the SFMS (right, Δ SFR< -0.6 dex). The median of each distribution is shown as a dashed line. Although Figure 2.6 showed that on average post-merger spaxels are biased to large $\Sigma_\star$, this diagram reveals that bias to be far more prominent for galaxies below the main sequence than those on it. If mergers can trigger bulge growth, there should be an observable build up of larger $\Sigma_\star$ in elliptical galaxies, as is seen here. 48

Figure 2.8 ΔO/H vs. $\Delta\Sigma_{\rm SFR}$ for all star-forming spaxels in the isolated MaNGA sample (top), pair sample (bottom left), and post-merger sample (bottom right). The diagram is broken into four quadrants depending on the sign of each offset parameter, with the percentage of spaxels in each quadrant displayed in the figure. Both pair and post-merger galaxies have a larger percentage of spaxels with positive $\Delta\Sigma_{\rm SFR}$ and negative ΔO/H compared to the isolated sample, as might be expected if low-metallicity gas inflows resulting from mergers trigger boosts in star formation. One would expect spaxels with positive $\Delta\Sigma_{\rm SFR}$ to have negative ΔO/H, and those with positive ΔO/H to have negative $\Delta\Sigma_{\rm SFR}$ (if low metallicity is any indicator for the molecular gas in a system). There is only a small Pearson's correlation coefficient (-0.2) between ΔO/H and $\Delta\Sigma_{\rm SFR}$. Although the two variables are not strictly correlated, there can still be a crucial physical connection between the two. 50

Figure 2.9 Data product maps for a post-merger (top), visual disturbed pair with the companion on the IFU (middle), and pair galaxy with a spectroscopic companion to the bottom right (bottom). From left to right: the SDSS *gri*-image (with MaNGA footprint overplot in magenta), stellar mass surface density (from PIPE3D), star formation rate surface density (derived from Hα), O3N2 metallicity, $\Delta\Sigma_{\rm SFR}$, and ΔO/H. For all data product maps besides $\Sigma_\star$, only star-forming spaxels are shown. Both the patchiness and complexity of the map varies greatly between galaxies. 52

Figure 2.10 Individual $\Delta\Sigma_{\rm SFR}$ profiles as a function of R_e for each post-merger within a particular ΔSFR bin, colour-coded from lowest (yellow) to highest (blue) ΔSFR within that bin. Examining all galaxy profiles reveals the magnitude of galaxy-to-galaxy variation, even for galaxies in a similar position on the star-forming main sequence. Note the fading strength of the central starburst with decreasing ΔSFR holds even when this diversity is considered. 54

Figure 2.11 Radial profiles of $\Delta\Sigma_{\rm SFR}$ for the post-merger sample, in bins of R_e (left) and kpc (right). Each spaxel is separated into bins of ΔSFR, and then the average $\Delta\Sigma_{\rm SFR}$ of those spaxels within a radial bin is computed. The average profile for all post-mergers is shown as a grey dashed line. The width of each line represents the error on the mean ($\sigma/\sqrt{N}$). Note that this error quantifies the number of spaxels contributing, not the number of galaxies. Single galaxy contribution is not an issue for most ΔSFR bins save for ΔSFR< -0.4, which is the most sparsely populated bin with only 3 galaxies contributing beyond $1.5R_e$. This is also why the $\Delta\Sigma_{\rm SFR}$ profile looks so different for ΔSFR< -0.4 galaxies when plotted against radii in kpc. 55

Figure 2.12 Individual ΔO/H profiles for each post-merger within a particular ΔSFR bin, colour-coded from lowest (yellow) to highest (blue) ΔSFR within that bin. Just as is seen for $\Delta\Sigma_{\rm SFR}$ profiles in Figure 2.10, there is a noticeable diversity between galaxy profiles even within a ΔSFR bin. Examining all post-merger profiles reveals many of the ΔSFR> 0 mergers have stronger metallicity deficits in their centres compared to their outskirts, implying inflows of low-metallicity gas often occur in mergers (but are clearly not the only possible scenario). Mergers with the strongest central deficit often have positive gradients in ΔO/H, whereas those with moderate suppressed central metallicity tend to be similar suppressed out to 2 R_e. 58

Figure 2.13 Radial profiles of $\Delta\Sigma_{\rm SFR}$ (blue) and ΔO/H (orange) for three example post-mergers with very different resolved behaviour, withe the SDSS *gri*-image next to each plot for comparison. The first galaxy (plate-ifu: 9090-3704) has both suppressed star formation and metallicity out to 2 R_e. The second (plate-ifu: 9511-6103) has profiles greater than zero for both properties. The third galaxy (plate-ifu: 7992-6102) agrees with the majority of post-merger spaxel offsets as shown in Figure 2.8, with $-\Delta$O/H corresponding to $+\Delta\Sigma_{\rm SFR}$. 59

Figure 2.14Radial profiles of ΔO/H for the post-merger sample, in bins of R_e (left) and kpc (right). Each spaxel is separated into bins of ΔSFR, and then the average ΔO/H of those spaxels within a radial bin is computed. The average profile for all post-mergers is shown as a grey dashed line. The width of each line represents the error on the mean ($\sigma/\sqrt{N}$). The same ΔSFR bins are used as in Figure 2.11, although note that the ΔSFR< -0.4 dex bin is even more sparsely populated in this figure (given fewer spaxels have accurate ΔO/H measurements than $\Delta\Sigma_{\rm SFR}$). All profiles besides the two lowest ΔSFR bins have suppressed metallicity, though the starbursts (ΔSFR$>$0.5 dex) have the greatest suppression. Note that this suppression is relatively flat, unlikely the distinct inside-out behaviour of the $\Delta\Sigma_{\rm SFR}$ profiles. 61

Figure 2.15*Left:* Radial profiles of $\Delta\Sigma_{\rm SFR}$ as a function of R_e for the interacting pair galaxies in bins of projected separation (r_p), with dark purple representing the closest pairs. The post-merger $\Delta\Sigma_{\rm SFR}$ profile is shown with a blue dashed line for comparison. *Right:* The same radial profiles, but now in bins of kpc for comparison. 62

Figure 2.16Radial profiles of $\Delta\Sigma_{\rm SFR}$ similar to Figure 2.15, but separated into three bins of ΔSFR to demonstrate the similarities between radial profiles for different r_p values. r_p and ΔSFR bins have changed slightly from previous figures, to maintain a relatively equal number of galaxies in each bin. All r_p bins seem to reflect the general behaviour as predicted by ΔSFR, with those above the main sequence (ΔSFR$>$ 0.2) having extended enhancements with the strongest enhancement in the centre, those on the main sequence ($-0.2 <$ ΔSFR$<$ 0.2) having only centralized SFR enhancements, and those below the main sequence (ΔSFR< -0.2) having mostly negative $\Delta\Sigma_{\rm SFR}$ values. 63

Figure 2.17 *Left:* Radial profiles of $\Delta\Sigma_{\rm SFR}$ for the interacting pair galaxies in bins of mass ratio μ, with red profiles showing targets much smaller than their companion, blue showing targets much larger than their companion, and green showing mergers between two like-sized galaxies. The average pair profile is shown as a grey dashed line for comparison. *Right:* The same radial profiles, but now in bins of kpc for comparison. When the target galaxy is much larger than the companion ($\mu > 2$) it is less likely to exhibit centralized enhancements in star formation, likely due to the limited gravitational impact of the companion. 64

Figure 2.18 *Left:* ΔSFR vs. the log mass ratio of the pair galaxies. There is no clear relationship that when the two galaxies are of similar size ($\log \mu \sim 0$) the offset from the star-forming main sequence is highest. Nor is there an obvious correlation between ΔSFR and μ, with a Pearson Correlation Coefficient of -0.08. *Right:* Distributions of ΔSFR for pairs with $\mu < 1$(blue) and $\mu > 1$(orange). Although our sample contains more pairs with $\mu > 1$ (the target is larger than the companion), both samples cover a similar range of ΔSFR values. 65

Figure 2.19 Radial profiles of $\Delta\Sigma_{\rm SFR}$ similar to Figure 2.17, but separated into three bins of ΔSFR to examine how μ dependence varies with global offset from the star-forming main sequence. As long as the merger is on or above the star-forming main sequence (Δ SFR> -0.2 dex), pairs with small μ values consistently create stronger central starbursts. Central starbursts are not seen in more passive galaxies, thus the μ dependence goes away for the Δ SFR< -0.2 dex bin. 66

Figure 2.20 *Left:* Radial profiles of ΔO/H for the interacting pair galaxies in bins of projected separation (r_p), with dark purple representing the closest pairs. The post-merger ΔO/H profile is shown with a blue dashed line for comparison. *Right:* The same radial profiles, but now in bins of kpc for comparison. Note that only the furthest pairs show enhancements in metallicity, but beyond that every stage of a merger has some degree of metallicity dilution. 68

Figure 2.21 *Left:* Radial profiles of ΔO/H for the interacting pair galaxies in bins of mass ratio (μ), with warm colours for targets smaller than their companion, and cool colours for targets larger than their companion. The average pair ΔO/H profile is shown as a grey dashed line for comparison. *Right:* The same radial profiles, but now in bins of kpc for comparison. The strongest central dilutions in metallicity occur in galaxies that are smaller than their companion, in agreement with the central star formation enhancement seen in Figure 2.17. 69

Figure 3.1 The steps through which realistic noise and resolution are applied to a simulated galaxy. Top-left: The stellar mass surface density of the simulated galaxy, from which intrinsic asymmetry and concentration are measured. Top-middle: A sample PSF applied to this galaxy, although values can range from 0.002"-7". Changing the PSF allows us to change the resolution to the simulated galaxies at a fixed distance. I have chosen to highlight this galaxy with a small angular size compared to the applied PSF, resulting in a small resolution value (smaller than has been examined in previous works), to highlight how significantly degrading the resolution changes the asymmetry and concentration. Top-right: Random noise generated from a Gaussian distribution, to be applied to the galaxy image. The desired (input) S/N is used to generate the width of the Gaussian distribution so that the measured S/N is of a similar (though not exactly the same) value. Bottom-left: The stellar mass surface density image of the galaxy with added noise. White values are where $\Sigma_\star$ is so small, adding negative noise results in a non-measurement. Bottom-middle: The image of the galaxy convolved with the PSF from the top-middle panel. Bottom-right: The image of the galaxy convolved with the PSF and with noise added, providing an image of the galaxy more similar to what would be seen with observations. . 79

Figure 3.2 The observed concentration (left) and asymmetry (right) compared to intrinsic values (which have no random noise contribution). From the left panel it is clear that the addition of noise has no effect on concentration measurements (save catastrophic cases at the lowest signal-to-noise). Asymmetry, on the other hand, is always overestimated once noise is added, although the degree of that overestimation scales with inversely with S/N. . 85

Figure 3.3 The standard noise subtraction method requires subtracting all of $A_{\rm noise}$ from $A_{\rm obs}$ to approximate the intrinsic asymmetry. The black dashed line represents the line of equality, with red dashed lines representing a 0.05 buffer from this line. Points are colour-coded by S/N, save for galaxies with $S/N < 10$, which are grey. By correcting for noise contribution to asymmetry the scatter between the measured and intrinsic asymmetry is lessened by a factor of 10, and 5% more galaxies have a good asymmetry measurement (within 0.05 of $A_{\rm int}$). However, the median offset using this correction is of a similar magnitude to doing no noise correction (see Figure 3.2), just in the opposite direction. The galaxies with asymmetries far less than $A_{\rm int} \pm 0.05$ are those with low S/N, in particular the galaxies with $S/N < 10$ have the greatest difference in asymmetry from noise. 86

Figure 3.4 Left: The mean difference between the intrinsic asymmetry and corrected asymmetry for increasing signal-to-noise. Each curve represents subtracting a different fraction of the noise asymmetry, where red has no subtraction, and purple subtracts the entire $A_{\rm noise}$ value. The width of each line is the standard error on the mean. See Figure 3.7 for a comparison of these plots to my fit correction. Right: The standard deviation of the difference between intrinsic and corrected asymmetry in each signal-to-noise bin, for each correction method. Thus to recover the intrinsic asymmetry at $S/N < 100$, subtracting a fraction of $A_{\rm noise}$ does better than subtracting the total noise contribution to asymmetry. Subtracting $A_{\rm noise}/1.2$ recovers the most asymmetry values (within $A_{\rm int} \pm 0.05$) and has the smallest scatter in the difference at all S/N values. 87

Figure 3.5 The asymmetry corrected for $A_{\rm noise}/1.2$ versus the intrinsic asymmetry. Points are colour-coded by S/N, except for galaxies with $S/N < 10$, which are grey. The scatter between the two is smaller than doing no noise correction, similar to the improvement from subtracting $A_{\rm noise}$ from the observed asymmetry (see Figure 3.3). However, the median offset is significantly less, and over 20% more of the simulated galaxies are within an accurate asymmetry measurement (within $A_{\rm int} \pm 0.05$). In fact, almost all galaxies with $S/N > 10$ are within 0.05 of $A_{\rm int}$, a much more forgiving S/N cut than the $S/N > 100$ cut necessary for the traditional $A_{\rm noise}$ correction. 89

Figure 3.6 Density contours for the predicted asymmetry based on the fit relationship from Equation 3.8 versus the intrinsic asymmetry, the dashed red line representing where the two would be equal to each other. Applying a correction for the random noise based on a fit function significantly decreases the scatter of the difference between the predicted and intrinsic asymmetry, while also removing any bias in the predicted asymmetry. The scatter in the fit is dominated entirely by low S/N galaxies. 91

Figure 3.7 Left: The mean difference between the intrinsic and observed asymmetry for increasing signal-to-noise bins. The red line represents performing no correction for the sky asymmetry, the purple line represents correcting by $A_{\rm noise}$, the green line for correcting by $A_{\rm noise}/1.2$, and the orange line for applying the fit correction from Equation 3.8. The width of each line is the standard error on the mean. Right: The standard deviation of the difference in asymmetry for the four asymmetry correction methods. All methods that perform some kind of correction for noise contribution to asymmetry result in lower standard deviations than doing no noise subtraction. One should note that the standard deviation of the difference for the LM Fit method is comparable to the two noise subtraction methods except at low signal to noise. Here the scatter of the LM Fit method is slightly larger, although still relatively small and a significant improvement from doing no noise correction. 93

Figure 3.8 A demonstration of how degrading resolution changes the asymmetry (left) and the concentration (right) compared to their intrinsic values (where resolution is functionally infinite). Degrading the resolution systematically decreases both asymmetry and concentration, and the magnitude of this difference increases inversely with the value of resolution. Note that the points with the lowest resolution are furthest from the black dashed line representing $A_{\rm Res}$=$A_{\rm int}$. Given the bias in the asymmetry/concentration measurement is clearly dependent on the intrinsic asymmetry/concentration and resolution value, just as with S/N the resolution effects can be corrected for to recover the intrinsic index. 95

Figure 3.9 Density contours of the asymmetry predicted by Equation 3.11, plotted against the intrinsic asymmetry, with the red dashed line representing where the two would be equal. Note the median difference between these two values, even for the smallest asymmetries measurements, is only a few percent of the measured value. Thus the intrinsic asymmetry is recovered (within reason) for the majority of the galaxies in the sample. 97

Figure 3.10A demonstration of how applying a PSF (and thus degrading the resolution) changes two of the asymmetry approximation methods from Figure 3.7. Left panel: How resolution changes the difference in asymmetry when no correction for the noise asymmetry is performed. The curve from Figure 3.7 is replicated here, labelled "No PSF". The other three curves represent the relationship between $A_{\rm int} - A_{\rm corr}$ for different resolution bins. Applying a PSF to $A_{\rm obs}$ always shifts the curve up, since $A_{\rm obs}$ will systematically increase. This shift upward is greater for smaller resolutions. Right panel: The same investigation, but for the $A_{\rm noise}/1.2$ subtraction method. The curve from Figure 3.7 is replicated here, labelled "No PSF", where as the other three curves are separated into resolution bins. The same systemic shift upward is seen as in both methods. Not only that, but beyond $S/N = 200$ the change in asymmetry is almost entirely due to worsened resolution. The fact that both no noise subtraction and subtracting $A_{\rm noise}/1.2$ have similar changes from resolution beyond $S/N > 200$ implies that above that S/N, asymmetry only needs to be corrected for resolution effects. 99

Figure 3.11Density contours of the asymmetry predicted by Equation 3.12 to correct for resolution and noise, plotted against the intrinsic asymmetry. The red dashed line represents where the two values would be equal to each other. The median difference is only a small fraction of the intrinsic asymmetry, although it is larger than the corrections for noise (Figure 3.6) or resolution (Figure 3.9) alone. Correcting for noise and resolution simultaneously is inherently more difficult because both artefacts change asymmetry in opposite directions, making it difficult to distinguish which fraction of the change in asymmetry stems from noise or resolution. Most of the galaxies that constitute the outer contours have both a small signal-to-noise and resolution, demonstrating a weakness of the combined fit correction for the worst quality asymmetries. However, a median offset of 0.0098 is still good enough quality to make decent asymmetry measurements for the majority of the sample. 101

Figure 3.12 The difference between intrinsic asymmetry and the asymmetry measured for four different noise correction methods with no resolution effects (the same as in Figure 3.7), with resolution effects, and after resolution correction. Given noise and resolution affect asymmetry in ways that can cancel out, it is difficult to disentangle the two observational effects. Thus the resolution corrected curve approximates the curve with no PSF, but not exactly (particularly at low S/N). The LM Fit method reproduces the intrinsic asymmetry at low S/N most accurately from the four methods. 102

Figure 3.13 The mean fractional difference between intrinsic and observed concentration as a function of resolution for different S/N bins. The three curves overlap each other, indicating that a single resolution correction can be applied to concentrations of varying S/N. This logically follows the results from Figure 3.2, which demonstrated that noise has a negligible effect on the concentration measurement. 103

Figure 3.14 Density contours for the concentration predicted by Equation 3.14 versus the intrinsic concentration, with the red dashed line representing $C_{\rm predict}$=$C_{\rm int}$ The small scatter about the line of equity demonstrates how effective the resolution correction is for this simulation. The median difference in concentration is less than 1% of the average measured concentration. 105

Figure 3.15 *Top row:* Density contours of the intrinsic morphologies compared to values predicted by the fits presented in this work for a set of previously unseen TNG galaxies, with the dashed green line representing where the predicted values equal the intrinsic values. The first panel shows the asymmetry predicted after noise correction, the 2nd shows asymmetry predicted after resolution correction, the 3rd shows asymmetry corrected for both resolution and noise, and the fourth shows concentration predicted after resolution correction (no noise correction for concentration is necessary). *Bottom row:* Density contours of the intrinsic morphologies compared to values predicted by the fits presented in this work for a set of Illustris Galaxies, with the dashed green line representing where the predicted values equal the intrinsic values. The order of whether noise, resolution, or a combination of both is corrected for is the same as in the top row. For the combined noise and resolution correction (third column) galaxies with asymmetries predicted to be greater than 1 (far beyond the scope of $A_{\rm int}$) are removed from the analysis (20 in the unseen TNG and 4 in Illustris). For both data sets there is no clear bias in the predicted values, and the scatter on the predicted values reflects that seen in the training data (see Figures 3.6, 3.9, 3.11 and 3.14). For comparison the initial median offset for noise correction of asymmetry is -0.001, for resolution correction of asymmetry is -0.0032, for resolution and noise corrected asymmetry is -0.0098, and for resolution correction of concentration is -0.033. The combined noise and resolution correction does have a broader distribution than the other corrections, where galaxies with both a small S/N and Res value result in poorer asymmetry predictions. But the same effect is seen in the original TNG sample (see Figure 3.11). The replicability of the difference between the intrinsic and predicted indices with both Illustris and TNG implies that the corrections are viable for different galaxy samples. 107

Figure 3.16Distributions of intrinsic asymmetry (left), intrinsic concentration (middle) and stellar half mass radius (right) for the 1000 galaxies selected from TNG (yellow) and Illustris (pink) galaxies. Note that Illustris galaxies are on average larger and more highly concentrated, but have similar asymmetries as those in TNG. TNG has more accurate sizes for low mass galaxies (reflected in the smaller median R_{half} in TNG compared to Illustris), which likely leads to lower concentration values than were observed in Illustris. 108

Figure 3.17The mean difference between the intrinsic and corrected asymmetry as a function of signal-to-noise for subtracting A_{noise} (top left), subtracting $A_{noise}/1.2$ (top right), predicting asymmetry from Equation 3.8 (bottom left), and doing no noise correction (bottom right) for both the TNG (the dark curve) and Illustris (the light curve) galaxy sets. All four correction methods match between the galaxy samples, implying that the relationship between the quality of correction and S/N is the same no matter which simulation is examined. 110

Figure 3.18The asymmetry of interacting galaxies in TNG as a function of their 3D separation from the nearest companion (r_{3D}). The intrinsic asymmetry measurement (navy, identical in all panels), the observed asymmetry measurement (red), the observed asymmetry corrected for A_{noise} (pink), the observed asymmetry corrected for $A_{noise}/1.2$ (green), and the asymmetry predicted by Equation 3.8 (yellow) are all included. The four panels represent four different signal-to-noise ranges applied to the same set of TNG galaxies, demonstrating how the trend between asymmetry and r_{3D} is obscured in observed asymmetry as signal-to-noise decreases. Ideally all curves would match the navy curve, but as the S/N regime decreases the different asymmetry measurements struggle to capture the true underlying trend between A_{int} and r_{3D}. 116

Figure 4.1 Position of the post-merger (orange circles) and pair (triangles) galaxies on the global star-forming main sequence defined by the rest of the MaNGA survey (grey hexbin). Pair galaxies are colour-coded by the projected separation from their closest companion (in kpc). Galaxies that were excluded due to a lack of viable CO spaxels are excluded from this diagram (see Table 4.2 and Section 4.2.2 for details). An inset histogram shows the distribution in ΔSFR for post-mergers (orange) and pair (blue) galaxies with respect to MaNGA (grey). Although this merger sample probes more highly star-forming galaxies than a random population, it still covers a broad range of ΔSFR values. 125

Figure 4.2 Data product maps for three of the galaxies in the ALMaQUEST merger sample (see Appendix A.2 for the remaining 28 galaxies in the sample), a post-merger (top), a visual pair (middle), and a spectroscopic pair with the companion out of frame (bottom). From left to right: the SDSS *gri*-image, inclination corrected stellar mass surface density (from PIPE3D), inclination corrected molecular gas surface density (computed from CO luminosity), inclination corrected star formation rate surface density (computed from Hα luminosity), inclination corrected star formation rate surface density (computed from Hα luminosity and sSFR-D4000 relation), molecular gas fraction ($\Sigma_{H_2}/\Sigma_\star$), and star formation efficiency ($\Sigma_{SFR}/\Sigma_{H_2}$). Note the significant increase in spaxel count when both Hα and D4000 Σ_{SFR} are used. The central gap still present in the combined Σ_{SFR} map for 8241-12705 (second row, fifth column) is the result of D4000 exceeding 1.4 in those spaxels. Including D4000-Σ_{SFR} measurements optimizes the overlap between Σ_{H_2} and Σ_{SFR} for this analysis. 130

Figure 4.3 The sSFR-D4000 distribution for all star-forming spaxels in MaNGA (shown as a density hexbin). The median sSFR value in each D4000 bin is shown as red line out to D4000=1.45; this value is used to approximate $\Sigma_{\rm SFR}$ based on D4000 for spaxels that do not meet are star-forming criteria. The standard deviation of sSFR within each bin is shown as a red dashed line. The median sSFR value steeply changes at high D4000, leading to vary different sSFR values in relatively close D4000 bins. I therefore only use the D4000-sSFR calibration when D4000<1.4 (vertical dashed line). 132

Figure 4.4 Resolved scaling relations for non-interacting ALMaQUEST galaxies (grey histogram), pairs (blue contours), and post-mergers (orange contours). The rSFMS is shown on the left, the rKS is shown in the middle, and the rMGMS is show on the right. All measurements required a CO $S/N > 3$, along with the quality criteria to measure $\Sigma_{\rm SFR}$ with either Hα or D4000 methods as described in Subsection 4.2.3.1. These cuts result in 22782 isolated spaxels, 7990 pair spaxels, and 4012 post-merger spaxels. Below each histogram distributions of $\Sigma_{\rm SFR}$, $\Sigma_{\rm H_2}$, and $\Sigma_\star$are included, separated into non-interacting, post-merger, and pair populations. The median value of each distribution is shown as a horizontal dashed line. Note that the non-interacting ALMaQUEST sample is biased towards higher $\Sigma_{\rm SFR}$ values resulting from the population of starbursts in the original ALMaQUEST sample (see Subsection 4.3.1 for clarification on how this differs from offset parameter controls). A KS-test reveals that all three populations are distinct from each other in $\Sigma_{\rm SFR}$, $\Sigma_{\rm H_2}$, and $\Sigma_\star$. The pair sample has a small offset to lower $\Sigma_{\rm SFR}$, $\Sigma_{\rm H_2}$, and $\Sigma_\star$, which is driven by two pair galaxies with uniquely low $\Sigma_\star$ and $\Sigma_{\rm H_2}$ values (8078-6104 and 8083-12703). Overall, all three populations cover a similar range of surface densities. 135

Figure 4.5 Resolved star-forming main sequence for all merger galaxies, with the MaNGA plate-ifu of the galaxy in the left corner and r_p (kpc) in the right corner (left blank for post-mergers). Star-forming spaxels are colour-coded by radius, and spaxels with $\Sigma_{\rm SFR}$ determined by D4000 are yellow (low Hα S/N) or brown (AGN contamination). The non-interacting galaxies in ALMaQUEST are shown as a grey histogram, for reference (including both Hα-$\Sigma_{\rm SFR}$ and D4000-$\Sigma_{\rm SFR}$). Note that there is a diversity of star formation behaviour in the merger sample. Some post-mergers and pairs are significantly offset from the rest of ALMaQUEST. Those that exhibit suppressed star formation (such as 8241-12705, 7975-6104, and 8078-6104) can be derived from both Hα- and D4000- $\Sigma_{\rm SFR}$ values, confirming the validity of the combined $\Sigma_{\rm SFR}$ method. 136

Figure 4.6 Resolved Kennicutt-Schmidt relation for all merger galaxies, with the MaNGA plate-ifu of the galaxy in the left corner and r_p (kpc) in the right corner (left blank for post-mergers). Star-forming spaxels are red and colour-coded by radius, and spaxels with $\Sigma_{\rm SFR}$ determined by D4000 are yellow (low Hα S/N) or brown (AGN contamination). The non-interacting galaxies in ALMaQUEST are shown as a grey histogram, for reference, (including both Hα-$\Sigma_{\rm SFR}$ and D4000-$\Sigma_{\rm SFR}$). Examining mergers on an individual basis reveals many mergers that are offset, both above and below, the non-interacting rKS. 138

Figure 4.7 Resolved molecular gas main sequence for all merger galaxies, with the MaNGA plate-ifu of the galaxy in the left corner and r_p (kpc) in the right corner (left blank for post-mergers). Star-forming spaxels are colour-coded purple by radius, and spaxels with $\Sigma_{\rm SFR}$ determined by D4000 are yellow (low Hα S/N) or brown (AGN contamination). The non-interacting galaxies in ALMaQUEST are shown as a grey histogram, for reference. Many merging galaxies have tails at the high mass end of the molecular gas main sequence, at times for AGN spaxels as well (supporting a paradigm where mergers fuel AGN). 139

Figure 4.8 Maps of the offset parameters for an example post-merger galaxy. 1st column: the SDSS *gri*-image of the galaxy, for reference. 2nd column: $\Delta\Sigma_{\rm SFR}$ distribution, with blue representing an enhancement in star formation. 3rd column: ΔSFE distribution, with blue representing enhanced star formation efficiency. 4th column: $\Delta f_{\rm H_2}$ distribution, with blue representing enhanced gas fraction in a spaxel. The correlation between a uniform enhancement in $\Sigma_{\rm SFR}$ and SFE, along with the patchy deficits of molecular gas, imply that the star formation in this galaxy is driven by an enhanced efficiency at which gas is converted to stars. 142

Figure 4.9 ΔSFE versus $\Delta f_{\rm H_2}$ for all spaxels that have $\Delta\Sigma_{\rm SFR}>0$, separated into spaxels which belong to isolated galaxies (left), pair galaxies (middle), and post-merger galaxies (right). Spaxels are colour-coded by $\Delta\Sigma_{\rm SFR}$. The line of equality is shown to delineate the efficiency-driven regime (where $\Delta{\rm SFE}>\Delta f_{\rm H_2}$) and the fuel-driven regime (where $\Delta{\rm SFE}<\Delta f_{\rm H_2}$). The percentage of isolated/pair/post-merger spaxels in each regime is overplotted on the figure, with the uncertainty in the percentage being propagated error of the number of spaxels above/below the line divided by the total number of spaxels. Based on these percentages there is a slight bias towards efficiency-driven star formation in post-mergers and pairs (though more so in the former), but other than that the amount of efficiency and fuelled spaxels with enhanced star formation is relatively even. 143

Figure 4.10 ΔSFE versus $\Delta f_{\rm H_2}$ for all spaxels with $\Delta\Sigma_{\rm SFR}>0$ in an example post-merger galaxy (MaNGA plate-ifu = 8156-3701). In this galaxy almost all spaxels are in the efficiency-driven regime, as might be expected from examining the distribution of offset parameters in Figure 4.8. 144

Figure 4.11 ΔSFE versus Δf_{H_2} for all spaxels with $\Delta\Sigma_{SFR}>0$ in each galaxy merger with more than 20 spaxels with $\Delta\Sigma_{SFR}>0$, the plate-ifu number of each galaxy is provided in the left corner of every plot. Spaxels are colour-coded by $\Delta\Sigma_{SFR}$. The percentage of spaxels above and below the line of equality are provided as well, which help discern whether the star formation in a galaxy is predominantly driven by enhanced SFE or enhanced f_{H_2}. Galaxies that are predominantly efficiency-driven (< 40% below the line) and fuel-driven (> 60% above the line) are labelled for reference. For some galaxies there is clearly a dominant mechanism driving star formation, but many galaxies have contributions from both efficiency and fuel-driven SFR enhancements. 146

Figure 4.12 Distributions of the fraction of fuel-driven spaxels for the merger sample (grey), along with the pair (blue) and post-merger (orange) sub-samples. The median of each distribution is shown with a vertical dashed line: 0.51 for the entire merger sample, 0.44 for pairs, and 0.52 for post-mergers. The median value of each sub-smaple being so similar, and so close to 0.5, confirms that there are an equal number of fuel- and efficiency-driven mergers. 148

Figure 4.13 Fraction of fuel-driven spaxels as a function of projected separation in kpc, with post-mergers in the grey region (since projected separation cannot be measured without a companion). All points are colour-coded by the galaxy's global offset from the star-forming main sequence, ΔSFR (bluer points have globally enhanced SFR, red points have globally suppressed SFR, compared with the global SFMS). Note that galaxies with negative ΔSFR can still have regions of enhanced star formation, which is used to compute a fuel fraction. Pairs that have tidal arms connecting the two galaxies are highlighted with orange. Neither projected separation, nor this secondary morphology characteristic, show any trend with the fraction of fuel-driven spaxels. . . 150

Figure 4.14Radial profiles of the median $\Delta\Sigma_{\rm SFR}$ in bins of effective radius for post-merger and pair galaxies included in my analyses, separated into groups of "Efficiency-Driven", "Both", and "Fuel-Driven" based on the fuel fraction value (the second column of Table 4.3). Each profile is also colour-coded by the fuel fraction. Radial profiles are plotted as a function of the effective radius, with the solid line representing the median in a bin of 0.1 R_e, and the faded width of the line representing the error on the mean. Efficiency-driven mergers tend to have the strongest and most extended enhancements in star formation, whereas fuel-driven mergers are more likely to have centrally concentrated bursts of star formation, likely due to an inflow of gas. 152

Figure 4.15*1st column: gri*-image of the merger galaxy. *2nd column:* ΔSFE versus $\Delta f_{\rm H_2}$ for all spaxels where $\Delta\Sigma_{\rm SFR}>0$, colour-coded by ΔSFE$-\Delta f_{\rm H_2}$. *3rd column:* spatially resolved map of ΔSFE$-\Delta f_{\rm H_2}$for spaxels where all three offset parameters are positive. The colour bars change slightly for each merger, which have different spans of ΔSFE$-\Delta f_{\rm H_2}$, but zero is always white. Note that ΔSFE-$\Delta f_{\rm H_2}$ scales with distance from the line of equality shown in the 2nd column. Within each galaxy there is distinct variability in the importance of ΔSFE and $\Delta f_{\rm H_2}$, particularly between the centre and outskirts of the galaxy. 155

Figure 4.16A replication of Figure 4.11, but now with a grey line indicating the 0.248 dex error on both offset parameters from using a constant $\alpha_{\rm CO}$. Spaxels within this grey region are not considered when calculating the fraction of fuel-driven spaxels. This biases the distribution of fuel fractions to the extreme ends (very high or very low), as spaxels further away from the line become more important in the calculation. 157

Figure 4.17The fuel fraction determined from Figure 4.16, considering uncertainties from not using $\alpha_{\mathrm{CO,\,met}}$, plot against the original fuel fraction determined from Figure 4.11. Note that efficiency-driven mergers move below the line of equality (black dashed line), and fuel-driven mergers move above the line; thus the dominant star-forming mechanism only appears more dominant when uncertainties in α_{CO} are considered. I have highlighted regions that indicate the dominant mechanism has not changed (ideally where all points would lie): where both fractions imply star formation is efficiency-driven (red), where both fractions imply star formation is fuel-driven (blue), and where both fractions imply star formation is driven by both (grey). Only two mergers change category (from "both" to "fuel-driven"), and both galaxies were already at the border between these two categories. 159

Figure 4.18sSFR versus D4000 for all star-forming spaxels in MaNGA. Density contours of this distribution are shown in grey, over a hexbin distribution colour-coded by the median $\Delta\Sigma_{\mathrm{SFR}}$ value in each bin. The median sSFR value in a D4000 bin is shown in red: these points are used to approximate Σ_{SFR} for spaxels that do not meet my star-forming criteria. Spaxels with D4000>1.4 are excluded, given the asymptotic nature of the sSFR-D4000 at high D4000. Note that there is significant scatter in this relation, which correlates with $\Delta\Sigma_{\mathrm{SFR}}$. 160

Figure 4.19 The fuel fraction determined from only Hα spaxels compared to the fuel fraction when both Hα and D4000 spaxels are included. Ideally all galaxies would lie on the line of equality, implying that the inclusion of D4000 spaxels does not drastically change my results. But realistically there is scatter about the line of equality as more spaxels are included in the analysis. Difference between the two fuel fractions is alright, so long as it does not change which mechanism predominantly drives star formation. I have highlighted regions that ideally the points should lie within: where both fractions imply star formation is efficiency-driven (red), where both fractions imply star formation is fuel-driven (blue), and where both fractions imply star formation is driven by both (grey). Only one point lies outside these acceptable regions: 8616-9101, which is efficiency-driven when both Hα and D4000 spaxels are included, but fuel-driven when only Hα spaxels are considered. 162

Figure 5.1 Molecular gas surface density versus stellar mass surface density for star-forming(blue) and AGN(red) pixels in a post-merger and a non-interacting galaxy taken from the archival data of ALMaQUEST. The resolved molecular gas main sequence for isolated ALMaQUEST galaxies is shown in grey. The non-interacting galaxy has suppressed gas fractions in the AGN pixels, as has been seen with other resolved molecular gas studies. However, in the post-merger, the gas fractions in AGN pixels range from regular to enhanced. This implies the relationship between an AGN and nuclear molecular gas is different in this post-merger than would be expected from a non-interacting system. 173

Figure A.1 206
Figure A.2 207
Figure A.3 208
Figure A.4 209
Figure A.5 210
Figure A.6 211
Figure A.7 212

Figure A.8 213
Figure A.9 214
Figure A.10 215
Figure A.11 216
Figure A.12 217
Figure A.13 218
Figure A.14 219
Figure A.15 220
Figure A.16 221
Figure A.17 222
Figure A.18 223
Figure A.19 224
Figure A.20 225
Figure A.21 226
Figure A.22 228
Figure A.23 229
Figure A.24 230
Figure A.25 231
Figure A.26 232

Figure A.27*Left:* Comparison of $\Delta\Sigma_{\rm SFR}$ determined from a control that only contains Hα-$\Sigma_{\rm SFR}$ (x-axis) to $\Delta\Sigma_{\rm SFR}$ determined from a control with both Hα-$\Sigma_{\rm SFR}$ and D4000-$\Sigma_{\rm SFR}$ (y-axis). Data are shown as a density hexbin, with a scatter plot in the background as grey dots representing individual spaxels. The black dashed line represents where the new and old $\Delta\Sigma_{\rm SFR}$ are equal, demonstrating how closely the two values follow each other. *Middle:* The difference in $\Delta\Sigma_{\rm SFR}$ (Hα control spaxels only minus Hα and D4000 controls) plot against the original $\Delta\Sigma_{\rm SFR}$ measurement. Again, data are shown as a density hexbin with a grey scatter plot representing individual spaxels in the background There is a small bias for the new $\Delta\Sigma_{\rm SFR}$ value to be larger (difference is positive). *Right:* A histogram showing the range of change possible in $\Delta\Sigma_{\rm SFR}$. The median change is very small, shown as a dashed line at 0.03 dex. $\Delta\Sigma_{\rm SFR}$ computed from a Hα and D4000 controls are usually higher because the D4000-$\Sigma_{\rm SFR}$ values bring down the average $\Sigma_{\rm SFR}$ of the control. 234

Figure A.28 *Left:* Comparing the original fuel fraction (x-axis) to the fuel fraction with $\Delta\Sigma_{\rm SFR}$ values using the new control (y-axis). Ideally the two fuel fractions would be equal, and thus lay on the dashed line. I have highlighted regions that indicate the dominant mechanism has not changed based on the criteria described in Chapter 4: where both fractions imply star formation is efficiency-driven (red), where both fractions imply star formation is fuel-driven (blue), and where both fractions imply star formation is driven by both (grey). Only 5 mergers change whether their dominant star-forming mechanisms, and these were already border cases (at the boundary for fuel-driven star formation). *Right:* The difference in fuel fraction (new - old) as a function of the number of spaxels used to determine fuel fraction. The galaxies with the most drastic change in fuel fraction are also those with the least spaxels, where only a handful of spaxels changing their $\Delta\Sigma_{\rm SFR}$ have a major impact on the final fuel fraction computed. There is also a small bias towards smaller fuel fractions, which is intuitive given when D4000-$\Sigma_{\rm SFR}$ are considered the average control $\Sigma_{\rm SFR}$ goes down, meaning both $\Delta\Sigma_{\rm SFR}$ and ΔSFE will be larger. 235

Figure A.29 A replication of Figure 4.11, where $\Delta\Sigma_{\rm SFR}$ and ΔSFE are based on a control which contains D4000-$\Sigma_{\rm SFR}$. Every panel shows ΔSFE versus $\Delta f_{\rm H_2}$ for all spaxels with $\Delta\Sigma_{\rm SFR}>0$ in each galaxy merger with more than 20 spaxels with $\Delta\Sigma_{\rm SFR}>0$, the plate-ifu number of each galaxy is provided in the left corner of every plot. Spaxels are colour-coded by $\Delta\Sigma_{\rm SFR}$. The percentage of spaxels above and below the line of equality are provided as well, which help discern whether the star formation in a galaxy is predominantly driven by enhanced SFE or enhanced $f_{\rm H_2}$. Galaxies that are predominantly efficiency-driven ($< 40\%$ below the line) and fuel-driven ($> 60\%$ above the line) are labelled for reference. . . 236

Figure A.30 239

Figure A.31 240

Figure A.32 241

Figure A.33 242

List of Abbreviations

A: Asymmetry
ALMA: Atacama Large Millimetre Array
ALMaQUEsT: ALMA MaNGA Quenching and Star formation Survey
BPT: Baldwin, Phillips & Telervich diagram, usually referring to subsequent classifications of star formation
C: Concentration
CALIFA: Calar Alto Legacy Integral Field Area (often also used to refer to the CALIFA survey)
CO: ^{12}CO $J = 1 \rightarrow 0$ molecular emission line, rest frame 115 GHz
$\mathbf{f_{H_2}}$: Molecular gas fraction ($M_{H_2}/M_\star$ or $\Sigma_{H_2}/\Sigma_\star$)
FMR: Fundamental Metallicity Relation (rFMR for the resolved relation)
FWHM: Full Width Half Maximum
IFS: Integral Field Spectroscopy
IFU: Integral Field Unit
kpc: Kiloparsecs
KS: Kennicutt-Schmidt relation (rKS for the resolved relation)
$\mathbf{M_{H_2}}$: Total molecular gas mass
$\mathbf{M_\star}$: Total stellar mass
$\mathbf{M_\odot}$: Solar mass
MAD: Median Absolute Deviation
MaNGA: Mapping Nearby Galaxies at Apache Point Observatory (often also used to refer to the MaNGA survey)
MGMS: Molecular Gas Main Sequence (rMGMS for the resolved relation)
MZR: Mass metallicity relation (rMZR for the resolved relation)
NSA: NASA Sloan Atlas
PSF: Point Spread Function
$\mathbf{r_p}$: Projected separation, between galaxy pairs specifically
$\mathbf{R_{half}}$: Stellar half mass radius
$\mathbf{R_e}$: Effective radius
Res: Apparent galaxy size with respect to PSF, defined as the stellar half mass radius over the PSF FWHM (both in arcseconds)
SAMI: Sydney-Australian Astronomical-Observatory Multi-object Integral Field Spectrograph (often also used to refer to the SAMI galaxy survey)

SDSS: Sloan Digital Sky Survey
SFE: Star Formation Efficiency
SFMS: Star-Forming Main Sequence (rSFMS for the resolved relation)
SFR: Total Star Formation Rate
S/N: Signal-to-noise ratio
z: Redshift
$\mathbf{\Delta f_{H_2}}$: Offset from the rMGMS
$\mathbf{\Delta}$O/H : Offset from the rMZR
$\mathbf{\Delta\Sigma}_{\rm SFR}$: Offset from the rSFMS
$\mathbf{\Delta}$SFE : Offset from the rKS
$\mathbf{\Delta}$v : Change in line-of-sight velocity between galaxy pairs
μ : Mass ratio between two galaxies (target mass / companion mass)
$\mathbf{\Sigma}_{\rm H_2}$: Molecular gas mass surface density
$\mathbf{\Sigma}_{\rm SFR}$: Star formation rate surface density
$\mathbf{\Sigma}_{\star}$: Stellar mass surface density

Author Contribution Statement

Chapter 2: Mallory Thorp designed and performed the analysis, along with creating a data structure to house various computed properties. Sara Ellison conceived various analysis tools, as is cited in the text, and provided guidance throughout the project. Jillian Scudder calculated dust-corrected emission flux and metallicity calibrations for MaNGA datacubes used in this work.

Chapter 3: Mallory Thorp conceived the analysis, collected the data, performed the analysis and wrote the eventual publication of this work in the *Monthly Notices of the Royal Astronomical Society*. Asa Bluck, Sara Ellison, and Roberto Maiolino provided insight and suggestions into that analysis from its conception to its completion, with the former committing the most time and the latter the least. Christopher Conselice provided important feedback in the late stages of this project. Maan Hani and Connor Bottrell provided support collecting and managing Illustris-TNG data. All listed authors reviewed the final results and provided editorial feedback on the published manuscript.

Chapter 4: The ALMaQUEST - Mergers sample was devised and collected by Hsi-An Pan, Lihwai Lin, Sara Ellison, and Mallory Thorp. Pan served as Principal Investigator (P.I.) on the Cycle 7 ALMA program targeting merging galaxies with Lin, Ellison, Thorp, and Jillian Scudder serving as Co-P.I.s (Bau-Ching Hsieh, Fangting Yuan, Ting Xiao, and Jorge Barrera-Ballesteros were also Co-P.I., but added no other contribution to the work in this thesis). ALMA data were reduced by Lin, Pan and Thorp. Dust corrected emission line fluxes and metallicity calibrators for the MaNGA data were computed by Scudder. Asa Bluck provided fits for the sSFR-D4000 relation in MaNGA, along with suggestions for testing the validity of this approximation. Thorp computed further dataproducts, and created a structured database combining ALMA and MaNGA data. Thorp designed and performed the analysis, with regular input from Ellison and David Patton. Thorp provided major interpretations of the results, with input from Ellison, Patton, Lin, and Pan. Dan Walters provided key insights on the analysis methods employed in Section 4.3.2. All listed authors reviewed the final results and provided editorial feedback on a manuscript eventually published in the *Monothly Notices of the Royal Astronomical Society*.

Acknowledgements

This thesis was conducted primarily at the University of Victoria, which stands on the traditional territory of the Lekwungen peoples. I would like to acknowledge with respect the Songhees, Esquimalt, and W̱SÁNEĆ peoples who were the first astronomers of this land and whose continued stewardship is crucial to its preservation.

I owe thanks to many mentors, collaborators, peers and friends who aided me on my PhD journey. First and foremost, I am immeasurably grateful for the guidance and support of my advisor **Sara Ellison**, without whom I would not be the scientist I am today. Furthermore, I am blessed to be part of a kind and inclusive academic family, whose discussion on this work bettered it at every step, in particular: **David Patton**, **Jillian Scudder**, **Joanna Woo**, **Salvatore Quai**, **Maan Hani**, **Connor Bottrell**, **Dan Walters**, **Scott Wilkinson**, and **Shoshannah Byrne-Mamahit**.

I would like to thank **Asa Bluck** and **Roberto Maiolino** who co-supervised a third of this work and helped steer me through a rather treacherous project, along with Roberto's group at the Kavli Institute for Cosmology in Cambridge who welcomed me with open arms.

My research would not be possible without the brilliant researchers of the ALMaQUEST collaboration, in particular **Lihwai Lin** and **Hsi-An Pan** who introduced me to ALMA and patiently taught me the ways of CASA.

I am indebted to **Ruth Digby**, **Ariane Trudeau**, and **Anne Hung**, who reminded me that writing well is much easier with a little help. And to my friends who kept me sane during the combined deluge of a global pandemic and a PhD dissertation: **Nic Loewen**, **Bobby Bickley**, **Asya Borukhovetskaya**, **Rory Coles**, and **Locke Patton**.

I also wish to thank the teachers who inspired me to follow this path in the first place: **Don Crider** and **Ana Larson**, know that your smallest actions made the biggest difference.

Finally, I must acknowledge **Marcus Vipsanius Agrippa (Grippy)**, who attended every zoom call with me and only typed in the chat once, and who has kept me smiling even to my final day of writing.

It's merging time!

Dedication

For my mother, who bought me my first telescope when I was only obsessed with star stories. And for Dad, Oscar, and Emma, who stood out in the cold with me.

Chapter 1

Introduction

If you can stay up until midnight on a crisp, October night, you can see the Andromeda galaxy directly overhead. You will have little luck spotting it from Victoria, with bright city lights washing out the finer features of the sky, so bring a set of binoculars. Better seen from one's peripherals than straight on, Andromeda looks more like a faint grey smudge on the eyepiece than anything as jaw dropping as our Milky Way. Up until the 20th century, most astronomers considered Andromeda and similar celestial objects to be unresolved nebulae. It was German philosopher Immanuel Kant, writing far ahead of his time in the 16th century, that pointed to the diffuseness of Andromeda as evidence that it may be composed of many stars. That Andromeda is an "island universe", much like our Milky Way, and that both are one of many islands in the vast sea of space.

As astronomical measurements improved, higher resolution images revealed these "nebulae" to be far more similar to the Milky Way than any planetary nebula, and more accurate astronomical distances confirmed they were extragalactic in origin. Hence Andromeda and like objects have been more aptly labelled "galaxies", from the Greek word for the Milky Way: $\gamma\alpha\lambda\alpha\xi\iota\alpha\iota$. At their most basic, galaxies are massive structures composed of gas, stars, and dark matter. But the growing detail of galaxy observations has only uncovered more complexities and multiplicities. Images from the most modern telescopes reveal a plethora of galaxies in varying sizes, shapes, and colours. The primary objective of extragalactic astronomy is to understand how different galaxy populations came to be, and how they relate to each other.

Edwin Hubble, who confirmed Andromeda's extragalactic nature, established many crucial ontological frameworks still essential to galactic studies. Hubble suggested that most galaxies can be sorted into one of two categories: disk-like spirals, and bulge-dominated ellipticals (Hubble, 1926). This dichotomy can be further di-

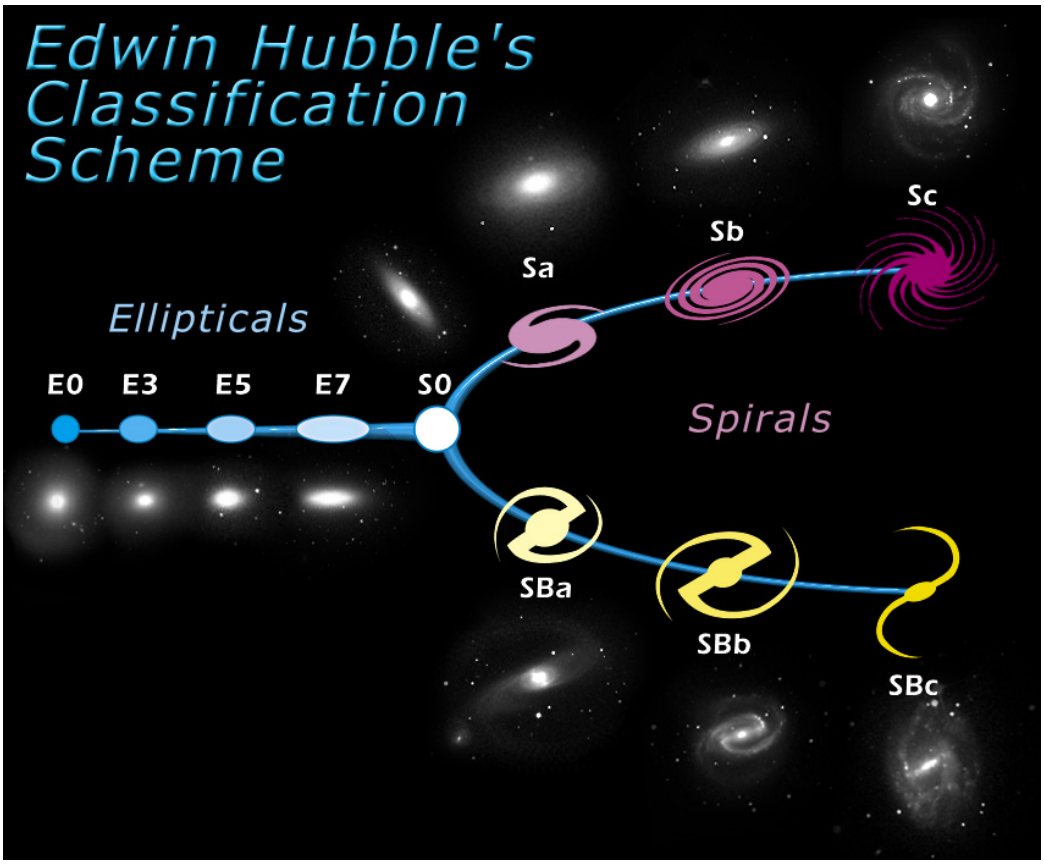

Figure 1.1: Hubble's classification scheme, summarized with both cartoons depicting basic galaxy structure and examples of real galaxy images. Es denote elliptical galaxies, with higher numbers corresponding to degree of elongation. Spiral galaxies are denoted with S, with S0 representing a disk galaxy with no spiral arm structure (lenticulars). Spirals are further separated into those with and without a bar (B), with additional subclasses (a,b,c) denoting the tightness of the spiral arms. Image Credit: NASA & ESA.

vided into sub-categories, differentiating ellipticals by the degree of elongation and spirals by the presence of stellar arms or a bar. Figure 1.1 provides visual aid for this classification scheme. Later editions were made to account for disks without spiral arms (lenticulars, Hubble 1936), inner/outer ring structures (De Vaucouleurs, 1959), and more subcategories for spiral arms (Elmegreen & Elmegreen, 1982). Although several updates to the Hubble Sequence of galaxies have been adopted to account for our growing observational knowledge (Elmegreen et al., 1992; van den Bergh, 1998; Kormendy & Bender, 2011), Hubble's initial taxonomy still shapes how we think about galaxies beyond our own.

1.1 Galaxy types and evolution

Though the initial Hubble galaxy types are distinguished solely on visual characteristics, there are further quantitative properties that have been utilized to better characterize these classes. For example, the Sérsic index quantifies galaxy structure by measuring the shape of the light intensity from a galaxy as a function of radius, quantifying the "bulginess" of that galaxy (Sérsic, 1963). A Sérsic profile can describe the surface brightness of a galaxy (I), the log of which falls off exponentially with distance from the galaxy's centre, or

$$\ln(I(R)) \propto R^{1/n} \tag{1.1}$$

where R is distance from the galaxy's centre and n is the Sérsic index. A Sérsic index of 1 describes an exponential disk of light, whereas a Sérsic index of 4 indicates a more bulge-like profile (a de Vaucouleurs profile, de Vaucouleurs 1948). Morphology measurements are then often combined with observations of galaxy colour to fully characterize the Hubble Sequence.

A galaxy's colour provides key insights to its nature, in particular that of the underlying stellar population. Blue (high frequency) light in a galaxy primarily comes from young, massive or metal-poor stars, whereas old, low-mass, or metal-rich stars are much cooler than their younger counterparts and emit red (low frequency) light. When comparing the colours of different galaxy types, spirals tend to be bluer in colour than elliptical galaxies (Bower et al., 1992; Bell et al., 2004; Schawinski et al., 2014). Thus galaxies can be conceptualized as existing in three populations: the red sequence (dominated by ellipticals), the blue cloud (dominated by spirals), and the green valley (representing an intermediate region with contributions from both galaxy types) (Strateva et al., 2001; Bower et al., 1992; Bell et al., 2004; Driver et al., 2006; Schawinski et al., 2014). Figure 1.2 shows a colour-mass diagram for galaxies from the Sloan Digital Sky Survey, revealing that old/red stellar populations dominate elliptical galaxies.

Initially Hubble proposed a framework where galaxies became more complex over time, with ellipticals being "early-type" galaxies and spirals being "late-type" galaxies. But this evolutionary theory does not coincide with evidence of older stellar populations in ellipticals compared to spirals. Ellipticals also have significantly less angular momentum than spirals (Bertola & Capaccioli, 1975; Illingworth, 1977; Chiosi & Carraro, 2002), existing in dense but dynamically relaxed cluster environments (Oemler,

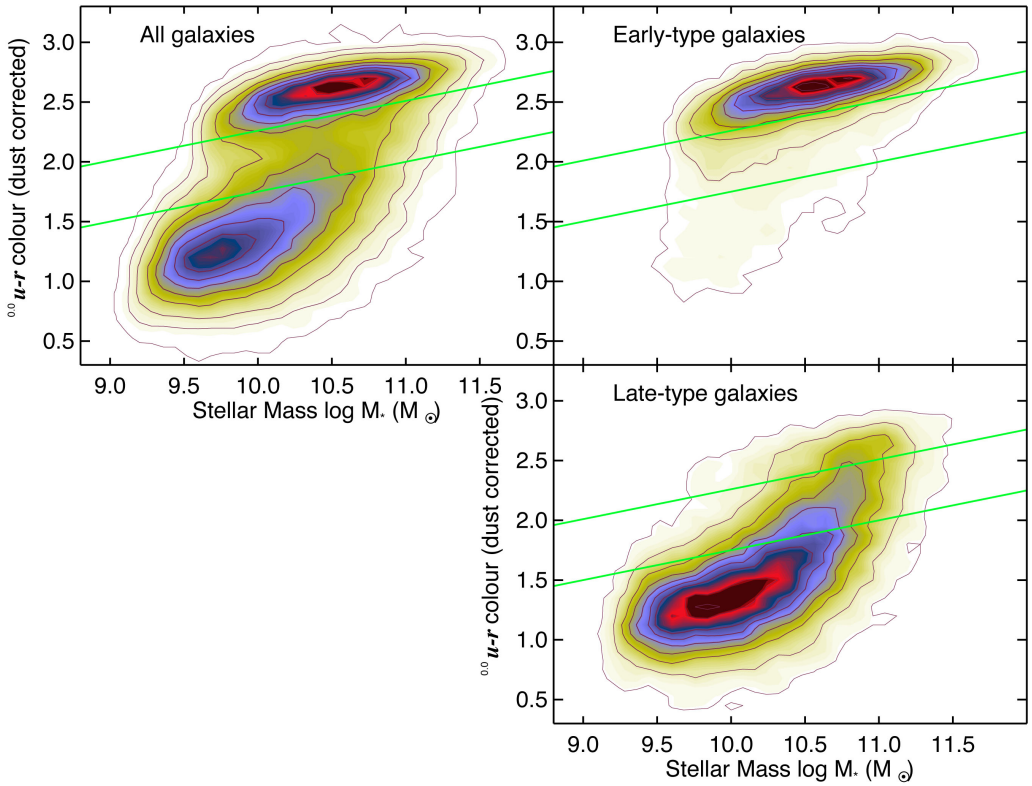

Figure 1.2: The u-r colour-mass diagram for galaxies in the Sloan Digital Sky Survey. All galaxies are shown in the top left panel, where two populations emerge: a tight red sequence (red being larger u-r values), and a more diffuse blue cloud (low u-r values). The green valley is sectioned off as the intermediate space between both populations. The top right and bottom right panel separate galaxies into early- and late-type, respectively. The early type galaxies (also called ellipticals) make up the majority of the red population, where as late-type (spiral) galaxies make up the blue cloud. Source: Schawinski et al. (2014).

1974; Dressler, 1980). One is hard-pressed to suggest a scenario in which ellipticals could start rotating rapidly to evolve into spiral galaxies; the inverse is likely more true. A framework where spirals become ellipticals is also supported by the increase in mass for the red sequence since redshift[1] z∼1, implying more red/elliptical galaxies are forming over time (Bell et al., 2004; Faber et al., 2007; Muzzin et al., 2013). One scenario through which ellipticals could transform into spirals is through hierarchical growth, where the merging of dark matter halos is accompanied with the merging of their baryonic counterparts (White & Rees, 1978; Blumenthal et al., 1984; Cole et al., 2000).

If elliptical galaxies form hierarchically from collisions of spiral galaxies, we might expect then to see a connection between ellipticals and the visual indicators of a recent merger event. There are many examples of elliptical galaxies showing signs of an interaction, such as stellar shells and asymmetries, decoupled cores, and cold gas orbiting at random inclinations (Schweizer, 1980, 1982; Malin & Carter, 1983). However, through physical models we know that not all products of galaxy collisions are elliptical galaxies (Toomre & Toomre, 1972; White, 1978, 1979; Baugh et al., 1996). Section 1.3 will outline how mergers help us understand bimodalities in morphology, colour, and star formation activity. To understand the physical impact of interactions, one must first understand the stars and gas within a galaxy that will be impacted by such an event.

1.2 Star formation in galaxies

Stars are born out of the gas and dust that exist between stars, often called the interstellar medium (ISM). The diffuse ISM is mainly in the form of neutral hydrogen gas (HI), within which there are clouds of molecular hydrogen gas (H_2) where over densities emerge to form stars. A complex balance of forces within a molecular cloud allow for this fragmentation. Gravity and external environmental pressures will cause molecular gas to condense, but internal pressures like turbulence, magnetic fields, and thermodynamics can work against these forces. Newly formed stars will eventually reshape the ISM; stellar feedback from winds/outflows and supernovae feedback can

[1]Redshift (z) is a term often used to delineate both a time and location in the Universe. Due to the expansion of the Universe, light from more distant galaxies appears redder as a result of the Doppler shift. And given the set speed of light, light from a galaxy further away from an observer will take longer to reach them, capturing an image from further in the past. Thus large redshifts represent light from distant galaxies emitted a long time ago.

hinder the fragmentation of molecular clouds, and re-enrich the ISM with heavier elements created in stellar fusion.

The youngest and most massive stars (called O and B types), which form in molecular clouds will emit UV radiation, ionizing the surrounding HI gas to HII. Areas that are actively forming new stars are thus called HII regions, which are an important tool for quantifying how many stars are currently being created within a galaxy. HII regions emit in a variety of nebular hydrogen recombination lines, including Hα, Hβ, Pα, Pβ, Brα, and Brγ. With the aid of evolutionary synthesis models, one can derive the number of stars formed in a unit of time based on these ionizing flux lines. Star formation rate (SFR) is defined as the mass of stars (in solar masses $M_{\odot}$) formed per year (Osterbrock & Ferland, 2006). The hydrogen recombination emission line flux is dominated by stars of mass greater than 10 $M_{\odot}$, with lifetimes less than 5 - 10 Megayears (Myr). As a result, hydrogen recombination lines can measure approximately instantaneous star formation rates (Kennicutt, 1983; Kennicutt et al., 2009; Hao et al., 2011; Flores Velázquez et al., 2021).

There are many alternative methods to measure SFR. For example, SFR scales linearly with ultraviolet (UV wavelength regime 1250 - 2500 Å) luminosity if the spectrum is dominated by young stellar populations (O and B stars are brightest at UV wavelengths) (Kennicutt, 1998a; Kennicutt & Evans, 2012; Calzetti, 2013). However, Earth's atmosphere absorbs most UV light, necessitating observations from costly space telescopes. UV light also suffers greatly from dust absorption within a galaxy. UV provides one of the most direct measurements of recent star formation, but observational limitations often require turning to other wavelengths.

The absorption cross-section of dust peaks in the UV, meaning that light from young massive stars can also be traced by its re-emission from interstellar dust (in the far-infrared, FIR, Kennicutt 1998a; Kennicutt & Evans 2012; Calzetti 2013). FIR approximations for star formation come with their own obstacles, in particular for elliptical galaxies where optical emission from old stars leads to dust heating that contaminates the FIR emission (Sauvage & Thuan, 1992; Walterbos & Greenawalt, 1996). For simplicity this chapter will not distinguish between different SFR measurements unless necessary, although most refer to SFR derived from Hα.

Similar to colour, a clear bimodality in galaxy populations appears when comparing global SFRs with galaxy stellar mass ($M_{\star}$). Figure 1.3 displays the SFR - $M_{\star}$ distribution for galaxies from the Sloan Digital Sky Survey (SDSS, York et al. 2000; Abazajian et al. 2009) in the cosmically "local" Universe ($0.02<z<0.085$), published

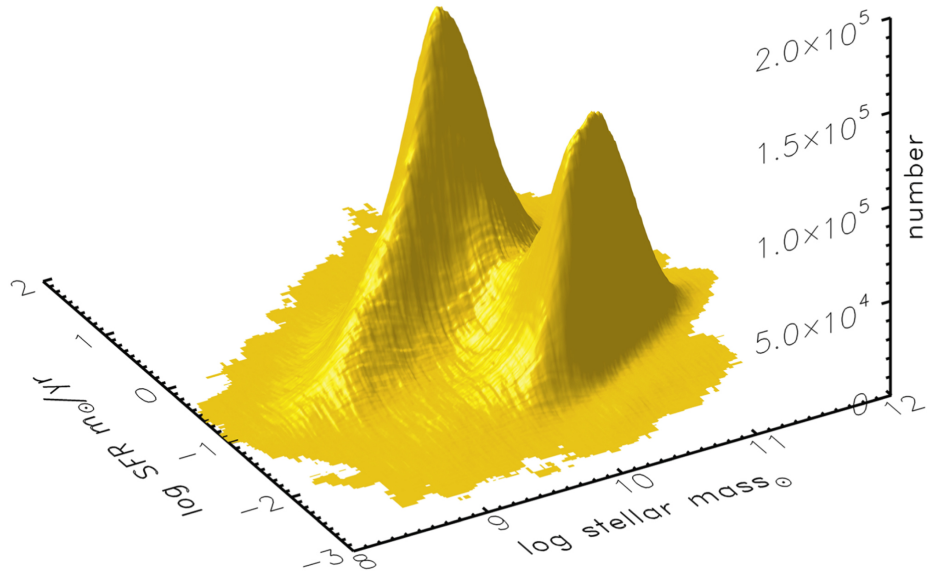

Figure 1.3: The SFR - $M_\star$ relation for SDSS galaxies between 0.02<z<0.085. The third dimension represents the number of galaxies in each bin, demonstrating the peaks that represent the star-forming and passive population of galaxies. Source: Renzini & Peng (2015).

in Renzini & Peng (2015). The number of galaxies in bins of SFR - $M_\star$ is shown as well, making the population bimodality quite clear. The first population with higher SFRs exhibits a positive correlation between $M_\star$ and SFR, otherwise known as the star-forming main sequence (SFMS, Brinchmann et al. 2004; Noeske et al. 2007a; Daddi et al. 2007; Elbaz et al. 2007; Pannella et al. 2009; Schreiber et al. 2015). The second population, often called passive galaxies, has very weak hydrogen recombination lines and thus very minimal star formation activity. Within the SFR - $M_\star$ relation there is an implied dependence on morphology, similar to what is observed in colour-mass space. Passive galaxies tend to be bulge dominated (measured by high Sérsic indices), whereas higher star formation rates tend to exist in disk galaxies (Strateva et al., 2001; Bell, 2008; Wuyts et al., 2011; Mendel et al., 2013; Schawinski et al., 2014). The clear bimodalities between SFR, colour, and morphology, along with the increasing number of red/passive galaxies at more recent times, implies the conversion from spiral to elliptical galaxies is accompanied by a suppression in star formation, often referred to as "quenching" (Drory et al., 2004; Faber et al., 2007; Pozzetti et al., 2010; Tacchella et al., 2015; Woo et al., 2015).

A comprehensive theory of star formation evolution on an extragalactic scale is

intertwined with physics of the ISM: both the initial molecular gas reservoir from which stars form, and the subsequent impact of stars on the surrounding medium. A complete review of the properties of the ISM would merit its own textbook. This thesis will focus on one in particular that is frequently paired with studies of the SFMS: the metal-content of interstellar gas.

1.2.1 Gas - phase metallicity

Global star formation rates are intrinsically entangled with the metallicity of a galaxy. Metallicity refers to the fraction of mass that consists of elements heavier than hydrogen and helium, traditionally oxygen for gas-phase metallicity and iron for stellar metallicity. As discussed previously, the majority of the ISM is made of up hydrogen gas, a result of the primordial matter created after the Big Bang (mostly hydrogen and helium-4, with smaller amounts of deuterium, helium-3, and lithium). Over time stars produce heavier nuclei, which are eventually injected into the ISM by supernova explosions, stellar winds, and planetary nebulae ejection. Throughout this work metallicity will refer specifically to the gas-phase oxygen abundance in a galaxy.

The gas-phase metallicity is often defined as the ratio between oxygen atoms to Hydrogen atoms, given oxygen is one of the more abundant metals in the ISM. Oxygen abundances are derived from the electron temperature (T_e), measured from faint auroral or nebular emission line intensities. The ratio between a higher energy line and a lower energy line reveals information about the temperature of the gas, with the higher energy line being more dominant at high temperatures. Most often this ratio is taken for the same element (so as not to worry about different ion abundances in the ISM) for two forbidden lines, such as [OIII]λ4363 (higher) and [OIII]λ5007 (lower). However the intrinsic weakness of these lines creates an obstacle for this more direct method. Oxygen serves as an effective radiative coolant, so as the oxygen abundance (metallicity) rises, the temperature of the gas will decrease (making it more difficult to excite the higher energy emission line like [OIII]λ4363) (Osterbrock & Ferland, 2006; Stasinska et al., 2012; Peimbert et al., 2017).

As an alternative, indirect abundance measurements can be made from stronger nebular emission lines of metals other than oxygen. Some common ratios used are [NII]λ6583/Hα, [OIII]λ50073/Hβ, [NII]λ6583/[OII]λ3727, and [OIII]λ5007/[OII]λ3727 (Mcgaugh, 1991; Zaritsky et al., 1994; Kewley & Dopita, 2002; Pettini & Pagel, 2004; Kobulnicky & Kewley, 2004; Marino et al., 2013a). These ratios are then calibrated

either based on measurements from the more direct method discussed previously, or on photoionization models (e.g. Mcgaugh 1991; Kewley & Dopita 2002; Kobulnicky & Kewley 2004). This alternative method is far more common than the more difficult direct metallicity measurement; most of the remaining works mentioned in this thesis which observe metallicity use the indirect method.

Three physical processes shape galactic gas-phase metallicity: internal enrichment from the injection of heavy elements from star formation (as discussed previously), galactic outflows in the form of winds, and gas inflows. Galactic winds, created by starbursts or active galactic nuclei (AGN), can move metals from the centre of the galaxy to the intergalactic medium, thus lowering the galaxy's total metallicity (Garnett, 2002; Veilleux et al., 2005; Weiner et al., 2009; Chisholm et al., 2018). Observations of galactic outflows have confirmed gas in these outflows have higher metallicities than their host ISM, and are particularly effective at transporting high-metallicity gas from low mass galaxies to their surrounding circumgalactic medium (Tremonti et al., 2004; Tumlinson et al., 2011; Chisholm et al., 2018). Metallicity can also be diluted by gas inflows, which transport metal-poor gas from the intergalactic medium into the galaxy. Non-axisymmetric structures within a galaxy can also cause gas to lose angular moment, transporting it from the outskirts to the centre of the galaxy and diluting the metallicity there (see Section 1.3 for further discussion) (Barnes & Hernquist, 1991, 1996; Kewley et al., 2006b, 2010).

Metallicity, similar to star formation rate, is strongly correlated with global stellar mass, often called the mass-metallicity relation (MZR) (Lequeux et al., 1979; Kinman & Davidson, 1981; Tremonti et al., 2004; Kewley & Ellison, 2008). Multiple hypotheses for this correlation have been put forward. One theory proposes that metals are more easily ejected by galactic outflows in low mass galaxies, due to their comparatively low gravitational potentials (Larson, 1974; Tremonti et al., 2004; Tumlinson et al., 2011; Chisholm et al., 2018). The greater gravitational potentials of high mass galaxies trap galactic winds that would otherwise remove metals from a galaxy. An alternative scenario suggests high-mass galaxies form stars earlier (at higher redshift) than low mass ones, allowing more time for stellar feedback to enrich the gas reservoir (Noeske et al., 2007b; Maiolino et al., 2008; Zahid et al., 2011). It is also possible that low mass galaxies are simply less efficient at converting gas into stars, leading to a similar lack of stellar enrichment. (Brooks et al., 2007; Mouhcine et al., 2008; Calura et al., 2009; Vincenzo et al., 2016).

The MZR appears to have a third dependence on star formation rate for most

galaxies: galaxies offset above the MZR (heightened metallicities for their $M_\star$) tend to have lower SFR values. The relationship between $M_\star$, metallicity, and SFR has been dubbed the Fundamental Metallicity Relationship (or FMR, Ellison et al. 2008b; Mannucci et al. 2010; Lara-López et al. 2010). One physical explanation of the FMR comes from a combination of inflows and outflows of gas within a galactic system. The infall of gas from the intergalactic medium moderates star formation and directly changes the integrated gas-phase metallicity of a galaxy, while outflows of metal-rich gas depend on the gravitational potential of the galaxy (thus metallicity depends on $M_\star$). Recently the FMR has been brought under scrutiny, as it could possibly be an artefact of aperture effects from single fibre spectroscopic surveys or simply limited to the central regions of galaxies (Barrera-Ballesteros et al., 2017; Sanders et al., 2017; Ellison et al., 2018a). However the FMR has been accurately reproduced in galaxy simulations, where the evolution of offsets from the SFMS and MZR (leading to offsets in the FMR) are linked to each other and to the evolution of the dark matter halo rather, than specific feedback physics (Lagos et al., 2016; Davé et al., 2017; De Rossi et al., 2017; Torrey et al., 2018)

The SFMS, MZR, and the FMR all stem from scaling relations on a kpc-scale. The following section will transition from integrated galaxy properties like SFR and $M_\star$, to resolved properties such as the star formation rate surface density ($\Sigma_{\rm SFR}$) and stellar mass surface density ($\Sigma_\star$). Along with this, the following section will introduce two new relations yet to be discussed: the Kennicutt-Schmidt relation, and the molecular gas main sequence.

1.2.2 Resolved scaling relations

The Kennicutt-Schmidt (KS) relation describes the correlation between total gas mass and SFR, with the later publications focusing on molecular gas mass in particular (Schmidt, 1959; Kennicutt, 1989, 1998b). Once resolved observations of star formation and gas improved (see Section 1.4.2 for details), studies confirmed the KS relation persisted on a kpc-scale (the resolved Kennicutt-Schmidt, or rKS; Bigiel et al. 2008; Leroy et al. 2008; Schruba et al. 2011; Usero et al. 2015; Utomo et al. 2017). Both the KS and rKS are intuitive given our understanding of star formation in the ISM: if molecular gas is the material from which new stars form, it follows that increasing molecular gas mass would subsequently increase SFR. There is scatter about the rKS due to local changes in the efficiency at which gas is converted into stars (also called

"star formation efficiency", or SFE) (Leroy et al., 2013; Bolatto et al., 2017; Utomo et al., 2017).

The rKS is often associated with another resolved relation, between the molecular gas surface density (Σ_{H_2}) and $\Sigma_\star$, also called the resolved molecular gas main sequence (rMGMS, Wong et al. 2013; Lin et al. 2019; Ellison et al. 2021a; Barrera-Ballesteros et al. 2020). Unlike the rKS, the origin of the rMGMS remains ambiguous. One possible origin requires the dark matter contribution to the gravitational potential of a galaxy is negligible compared to baryonic matter and that there is much more mass in stars than in molecular gas in a galaxy, such that $\Sigma_\star$ drives the local potential that Σ_{H_2} must then follow. In such a scenario the molecular gas main sequence will disappear at larger redshifts, when gas masses surpass stellar masses (Isbell et al., 2018; Tacconi et al., 2018). Alternatively, both Σ_{H_2} and $\Sigma_\star$ could be following the underlying gravitational potential shaped by dark matter; further studies of the MGMS through cosmic time will help reveal which scenario is more plausible (Lin et al., 2019).

The rKS and rMGMS combined are responsible for a resolved star-forming main sequence (rSFMS, Lin et al. 2019; Ellison et al. 2021a; Baker et al. 2022). Figure 1.4 helps visualize the interconnections between the rKS, rMGMS, and rSFMS. Each 2D relation describes an aspect to a 3D distribution of surface densities. The rSFMS has a larger scatter than the other two relations, as well as a weaker correlation between the two primary variables (Lin et al., 2019). The secondary nature of the rSFMS is a relatively new paradigm. Negative gradients in Σ_{SFR}, stemming from negative gradients in HII region density, demonstrated that larger $\Sigma_\star$ values corresponded to larger Σ_{SFR} as would be expected for kpc-scale SFMS (Pagel & Edmunds, 1981; Evans, 1986; Garnett & Shields, 1987; Shields, 1990). Eventually resolved spectroscopic observations would better characterize the tight positive correlation between Σ_{SFR} and $\Sigma_\star$(Rosales-Ortega et al., 2012; Sánchez et al., 2013; Cano-Díaz et al., 2016; González Delgado et al., 2016; Hsieh et al., 2017; Medling et al., 2018; Vulcani et al., 2019). The proven connection between the rKS, rMGMS, and rSFMS later implied that scatter in the rSFMS stems from offsets in either the rKS (from changes in SFE) or the rMGMS (from changes in molecular gas fraction). However, environmental effects independent of the rKS and rMGMS can also alter the $\Sigma_\star$ profile and boost star formation (Usero et al., 2015; Gallagher et al., 2018; Jiménez-Donaire et al., 2019).

The MZR also has an underlying resolved component as well (rMZR, González Delgado et al. 2014; Barrera-Ballesteros et al. 2016; Belfiore et al. 2018; Curti et al. 2020,

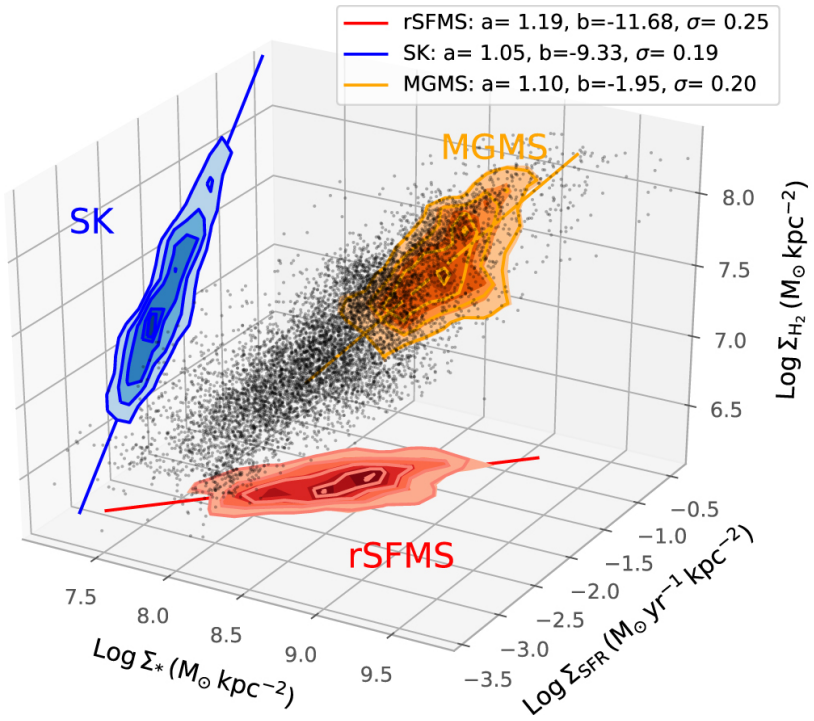

Figure 1.4: A 3D distribution of $\Sigma_\star$, $\Sigma_{\rm H_2}$, and $\Sigma_{\rm SFR}$ for star-forming regions in main-sequence galaxies. Each individual scaling relation is shown on a 2D plane: red for the rSFMS, blue for the rKS (called Schmidt-Kennicutt, or SK, here), and orange for the rMGMS. Contours show levels corresponding to 20%, 40%, 60%, 80%, and 90% of the density peaks. Fits for each scaling relation are calculated, shown as a solid dashed line, with parameters (a,b) and associated scatter (σ) shown in the legend. Through a 3D representation it becomes clear that all three scaling relations are merely one component of a more complex relationship between gas and stars. Source: Lin et al. (2019).

although global galaxy properties such as $M_\star$ still have significant impacts on the global MZR (D'Eugenio et al., 2018; Barrera-Ballesteros et al., 2018). If the rSFMS can itself be the by-product of two more fundamental scaling relations, one may expect a resolved FMR (rFMR) to manifest as a result from the rSFMS and rMZR. However many initial studies hypothesized the global FMR might stem not from a rFMR, but from aperture effects of single slit spectroscopy (Sánchez et al., 2013; De Los Reyes et al., 2015; Barrera-Ballesteros et al., 2017; Sanders et al., 2017). But through careful analysis of resolved spectroscopic data, paying particular attention to which metallicity calibration and SFR indicator are chosen, more recent studies appear to agree that a resolved FMR exists (Salim et al., 2014; Gao et al., 2018; Cresci et al., 2019; Sánchez Almeida & Sánchez-Menguiano, 2019).

Explaining variations in these resolved relations is essential to our broader understanding of galactic star formation evolution, and thus what has led to the observed diversity of galaxy populations. Some of the most extreme star-forming environments occur when galaxies interact with one another. Thus galaxy interactions can be used both as a laboratory for extreme star-forming conditions, as well as aiding our understanding of how galaxies evolve to extremely high (and extremely low) global star formation rates.

1.3 Galaxy mergers as a keystone for cosmic evolution

There is extensive evidence to establish galaxy mergers as a critical component of galaxy evolution over time. From a cosmological perspective, hierarchical growth should lead to the merging of dark matter halos, and thus their baryonic counterparts (White & Rees, 1978; Blumenthal et al., 1984; Cole et al., 2000). Hierarchical growth has also helps explain the apparent bimodality in galaxy populations: between star-forming spiral disks and red-and-dead ellipticals (Bower et al., 1992; Bell et al., 2004; Schawinski et al., 2014; Renzini & Peng, 2015). Theoretically, major galaxy mergers can trigger a strong starburst, moving a galaxy in both colour-space and about the SFMS (Barnes & Hernquist, 1991; Mihos & Hernquist, 1994, 1996). The bluer colour of peculiar galaxies proves this in the most fundamental way (Larson & Tinsley, 1978; Barton Gillespie et al., 2003a; Lambas et al., 2012), followed by the excess Hα emission seen in interacting pairs (Kennicutt et al., 1987; Knapen & James, 2009). Some observational studies suggest that there exists a link between merger fraction and the build-up of early-type galaxies, further connecting mergers to the formation

of red elliptical galaxies (Hopkins et al., 2007, 2008). Section 1.4 will review the observational studies that have revealed the impact of interactions on global and resolved galaxy properties. Before that can be discussed, we must review the physical processes which impact a galaxy during and after an interaction.

1.3.1 What happens when galaxies collide?

When galaxies collide there is very little chance of any collision between stars within those galaxies, given how far apart stars are even within their own galaxy. But stars will react gravitationally to each other. Chandrasekhar (1943) first proposed the concept of dynamical friction: that as a star moves through a dense stellar medium it will experience small gravitational tugs by neighbouring stars. Only neighbouring stars moving slower than the target star will experience this effect, as they are the ones that can be accelerated by a faster moving target star. Over time, kinetic energy will be transferred from the target star to the acceleration of its slower neighbours, slowing the target star and creating a high-density "wake" trailing the target (Carroll & Ostlie, 2007). This physical mechanism can also be applied to galaxies, where all the stars in the target galaxy experience gravitational pulls from the neighbouring galaxy's stars.

Dynamical friction helps us determine how quickly two galaxies will coalesce, and depends on the mass and velocity of the target, as well as the stellar density of the companion it must pass through. A low mass galaxy will lose energy to dynamical friction to a larger companion much more slowly than if the two were of similar size. Likewise, if a galaxy has a large velocity, it will spend less time near a neighbouring object, lessening the time dynamical friction can have an impact. The density of the neighbouring galaxy will impact time to coalescence, as kinetic energy is more easily transferred in dense stellar environments. Dynamical friction is also at its core a gravitational effect, and thus has greater influence when the two galaxies are closer together. All of these factors can influence whether two galaxies merge in a single free-fall event, or whether they experience multiple close encounters before coalescing (Carroll & Ostlie, 2007). The interaction stage can last up to $\sim$1Gyr (Giga-year, a billion years) (Jian et al., 2012). During this process gravitational forces between the galaxies can create highly asymmetric structures such as tidal arms, bridges between galaxies, stellar streams, and shells (Toomre & Toomre, 1972; Barnes, 1988; Barnes & Hernquist, 1992).



Figure 1.5: *Left:* Image of NGC 4676, two interacting galaxies also known as the Mice, taken with The Advanced Camera for Surveys (ACS) on the Hubble Space Telescope. The Mice are a textbook example of both bridge features (between the two nuclei), and tidal tails (streaming to the left and right of each). Image credit: NASA, H. Ford (JHU), G. Illingworth (UCSC/LO), M.Clampin (STScI), G. Hartig (STScI), the ACS Science Team, and ESA. *Right:* Image of NGC 474, taken with the MegaCam camera on the Canada-France-Hawaii Telescope (CFHT). The CFHT observation picks up faint galactic features, and fantastically captures both stellar shells and streams that are often less obvious than tidal tails. Image credit: CFHT, Coelum, MegaCam, J.C. Cuillandre (CFHT) & G. A. Anselmi (Coelum).

Visual indicators of an interaction can emerge as early as the first close approach (pericentric passage), and can last from 0.1-1.2 Gyr (Lotz et al., 2008). Such features have been noted for a variety of observed galaxies (e.g., the Atlas of Peculiar galaxies, Arp 1966). Figure 1.5 provides two example galaxies that have some of the most striking merger features, with NGC 4676 displaying tidal tails and bridges from a close interaction and NGC 474 exhibiting shells and stellar streams from a more recent coalescence. However, of the observed galaxies within $z < 1$, only between $4 - 6\%$ have such features to indicate an interaction has occurred within 1 Gyr or less (Darg et al., 2010). The rarity of visible merger events does not prove they are unimportant to galaxy evolution on a cosmic timescale. N-body simulations suggest that a typical galaxy at $z{\sim}3$ ($M_\star > 10^{10} M_\odot$) undergoes over 4 mergers before $z = 1$ (Conselice, 2006; Rodriguez-Gomez et al., 2015).

The asymmetric structures created by close interactions cause gravitational torques in a galaxy, which causes gas to lose angular momentum and fall towards the centre of a galaxy (Hernquist, 1989; Barnes & Hernquist, 1991; Mihos & Hernquist, 1996; Iono et al., 2004; Hopkins et al., 2009). Even a non-axisymmetric gravitational potential,

created by the presence of a close companion, can spur bar instabilities in the nucleus of a galaxy, the stellar and gaseous components of which are usually misaligned by a few degrees (Barnes & Hernquist, 1996; Hopkins et al., 2009). The stellar bar is still non-collisional (stars are not close enough for a likely collision), but the gaseous component is collisional. The misalignment will cause a torque exerted by the stellar component onto the gaseous one; creating a drag on the gas as kinetic energy is transferred between the two and gas loses its angular momentum. As the interaction progresses these torques grow, and gas loses the angular momentum necessary to stay at its set radius, falling into the centre of the galaxy (Barnes & Hernquist, 1991, 1996; Mihos & Hernquist, 1996). Simulations have improved over years to not only replicate this process, but to help us understand how interactions effect gas and subsequent star formation throughout the entire interaction.

1.3.1.1 Results from galaxy simulations

The timescales on which galaxy mergers occur (Gyrs) are unobservable, meaning simulations play an essential role to examine the effects of an interaction in real time. Although early N-body simulations that modelled gravitational forces could help us constrain how tidal forces changed the structural and dynamical qualities of a galaxy (Toomre & Toomre, 1972; White, 1978, 1979), more complicated radiative processes govern the gas dynamics of an interaction (Hernquist, 1989; Barnes & Hernquist, 1991). Incorporating hydrodynamics into simulations has permitted the examination of complex effects like star formation feedback for both isolated and interacting galaxies (Tissera et al., 1997; Springel, 2000; Hopkins et al., 2006; Keller et al., 2014).

Simulations have demonstrated that interactions continuously alter galaxy morphology, resulting in unique structural characteristics for each merger stage (Mihos & Dubinski, 1998; Bournaud et al., 2005; Lotz et al., 2008; Hopkins et al., 2009; Rodriguez-Gomez et al., 2017). Such structures can occur both at large radii as described previously, as well as small scale changes (10pc) such as eccentric and lopsided disks that end up impacting the gravitational potential (Hopkins & Quataert, 2011). These non-axisymmetric structures give way to misalignments between stellar and gaseous components and the subsequent infall for the gaseous component previously discussed (Barnes & Hernquist, 1996; Mihos & Hernquist, 1996; Iono et al., 2004; Hopkins et al., 2009, 2013).

Gaseous inflows from a merger can fuel an active galactic nucleus (AGN), ex-

tremely luminous emission from gas and dust as it falls into the central supermassive black hole in a galaxy (Cattaneo et al., 2005; Di Matteo et al., 2005; Capelo et al., 2015). Feedback from AGN has the potential to remove gas from the galactic reservoir and halt star formation (Springel et al., 2005; Boylan-Kolchin et al., 2009; Somerville & Davé, 2015). Thus through AGN mergers could be a possible route for galaxy quenching (Di Matteo et al., 2005; Hopkins et al., 2008; Somerville et al., 2008; Quai et al., 2021). However gaseous inflows can also trigger a burst of star formation (Cox et al., 2008; Di Matteo et al., 2007, 2008; Montuori et al., 2010; Torrey et al., 2012), thus there is a unique interplay between processes regulating star formation in a merger.

Simulations demonstrate that merger-induced enhancements in star formation begin early in the pair stage of an interaction (Mihos & Hernquist, 1996; Springel & Hernquist, 2005; Torrey et al., 2012; Hopkins et al., 2013), with the enhancement peaking at a factor of 2 for small separations (Patton et al., 2020). The star formation enhancement is greatest when the two galaxies coalesce, but those enhancements will eventually decay over $\sim$0.5 Gyr (Hani et al. 2020, see also Moreno et al. 2015; Rodríguez-Montero et al. 2019). The central starburst is accompanied by a dilution in gas-phase metallicity, due to the inflow of low-metal gas that concentrates in the centre of the galaxy (Rupke et al., 2010; Montuori et al., 2010; Perez et al., 2011; Torrey et al., 2012; Bustamante et al., 2018). High resolution simulations have allowed us to split gas into different physical phases, such as ionized, atomic, and molecular. This has helped demonstrate that the star formation enhancement, which can persist up to 4 Gyr after first pericentric passage, is accompanied by a build up in the dense molecular gas reservoir (Moreno et al., 2019). Eventually supernova feedback will re-enrich the ISM and mitigate previous dilutions in metallicity (Perez et al., 2011).

The effects discussed thus far are all inherently sensitive to the properties and orientation of merger progenitors. For example, simulations have demonstrated that galaxies rotating in opposite directions with respect to each other can enhance the efficiency at which gas is converted to stars by a factor of two, compared to a scenario where galaxies are rotating in the same direction (Di Matteo et al., 2007; Cox et al., 2008; D'Onghia et al., 2010). Greater perturbations in a merging system can also occur when a galaxy's rotation speed is similar to the peak angular speed of the encounter (D'Onghia et al., 2010). The angle of approach between galaxies can also alter the strength of the resulting starburst (Cox et al., 2008; Di Matteo et al., 2008; Torrey et al., 2012), as well as the star formation activity at the outskirts of the

galaxy (Moreno et al., 2015). The ability to know the pre- and post- coalescence properties of a galaxy in a simulation helps constrain which properties shape the post-coalescence state. For example, the closer in mass two interacting galaxies are, the greater post-coalescence enhancement in SFR (Woods & Geller, 2007; Cox et al., 2008; Lotz et al., 2010b; Lambas et al., 2012). Large gas fractions also tend to lead to weaker and short lived SFR enhancements (relative to a similar but isolated galaxy) (Bournaud et al., 2011; Perez et al., 2011; Scudder et al., 2015; Fensch et al., 2017).

Simulation results can help us interpret real world observations, where the full time-lapse of an interaction is so dearly missed. However the works described thus far are still theoretical frameworks with their own assumptions and shortfalls. Real world observations of mergers allow us to assess the validity of simulations and improve them with our extended knowledge. Both approaches depend fundamentally on each other to complete our understanding of merger events.

1.4 Statistical observational studies of merging galaxies

Alternative to galaxy simulations, one can attempt to reconstruct the merging process with observations of many galaxies at different stages of interaction. With a bit of detective work, one can piece together what happens during an interaction, similarly to how animations are made of many different individual images. Although targeted studies of individual mergers provide insights into the drastic changes an interaction can induce, to create a comprehensive understanding of the impact of interactions requires large data sets of multiple kinds of mergers.

1.4.1 Integrated Studies

Large photometric surveys have allowed for the collection of extensive merger sets, despite the rarity of merger events in a single population. As discussed previously, photometry can be used to quantify whether a galaxy is "redder" or "bluer", with stronger starbursts being bluer in colour.[2] Peculiar galaxies tend to be bluer in colour, implying that an interaction which has disturbed the morphology of the galaxy can also create a burst of star formation (Larson & Tinsley, 1978; Barton Gillespie et al., 2003b; Lambas et al., 2012). Galaxies that have a close enough companion to

[2]Not all starbursts are necessarily bluer in colour. For example, ultraluminous infrared galaxies (ULIRGs) have intense star formation activity (most often triggered by mergers), but are so dusty they appear "redder" in colour (Sanders et al., 1988; Clements et al., 1996; Farrah et al., 2001).

confirm that an interaction is either imminent or in progress (called "pair" systems) tend to exist in denser environments, and thus have a larger fraction of red galaxies (Ellison et al., 2010; Patton et al., 2011; Alonso et al., 2012). However, on average galaxies become comparatively bluer as the separation between galaxy pairs decreases (Barton Gillespie et al., 2003b; Patton et al., 2011; Tonnesen & Cen, 2012), with the bluest galaxies being those with prominent tidal features (Lambas et al., 2012).

One can more directly measure SFR from Hα luminosity (see Section 1.2). Hα flux can be measured using either a long-slit spectrograph, which gathers flux as a function of wavelength along a fixed position angle on the sky, or with a fibre which collects light through an aperture to be sent to a spectrograph. Both create a single spectrum from which one can derive a global SFR value. Imaging is often used in conjunction with this method to help correct for flux lost if the galaxy extends beyond the fibre/slit (Brinchmann et al., 2004). Large spectroscopic surveys like SDSS provide integrated spectra for hundreds of thousands of galaxies (Abazajian et al., 2009), allowing for statistical analysis of SFR for different merger stages. On average galaxy pairs with smaller separations have larger SFRs, implying that the merger event is triggering this star formation (Barton et al., 2000; Nikolic et al., 2004; De Propris et al., 2005; Woods et al., 2010; Ellison et al., 2008a; Scudder et al., 2012; Yuan et al., 2012; Patton et al., 2016; Bickley et al., 2022). Figure 1.6 provides an example of this from Ellison et al. (2013a), illustrating the change in SFR with projected separation between pairs by quantifying an enhancement in SFR with respect to a control sample of isolated galaxies (ΔSFR), confirming that ΔSFR increases as the interaction progresses and peaks at coalescence.

Gaseous inflows can also trigger AGN, although observational evidence for this is less clear than for triggered star formation. Many studies have found a connection between merger features and the presence of an AGN (Alonso et al., 2007; Woods & Geller, 2007; Ellison et al., 2011; Satyapal et al., 2014; Goulding et al., 2018; Gao et al., 2020); but just as many find no connection between the two phenomena (Grogin et al., 2005; Gabor et al., 2009; Cisternas et al., 2011; Sabater et al., 2015; Marian et al., 2019). Current dissension between AGN-merger studies likely stems from a variety of methodology and AGN selection. For example, mergers are in greater excess in mid-infrared selected AGN compared to optically selected AGN, meaning merger AGN are more highly obscured (Satyapal et al., 2014; Goulding et al., 2018; Ellison et al., 2019).

Mergers not only trigger gaseous inflows, but can also have overall larger molecular

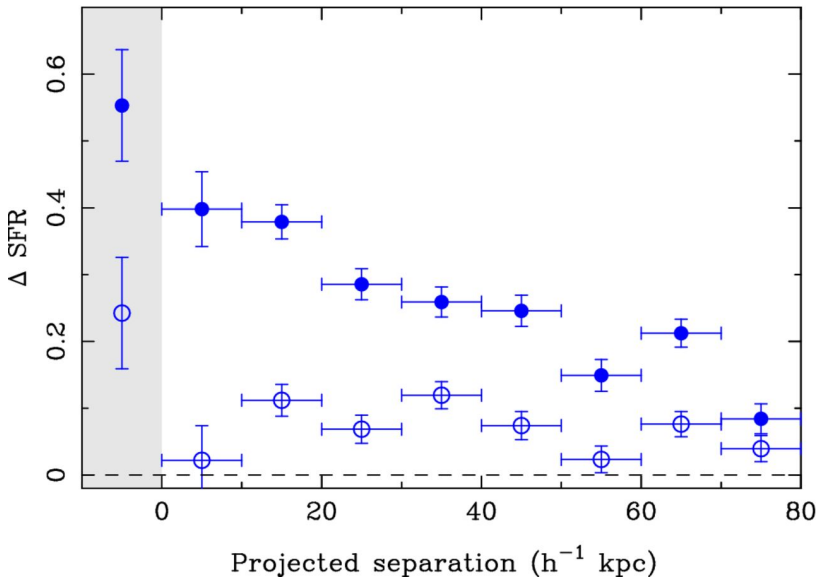

Figure 1.6: Enhancements in SFR compared to a control sample (ΔSFR) for star-forming galaxies in close pairs, shown as a function of projected separation between pairs. Enhancements for a post-merger sample are shown in the grey shaded box. Note how as galaxy pairs get closer the star formation enhancement increases, with the greatest enhancement at the moment of coalescence. Filled circles show the fibre SFR, whereas empty circles show the SFR outside the fibre. Source: Ellison et al. (2013b).

gas fractions than their non-interacting counterparts. There is some bias to gas studies of mergers, given mergers with high gas fractions tend to have longer lasting morphological disturbances (and are thus more easily selected as mergers) (Lotz et al., 2008, 2010b). Statistical studies of the molecular gas mass demonstrate that mergers tend to have higher molecular gas fractions than non-interacting galaxies (Braine & Combes, 1993; Combes et al., 1994; Casasola et al., 2004; Larson et al., 2016). More careful considerations for how H_2 mass is derived from observations (details in Chapter 4), along with comparing interacting galaxies to well picked controls, has mostly confirmed that gas fraction increases as an interaction progresses (Violino et al., 2018; Pan et al., 2018b). The heightened gas fraction is often accompanied with a boost in star formation, resulting in many mergers having an enhanced star formation efficiency as well (SFE= SFR / gas mass, Solomon & Sage 1988; Saintonge et al. 2012; Michiyama et al. 2016). There is more contention for whether mergers also trigger enhanced atomic gas fraction, with some studies finding no difference between merger and non-merger atomic gas fractions (Braine & Combes, 1993; Ellison et al., 2015; Zuo et al., 2018), while others find a clear enhancement in the pair and post-merger stage (Casasola et al., 2004; Huchtmeier et al., 2008; Scudder et al., 2015; Ellison et al., 2018b).

Given the observed changes in SFR and gas fraction, it naturally follows that gas-phase metallicity will also be diluted in galaxy pairs and post-mergers. Differences between a merger metallicity and a well matched control (ΔO/H) tend to be much smaller in magnitude compared to offsets in SFR, usually of a order of $0.03-0.05$ dex (Cooper et al., 2008; Ellison et al., 2008a). Nonetheless mergers with enhanced star formation activity on a global scale are accompanied by a suppressed metallicity (Kewley et al., 2006a; Ellison et al., 2008a; Michel-Dansac et al., 2008; Peeples et al., 2009). Beyond a projected separation of $\sim$ 60 kpc, most merger metallicities are consistent with a control sample (Scudder et al., 2012).

Integrated studies have provided a comprehensive picture of the impact interactions have on global galaxy properties. As demonstrated by simulations, interactions lead to enhanced gas fractions that dilute metallicity and boost star formation. Nevertheless, integrated studies remain blind to the changes that occur within a galaxy. Are gaseous inflows and central starbursts the only ramifications of a merger event? Or are more complex processes at play in a galaxy? To answer these questions one must move beyond global spectroscopic studies to full spatially resolved investigations of merger properties.

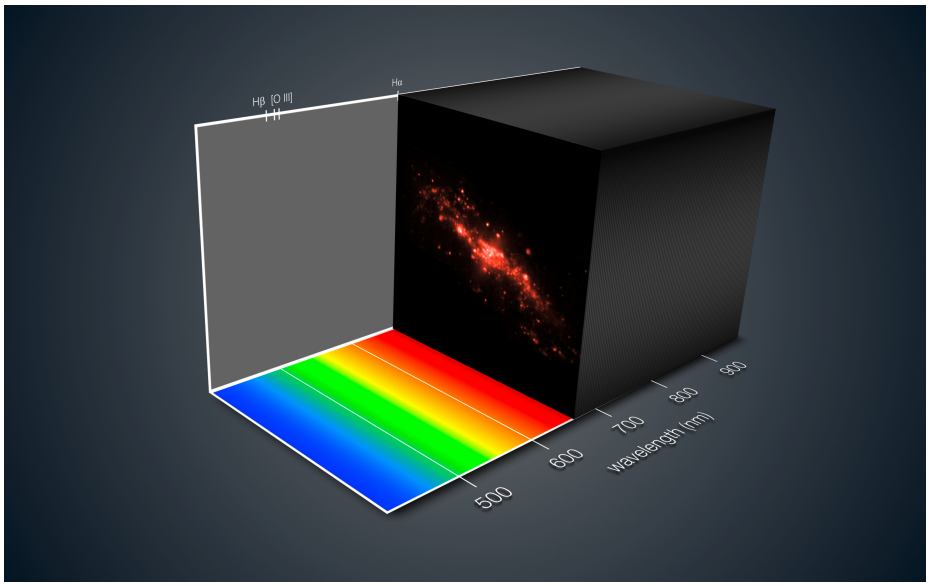

Figure 1.7: An illustration of the data cube produced by integral field spectroscopy, made specifically for the Multi-Unit Spectroscopic Explorer (MUSE) instrument. The data cube is split into different wavelengths of light, such that every wavelength interval has a complete image of NGC 4650A (an Hα emission map is shown here). Image Credit: ESO/MUSE consortium/R. Bacon/L. Calçada

1.4.2 Resolved spectroscopic studies

The advent of integral field spectroscopy (IFS) surveys have allowed for the collection of resolved spectroscopic data for a large sample of galaxies. Rather than place a single long-slit or fibre spectrograph on a galaxy, IFS techniques create a map of spectra using bundles of spectroscopic fibres, lenslet arrays, or image slicers. From this set up a three dimensional data cube is created, where for every wavelength of a spectrum there is an image of a galaxy (see Figure 1.7 for a visualization). In the past integral field spectroscopy was used to study a few nearby galaxy interactions, such as the NGC 7771 + NGC 7770 galaxy pair or the Mice interacting system (Alonso-Herrero et al., 2012; Wild et al., 2014). Both remarked on the central and extended starburst behaviour for interacting galaxies undergoing their first pericentric passage. Targeted studies like these have been combined more recently with spatially resolved molecular gas measurements, revealing over two orders of magnitude variation in SFE (Tomičić et al., 2018).

Targeted IFS studies have shown great promise, but larger data sets are necessary to investigate the diversity of merger scenarios. The following section will briefly review the earliest IFS surveys that served as the forerunners for contemporary large

IFS surveys, before addressing more recent results concerning the resolved properties of mergers.

1.4.2.1 Integral field spectroscopy surveys

Though IFS was used in scientific projects throughout the 1980s and 1990s, the Spectroscopic Areal Unit for Research on Optical Nebulae (SAURON) is often quoted as the first attempt of an IFS galactic survey (Sánchez, 2020). SAURON explored a representative sample of 72 early-type galaxies in the nearby universe (Tim De Zeeuw et al., 2002). SAURON paved the way for ATLAS^{3D}, which used the same instrument as SAURON (along with radio and millimetre observations) to create a multi-wavelength study of 260 elliptical/lenticular galaxies (Cappellari et al., 2011). Both surveys were able to explore stellar populations, stellar composition, and galaxy dynamics. Following dynamical studies completed with SAURON, the DiskMass Survey analyzed mass-to-light ratios in disk-like galaxies to better understand dark matter fractions within such galaxies (Bershady et al., 2010).

These initial studies inspired second generation IFS surveys with more narrowly focused science goals. Such follow-up was necessary, given the relatively small sample size of SAURON and ATLAS^{3D} limited the number of different galaxy types. The VIRUS-P Exploration of Nearby Galaxies (VENGA) Survey prioritized high spatial resolution and deep observations to constrain star formation in nearby spirals (Blanc et al., 2013). The SAGES Legacy Unifying Globulars and GalaxieS (SLUGGS) Survey focused on investigating the chemical compositions and kinematics of 25 early-type galaxies at large radii (out to ∼8 effective radii) (Brodie et al., 2014). The MASSIVE Survey observed some of the largest galaxies ($M_\star \gtrsim 10^{11.5} M_\odot$) with IFS (Ma et al., 2014). Merger-focused IFS surveys were completed as well, with the Wide Field Spectrograph (WiFeS) Great Observatory All-Sky LIRG Survey(GOALS) (WiGS) investigating the resolved emission and kinematic information for interacting and post-merger luminous infrared galaxies (LIRGs) (Rich et al., 2012, 2014, 2015).

Only within the last decade have IFS surveys expanded to an order of hundreds or thousands of galaxies, providing more holistic samples from which focused studies can be performed. The first of these surveys launched was the Calar Alto Legacy Integral Field Area (CALIFA) survey, using the same Potsdam Multi-Aperture Spectrograph fibre package (PMAS/PPAK) employed for case studies of the Mice galaxies described previously. CALIFA observed roughly ∼600 galaxies between 2011 and

2016 (Sánchez et al., 2012). More recent surveys have significantly larger samples than CALIFA. The Sydney-Australian Astronomical-Observatory Multi-object Integral Field Spectrograph (SAMI) survey observed ∼3000 galaxies (Allen et al., 2015), enabling a rather substantial merger study despite the rarity of merger events. The largest IFS survey to date is the Mapping Nearby Galaxies at Apache Point Observatory (MANGA) survey, which has collected over 10,000 observations of individual galaxies (Bundy et al., 2015; Law et al., 2015; Abdurro'uf et al., 2022). Given the rarity of merger events, most statistical IFS studies of mergers have been limited to these three galaxy surveys.

1.4.2.2 Statistical IFS studies of mergers

The first large IFS study of mergers was completed with CALIFA, where 103 mergers were selected by either visual classification (highly disturbed morphologies) or by the presence of a companion (within a projected separation $r_p < 106$ kpc and a line-of-sight velocity difference $\Delta v < 600$ km/s (Barrera-Ballesteros et al., 2015). 2D maps from CALIFA were then separated into "central" and "extended" apertures (5" and 30" respectively), simplifying resolved properties into what is happening in the centre of a galaxy vs. its outskirts. Using the equivalent width (EW) of Hα emission lines as a proxy for specific star formation rate (sSFR=SFR/M$_\star$), Barrera-Ballesteros et al. (2015) found interacting galaxies have higher sSFR values in their centre compared to a control sample, and compared to their outskirts. At the edge of the galaxy sSFR could be similar to or even smaller than that in a control sample, depending on how the control was selected. CALIFA was also used to measure the gas-phase metallicitiy gradients in mergers, which are flatter than their non-interacting counterparts, suggesting the inflow of low-metal gas homogenizes the galaxy's metallicity (Sánchez et al., 2014).

MaNGA has been used more recently to measure star formation radial profiles, rather than aperture values. Radial profiles are created by azimuthally average values in a 2D map in radial bins, capturing any continuous changes in star formation. Pan et al. (2019) created radial profiles of star formation enhancements for a set of merging galaxies in MaNGA (only half the final MaNGA sample was public at the time), which are shown for reference in Figure 1.8. These profiles make clear that the merger-induced starburst at apocentre and coalescence are not limited to the centre of a galaxy. Although seemingly contrary to results found in Barrera-Ballesteros et al.

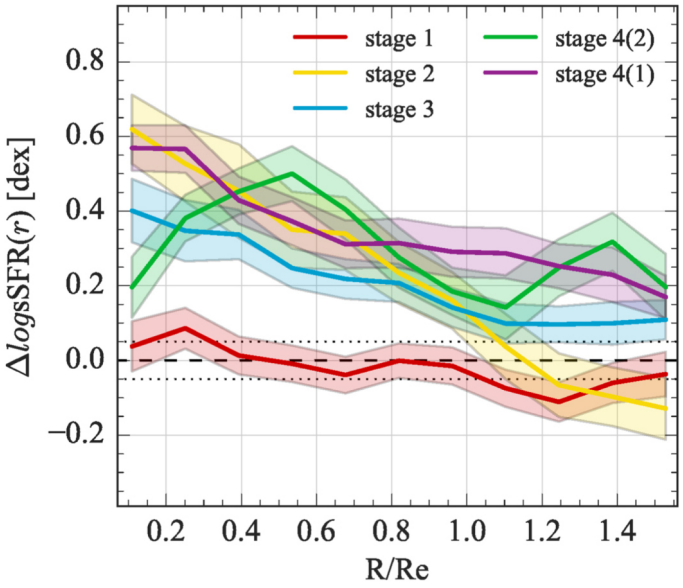

Figure 1.8: Radial profiles of the enhancement in sSFR compared to a control population (Δ logsSFR) for merging galaxies, separated into different interaction stages. The shaded area around each line represents the standard error of the mean. Stage 1 (red) are well separated galaxies with no morphology distortion, indicating they are likely incoming galaxy pairs. Stage 2 (yellow) are close pairs with strong morphological signs of an interaction, such as tails or bridges, assumed to be close to first pericentric passage. Stage 3 (blue) are well separated pairs with weak morphology distortions, implying that first passage has already occurred and galaxies are either approaching or just passing apocentre. Stage 4 represents galaxies near coalescence, with either two highly distorted components overlapping (green) or a single galaxy with obvious tidal features (purple). Source: Pan et al. (2019).

(2015), Figure 1.8 proves how the current stage of an interaction can have significant impact on the resolved star-forming properties of a galaxy, which is concealed when all pair galaxies are considered together.

Even within a single stage of interaction, there is considerable variability. Figure 1.9 shows individual radial profiles of star formation enhancement for a sample of post-merger galaxies in MaNGA (again, only a subset of MaNGA was available at the time of this work), illustrating how mergers with similar central starburst strength can have a variety of extended star-forming behaviour (Thorp et al., 2019). Other properties of a merger can impact resolved radial profiles as well: mergers with a small absolute mass ratio (stellar mass ratio between a target and companion, without assuming which is in the numerator of that ratio) have stronger central enhancements in sSFR

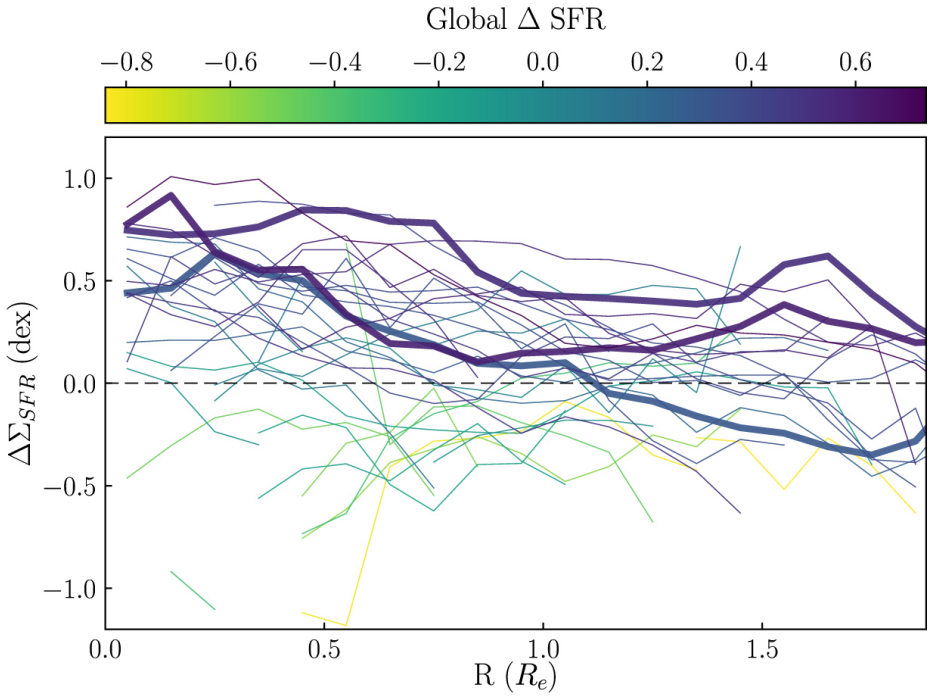

Figure 1.9: Radial profiles of the enhancement in $\Sigma_{\rm SFR}$ ($\Delta\Sigma_{\rm SFR}$) for a sample of 48 post-merger galaxies, each colour-coded by the global offset from the star-forming main sequence. Note that although strong central enhancements in star formation are most common, there is a wide range of changes in resolved star formation. Three profiles with similar central starbursts are highlighted, to demonstrate how much they differ at larger radii. Source: Thorp et al. (2019).

(Steffen et al., 2021). Similarly, if the target is the less massive of the two galaxies it is more likely to exhibit suppression in sSFR at large radii.

Recent MaNGA studies such as Thorp et al. (2019); Pan et al. (2019); Steffen et al. (2021) have focused on examining the radial profiles of resolved merger properties, which can lead to complicated analysis given the highly disturbed morphologies of mergers lack the axisymmetry necessary for interpreting radial profiles. For example, Hwang et al. (2018) looked for anomalously low metallicity (ALM) regions in galaxies and found a handful of mergers where ALM regions were biased towards the side closer to the interacting companion. That kind of complexity is obscured when averaging in radial bins. Merger asymmetry is also reflected in the gas kinematic information provided by MaNGA; Feng et al. (2020) found that mergers with enhanced SFR consistently exhibited kinematic asymmetries. Examining the resolved changes induced in mergers for such large data sets is an ever-growing field of study, with contemporary works learning how to take these finer details into consideration.

There is a growing effort to pair IFS surveys with measurements of molecular gas, derived from ^{12}CO emission, to complement resolved SFR studies. A subsample of 126 CALIFA galaxies were observed with the Combined Array for Research in Millimeter-wave Astronomy (CARMA) to collect ^{12}CO emission line maps, forming the Extragalactic Database for Galaxy Evolution (EDGE) survey (Bolatto et al., 2017). The key synergy between these two instruments allowed for direct comparisons between the star formation and gas content in mergers, revealing that a central concentration of molecular gas existed in interacting galaxies regardless of the degree (or even existence) of a central burst of star formation (Chown et al., 2019). Only 20 of the EDGE-CALIFA galaxies show sign of mergers, making it difficult to probe different interaction properties with this data set.

Molecular gas information was collected for a sample of MaNGA targets in the ALMaQUEST survey (ALMA - MaNGA QUEnching & STar formation survey), similarly bridging the gap between star formation and molecular gas studies as EDGE-CALIFA had (Lin et al., 2020). ALMaQUEST has a small sample size of 46 galaxies, but they are selected with the intent to cover a broad range of specific star formation rates. None of their studies have focused on mergers yet, although Ellison et al. (2020a) found a handful of mergers in their starburst sample that had some of the greatest enhancements in SFE. Given that the goal of ALMaQUEST is to understand how galaxies come to have extremely enhanced or suppressed star formation, a component dedicated to sampling various merger properties is clearly the next crucial addition to this survey.

The resolved study of galaxy mergers is a quickly growing field in astronomy, and the synergy between multi-wavelength observations is opening the door to truly pin down the interplay between star formation and gas in mergers. There are countless unexplored avenues within this field. For example, most of the resolved spectroscopic studies listed thus far focus on studying single values within an aperture or a condensed radial profile. And although extremely beneficial for combining large samples of mergers and making one-to-one comparisons, these methods obscure some of the most interesting 2D information provided by integral field spectroscopy. Although EDGE-CALIFA and ALMaQUEST are opening the doors for combined H_2-SFR studies, little work has been done to investigate the mergers in these samples.

1.5 Thesis outline

The work described herein begins to address the current gaps in our understanding of the resolved properties of interacting galaxies, while simultaneously introducing novel analysis methods for resolved astronomical data. Chapter 2 is an extension from aforementioned studies of radial profiles of merging galaxies (Thorp et al., 2019; Pan et al., 2019; Steffen et al., 2021), but with a sample 8 times larger than what has been used in previous works. Using the largest IFS merger study to date I will investigate resolved trends in star formation as a function of mass ratio and pair separation, truly capturing the diversity of behaviour even for interactions with similar qualities. In conjunction I will examine resolved changes in gas-phase metallicity as it pertains to interaction properties, an area that remains relatively unexplored compared to recent $\Sigma_{\rm SFR}$ studies.

Radial profiles present their own issues for merger studies, as discussed previously. In Chapter 3 I will propose alternative metrics to quantify resolved variations: asymmetry and concentration. This chapter is devoted to testing whether such metrics can be applied to IFS data, implementing levels of realism in simulated galaxies to measure how asymmetry and concentration measurements are impacted by realistic observational conditions. Although I find MaNGA IFS data is of too poor signal-to-noise and resolution to employ such measurements, my analysis provides a layout for what would be required to make such measurements in the future. Additionally, I provide warnings for how current merger studies that use asymmetry and concentration are assuming dangerous equivalencies that could lead to false results.

Chapter 4 will shift focus to multiwavelength studies of mergers. I will present new observations of molecular gas maps acquired with ALMA and mapped to the resolution of MaNGA, as an extension of the ALMaQUEST survey. The 31 mergers observed makes up the largest multiwavelength study of mergers to date, which are specifically selected to sample a broad range of interaction stages. Such a sample can answer a question that evades case studies of gas and star formation in mergers: is merger-induced star formation more likely to be driven by an excess of molecular gas to fuel a starburst, or an enhanced rate at which gas is converted to stars?

Finally, Chapter 5 will review major conclusions from this thesis, and postulate some key science questions that remain to be answered. Astronomers are currently at the forefront of large multiwavelength surveys of mergers, and thus are still experimenting with the best ways to approach these data sets. The diversity of merger

behaviour on a resolved scale continues to exceed expectations, evading our more straightforward models of what occurs during an interaction. Evidence suggests this diversity persists on a kpc-scale, with variations due to local galaxy structure, and perhaps the presence of an AGN. Continued targeted molecular gas studies are necessary to meet the extensiveness of IFS surveys like MaNGA. As these surveys grow, we will need to create novel analysis methods that can quantify resolved trends that have remained difficult for us to capture.

Chapter 2

Star formation and metallicity of mergers in MaNGA

Only recently have integral field spectroscopy (IFS) surveys becomes large enough to perform statistical studies of resolved merger properties, with past studies being limited to dedicated observations and case studies. As the largest IFS survey of its kind, MaNGA (described in detail in the following section) is the optimal data set from which to collect a substantial merger sample. The first large statistical study of post-merger galaxies was completed using the 14th MaNGA data release in Thorp et al. (2019), using a set of 48 post-merger galaxies to investigate the impact of coalescence on resolved star formation rates and gas-phase metallicities. Interacting pairs were analyzed in the 15th data release of MaNGA, with Pan et al. (2019) and Steffen et al. (2021) examining the impact of interaction stage and galaxy mass on $\Sigma_{\rm SFR}$ for $\sim$200 interacting galaxies. The work described in this chapter is a natural continuation of those previous studies, but uses the complete MaNGA survey (data release 17, or DR17), increasing both the post-merger and pair sample by a factor of 8.

The goal of this work is to determine whether merging galaxies have differences in their star formation and metallicity properties on a kpc scale compared to their isolated counterparts. Section 2.1 describes the MaNGA survey in detail, reviewing instrumentation and science goals, along with the spectral reduction pipeline used to convert those observations into physical parameters (PIPE3D, see Section 2.1.1). Although many data products used in this work are taken from public releases, I have additionally computed numerous additional properties required for this work (recounted in Section 2.1.2). I selected a sample of galaxy mergers from MaNGA through visual inspection and galaxy pair catalogues, the properties of which are

described in Section 2.2. Finally I present analysis of the resolved star formation and metallicity properties of mergers in Section 2.3, separating the analysis of post-merger and pair galaxies for clarity, and summarize these results in Section 2.4.

2.1 MaNGA survey

The Mapping Nearby Galaxies at Apache Point Observatory (MaNGA) survey is the largest integral field spectroscopy survey of galaxies to date, thus perfect for the statistical study of resolved merger properties this work will pursue. One of the core programs of the fourth-generation Sloan Digital Sky Survey (SDSS-IV), MaNGA was launched on July 1st 2014 and completed observations of roughly 10,000 nearby (z$\sim$0.03) galaxies over six years, obtaining a galaxy sample with a relatively flat stellar mass distribution (Bundy et al., 2015; Wake et al., 2017; Abdurro'uf et al., 2022). MaNGA uses integral field units (IFUs), hexagonal bundles of individual 2" diameter fibres. The bundles range in diameter from 12" (19 fibres) to 32" (127 fibres). IFUs are attached to aluminum plug plates specifically drilled for particular fields and targets, which are then mounted on the 2.5m Sloan Telescope at the Apache Point Observatory (Gunn et al., 2006). These fibres are fed into the Baryon Oscillation Spectroscopic Survey (BOSS) spectrograph, which covers wavelengths 3600Å - 10300Å with an average spatial resolution of R$\sim$2000. (Smee et al., 2013). A relative spectrophotometric accuracy of 7% from [OII]λ3727 to Hα and 2.4% from Hβ to Hα is required to minimize calibration errors on the SFR and nebular metallicity measurements. Figure 2.1 provides a helpful simplification for IFUs and how they observe galaxy spectra.

MaNGA data must be corrected for flux loss due to system throughput and the atmosphere. Twelve seven-fibre "mini-bundles" are used to target spectrophotometric standards, observations of which can be used to fit the fraction of light covered by the central fibre as a function of wavelength and measure the flux loss due to system throughput (Yan et al., 2016). Sky subtraction is achieved by constructing a highly sampled model background sky based on observations from sky fibres, which can then be subtracted from the science fibre observation. Two sky fibres are added onto every v-groove block of the science IFU (the corners of the hexagon). This set up allows MaNGA to reach $\sim$1% level sky subtraction in the continuum (as is achieved with the BOSS reduction pipeline, Bolton et al. 2012).

The MaNGA survey has both technological and design advantages over other IFS

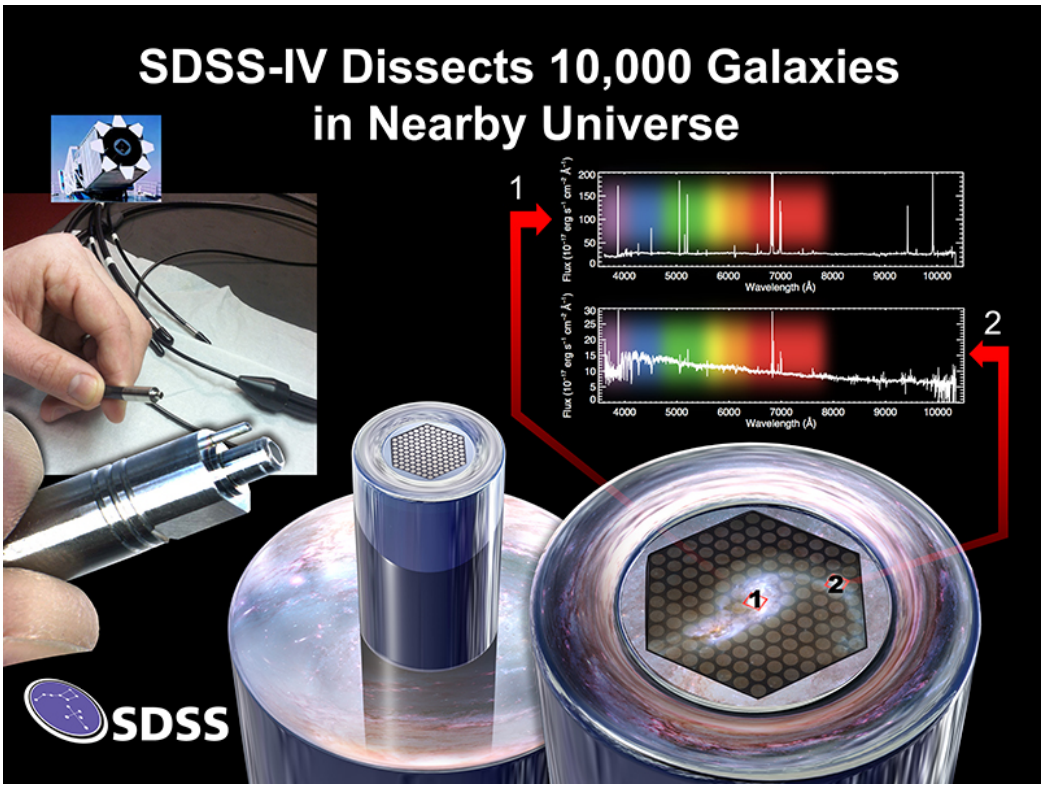

Figure 2.1: Infographic describing the MaNGA IFU, and how it is used to collect data, provided by the SDSS official website. A picture of an IFU, ready to be plugged into an SDSS plate, is shown at left. To the right a zoom-in is provided to show the structure of fibres within the IFU, and how they cover an example galaxy. The infographic demonstrates how each fibre outputs a separate spectrum for different points on the galaxy. The SDSS telescope is shown in the top left. Image Credit: Dana Berry/SkyWorks Digital Inc., David Law, and the SDSS collaboration. Available on the SDSS official website: https://www.sdss.org/surveys/manga/

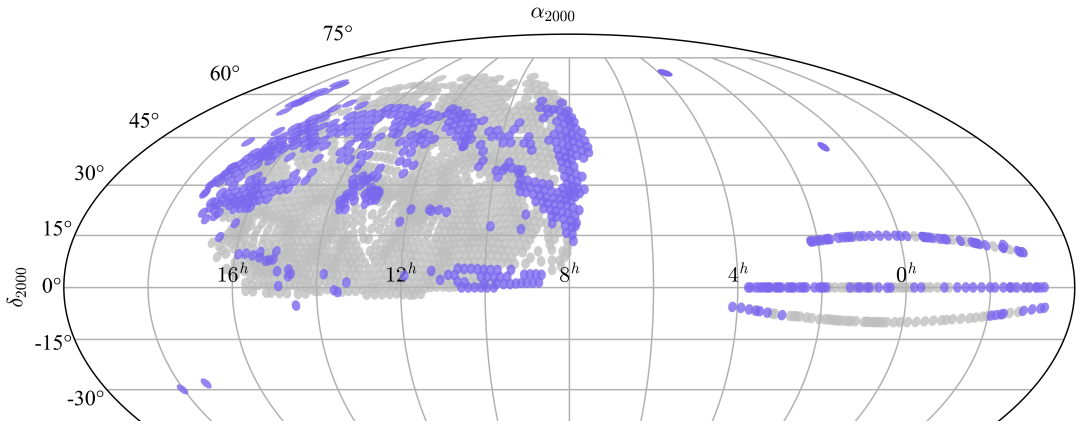

Figure 2.2: MaNGA footprint for the 17th data release, with possible MaNGA sky plates shown in grey and observed sky plates shown in blue. Image available on the SDSS official website: https://www.sdss.org /dr17/manga/manga-survey-strategy/footprint/

surveys. It has a larger wavelength range (3600Å - 10300Å) than other IFS surveys of comparable size such as CALIFA (3750Å - 7000Å) and SAMI (3700Å - 5700Å), as well as a continuous wavelength coverage rather than one which is split over different wavelengths such as SAMI (Sánchez et al., 2012; Allen et al., 2015; Croom et al., 2021). The MaNGA sample size is the largest to date, allowing for studies of much rarer galaxy populations such as post-starbursts, galactic outflows, and major galaxy mergers. The MaNGA sky distribution is displayed in Figure 2.2, with observed sky plates shown in blue and possible sky plates shown in grey. MaNGA target selection requires SDSS imaging and redshifts from the SDSS main spectroscopic sample (Bundy et al., 2015). There is a concentration of plates around a declination of ∼45°, where high altitudes that are not too close to zenith (where tracking is an obstacle for the Altitude-Azimuth SDSS telescope) makes them easiest to observe (Law et al., 2015). Thus every MaNGA observation has single-fibre spectroscopic information and photometric imaging to accompany IFS data.

The MaNGA sample was also designed such that principal components of a galaxy population (i.e., stellar mass, SFR, environment) could be divided into 6 bins, where the number of galaxies in each bin (n) ensures the single-measurement precision is approximately equal to the difference in signal from bin to bin ($\sqrt{n/2}$ quantifies the significance of detected differences between bins). To use a physical example, the precision required for the stellar age gradient is 0.1 dex per decade in R_e, based on variations in the stellar age gradient among currently studied galaxies (Kuntschner

et al., 2010; Spolaor et al., 2010). Thus 50 galaxies per bin are required to achieve a 5σ detection for our three considered principal components. Multiplying 50 by the number of bins to sample all galaxy populations (6^3) results in a sample size of 10,800 galaxies.

MaNGA observations concluded at the end of August 2020, with a two month delay due to COVID-19 closures. 11,273 datacubes were acquired as part of DR17 and released to the public in late December 2021, 10,296 of which are traditional MaNGA-type galaxy observations and 977 from ancillary programs. Within this set only 10,010 unique targets exist, with some repeat observations taken for cross-calibration purposes (Abdurro'uf et al., 2022). Datacubes for each galaxy provide the flux for each spatial pixel (spaxel) as a function of wavelength, calibrated and reduced as part of the MaNGA Data Reduction Pipeline (DRP, Law et al. 2016, 2021). To simplify comparisons to other studies and save research time, rather than performing our own spectral analysis I use publicly released analysis of emission lines and stellar population fits provided by PIPE3D (Sánchez et al., 2016b, 2022).

2.1.1 Spectral reduction and PIPE3D

Optical spectra arise from multiple emitting sources, mainly stars and ionized gas, which need to be decoupled to study individually. The stellar population emission dominates the continuum, thus one can assume the stellar emission results from one or a combination of many single stellar populations (SSP). One can generate synthetic SSPs that replicate key properties of the population (such as initial mass function, star formation rate, and stellar isochrones) to predict the theoretical populations that comprise an observed spectrum. However most galaxies have complex star formation histories, with multiple episodes of star formation activity leading to multiple stellar populations of varying age and metallicities (Worthey, 1994; Gil de Paz & Madore, 2002). A large wavelength range, like MaNGA has, can help minimize these degeneracies by probing multiple stellar populations. The synthesized stellar continuum must also be corrected for dust attenuation, redshifted to account for kinematic effects, and smoothed for velocity dispersion effects (Sánchez et al., 2016a). Once all these factors are accounted for, the modelled stellar spectrum can be subtracted from the observed spectrum to attain the emission lines from ionized gas only.

PIPE3D is a spectroscopic analysis pipeline used on a variety of IFS data sets including MaNGA (Bundy et al., 2015; Sánchez et al., 2018), CALIFA (Sánchez et al.,

2012; Sánchez-Menguiano et al., 2016), SAMI (Croom et al., 2012; Sánchez et al., 2019), and the Multi Unit Spectroscopic Explorer (MUSE, López-Cobá et al. 2020). It uses the SSP analysis tool FIT3D[1] introduced in Sánchez et al. (2006), but updated to iterate over randomized versions of the input spectrum in a Monte-Carlo procedure that provides mean weights for different populations in the stellar component of the spectrum. This methodology also provides uncertainties on these weights and on the final model (Sánchez et al., 2016a). Once the stellar spectrum is subtracted, emission lines are fit with a Gaussian function that accounts for the velocity, velocity dispersion, and intensity of the line. Emission lines are also fit with a low order polynomial to characterize the continuum. Thus PIPE3D can provide information for both emission line parameters from the Gaussian (required to calculate Σ_{SFR} and metallicity), as well as stellar population properties like $\Sigma_{\star}$that are used extensively in this work.

Integrated properties from PIPE3D spectral analysis are provided in a value added catalogue (VAC) (Sánchez et al., 2018, 2022). In this work I will use the total stellar masses ($M_{\star}$) and total star formation rates (SFR) provided by this catalogue. The integrated spectrum and best fitted model are visually inspected, along with emission line maps, by the PIPE3D team to hand remove any galaxy fits that are critical failures (only 6 of the unique galaxies are removed). The remaining galaxies serve as the fundamental sample of this work. Other global properties required such as redshift, galaxy axial ratio, and half-light radius, are provided by the NASA-Sloan Atlas (NSA) (Blanton et al., 2011).

2.1.2 Extended data products

Key data products derived from emission line fluxes are not provided in PIPE3D, in particular star formation rate surface density (Σ_{SFR}) and gas-phase metallicity. I compute these properties from PIPE3D emission lines with my own methodology to have complete control over the quality cuts and corrections made, ensuring data are treated uniformly throughout the process.

Before additional data products can be derived, emission lines need to be corrected for dust effects. Dust grains in a galaxy will absorb more light at shorter wavelengths, thus dust absorption can be measured from the ratio between Hα and Hβ (also called the Balmer decrement, given both lines are part of the Balmer series of emission lines). Given no dust extinction the ratio between these emission lines

[1] http://www.astroscu.unam.mx/sfsanchez/FIT3D

should be fixed (Hα/Hβ = 2.86, Osterbrock & Ferland 2006), any increase in that ratio result from dust reddening. Dust attenuation curves (or how dust impacts a variety of wavelengths) have been well categorized for the Small Magellanic Cloud, the Large Magellanic Cloud, and the Milky Way (Cardelli et al., 1989; Pei, 1992; Gordon et al., 2003). Thus dust reddenning can be corrected for by picking one of these well established attenuation curves to apply to an observed galaxy and measuring the Balmer decrement. For this work I assume a Milky-Way like extinction curve (Cardelli et al., 1989).

Dust corrected Hα fluxes are then used to measure star formation rate surface densities. $\Sigma_{\rm SFR}$ is derived from Hα luminosity, itself determined by multiplying the Hα flux by $4\pi D_L^2$, where D_L is the luminosity distance. Hα luminosity (in erg/s) is then multiplied by 7.9×10^{-42}, a constant derived in Kennicutt et al. (1994), resulting in $\Sigma_{\rm SFR}$ in units of $M_\odot$ yr^{-1} arcsec^{-2}. Units of $\Sigma_{\rm SFR}$ are then converted from $M_\odot$ yr^{-1} arcsec^{-2} to $M_\odot$ yr^{-1} kpc^{-2} using the angular diameter distance, which provides the ratio of physical size in kpc to angular size in arcsec for a given redshift. The constant in the Kennicutt et al. (1994) conversion from luminosity to $M_\odot$ yr^{-1} carries with it a handful of assumptions: that star formation declines exponentially over time, that stellar growth can be defined by the Schaller et al. (1992) stellar evolutionary tracks, that all ionizing flux stems from massive star formation (i.e., the escape fraction of ionizing photons is less than 3%, Leitherer et al. 1995), and that the Salpeter (1955) initial mass function (IMF) describes the total number of stars per unit mass interval.

IMFs are crucial to our analysis of stellar growth in a galaxy and its contribution to the ISM. The IMF is estimated from the luminosity function of a galaxy, and is thus dependent on different stellar evolution theories applied to mass-age-luminosity relations (Chabrier, 2003). I adopt the Salpeter (1955) IMF, the same as is used for PIPE3D data products (Sánchez et al., 2022), which can be described as follows:

$$\xi(M) = \xi_0 M^{-2.35} \tag{2.1}$$

where ξ_0 is a constant that sets the local stellar surface density. The Salpeter IMF assumes most of the galaxy's mass exists in low mass stars, but most of the galaxy's luminosity comes from high mass stars. It has proven consistent with resolved stellar populations in nearby galaxies, though works best for normal disks (Massey, 1998). Later investigations of stellar populations suggest the IMF should flatten at masses lower than 0.5$M_\odot$ (Scalo, 1986; Kroupa, 2002; Chabrier, 2003). But to remain con-

sistent with PIPE3D I elect to use the Salpeter prescription.

Beyond $\Sigma_{\rm SFR}$, gas-phase metallicities are also measured from optical emission lines. Many metallicity calibrations have been suggested, the effectiveness of which can depend highly on the science question one wishes to answer. I elect to use the Marino et al. (2013a) O3N2 technique, which uses the ratio of optical emission lines ([OIII]λ5007/Hβ)/([NII]λ6584/Hα). O3N2 was first introduced by Pettini & Pagel (2004), minimizing extinction effects due to the ratio of close together, strong optical emission lines. Marino et al. (2013a) updated the calibration method using photoionization models of oxygen abundance at a much higher metallicity range, then recalibrated using direct measurements of oxygen abundances from HII regions (Pérez-Montero & Contini, 2009; Pilyugin et al., 2012) and IFS (Marino et al., 2013b). A signal to noise (S/N) greater than 3 is required in all emission lines as well to ensure accurate measurements.

All data products, both those provided by PIPE3D and computed by myself for this work, are inclination corrected using the same b/a axial ratio from the NSA catalogue (Blanton et al., 2011). Very few galaxies appear perfectly face-on in the sky; the degree of this inclination can be approximated using the apparent ellipticity of the galaxy disk (thus the ratio between the minor and major axis, or b/a). I use the b/a axial ratio derived from single Sérsic fits to compute an inclination corrected galactocentric radius for each spaxel.

Along with emission line data products, I also compute my own radius measurements per spaxel in arcseconds and kiloparsecs (kpc). Given each MaNGA spaxel has a set diameter of 0.5", I can convert any distance from the centre of the observation in spaxels to a distance in arcseconds, and thus a distance as a fraction of half-light radii[2]. If the V-band centre of the MaNGA map is more than 10% the total IFU width away from the observed centre, then the V-band centre is used as the true centre for radius measurements. Arcsecond distances are then converted to kiloparsec assuming a cosmology $H_0 = 70$km/s/Mpc, $\Omega_M = 0.3$, and $\Omega_\lambda = 0.7$.

2.1.3 Star-forming criteria

This analysis will only use $\Sigma_{\rm SFR}$ and metallicity values measured from truly star-forming regions, without contamination from AGN or other ionizing sources like shocks and LINERS (Low-ionization nuclear emission regions). Emission is attributed

[2]Half-light radii are determined from single-component Sérsic fits provided by the NSA catalogue, which is provided in arcseconds (Blanton et al., 2011).

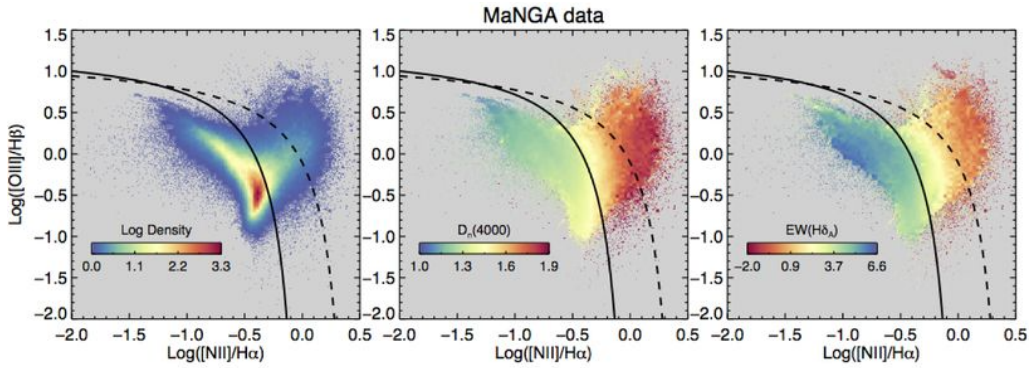

Figure 2.3: A BPT diagnostic diagram for global galaxy emission using emission line data from MaNGA data release 13, published in Belfiore et al. (2016). The Kauffmann et al. (2003) line is shown in solid black, and the Kewley et al. (2001) line is dashed. Within each diagram each axis is divided into 100 bins to create 2D histogram, the first column is colour coded by the log density of these bins. The second and third column are colour-coded by the 4000 Å break index (D4000) and Hδ_A equivalent width (EW); bins with more than 20 galaxies take the average of the bin, those with less show a point for each galaxy. Both D4000 and Hδ_A scale with stellar population age, demonstrating how younger stellar populations lie to the left of the Kauffmann et al. (2003) demarcation.

to the appropriate source by using a Baldwin, Phillips & Telervich (BPT) diagram, which employs ratios of emission lines to categorize Hα flux (Baldwin et al., 1981).

Many studies have published their own star-forming criteria, which can vary significantly based on the goals of that work. I elect to use Kauffmann et al. (2003) BPT emission criterion, an example of which is provided in Figure 2.3. The Kauffmann et al. (2003) criterion was created based on a semi-empirical fit of emission line ratios [OIII]λ5007/Hβ and [NII]λ6584/Hα for over 20,000 SDSS galaxy spectra to distinguish star-forming and AGN emission. Galactic AGN emission tens to have higher [OIII]λ5007/Hβ and [NII]λ6584/Hα than HII regions, given the higher-energy photons produced in the AGN accretion disk induce heating in the narrow line region and thus collisionally excited lines ([NII] and [OIII]) emit more strongly than Balmer recombination lines (Stasińska et al., 2006).

The Kewley et al. (2001) method is an earlier alternative to the Kauffmann et al. (2003) criterion, based on photoionization models. If star-forming regions have emission line ratios similar to HII regions, then photoionization models of O and B star emission (the largest and most massive stars) can provide the maximum emission for

a starburst, beyond which emission must be caused by an AGN. The region between the conservative Kauffmann et al. (2003) and the extended Kewley et al. (2001) criteria is often called the "composite" region, having contribution from both AGN and star formation. More recent works have delved into contamination from AGN in the traditional "star-forming" regions of the BPT diagram, and the viability of the BPT diagram as an AGN classifier in general (Stasińska et al., 2008; Belfiore et al., 2016; Agostino & Salim, 2019). One can also replace the [NII]λ6584 line with [SII]λ6717 or [OI]λ6300 to distinguish low luminosity AGN (Sefert emission) and LINERs, which are similar to Seyfert but with much stronger low-ionization lines (Veilleux & Osterbrock, 1987; Kewley et al., 2006b). But given our focus on star formation alone I elect to stick with the original Kauffmann et al. (2003) criteria.

Additional quality cuts are applied to the spaxel data as well, such as requiring each diagnostic emission line from the BPT diagram have signal-to-noise ratio (S/N) greater than 3 to ensure accurate classification. The S/N cut is also important for measurements of $\Sigma_{\rm SFR}$, where large S/N ratios in Hα emission are necessary for accurate measurements. A secondary cut in Hα equivalent width (EW) $>$ 6Å is also necessary to ensure only young massive stars contribute to Hα emission. For the remainder of this chapter only star-forming spaxels will be considered when examining $\Sigma_{\rm SFR}$ and metallicity, although alternatives to this method will be addressed in Chapter 4.

2.2 Merger classification algorithm and sample characteristics

To complete a study of merging galaxies, they must first be distinguished from non-interacting galaxies that make up the majority of the MaNGA sample. Galaxy classification techniques can differ significantly with the goals of the project: whether the study prioritizes purity or completeness, as well as how much time one can commit to a classification scheme. The following section will review these techniques, highlighting their advantages and drawbacks which lead to our final choice of a visual classification scheme. Following this, I will introduce the final MaNGA merger sample and its properties.

2.2.1 Review and evaluation of merger classification methods

The most automated merger selection method, with minimal user adjustment, would be to use non-parametric morphology measurements to characterize how likely it is for

a recent merger event to have occurred. There are a few non-parametric measurements that can be used that will be discussed below, the most popular being combinations of asymmetry and concentration (A+C) or Gini and M_{20} (G+M_{20}).

A combination of concentration and asymmetry measurements can be used to identify whether a recent catastrophic merger has occurred, with asymmetry capturing asymmetric structures caused by a merger event, and concentration capturing the central gas accretion and subsequent starburst (Conselice et al., 2000, 2003; Lotz et al., 2004, 2008). Shape asymmetry, introduced by Pawlik et al. (2016), serves as a useful alternative to regular asymmetry given it is not weighted by light from the galaxy, and thus is optimized to capture faint asymmetric features. Alternatively, the Gini coefficient, originally developed to quantify wealth disparities, has been adopted to measured the distribution of flux within a galaxy in a similar manner to concentration (without relying on the geometric centre overlapping with the centre of the distribution, Abraham et al. 2003). Gini is paired with M_{20}, a morphology parameter which quantifies the second order moment of the brightest 20% of the galaxy, resulting in a combined merger classifier more sensitive to interactions with large mass ratios than other non-parametric morphology measurements (Lotz et al., 2010a).

Non-parametric morphology measurements can be used in a completely automated fashion, making them extremely useful for classification of large galaxy surveys. But their sensitivity to the data quality and heavy biases to particular galaxy types can seriously impact any results from a merger study. Asymmetry and concentration in particular are heavily biased towards galaxies that have just coalesced, in addition to being strongly correlated with (B-V) colour and Hubble type (Lotz et al., 2008; Hambleton et al., 2011). Non-parametric morphologies also only probe the most recent merger events: when IllustrisTNG galaxies are degraded to CFIS image quality, over 70% of galaxies that have had a merger event within ∼200 Myr are missed by Gini-M_{20}, asymmetry, and shape asymmetry classifiers (Wilkinson et al., 2022). Chapter 3 discusses in detail how the resolution and measurement uncertainty of an observation can drastically impact non-parametric morphology measurements and hinder merger studies. As the shortfalls of non-parametric morphologies have become more obvious, extragalactic astronomers have searched for alternative methods that can provide a more complete classification.

There is a growing foundation of studies which use machine learning to identify galaxy mergers. Machine learning techniques have already be applied to identify different Hubble types (De La Calleja & Fuentes, 2004; Banerji et al., 2010) and irreg-

ular vs disk galaxies (Huertas-Company et al., 2015). Convolutional Neural Networks (CNN) are a subset of machine learning that are trained to classify galaxies based on an initial data set - usually a cosmological simulation where one can know with certainty a merger has occurred within a very large sample (Domínguez Sánchez et al., 2019). CNNs have proven to be more effective than non-parametric morphologies at identifying merger samples (Ackermann et al., 2018; Walmsley et al., 2019; Bickley et al., 2021). However, the quality of the training set can have a serious impact on CNN performance. For example, a CNN trained on SDSS data can identify visually classified mergers with 91.5% accuracy, but only attains 64.6% accuracy when applied to galaxies in the Evolution and Assembly of GaLaxies and their Environments (EAGLE) simulations (Pearson et al., 2019a). When using a simulation as a training set, the application of realistic observational effects such as sky noise, PSF, and background objects, are crucial to developing an accurate CNN classifier (Bottrell et al., 2019b; Huertas-Company et al., 2019). Even if the accuracy of a CNN is exceptionally high, the intrinsic rarity of mergers will result in even a small inaccuracy leading to a highly impure sample. Bickley et al. (2021) demonstrated that even with the default CNN detection threshold, resulting in 89% completeness, a CNN merger sample would only have 6% purity. Only visual classifications completed by astronomers surpassed the CNN purity, although the completeness of the CNN classification was much higher.

Given the limitations of the methods described above, I elect to use a visual classification. The demonstrated incompleteness of non-parametric morphology indicators eliminates this method as useful to this work. A CNN could provide excellent classification, but the time it would take to train a CNN on SDSS like data, apply it to the new MaNGA sample, and do a manual review to mitigate issues of impurity would constitute an entirely separate project. Given I had already classified roughly half of the MaNGA sample (both DR14 and DR15) as part of my Master's project, manual classification of the remaining $\sim$5000 was not unmanageable (I average 1 classification every 7 seconds). By combining visual classification with well established catalogues of interacting galaxy pairs, I can create a large but representative merger sample in a relatively small amount of time considering the manual work necessary.

2.2.2 MaNGA sample selection and characteristics

My sample of merging galaxies is collected through two major steps. First I complete visual classification of SDSS *gri*-images (r-band half-light surface brightness limit of 23.0 mag arcsec^2, Strauss et al. 2002). Post-merger galaxies are identified by clear morphological disturbances likely to stem from a recent interactions, such as tidal tails or shells. Galaxies with similar structures, but a clear companion either on the IFU or visually connected to the target are considered visual pairs.

The second step is to collect spectroscopic galaxy pairs, where a visual connection between a galaxy and its possible companion is unclear, but the 3D spatial information available with spectra reveals the two are close enough that a recent or incoming interaction is highly likely. This is a crucial step to include galaxies on their first approach in our sample, which will have little to no morphological indications of an interaction. One can identify how close two galaxies are using the on-sky separation between the two (projected separation, or r_p), along with the difference in velocity between two galaxies (Δv) from spectral redshift. A combined r_p and Δv selection has been used extensively in other observational studies of interacting galaxies (Barton et al., 2000; Alonso et al., 2004; Ellison et al., 2008a; Patton et al., 2011; Scudder et al., 2012; Fu et al., 2018).

I select spectroscopic pairs from the Patton et al. (2016) catalogue, which provides information on the closest companion for each galaxy in SDSS DR7, with a companion boundary at $r_p = 1$ Mpc and Δv=1000 km/s. I match the Patton et al. (2016) catalogue to MaNGA based on the right ascension (RA) and declination (DECL) provided by both catalogues, using the Astropy[3] match-to-catalog-sky package (The Astropy Collaboration et al., 2013, 2018). If the RA/DECL position in MaNGA and within the Patton et al. (2016) catalogue match within 2", I consider them to be the same galaxy.

I then limit our spectroscopic pairs to those with $r_p < 100$ kpc and Δv<500 km/s. Most studies agree that within 50-100 kpc a companion galaxy will begin to influence the primary galaxy, even on a first encounter (Barton et al., 2000; Wong et al., 2011; Scudder et al., 2012; Patton et al., 2013; Ellison et al., 2013b). At close separations (< 20 h^{-1}kpc) galaxies with Δv< 500 km/s will show the morphological indicators of a merger event (Lin et al., 2004), though enhancements in star formation activity often do not occur until Δv$< 100 - 300$ km/s (Yang et al., 2007; Von Der Linden

[3]http://www.astropy.org

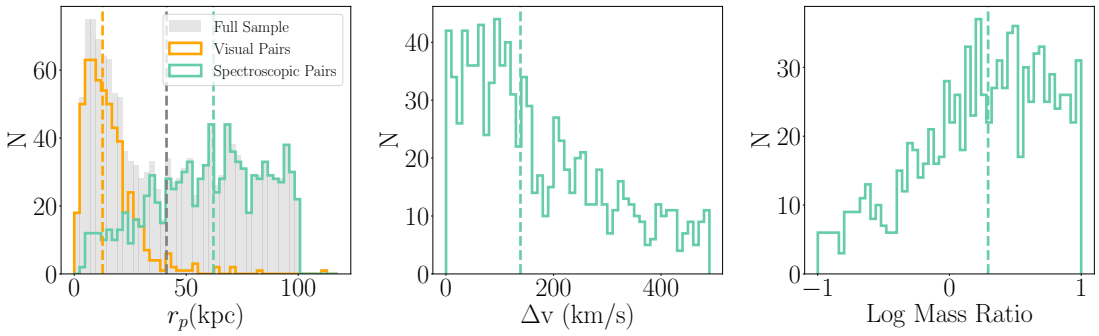

Figure 2.4: *Left:* The distribution of projected separation in kpc between a target galaxy and its companion, separated into visual pairs (orange) and spectroscopic pairs (green). The r_p distribution for the full sample is shown as a shaded grey histogram. The median of each distribution is shown as a vertical dashed line. Note that the visual pair sample is heavily biased to close pairs, which are undersampled by the spectroscopic pairs. *Middle:* The distribution of change in line of sight velocity for the spectroscopic pairs (visual pairs do not have Δv or μ information) in km/s. *Right:* The distribution of mass ratio for the spectroscopic pairs. Log $\mu = 0$ means that the two galaxies interacting galaxies are the same size, log $\mu < 0$ means the target MaNGA galaxy is the smaller of the two, and log $\mu > 0$ means the target is the larger of the two.

et al., 2007). I also limit the spectroscopic sample to galaxies interacting with a companion no more than 10 times larger or smaller in mass, by setting the mass ratio ($\mu = \mathrm{M_{target}/M_{companion}}$) to be greater than 0.1 and less than 10. Both simulations (Cox et al., 2008; Lotz et al., 2010b) and observations (Barton et al., 2000; Lambas et al., 2003; Patton et al., 2011) have used mass ratio to constrain merger studies to those that will substantially effect the galaxy.

The distributions for these key pair properties along with pair mass ratio ($\mu = \mathrm{M_{target}/M_{companion}}$) are displayed in Figure 2.4. The spectroscopic pair sample has fewer objects at small r_p than larger r_p. This is due to the design of SDSS DR17: the size of single spectroscopic fibre plugs requires a minimum separation of 55" between each target. This can constitute anywhere between 10 kpc and 100 kpc, depending on the redshift of the galaxy. Therefore the visual pairs are essential to investigate interactions with small r_p. For the rest of this work I will refer to visual and spectroscopic pairs as a single "interacting pair" sample.

The final merger sample is composed of 400 post-mergers and 1523 interacting pairs (551 of which are visually confirmed, with no spectroscopic information of the companion). Images of each merger galaxy are provided in Appendix A.1. Given I

intend to investigate the evolution of star formation with this sample, both the pair and post-merger samples need to cover a comprehensive range of star formation and mass properties. The position of both the pair and post-merger sample in the SFR - $M_\star$ plane are displayed in Figure 2.5, using values from the PIPE3D VAC (see Section 2.1.1 for details). Mergers are found both above, on, and far below the star-forming main sequence (though post-mergers are more heavily biased to on or above). There is a slight tendency for high mass mergers to have smaller projected separations, which may be due to massive galaxies in cluster environments where r_p is very small (Ellison et al., 2010; Patton et al., 2011; Alonso et al., 2012).

The bottom panel of Figure 2.5 compares the offset from the star-forming main sequence (ΔSFR) for our pair and post-merger sample. ΔSFR is measured by taking the difference between a galaxy's SFR and the average SFR of all galaxies "on" the star-forming main sequence within 0.1 dex $M_\star$ and 0.05 z of the target. To define the star-forming main sequence I first make a by-eye cut based on the grey histogram in Figure 2.5. I then fit galaxies above that cut with a 1st order polynomial. Any galaxy within 2σ (roughly 0.6 dex difference in SFR) of that fit is considered "on" the star-forming main sequence.

The pair sample has a lower median ΔSFR than the rest of MaNGA, as displayed in the bottom panel of Figure 2.5, likely due to the fact that galaxies in denser environments have lower star formation rates than those in the field (Ellison et al., 2010; Patton et al., 2011; Alonso et al., 2012). This bias for close red pairs is also why the pair sample has a lower median ΔSFR than the rest of MaNGA. The post-merger sample, on the other hand, has a larger median ΔSFR value, confirming that on average post-mergers boost star formation in their constituents. A heightened ΔSFR could also stem from the visual classification of the post-mergers, as gas-rich mergers will have longer lasting morphological features and stronger starbursts (Lotz et al., 2008, 2010b).

2.3 Results: resolved properties of mergers

The goal of this work is to determine whether merging galaxies have different star formation and metallicity properties on a kpc scale compared to their isolated counterparts. If the star formation in mergers is distinct from that triggered by regular environmental factors, there should be changes in magnitude or location within a merger. Previous merger studies have found merging galaxies can have far more ex-

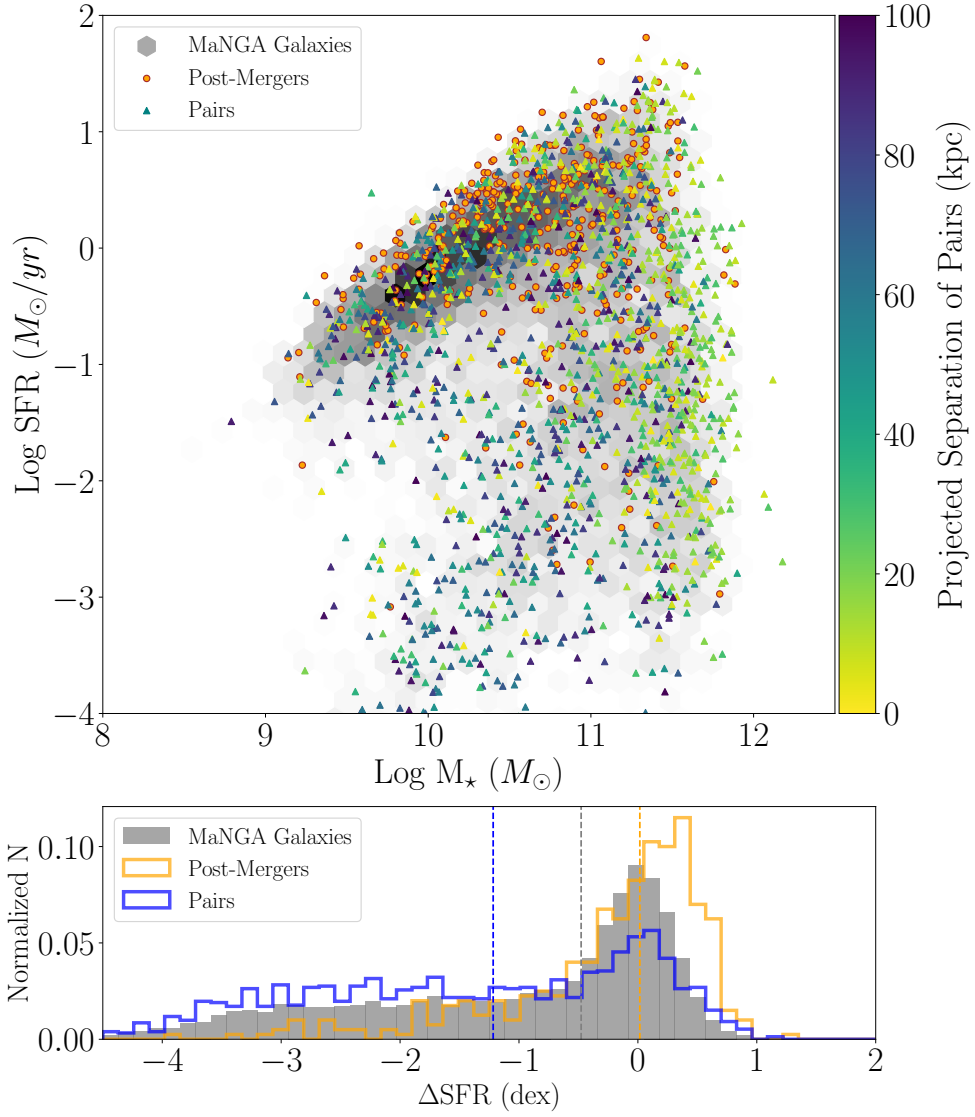

Figure 2.5: *Top:* Total star formation rate versus total stellar mass for the entire MaNGA survey (grey), with the post-merger (circles) and pair (triangle) galaxies select for this work over plot. Pair galaxies are colour-coded by the projected separation between the target and its companion (in kpc). Note that both the pre- and post-coalescence sample cover a broad range of SFRs and M$_\star$s. *Bottom:* Distribution of global ΔSFR values for non-interacting MaNGA galaxies (grey), post-mergers (orange), and pair galaxies (blue). The median ΔSFR of each sample are -0.49, 0.02, and -1.17 dex respectively (represented as dashed vertical lines). The pair sample is likely biased towards lower ΔSFR than the rest of MaNGA because it oversamples dense environments where star formation is overall lower. The post-merger sample is offset to larger ΔSFR, confirming that merger events on average boost star formation (at least in the timescale for which mergers can be visually identified).

tended star formation than their isolated counterparts (Thorp et al., 2019; Pan et al., 2019; Steffen et al., 2021). Additionally, Hwang et al. (2018) found that for a handful of interacting galaxy pairs in MaNGA, there was a clear bias towards lowered metallicities on the side closest to the companion. The following section will investigate how mergers differ from expected star-forming behaviour and metallicity content based on established scaling relations.

2.3.1 Resolved scaling relations for merging galaxies

Isolated, pair, and post-merger galaxies can be better compared using well established scaling relations, such as the resolved star-forming main sequence (rSFMS, Sánchez et al. 2013; Cano-Díaz et al. 2016; González Delgado et al. 2016) and the resolved mass-metallicity relation (rMZR, Rosales-Ortega et al. 2012; Sánchez et al. 2013; Barrera-Ballesteros et al. 2016). As discussed in Chapter 1, isolated galaxies exhibit considerable scatter on the rSFMS and rMZR (Ho et al., 2017; Lin et al., 2019). Different morphological environment appears to create significant variation about these relations even within a single galaxy (Pessa et al., 2021; Querejeta et al., 2019). But scatter can also be tied to changes in gas fraction and star formation efficiency (SFE), both of which change drastically with a galaxy merger (see Chapter 4 for details). Examining the resolved scaling relations of both populations will unveil whether mergers create a unique shift in properties.

Figure 2.6 compares the rSFMS and rMZR for the post-merger (orange) and pair (blue) sample to a control sample of non-interacting star-forming spaxels from MaNGA. All control spaxels are chosen to match at least one post-merger and pair galaxy within 0.1 dex $\Sigma_\star$, 0.1 dex $M_\star$, and 0.1R_e (further description of the matching criteria is provided in Subsection 2.3.1.1). All three populations have considerable overlap in both relations, indicating that the merger event does not impact all spaxels in a strong enough way to shift the entire population. To test whether the pair and post-merger sample could be drawn randomly from our non-interacting sample I perform a Kolmogorov-Smirnov (KS) test, where a lower P_{KS} value means low probability for this initial hypothesis. Both the pair and post-merger sample have $P_{KS} \approx 0$ for both $\Sigma_\star$, $\Sigma_{\rm SFR}$, and metallicity, so there may be a truly distinct quality between the two that is obscured by the scatter on both relations.

There is a small bias for pair and post-merger galaxies to have higher $\Sigma_{\rm SFR}$ and $\Sigma_\star$ than their control, although more so for post-mergers than pairs. The difference in the

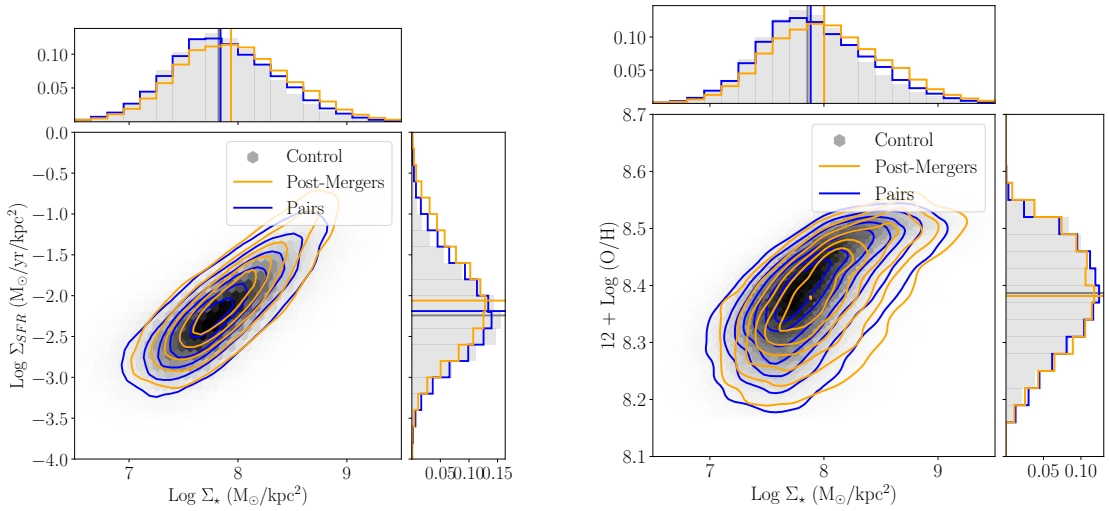

Figure 2.6: *Left:* $\Sigma_{\rm SFR}$ vs. $\Sigma_\star$ for all star-forming spaxels in the MaNGA survey (grey hexbin representing density of spaxels in each bin, with the distribution of the post-merger (orange) and pair (blue) sample overplot. Histograms for each variable are provided on the x and y axis, with a vertical line indicating the mean of the distribution. *Right:* The same as the left diagram, but with metallicity plot on the y-axis to show the mass-metallicity relation. Note that post-mergers seems to be biased towards larger $\Sigma_\star$ and $\Sigma_{\rm SFR}$ values, but not lower metallicities. For the rMZR, this bias for larger $\Sigma_\star$ not corresponding to a bias towards higher metallicities implies that post-mergers have lower metallicities than is expected given the average relation established by the rMZR.

median $\Sigma_{\rm SFR}$ value is 0.02 dex for pairs and 0.11 dex for post-mergers. $\Sigma_\star$ is also offset for both populations, with the difference between median $\Sigma_\star$ values being 0.05 dex for pairs and 0.18 dex for post-mergers. A shift in $\Sigma_\star$ is also seen in the rMZR, shown in the right panel of Figure 2.6. Although the median metallicity values are almost identical, the merger $\Sigma_\star$ values are shifted to the right, with a median difference of 0.03 dex for pairs and 0.14 dex for post-mergers. As a result it also looks as if the post-merger sample is shift to the right of the zMZR, exhibiting a lower metallicity range for the given $\Sigma_\star$ values.

Given a sizeable bias towards large $\Sigma_\star$ is only present for the post-merger galaxies, this could be evidence that mergers can induce bulge growth. Many galaxy evolution models rely on mergers for black hole and bulge growth (Hopkins et al., 2010; Somerville & Davé, 2015), though this is not the only route through which bulges build up mass (Johansson et al., 2012; Ceverino et al., 2015; Bell et al., 2017). Observations appears to support mergers as a route of bulge growth, as some bulge-dominated ellip-

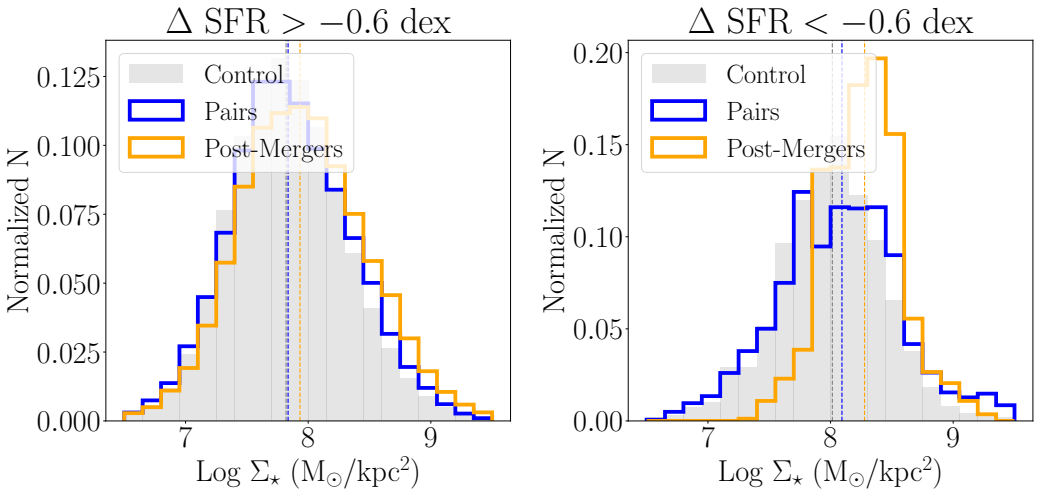

Figure 2.7: $\Sigma_\star$ distribution of spaxels from control galaxies (grey), pair galaxies (blue), and post-mergers (orange). Spaxel distributions are separated into two groups: those belonging to galaxies roughly on or above the SFMS (left, Δ SFR> -0.6 dex), and those belonging to galaxies below the SFMS (right, Δ SFR< -0.6 dex). The median of each distribution is shown as a dashed line. Although Figure 2.6 showed that on average post-merger spaxels are biased to large $\Sigma_\star$, this diagram reveals that bias to be far more prominent for galaxies below the main sequence than those on it. If mergers can trigger bulge growth, there should be an observable build up of larger $\Sigma_\star$ in elliptical galaxies, as is seen here.

ticals exhibit clear signs that a merger occurred in the past (Toomre, 1977; Schweizer, 1982; Malin & Carter, 1983). If post-mergers in our sample are accruing mass in the bulge of the galaxy, we might expect a bias in large $\Sigma_\star$ post-coalescence. This effect will be more prevalent in green valley and quenched post-mergers, long after the subsequent starburst when a galaxy has had time to time to build bulge mass. Figure 2.7 shows the $\Sigma_\star$ distribution for the control, pair, and post-merger galaxies that are roughly on (left, ΔSFR > -0.6 dex[4]) or below (right, Δ SFR< -0.6 dex) the star forming main sequence. The post-mergers below the SFMS are more strongly biased towards large $\Sigma_\star$ than those on or above the SFMS, alluding to a possible connection between post-coalescence of bulge-growth.

Although examining the resolved scaling relations of each population is informative, more can be revealed by quantifying the spaxel by spaxel offsets from scaling relations. I.e., where is $\Sigma_{\rm SFR}$ /metallicity greater than or less than you might expect

[4]For the computation of ΔSFR the star-forming main sequence is defined as galaxies within 2σ of a fit to the star-forming galaxies (see Section 2.1 for details). 2σ roughly corresponds to 0.6 dex ΔSFR, hence the choice of ΔSFR=-0.6 dex to define the bottom of the SFMS

from the control population? The following section will compute such offsets, and explore what they can tell us about merger star formation and gas-phase metallicity.

2.3.1.1 Offsets from scaling relations

Although comparing these scaling relations directly can be revealing, it can be more useful to quantify the offset from each relation for each spaxel. Measuring offsets at fixed stellar mass has been done extensively for global SFR and O/H (e.g. Ellison et al. 2008a; Scudder et al. 2012; Patton et al. 2013). More recently such methods have been applied to resolved scaling relations as well (Ellison et al., 2018a; Barrera-Ballesteros et al., 2018; Rowlands et al., 2018). Quantifying the offset in scaling relations can help us better pick out regions of anomalously high/low star formation activity or metallicity. Given recent studies have found the FMR holds on a kpc-scale, one would expect spaxels with heightened $\Sigma_{\rm SFR}$ to also have diluted metallicities (Salim et al., 2014; Gao et al., 2018; Cresci et al., 2019; Sánchez Almeida & Sánchez-Menguiano, 2019). However both post-mergers and interacting pairs are outliers from the global FMR, with greater metallicity dilution than is expected based on the FMR and each galaxy's total mass and star formation rate. One could postulate, then, that mergers must be outliers on the resolved FMR as well.

Offsets from the rSFMS ($\Delta\Sigma_{\rm SFR}$) and rMZR (ΔO/H) are determined based on a specific control sample of spaxels for each measurement. This control is taken from all star-forming spaxels in MaNGA, defined by the criteria established in Section 2.1.3, with b/a>0.34 (excluding galaxies with inclination greater than 70°). From this control pool I select spaxels that match the target spaxel within 0.1 dex of $\Sigma_\star$. The control sample is also matched within 0.1 dex of $M_\star$ to account for the bias towards low metallicities at $M_\star \lesssim 10^{9.5} M_\odot$ (Barrera-Ballesteros et al., 2016) and metallicity gradient dependencies on $M_\star$ (Belfiore et al., 2017). Considering each galaxy has a gradient in $\Sigma_{\rm SFR}$ and O/H dependent on radius, the control is also matched within 0.1 R_e (Rupke et al., 2010; Montuori et al., 2010; Perez et al., 2011). Thus for every spaxel with accurate $\Sigma_{\rm SFR}$ and O/H, I measure an offset $\Delta = \log(\text{spaxel}) - \log(\text{control})$, so long as there are at least 5 spaxels in the control pool that meet these criteria. If less than 5 control spaxels are found the tolerance is increased by 0.1 dex $\Sigma_\star$, 0.1 dex $M_\star$, and 0.1 R_e. Over 96% of spaxels have a minimum of 5 spaxels within the minimum matching criteria, and over 99% only require one growth of the matching criteria (those that require more than one growth are excluded).

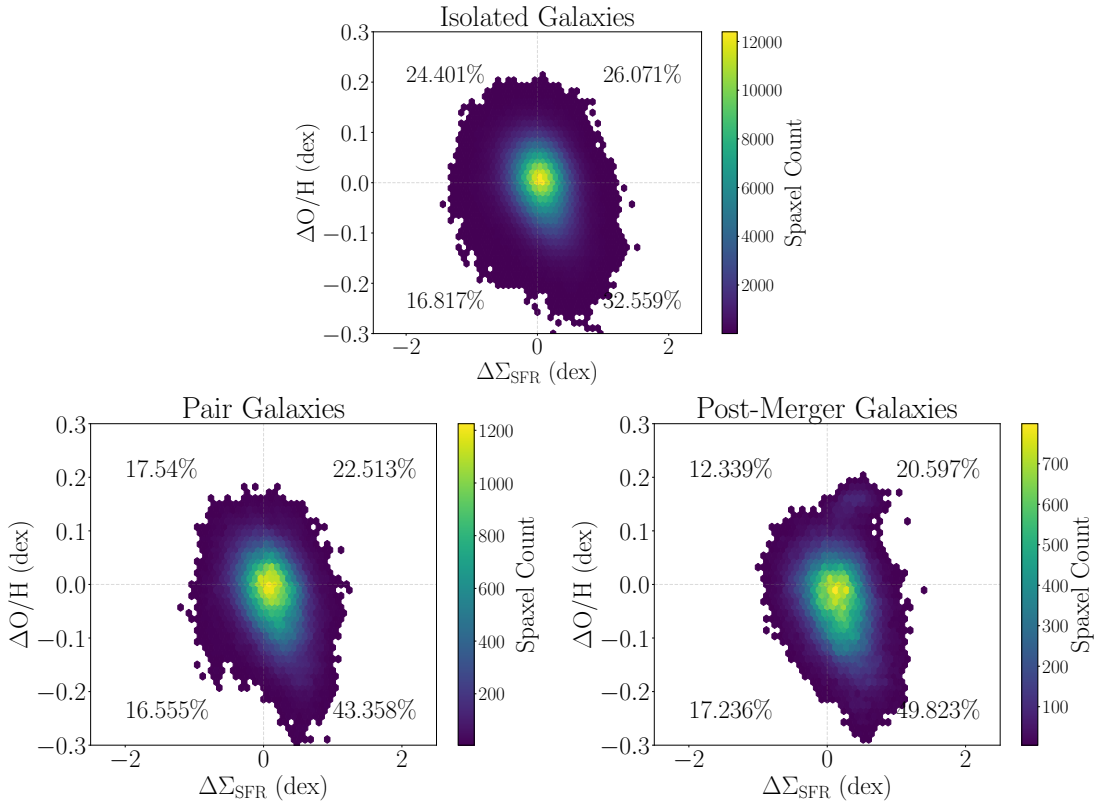

Figure 2.8: ΔO/H vs. $\Delta\Sigma_{\mathrm{SFR}}$ for all star-forming spaxels in the isolated MaNGA sample (top), pair sample (bottom left), and post-merger sample (bottom right). The diagram is broken into four quadrants depending on the sign of each offset parameter, with the percentage of spaxels in each quadrant displayed in the figure. Both pair and post-merger galaxies have a larger percentage of spaxels with positive $\Delta\Sigma_{\mathrm{SFR}}$ and negative ΔO/H compared to the isolated sample, as might be expected if low-metallicity gas inflows resulting from mergers trigger boosts in star formation. One would expect spaxels with positive $\Delta\Sigma_{\mathrm{SFR}}$ to have negative ΔO/H, and those with positive ΔO/H to have negative $\Delta\Sigma_{\mathrm{SFR}}$ (if low metallicity is any indicator for the molecular gas in a system). There is only a small Pearson's correlation coefficient (-0.2) between ΔO/H and $\Delta\Sigma_{\mathrm{SFR}}$. Although the two variables are not strictly correlated, there can still be a crucial physical connection between the two.

Figure 2.8 shows plots of ΔO/H vs. $\Delta\Sigma_{\rm SFR}$ for all three samples. If galaxies obey a resolved FMR, the majority of spaxels should be in the top-left or bottom-right quadrant (where diluted metallicity corresponds to a boost in star formation). Instead of such a tendency, there is a relatively even distribution between the four quadrants in Figure 2.8, with 24.412% with $-\Delta\Sigma_{\rm SFR}$ $+\Delta$O/H, 26.006% with $+\Delta\Sigma_{\rm SFR}$ $+\Delta$O/H, 16.931% with $-\Delta\Sigma_{\rm SFR}$ $-\Delta$O/H, and 32.4971% with $+\Delta\Sigma_{\rm SFR}$ $-\Delta$O/H. Such a distribution does not negate the existence of a rFMR, but rather captures the scatter around such a relation. Pair galaxies and mergers have similar percentages of spaxels in the $+\Delta\Sigma_{\rm SFR}$ $+\Delta$O/H and $-\Delta\Sigma_{\rm SFR}$ $-\Delta$O/H regions. Where they differ, however, is with a strong partiality for $+\Delta\Sigma_{\rm SFR}$ $-\Delta$O/H and away from $-\Delta\Sigma_{\rm SFR}$ $+\Delta$O/H. Pairs and post-mergers have 43.405% and 49.798% of spaxels in the $+\Delta\Sigma_{\rm SFR}$ $-\Delta$O/H, respectively, compared to the much smaller 32.4971% for isolated galaxies.

To evaluate whether these differences in percentage are significant, I test how likely a random sample of isolated galaxy spaxels could reach these high percentages in the $+\Delta\Sigma_{\rm SFR}$ $-\Delta$O/H . I select a random sample of spaxels the size of the post-merger set, then recompute the percentage of spaxels in the $+\Delta\Sigma_{\rm SFR}$ $-\Delta$O/H regime. Of 10,000 randomly selected isolated spaxel samples, none can reach 49.798% in the $+\Delta\Sigma_{\rm SFR}$ $-\Delta$O/H . Repeating this process with the pair sample yields similar results, verifying that the excess of spaxels in $+\Delta\Sigma_{\rm SFR}$ $-\Delta$O/H is significantly different than that in the isolated set. Overall merging galaxies have more spaxels with diluted metallicity than isolated galaxies (as was seen in Bustamante et al. 2018), as well as being more likely to have enhanced $\Sigma_{\rm SFR}$.

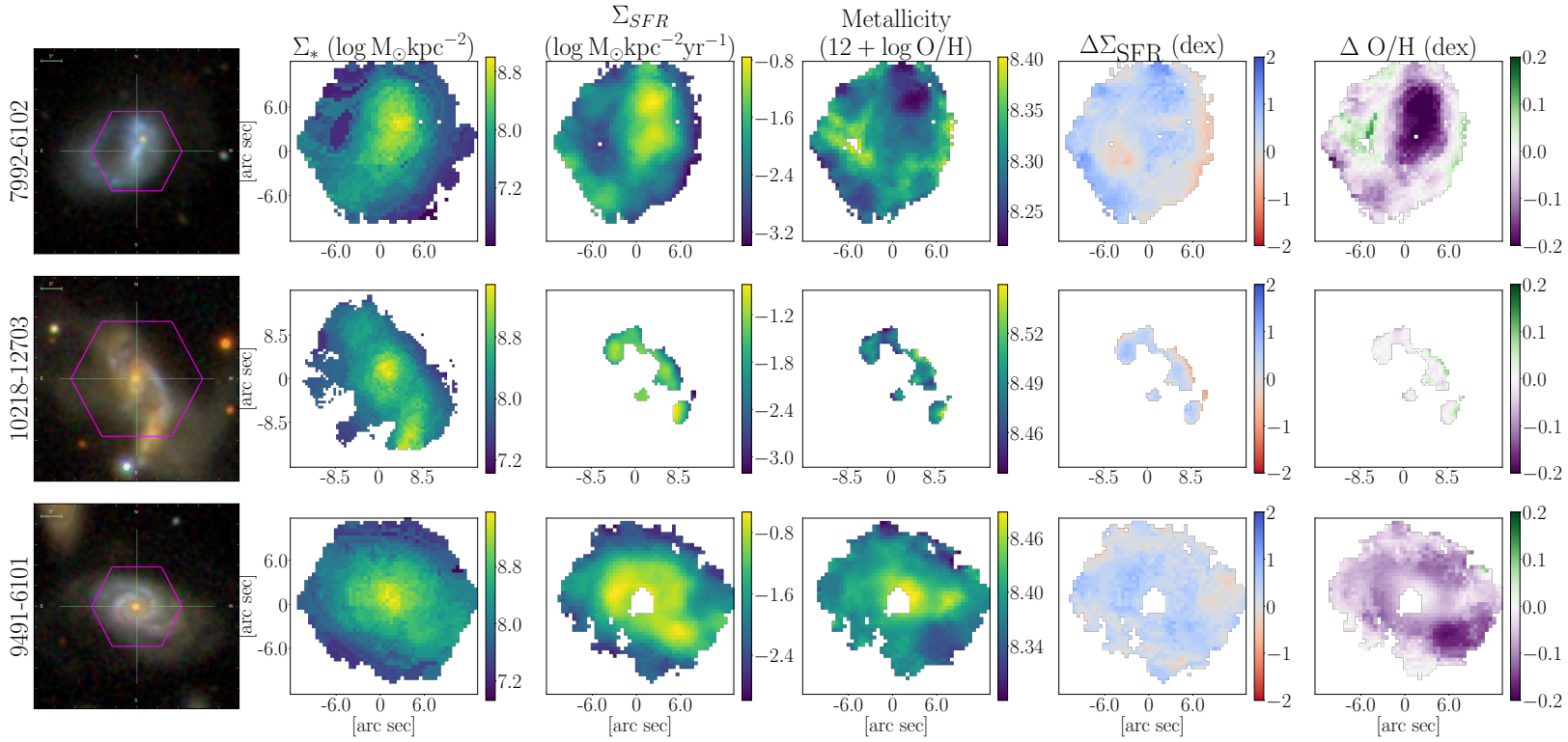

Figure 2.9: Data product maps for a post-merger (top), visual disturbed pair with the companion on the IFU (middle), and pair galaxy with a spectroscopic companion to the bottom right (bottom). From left to right: the SDSS *gri*-image (with MaNGA footprint overplot in magenta), stellar mass surface density (from PIPE3D), star formation rate surface density (derived from Hα), O3N2 metallicity, $\Delta\Sigma_{\rm SFR}$, and ΔO/H. For all data product maps besides $\Sigma_\star$, only star-forming spaxels are shown. Both the patchiness and complexity of the map varies greatly between galaxies.

Concealed in both the resolved scaling relations and offset parameters is the spatial information that is so crucial to our understanding of merger-driven star formation. Figure 2.9 shows some of the resolved properties of three different galaxy mergers: a post merger (top), a visually disturbed pair (middle), and a pair with a spectroscopically identified companion (bottom). From three examples alone one can see the obvious spatial variations missed when all spaxels are examined together. The post-merger in the top row is so highly disturbed a tidal arm creates extreme star formation activity even at large radii. The middle galaxy has far fewer spaxels with star-forming regions, due to central AGN contamination, and thus has a much patchier map of offset properties. And the final galaxy, despite having a comparatively normal morphology and complete map, has an anomalously low-metallicity region on one side of the galaxy (in the direction of the spectroscopic pair, which is off to the bottom right). The following section investigates trends in star formation and metallicity as a function of radius to attempt to capture this complexity.

2.3.2 Post-merger radial profiles

Figure 2.12 shows radial profiles of $\Delta\Sigma_{\rm SFR}$ for all post-merger galaxies with more than 10 spaxels, broken into bins of ΔSFR. Radial profiles are created by azimuthally averaging information on a data product map, in this case taking the median of all $\Delta\Sigma_{\rm SFR}$ values within a bin of $0.1R_e$. Given this work only examines star-forming spaxels, many galaxies have patchy maps and have no valid $\Delta\Sigma_{\rm SFR}$ measurement in an R_e bin. Such incomplete data is most detrimental in the lower ΔSFR bins; given these galaxies are not on the star-forming main sequence, S/N cuts become a more prominent factor. This leads to many of our profiles ending prematurely or having gaps. But besides the $\Delta\text{SFR} < -0.4$ bin, all other ΔSFR bins have a sufficient number of galaxies to compensate for patchiness and capture differing radial profiles.

Even within a single ΔSFR bin there is a diversity of radial profile behaviour. Such variety has been noted in past studies despite having samples a magnitude smaller (see Thorp et al. 2019); the large sample size only emphasizes this point. However, there is a developing trend of strong central starbursts for $\Delta\text{SFR} > 0.3$ dex. Although the diversity in merger behaviour has its own merit, further analysis will use average profiles in bins of ΔSFR to better understand this trend in particular.

Figure 2.11 shows the same spaxels as in Figure 2.10, but now spaxels from galaxies within the same ΔSFR bin are combined. The width of these radial profiles

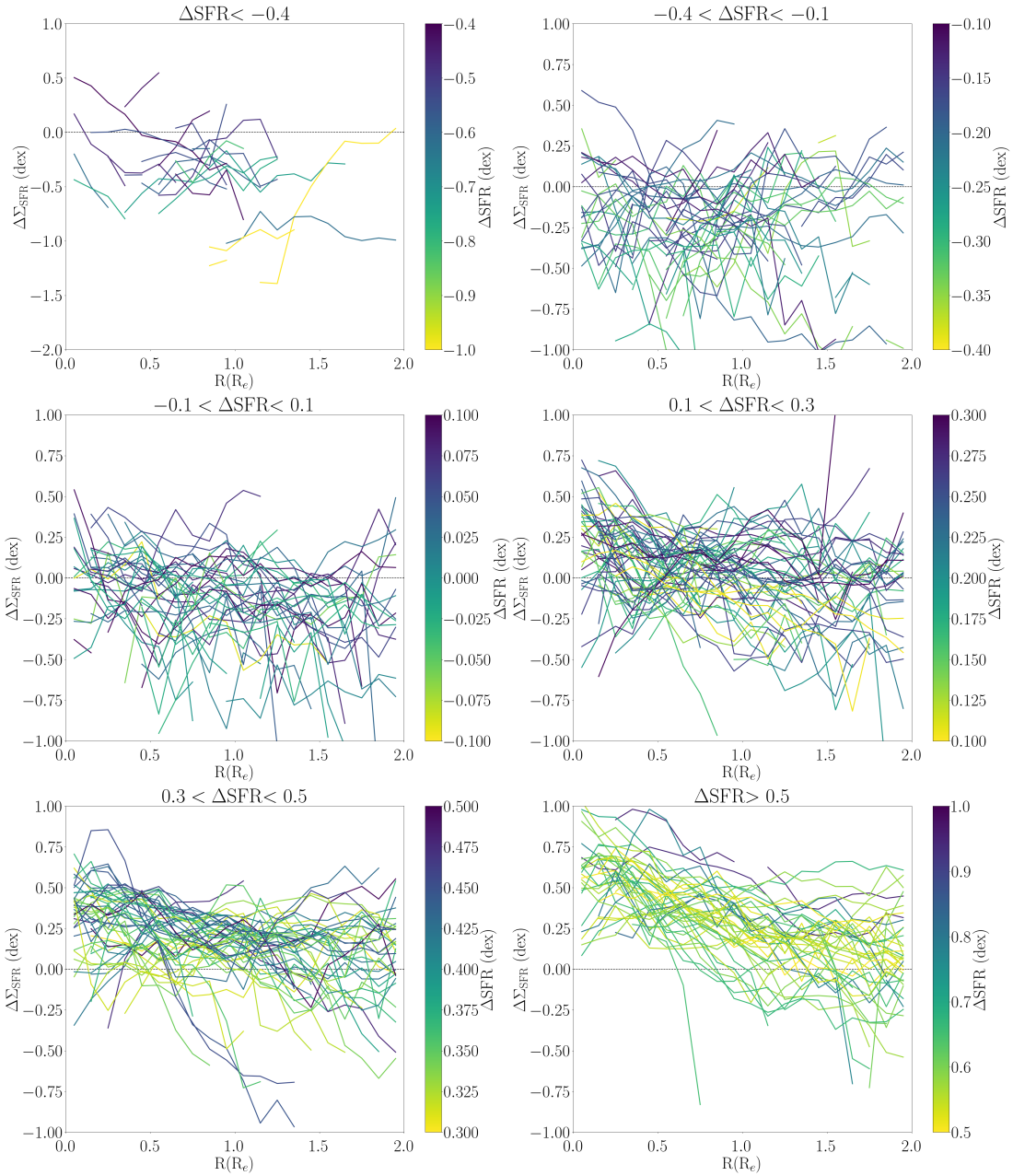

Figure 2.10: Individual $\Delta\Sigma_{\rm SFR}$ profiles as a function of R_e for each post-merger within a particular ΔSFR bin, colour-coded from lowest (yellow) to highest (blue) ΔSFR within that bin. Examining all galaxy profiles reveals the magnitude of galaxy-to-galaxy variation, even for galaxies in a similar position on the star-forming main sequence. Note the fading strength of the central starburst with decreasing ΔSFR holds even when this diversity is considered.

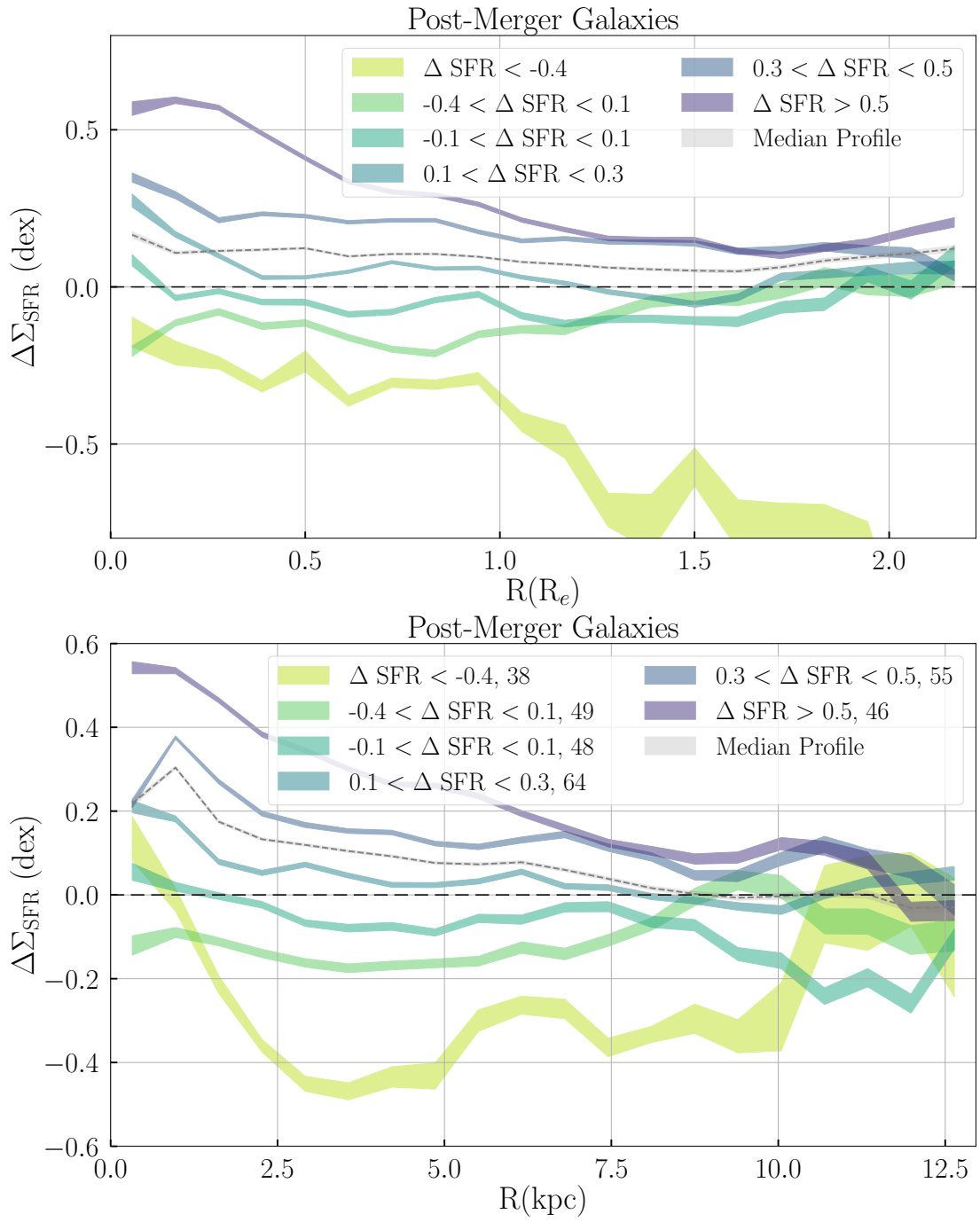

Figure 2.11: Radial profiles of $\Delta\Sigma_{\rm SFR}$ for the post-merger sample, in bins of R_e (left) and kpc (right). Each spaxel is separated into bins of ΔSFR, and then the average $\Delta\Sigma_{\rm SFR}$ of those spaxels within a radial bin is computed. The average profile for all post-mergers is shown as a grey dashed line. The width of each line represents the error on the mean ($\sigma/\sqrt{N}$). Note that this error quantifies the number of spaxels contributing, not the number of galaxies. Single galaxy contribution is not an issue for most ΔSFR bins save for ΔSFR< -0.4, which is the most sparsely populated bin with only 3 galaxies contributing beyond $1.5R_e$. This is also why the $\Delta\Sigma_{\rm SFR}$ profile looks so different for ΔSFR< -0.4 galaxies when plotted against radii in kpc.

represents the error on the mean, better quantifying where the majority of spaxels lie but failing to capture the galaxy-to-galaxy diversity. The lowest ΔSFR bin is so sparsely populated that only a handful of galaxies contribute to each radial bin, thus it is much more sensitive to galaxy-to-galaxy variability. In this format there is an obvious trend of the central star formation enhancement increasing as ΔSFR increases. I.e., galaxies with globally heightened star formation activity tend to have this activity concentrated in the centre. Such inside-out starbursts have been noted in past studies (Ellison et al., 2018a; Liu et al., 2018; Medling et al., 2018; Wang et al., 2019). Galaxies with ΔSFR$>$ 0.3 dex are more likely to have extended enhancements in star formation (though smaller compared to the central starburst). Interestingly, almost all mergers return to $\Delta\Sigma_{\rm SFR} = 0$ at 2 R_e, as would be expected for isolated galaxies (which also starburst/quench from the inside-out). That means galaxies with continuous enhancements in star formation are more rare within their population, and may represent a stage closer to coalescence where the changes in star formation are strongest (Hani et al., 2020).

Profiles are replicated in bins of kpc for comparison. Binning in effective radius better captures the total structure of a galaxy: 2 R_e for a small galaxy may be at a much smaller physical distance from its centre than a large galaxy, but represents the "edge" of the system in the same way 2 R_e does for our most massive galaxies. Alternatively, binning in kpc captures the actual physical extent of enhancements, and can be particularly important later when considering the influence of a companion. Reassuringly, the trend that central SFR enhancements correlates with ΔSFR persists with physical units. On average most post-mergers have $\Delta\Sigma_{\rm SFR} = 0$ beyond 10 kpc.

To inform interpretations of $\Delta\Sigma_{\rm SFR}$, we can next examine profiles of ΔO/H. Figure 2.12 replicates Figure 2.10 but with ΔO/H on the y-axis. One will note there are fewer ΔO/H profiles than $\Delta\Sigma_{\rm SFR}$ profiles, particularly in the lowest ΔSFR bins, given our stricter cuts for metallicity measurements. The overall change in metallicity is much smaller in magnitude than SFR, with maximum magnitudes around 0.2 dex rather than 1 dex. However, there is just as much diversity between galaxies. Even within a single ΔSFR bin, there exist post-mergers with central metallicity depletion up to −0.2 dex alongside post-mergers that have no changes in metallicity at all. Stronger metallicity deficits are more common for galaxies on or above the main sequence, and those with ΔSFR$>$ 0.5 dex are more likely to have −ΔO/H out to 2 R_e. Such a result makes intuitive sense if $\Sigma_{\rm SFR}$ and metallicity are anti-correlated as the rFMR suggests (Salim et al., 2014; Gao et al., 2018; Cresci et al., 2019; Sánchez Almeida &

Sánchez-Menguiano, 2019), given Δ SFR$>$ 0.5 dex galaxies also experience stronger central starbursts and more extended $+\Delta\Sigma_{\rm SFR}$ as shown in Figure 2.10.

But just as Figure 2.8 demonstrated that $+\Delta\Sigma_{\rm SFR}$ does not always correspond to $-\Delta$O/H, profiles with extended suppression in metallicity do not always have extended enhancements in $\Sigma_{\rm SFR}$. Figure 2.13 shows $\Delta\Sigma_{\rm SFR}$ and ΔO/H profiles of three post-mergers as examples of this phenomena. 9090-3704 has $-\Delta$O/H and $-\Delta\Sigma_{\rm SFR}$ out to 2 R_e. 9511-6103, alternatively, has enhancements in both properties. Only the third galaxy, 7922-6102, has a central burst in $\Sigma_{\rm SFR}$ accompanied by a central dilution in metallicity (as one might expect from the rFMR). Therefore, even though Figure 2.12 implies centralized dilutions in metallicity are on average tied to the central bursts of star formation seen in Figure 2.11, this is not the case for all post-mergers. It may not be the case that most galaxies with ΔSFR$>$0.5 dex have positive gradients in ΔO/H corresponding to the negative gradients in $\Delta\Sigma_{\rm SFR}$.

Figure 2.11 shows ΔO/H profiles averaged in bins of ΔSFR, similar to what is done in Figure 2.11. The expected trend of dilution strengthening with ΔSFR is far less obvious than the central starburst counterpart. Post-mergers on or above the main sequence are more likely to have central deficits than those below it, confirming what one can surmise from Figure 2.12. On average ΔO/H profiles for all ΔSFR bins are also relatively flat, meaning metallicity is uniformly diluted across most post-mergers. Given the steep gradients in some $\Delta\Sigma_{\rm SFR}$ profiles, one might expect similar changes in ΔO/H with increasing radii. However just as Figure 2.8 proved that a third of post-merger spaxels with $+\Delta\Sigma_{\rm SFR}$ have $-\Delta$O/H, the resolved star-forming behaviour of a post-merger is not strictly correlated with the gas-phase metallicity.

Though simulations have demonstrated that mergers can create gaseous inflows that dilute the central metallicity and boost star formation (Rupke et al., 2010; Torrey et al., 2012; Hani et al., 2018), they are not the only physical process that can impact gas-phase metallicity. Outflows from galactic winds can remove metals from a galaxy (Veilleux et al., 2005; Rupke, 2018; Chisholm et al., 2018). Metals can also be transported within a galaxy by the bulk flow of gas, or through turbulent mixing of gas with irregular metal concentration, both of which play a key role in forming galactic metallicity gradients (Greif et al., 2009; Yang & Krumholz, 2012; Forbes et al., 2012; Rennehan et al., 2019). Although globally metallicity is anti-correlated with atomic and molecular hydrogen gas mass (Bothwell et al., 2013; Lara-López et al., 2013; Bothwell et al., 2016), the lack of strong metallicity deficits does not negate the presence of gaseous inflows. In Chapter 4 I will investigate the resolved molecular

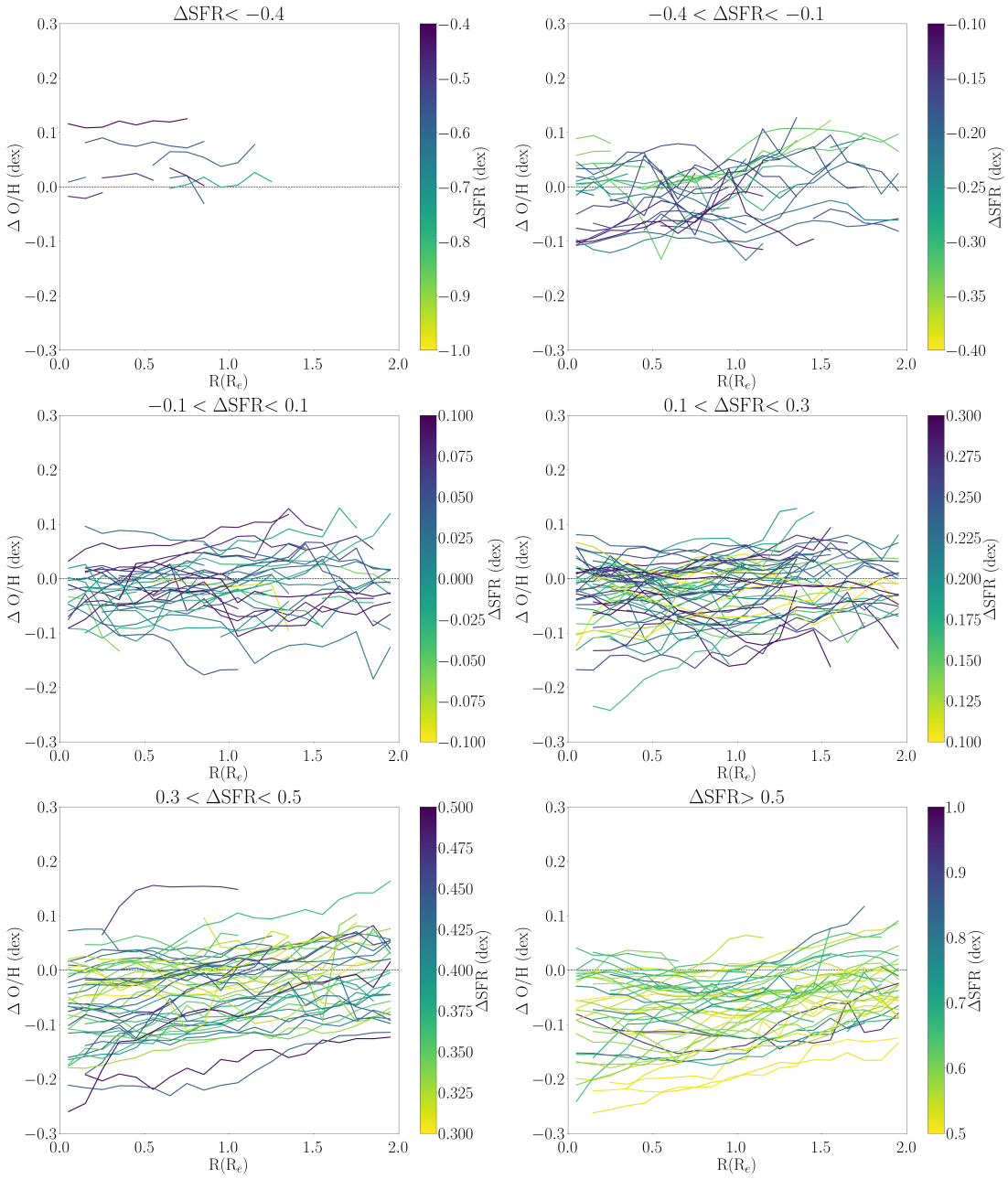

Figure 2.12: Individual ΔO/H profiles for each post-merger within a particular ΔSFR bin, colour-coded from lowest (yellow) to highest (blue) ΔSFR within that bin. Just as is seen for $\Delta\Sigma_{\rm SFR}$ profiles in Figure 2.10, there is a noticeable diversity between galaxy profiles even within a ΔSFR bin. Examining all post-merger profiles reveals many of the ΔSFR> 0 mergers have stronger metallicity deficits in their centres compared to their outskirts, implying inflows of low-metallicity gas often occur in mergers (but are clearly not the only possible scenario). Mergers with the strongest central deficit often have positive gradients in ΔO/H, whereas those with moderate suppressed central metallicity tend to be similar suppressed out to 2 R_e.

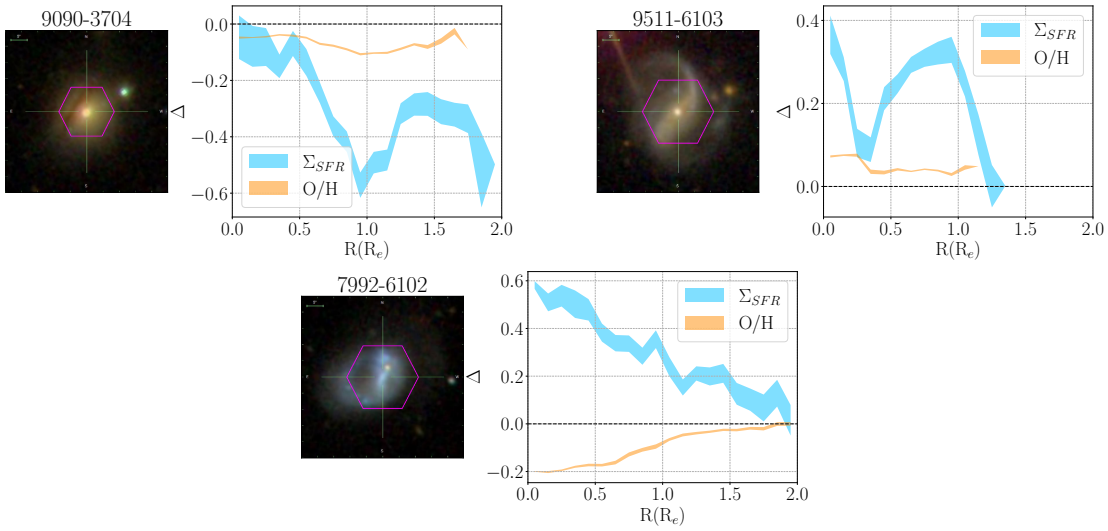

Figure 2.13: Radial profiles of $\Delta\Sigma_{\rm SFR}$ (blue) and ΔO/H (orange) for three example post-mergers with very different resolved behaviour, withe the SDSS *gri*-image next to each plot for comparison. The first galaxy (plate-ifu: 9090-3704) has both suppressed star formation and metallicity out to 2 R_e. The second (plate-ifu: 9511-6103) has profiles greater than zero for both properties. The third galaxy (plate-ifu: 7992-6102) agrees with the majority of post-merger spaxel offsets as shown in Figure 2.8, with $-\Delta$O/H corresponding to $+\Delta\Sigma_{\rm SFR}$.

gas properties for a subset of these mergers, to better pinpoint how merger-induced gaseous inflows impact the resolved star formation properties.

2.3.3 Pair radial profiles

There are far more interacting pair galaxies than there are post-mergers, at various stages of merger progression. The projected separation between galaxy pairs can be used as a proxy for merger progression, and help reveal any trends in spatially resolved changes related to merger stage. Figure 2.15 creates $\Delta\Sigma_{\rm SFR}$ profiles for pair galaxies in r_p bins of 20 kpc. In this figure any observations for which the companion galaxy is on the IFU are excluded, and they will be for the remaining radial profile analysis. IFU pairs suffer from significant overlap between two galaxies such that both will contribute flux to the same spaxel, and thus it is unwise to compare $\Delta\Sigma_{\rm SFR}$ radial variations in such cases to galaxies that are alone on the IFU.

Figure 2.15 demonstrates how the central star formation enhancement is stronger for pairs with smaller separations. Pairs at small separation are either experiencing their first passage, or are approaching coalescence. Either way, the gravitational forces between the two galaxies will be strongest at small r_p, leading to stronger morphological disturbances and (after first passage) exchange of material between the two targets. As a result, on average pairs with small r_p have stronger central enhancements in star formation, although profiles quickly return to $\Delta\Sigma_{\rm SFR}= 0$ beyond $1.5{\rm R}_e$. The only exception is $r_p < 20$ kpc, where after returning to normal a second enhancement in $\Sigma_{\rm SFR}$ is seen at large radii. This second boost is not as obvious when $\rm R_e$ is replaced with kpc-radii, although the $r_p < 20$ kpc are still the only pairs to have continuous enhancement out to 13 kpc.

Using r_p as an indicator for interaction stage has some key limitations. Firstly, r_p is not a perfect tracer of merger progression - one galaxy may be approaching a companion 30 kpc away for the first time, whereas another pair with the same r_p could have already taken its first passage and be experiencing the dynamical effects of a close encounter. Another factor to consider is that within a bin of r_p there are a variety of galaxy types (both for the target and companion galaxy). Galaxies on different positions on the SFMS have distinct star formation profiles (Ellison et al., 2018a; Medling et al., 2018; Belfiore et al., 2018). Thus it is worth examining galaxies on, above, and below the SFMS separately.

Deconstructing Figure 2.15 into separate bins of ΔSFR, now shown as a new Fig-

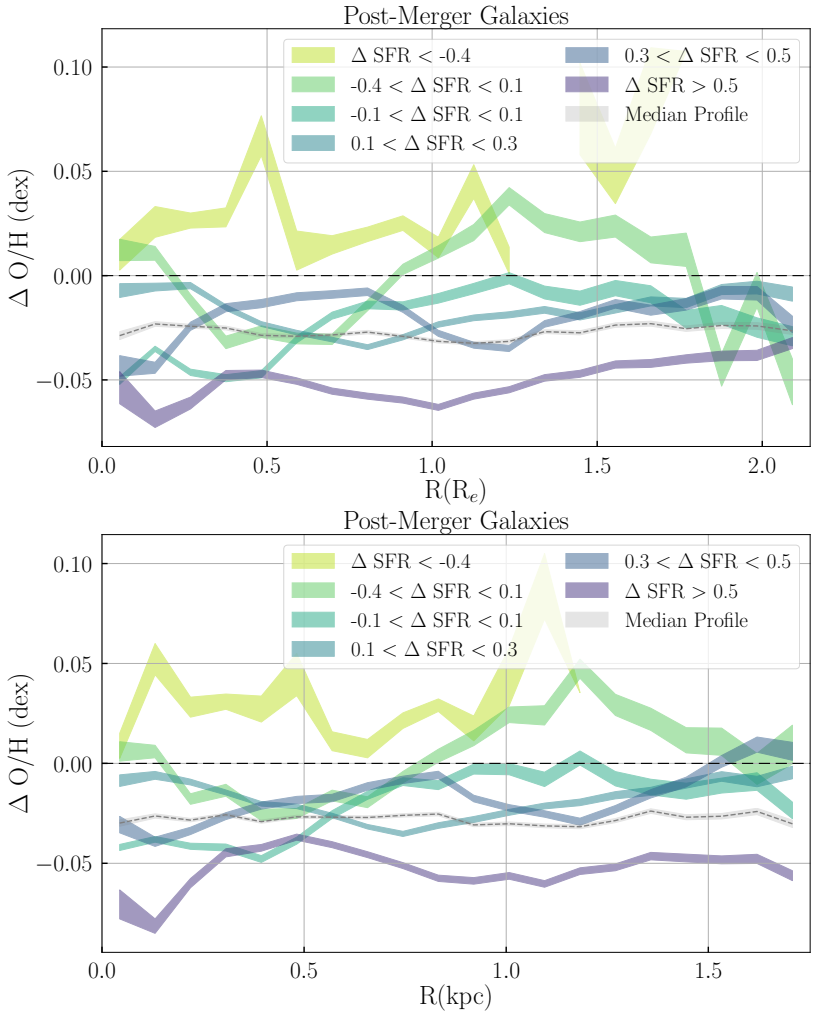

Figure 2.14: Radial profiles of ΔO/H for the post-merger sample, in bins of R_e (left) and kpc (right). Each spaxel is separated into bins of ΔSFR, and then the average ΔO/H of those spaxels within a radial bin is computed. The average profile for all post-mergers is shown as a grey dashed line. The width of each line represents the error on the mean ($\sigma/\sqrt{N}$). The same ΔSFR bins are used as in Figure 2.11, although note that the ΔSFR< -0.4 dex bin is even more sparsely populated in this figure (given fewer spaxels have accurate ΔO/H measurements than $\Delta\Sigma_{\rm SFR}$). All profiles besides the two lowest ΔSFR bins have suppressed metallicity, though the starbursts (ΔSFR>0.5 dex) have the greatest suppression. Note that this suppression is relatively flat, unlikely the distinct inside-out behaviour of the $\Delta\Sigma_{\rm SFR}$ profiles.

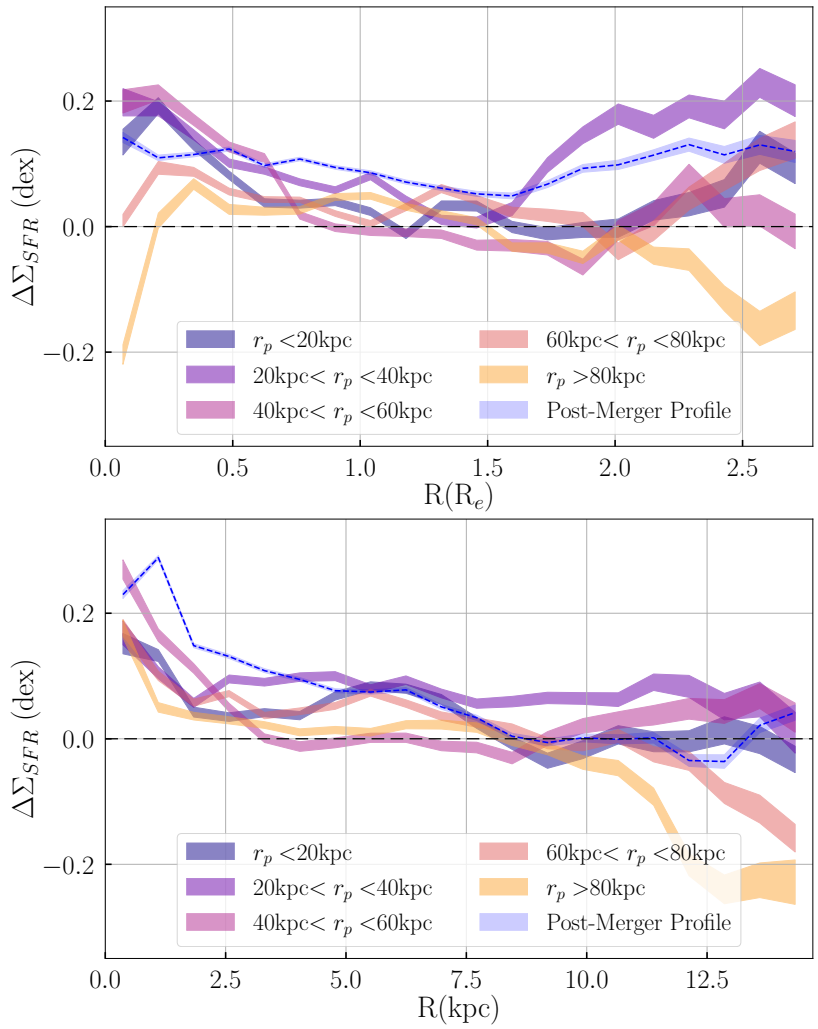

Figure 2.15: *Left:* Radial profiles of $\Delta\Sigma_{\rm SFR}$ as a function of R_e for the interacting pair galaxies in bins of projected separation (r_p), with dark purple representing the closest pairs. The post-merger $\Delta\Sigma_{\rm SFR}$ profile is shown with a blue dashed line for comparison. *Right:* The same radial profiles, but now in bins of kpc for comparison.

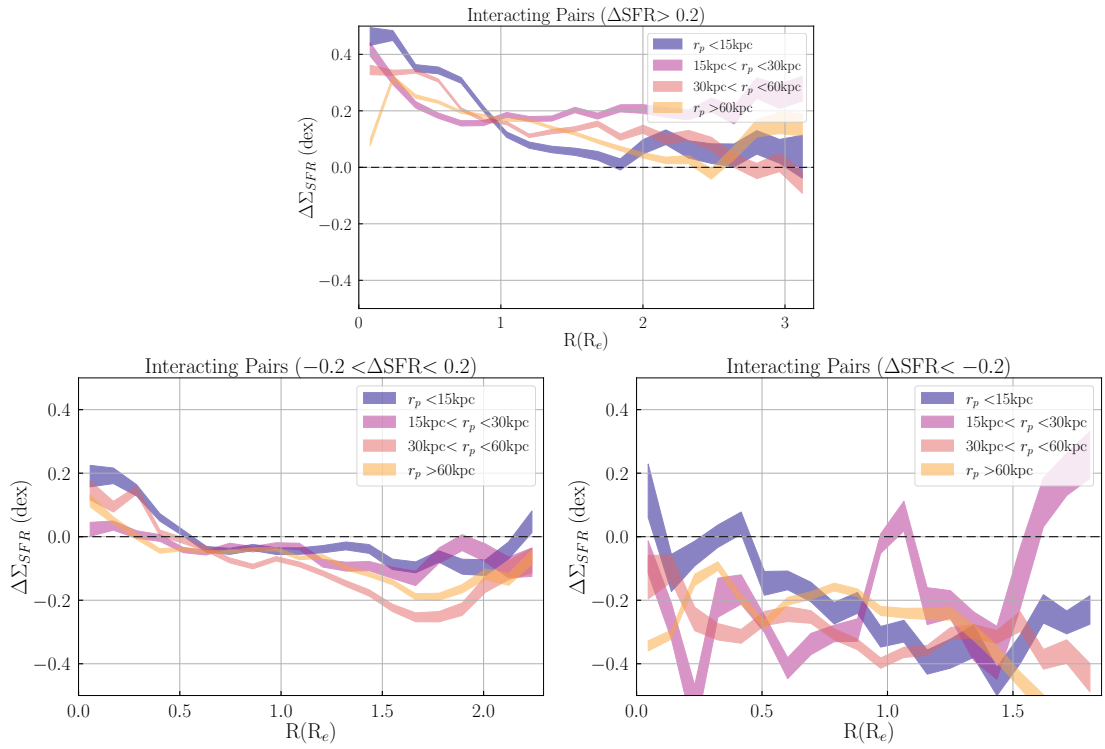

Figure 2.16: Radial profiles of $\Delta\Sigma_{\rm SFR}$ similar to Figure 2.15, but separated into three bins of ΔSFR to demonstrate the similarities between radial profiles for different r_p values. r_p and ΔSFR bins have changed slightly from previous figures, to maintain a relatively equal number of galaxies in each bin. All r_p bins seem to reflect the general behaviour as predicted by ΔSFR, with those above the main sequence (ΔSFR> 0.2) having extended enhancements with the strongest enhancement in the centre, those on the main sequence ($-0.2 <$ ΔSFR< 0.2) having only centralized SFR enhancements, and those below the main sequence (ΔSFR< −0.2) having mostly negative $\Delta\Sigma_{\rm SFR}$ values.

ure 2.16, demonstrates how within a narrower range of ΔSFR mergers with differing r_p have very similar $\Delta\Sigma_{\rm SFR}$ profiles. Pairs separated by 15 kpc can be boosted above the main sequence just as much as those separated by 60 kpc, and the resolved $\Delta\Sigma_{\rm SFR}$ profiles are not substantially different. Thus other properties of an interaction are required to explain the diversity of $\Delta\Sigma_{\rm SFR}$ profiles.

Another parameter that characterizes the interaction is μ, the mass ratio. The lower mass galaxy in an interaction tends to have a greater subsequent enhancement in integrated SFR (Woods & Geller, 2007; Ellison et al., 2010; Lambas et al., 2012; Scudder et al., 2012; Pan et al., 2018a). Simulations predict that this enhancement is concentrated in the centre of the galaxy, with the smaller of two interacting galaxies

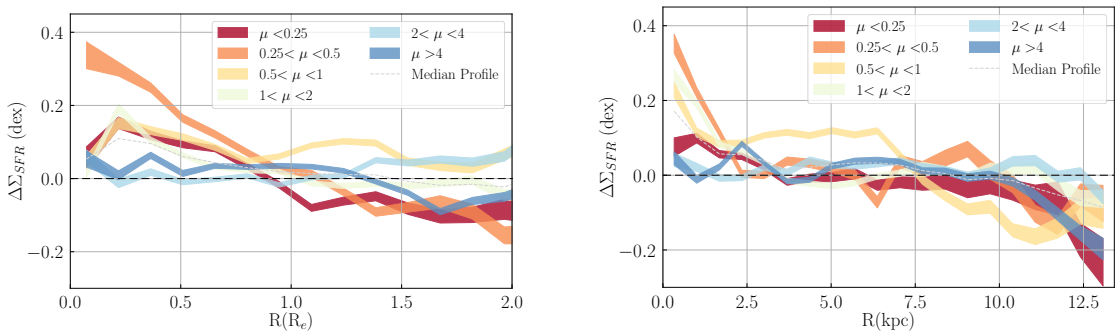

Figure 2.17: *Left:* Radial profiles of $\Delta\Sigma_{\rm SFR}$ for the interacting pair galaxies in bins of mass ratio μ, with red profiles showing targets much smaller than their companion, blue showing targets much larger than their companion, and green showing mergers between two like-sized galaxies. The average pair profile is shown as a grey dashed line for comparison. *Right:* The same radial profiles, but now in bins of kpc for comparison. When the target galaxy is much larger than the companion ($\mu > 2$) it is less likely to exhibit centralized enhancements in star formation, likely due to the limited gravitational impact of the companion.

actually experiencing a suppression of star formation at outer radii (Moreno et al., 2015, 2021). A recent study of interacting pairs in MaNGA confirmed this prediction, while also demonstrating that the more massive galaxy in a pair is more likely to exhibit enhanced star formation beyond $1.5R_e$ (Steffen et al., 2021).

I perform a similar investigation in Figure 2.17, where averaged radial profiles of $\Delta\Sigma_{\rm SFR}$ are binned by mass ratio. Warm colours represent cases where the target is much smaller than the companion, and cool colours represent cases where the target is much larger. Similar to what was found in Steffen et al. (2021), galaxies with $\mu > 1$ (larger than their companion) have stronger central enhancements in star formation. Those with $\mu > 0.5$ also have suppressed star formation in the outskirts as was seen in Steffen et al. (2021) (as well as simulations), but such behaviour is not limited to $\mu > 0.5$ pairs. In fact this merger sample shows no clear trend with μ and the extended star formation; on the contrary, galaxies that are over 4 times the size of their companion on average have suppressed star formation beyond $1.5R_e$. Such contradictions could be the result of different sample selection; (Steffen et al., 2021) limit their analysis to star-forming galaxies while this work probes well below the SFMS and green valley. By including these galaxies, this sample has no strong correlation between μ and ΔSFR as has been found in past studies, the two only having a Pearson correlation coefficient of -0.08. Indeed, when ΔSFR is plotted against μ in Figure 2.18, there is no obvious trend between the two. Pairs where

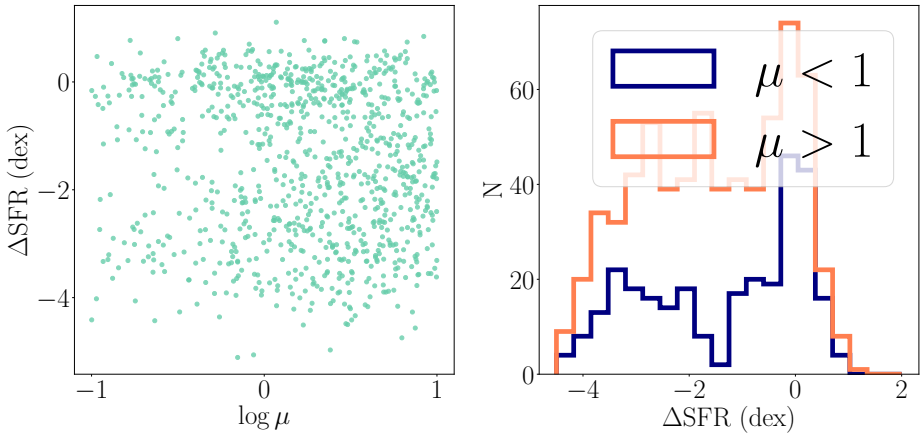

Figure 2.18: *Left:* ΔSFR vs. the log mass ratio of the pair galaxies. There is no clear relationship that when the two galaxies are of similar size ($\log \mu \sim 0$) the offset from the star-forming main sequence is highest. Nor is there an obvious correlation between ΔSFR and μ, with a Pearson Correlation Coefficient of -0.08. *Right:* Distributions of ΔSFR for pairs with $\mu < 1$(blue) and $\mu > 1$(orange). Although our sample contains more pairs with $\mu > 1$ (the target is larger than the companion), both samples cover a similar range of ΔSFR values.

the target is larger than the companion ($\mu > 1$) sample the same range of ΔSFR values as those where the companion is larger ($\mu < 1$), is is demonstrated by the right panel of Figure 2.18. Although galaxies of similar μ values can trigger the same magnitude of ΔSFR, galaxies of similar ΔSFR values may have different $\Delta\Sigma_{\rm SFR}$ properties depending on μ.

Figure 2.19 displays radial profiles binned by μ separately for galaxies above, on, and below the main sequence. Evidently, pairs with smaller μ (are the smaller of two galaxies) have stronger central star formation enhancements than those with large μ even if the galaxies being compared have similar offsets from the SFMS. Thus μ has a unique influence over the resolved star-forming properties of a merger, in contrast to projected separation where different r_p values had very similar $\Delta\Sigma_{\rm SFR}$ profiles within a ΔSFR bin. Mass ratio has no clear relationship with $\Delta\Sigma_{\rm SFR}$ profiles below the SFMS (Δ SFR< -0.2 dex). But such dependencies could be hidden by other properties of an interaction that influence star formation rate, such as the orbital parameters (Di Matteo et al., 2008; Moreno et al., 2015, 2021).

The pair sample is further explored with ΔO/H profiles. Figure 2.20 is similar to Figure 2.15, but now with ΔO/H on the y-axis. The spaxel population is also slightly different, given the stricter cuts on metallicity measurements than $\Sigma_{\rm SFR}$. Similar to

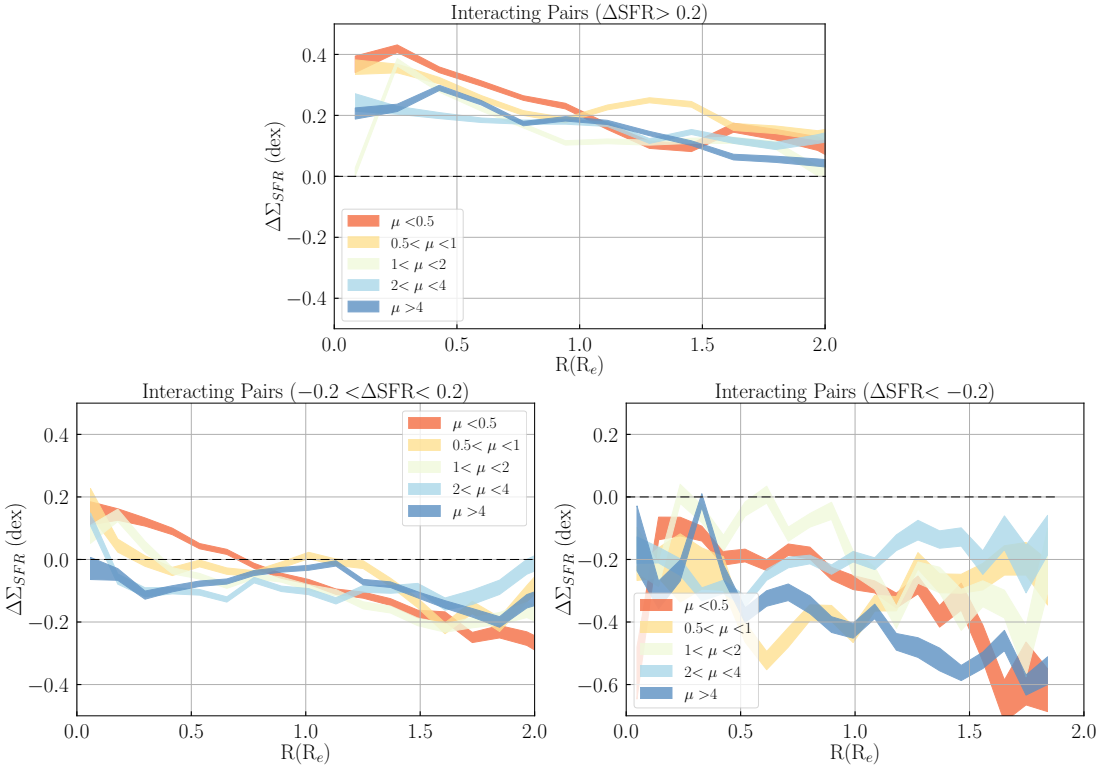

Figure 2.19: Radial profiles of $\Delta\Sigma_{\rm SFR}$ similar to Figure 2.17, but separated into three bins of ΔSFR to examine how μ dependence varies with global offset from the star-forming main sequence. As long as the merger is on or above the star-forming main sequence (Δ SFR> -0.2 dex), pairs with small μ values consistently create stronger central starbursts. Central starbursts are not seen in more passive galaxies, thus the μ dependence goes away for the Δ SFR< -0.2 dex bin.

$\Delta\Sigma_{\rm SFR}$, it is difficult to find any trend with ΔO/H profiles and r_p. The only key feature is galaxies with $r_p > 80$ kpc are more likely to have enhanced metallicity than other r_p bins. There is only one galaxy pair identified by visual disturbance (not spectroscopic redshift) with $r_p > 80$ kpc; thus this bin is likely biased towards galaxy pairs on their first approach. One scenario that could explain such behaviour is metallicity dilution coming later in an interaction, when stronger gravitational forces lead to larger structural impacts.

Even more interesting results arise when ΔO/H profiles are separated by mass ratio, as is displayed in Figure 2.21. The strongest central dilution in metallicity occurs for galaxies with $0.25 < \mu < 1$, meaning the target galaxy is the smaller of the pair, but is still at least one quarter the size of the companion. This central dilution is in agreement with the enhanced central star formation seen for pairs of similar μ values. But lowered metallicity does not automatically imply $\Delta\Sigma_{\rm SFR} > 0$. For $\mu > 2$, ΔO/H seems to decrease with radius, implying metal dilution in the outskirts despite the $\Delta\Sigma_{\rm SFR}$ profiles for this μ bin showing no significant enhancement in star formation at large radii (see Figure 2.17). $\mu > 2$ means that the companion galaxy is less than 50% the mass of the target galaxy. Hypothetically, a small galaxy might not create the tidal torques necessary to funnel central gas (at least, for the majority of galaxies). However, as it approaches the much larger target material from the companion is pulled onto the observed galaxy, leading to new material at the edge of the galaxy that could dilute the local metallicity. But the excess of gas now present at the outskirts of the galaxy does not lead to a greater number of stars formed. Previous resolved metallicity studies of mergers have found close pairs are more likely to have outer dilutions in metallicity than those that coalesce (those have larger dilutions in the centre) (Hwang et al., 2018). What is novel about the result from this thesis is it demonstrates metallicity dilution does not on average lead to heightened star formation rates as might be expected from a resolved FMR. Chapter 4 will reveal a similar predicament, where many post-mergers have enhanced gas fractions despite regular or suppressed star formation.

2.4 Summary & future work

The work described herein has demonstrated that mergers exhibit a diverse range of star formation and metallicity characteristics. Both post-merger and pair galaxies show as much scatter in the rSFMS and rMZR as the complete MaNGA sample,

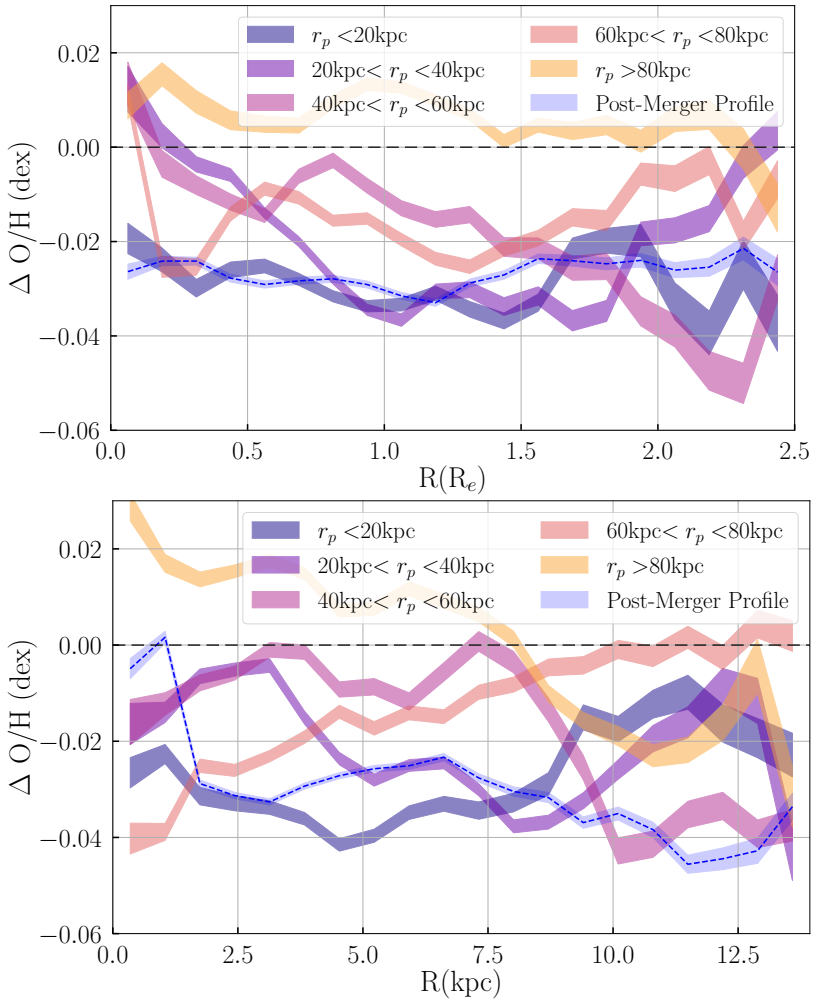

Figure 2.20: *Left:* Radial profiles of ΔO/H for the interacting pair galaxies in bins of projected separation (r_p), with dark purple representing the closest pairs. The post-merger ΔO/H profile is shown with a blue dashed line for comparison. *Right:* The same radial profiles, but now in bins of kpc for comparison. Note that only the furthest pairs show enhancements in metallicity, but beyond that every stage of a merger has some degree of metallicity dilution.

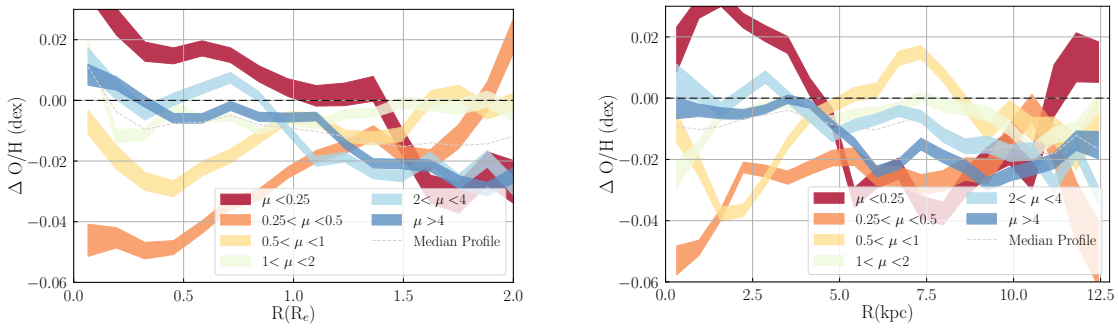

Figure 2.21: *Left:* Radial profiles of ΔO/H for the interacting pair galaxies in bins of mass ratio (μ), with warm colours for targets smaller than their companion, and cool colours for targets larger than their companion. The average pair ΔO/H profile is shown as a grey dashed line for comparison. *Right:* The same radial profiles, but now in bins of kpc for comparison. The strongest central dilutions in metallicity occur in galaxies that are smaller than their companion, in agreement with the central star formation enhancement seen in Figure 2.17.

though post-mergers are slightly biased towards higher star formation rates and stellar masses (Figure 2.6). Although the majority of spaxels in mergers where star formation is measured have star formation boosted above the rSFMS ($+\Delta\Sigma_{\rm SFR}$) and a deficit in gas-phase metallicity ($-\Delta$O/H), ΔO/H and $\Delta\Sigma_{\rm SFR}$ are not necessarily always anti-correlated as one might expect (Figure 2.8). What this implies is regions can have heightened star formation without the corresponding dilution from unprocessed gas (not necessarily what is expected for a gas-rich HII region), and regions flush with metal-poor gas can have low star formation rates.

I explore this diversity by creating radial profiles of $\Delta\Sigma_{\rm SFR}$ and ΔO/H, noting some well-defined trends with global offset from the SFMS persist despite a wide variety of profile behaviours. Post-mergers that have triggered a global starburst tend to have that star formation concentrated to the centre (Figure 2.11). Counter intuitively, this does not lead to a stronger depletion in gas-phase metallicity in the central regions of the galaxy. Rather post-mergers profiles of ΔO/H are relatively flat (Figure 2.14).

When examining galaxy pairs, I find that projected separation (often used as a proxy for the progression of the interaction) has little impact on radial profile trends. Galaxies as far apart as 60 kpc can have central enhancements in star formation as strong as those 15 kpc away, but both can also have suppressed star formation across the galaxy (Figure 2.16). Mass ratio plays a more important role; galaxies of similar size or smaller than their companion tend to have stronger central starburst, and those less than half the size of their companion having lowered $\Sigma_{\rm SFR}$ values in their outskirts (Figure 2.17). Galaxies more than twice as big as their companion are less likely to have a central starburst, or a central dilution of metallicity (Figure 2.21). This would imply that when the companion galaxy is much smaller than the target the lack of gravitational influence results in fewer asymmetric structures, hence no funnelling of low-metal gas to fuel a central starburst. The central gas depletion is actually strongest when the companion is of similar or larger mass, causing a strong disruption in galactic structure.

Using the largest IFS sample of interacting pair and post-merger galaxies to date, this analysis exposes just how difficult it is to generalize merger behaviour in the observable universe. Many key features that impact the galaxy merger, such as galaxy orientation, orbital parameters, and gas mass ratio are unavailable to this work. These factors, along with mass ratio and projected separation, all combine to make highly unique merger remnants. Thus one cannot necessarily prescribe one likely

evolutionary route for a pair galaxy, or hypothesize a single scenario that would lead to an observed post-merger. Future studies will need to focus on using observable quantities to account for factors only available in simulations, and thus will require intense synergy between observational and theoretical works.

Another limitation from this work arises from equating gas-phase metallicity to dilution from the inflow of low-metal gas. Most models predict that variations in the MZR stem from variations in gas fraction, which dilute metallicity and lead to heightened SFRs (Lagos et al., 2016; Segers et al., 2016). Observational studies have confirmed that gas-phase metallicity has a secondary dependence on global gas fraction, with the primary driver being total stellar mass (Peeples et al., 2008; Bothwell et al., 2016). More recent studies have confirmed this to be true on a resolved scale as well (Barrera-Ballesteros et al., 2018). But an inflow of gas will eventually lead to bursts of star formation, which subsequently enriches the interstellar medium through supernova outflows (Dalcanton, 2007; Maiolino & Mannucci, 2019). Observations of the molecular gas properties in mergers can more accurately contextualize the behaviour of gas in a galaxy, without suffering these degeneracies.

I address two of these obstacles in the following chapters of my thesis. In Chapter 4 I present molecular gas maps of a subset of this merger sample, investigating the true interplay between star formation and gas as a merger progresses without depending on metallicity. In the next Chapter, I use simulations to evaluate the impact of observational limitations on some key merger diagnostics. Although not all-inclusive to the limitations discussed here, this study provides a case study of how popular observational techniques to classify mergers pose substantial obstacles when applied to varying data sets and simulations.

Chapter 3

Robust determinations of non-parametric morphologies in marginal astronomical data

Spectroscopic maps like those provided by MaNGA have introduced a difficulty in how large galaxy surveys are analyzed. Historically, galaxy surveys were limited to global studies, making for relatively straightforward comparisons between different galactic properties. The maps of galaxy properties provided for each target in IFS surveys can be enlightening, but it is impossible to examine a thousand-galaxy survey map by map (and even more improbable to pull a quantitative result out of such an analysis).

One solution to this conundrum is to compress a 2-dimensional map into a radial profile averaged azimuthally, as was completed in Chapter 2. However, this method assumes that galaxies are axisymmetric: that they behave uniformly as a function of azimuthal angle. Both works studying galaxy mergers through simulations (e.g. Moreno et al. 2015, 2021) and IFS observations (e.g. Thorp et al. 2019; Pan et al. 2019; Steffen et al. 2021) use radial profiles to help quantify changes in merging galaxies as a function of radius. However, if a galaxy is morphologically disturbed a circular or elliptical radius can over or under estimate the true distance from the galaxy's nuclei, leading to a misinterpretation of data averaged over one or multiple galaxies.

Not only that, but there is crucial information encoded in azimuthal changes within a galaxy. Resolved studies of galaxy metallicity have revealed anomalously low metallicities in the direction of an interacting companion for a small sample of merging galaxies (Hwang et al., 2018). When resolved molecular gas maps are also available, some case studies have found gradients in SFE across a galaxy merger (Tomičić et al., 2018; Bemis & Wilson, 2019). These studies were possible as they

examined a few individual cases; ideally one would hope to create a statistical study of these asymmetric features.

Many studies based on photometric observations have utlized non-parametric morphologies to quantify the peculiar structure of mergers (Conselice et al., 2000; Lotz et al., 2004; Conselice et al., 2003; Lotz et al., 2006; Huertas-Company et al., 2009; Holwerda et al., 2013; Conselice, 2014). No such analysis has been undertaken to determine whether IFS data reflects the asymmetric nature of its corresponding photometric image for a large and comprehensive merger sample, in particular how that asymmetry may vary with different IFS data products.

This chapter will test whether two key non-parametric morphology measurements used extensively in photometric studies, asymmetry and concentration, could be applied to IFS data products. These parameters were designed for photometric data, which has different resolution and measurement uncertainty. Using simulated galaxies, for which the true asymmetry and concentration measurements are known, I set out to test whether comparably accurate asymmetry and concentration measurements could be made for data with IFS like noise and resolution. Section 3.1 provides a brief overview of galaxy morphology and how non-parametric morphologies have been used. Section 3.2 will introduce the simulation used in this experiment, Illustris-TNG, which defines the true/intrinsic asymmetry and concentration measurement. Following this, Section 3.3 will describe the asymmetry and concentration measurements in detail, including how observational effects are traditionally corrected. Finally, I design new methods to correct for uncertainty and resolution in Section 3.4, providing a route through which accurate asymmetry and concentration measurements can be made for a variety of data sets. I will then test these methods in alternative simulated galaxy sets (Section 3.5) and discuss the impact these corrections can have on contemporary merger studies (Section 3.6).

3.1 Morphology and non-parametric indices

The importance of morphology in galaxy evolution is supported by an abundance of observational and theoretical evidence. For example, a galaxy's internal structure is observed to strongly correlate with its global star formation rate (e.g. Wuyts et al., 2011; Bluck et al., 2014; Morselli et al., 2017; Bluck et al., 2019; Cano-Díaz et al., 2019; Cook et al., 2020; Sánchez, 2020; Leslie et al., 2020), as well as star formation efficiency (Saintonge et al., 2012; Leroy et al., 2013; Davis et al., 2014; Colombo et al.,

2018; Dey et al., 2019; Ellison et al., 2021b). The role of morphology in regulating star formation is also reproduced in simulations (e.g. Martig et al., 2009; Gensior et al., 2020). Other properties found to depend on morphology include gas fraction (e.g. Saintonge et al., 2017) and metallicity (e.g. Ellison et al., 2008b). Measuring and classifying galaxy morphologies are therefore a fundamental component of any modern galaxy survey.

Whereas early morphological measurements relied on expert visual classifications, often done by individual professional astronomers, this approach has become untenable in the era of large galaxy surveys. The deluge of galaxy images has therefore been tackled in two principal ways. The first is through crowd-sourcing, whereby the power of the human brain continues to be tapped, through the contributions of citizen scientists (Darg et al., 2010; Lintott et al., 2011; Casteels et al., 2014; Simmons et al., 2017; Willett et al., 2017). Recently, artificial intelligence is replacing humans and machine learning algorithms are increasingly being applied to the challenge of large imaging data sets, either for general morphological classification (Huertas-Company et al., 2015; Domínguez Sánchez et al., 2019; Cheng et al., 2020; Walmsley et al., 2021) or the identification of particular galaxy types/features (Bottrell et al., 2019b; Pearson et al., 2019b; Ferreira et al., 2020; Bickley et al., 2021). An alternative automated approach, which has been in use for several decades, is to compute some metric of the galaxy's light distribution, a technique that is readily applicable to large data sets. Such quantitative morphology metrics (usually) yield a continuous distribution, as opposed to placing galaxies in distinct classes.

There are numerous quantitative morphology metrics that have been developed over the years. One of the oldest methods is the definition of a characteristic radial profile of light in a given waveband (Sérsic, 1963). Modern fitting applications of the Sérsic profile often decompose the galaxy into two (or more) components, in recognition that bulges and disks, which commonly co-exist in a given galaxy, are characterized by distinct indices (e.g. Simard et al., 2011; Lackner & Gunn, 2012; Mendel et al., 2014; Bottrell et al., 2019a; Meert et al., 2015). Other metrics have been developed for specific applications, such as the identification of recent merger activity (e.g. Lotz et al., 2008; Pawlik et al., 2016). One of the most commonly used quantitative morphology systems is the 'CAS' approach (Conselice, 2003), which computes concentration, asymmetry and smoothness (Conselice et al., 2000, 2003; Lotz et al., 2004). The non-parametric approach of CAS is particularly useful for identifying galaxy mergers, whose disturbed structures often do not conform to pre-defined

parametric descriptions. Together, CAS and other non-parametric indices capture information that can be used to broadly distinguish early and late type galaxies, as well as possible mergers (Conselice et al., 2003; Lotz et al., 2004, 2008; Conselice et al., 2009).

All of these quantitative morphology metrics and classifications were initially envisioned to work on flux maps originating from galactic starlight. Although some work has extended the application of traditional non-parametric indices (such as asymmetry) to the distribution of galactic gas mass (e.g. Holwerda et al., 2011; Giese et al., 2016; Reynolds et al., 2020) and stellar mass from Hubble photometry (Lanyon-Foster et al., 2012), there has been little application to date on maps of other galactic properties, particularly the variety of properties provided by resolved spectroscopy. The widespread applicability of non-parametric morphology indicators is particularly pertinent in the era of large integral field unit (IFU) surveys wherein maps of a myriad of properties are available, i.e. the MaNGA Survey (Bundy et al., 2015; Law et al., 2015), the SAMI Survey (Allen et al., 2015; Croom et al., 2021), and the CALIFA Survey (Sánchez et al., 2012). Indeed, the technical challenge of effectively capturing the complexity of the spatial properties for large numbers of galaxies often leads to the use of averaged profiles, which loses much of the valuable information encoded in the IFU data (e.g. Ellison et al., 2018a; Thorp et al., 2019). There is a clear need to explore the application of traditional techniques, and potentially develop new ones, that are capable of capturing in an effective, statistical way, the high order structure in IFU data product maps (e.g. Bloom et al., 2017).

Most importantly, the biases in non-parametric morphology measurements created by different resolutions and signal-to-noise ratio values have not been investigated for IFU data product maps. These biases have been investigated in detail for photometry. Conselice et al. (2000) demonstrated that adding simulated random noise to a galaxy image will systematically increase the measured asymmetry, and that the change in asymmetry is inversely proportional to the signal-to-noise ratio. On the same galaxy sample they also investigate the effects of degraded resolution on asymmetry, by simulating their real galaxy images as if they are observed at a larger distance, and find that asymmetry artificially decreases with distance. Degraded resolution can also alter the concentration measurement, as Bershady et al. (2000) demonstrated by artificially degrading their spatial sampling. The most commonly used concentration and asymmetry measurements have been constructed to mitigate these effects, and reasonable cuts in signal-to-noise and resolution can be made to

make accurate asymmetry and concentration measurements within acceptable error (Bershady et al., 2000; Conselice et al., 2000, 2003). However, the same investigation has not been completed to see how these measurements and the necessary signal-to-noise/resolution limitations would work beyond photometric data, such as the IFU data products.

In the following work I use cosmological hydrodynamical simulations to explore the applicability of the most commonly used non-parametric indices (asymmetry and concentration) on the kind of products available in IFU surveys. This experiment focuses on simulated maps of stellar mass, although the lessons learned from this test case can be generalized to many IFU data products.

3.2 TNG simulation and sample selection

My goal is to assess the robustness of non-parametric morphology indicators on data products other than the standard application to starlight (e.g., stellar mass maps, SFR maps, metallicity maps). Although there is no mathematical reason that such indicators could not be applied to any 2-dimensional distribution, the limitations of realistic data may impose practical impediments. For this reason, it has become a common approach to add observational realism to simulated data, in order to fairly compare derived properties (Bottrell et al., 2017a,b; Huertas-Company et al., 2019; Bottrell et al., 2019b; Zanisi et al., 2020; Ferreira et al., 2020). My approach is therefore to use simulations of galaxies, for which I can measure "true" values of a given morphology metric, before adding noise (e.g. in the form of measurement uncertainty) and the effects of degrading resolution, and comparing to the idealized measurements.

Specifically, this work makes use of the IllustrisTNG (hereafter TNG) simulation (Weinberger et al., 2017; Pillepich et al., 2018a), as well as its predecessor, Illustris (Vogelsberger et al., 2014; Genel et al., 2014; Sijacki et al., 2015), in particular TNG100-1 and Illustris-1, which have comparable volumes and resolutions. The motivation for using two different simulations is to assess whether the results are sensitive to the details of the physics model used, or whether they are generalizable to different simulations or observational data sets (see Section 3.5 for details). The use of Illustris and TNG is ideal in this regard, since they both represent a suite of magneto-hydrodynamic (just hydrodynamic, in the case of Illustris) cosmological simulations (Marinacci et al., 2018; Naiman et al., 2018; Nelson et al., 2018; Pillepich et al., 2018b;

Springel et al., 2018; Nelson et al., 2019) run with the moving-mesh code AREPO (Springel, 2010; Pakmor et al., 2011, 2016).

Both simulations have runs with similar volumes and resolutions, but employ different physical models, such as the implementation of AGN feedback (Weinberger et al., 2017). The AGN feedback model used in TNG allows for more efficient quenching of high mass galaxies, leading to dissipationless processes that alter the morphology of quenched galaxies (Rodriguez-Gomez et al., 2017). Additionally, the reparameterization of galactic winds in TNG (Pillepich et al., 2018a) results in more accurate sizes of low-mass galaxies than in Illustris. These two changes to the physical model have resulted in more realistic morphologies of TNG galaxies, as opposed to Illustris, when compared to observational data sets (e.g. Bottrell et al. 2017b compared with Rodriguez-Gomez et al. 2019). Thus, for the work presented here, TNG100-1 serves as the fiducial simulation, the highest resolution run of the $(110.7\text{Mpc})^3$ volume, with a baryonic mass resolution of order $\sim 10^6 M_\odot$. Then Illustris-1 (hereafter Illustris), which has similar volume and resolution to TNG100-1, is used as a comparison sample to test the universality of the results determined from TNG.

One thousand galaxies are randomly selected each from TNG and Illustris, all of which are drawn from the final $z = 0$ snapshots and have stellar masses $M_\star/M_\odot \geq 10^9$. Any galaxies with $M_\star < 10^9 M_\odot$ are not reliably resolved. Given the random selection, the $M_\star$ distribution is biased towards low mass galaxies; Section 3.4 will demonstrate these methods still recover a realistic range of asymmetry and concentration values (Rodriguez-Gomez et al., 2019). Maps of the stellar mass distribution are generated from the simulation particle data, with a gravitational softening length for stars of 0.7 kpc at z=0 (Nelson et al., 2018). This idealized stellar mass map allows us to measure non-parametric morphologies without having to consider sensitivities to the mass-to-light ratio that would lead to uncertainties for an observed galaxy. Each simulated galaxy is projected along a random axis, with a FOV ten times the stellar half mass radius of the galaxy and 512 pixels on each side to achieve high spatial resolution for every galaxy (compared to the resolution degradation explored in Section 3.4.2).

3.2.1 Adding observational effects to simulated galaxies

Having generated the idealized stellar mass maps, observational realism is added in two steps. First, I consider the effect of degrading the resolution of the stellar mass map, which will reduce the contrast of asymmetry structures and alter the

concentration measurement (Conselice et al., 2000; Bershady et al., 2000). Such degradation is achieved by convolving the stellar mass map with a Gaussian PSF that has a full width at half maximum (FWHM) ranging between 0.002" - 7" (with the goal of ranging from a negligible PSF to some of the largest PSFs in current observational surveys). An arcsecond PSF value is chosen by assuming each galaxy is at the average distance of a MaNGA survey galaxy z = 0.037 (the applicable distance for comparing this analysis to IFU data), along with a cosmology in which $H_0 = 70$ km s^{-1} Mpc^{-1}, $\Omega_m = 0.3$, and $\Omega_\Lambda = 0.7$.

The PSF is only a component of the more fundamental resolution of the image, which itself is the relationship between the convolving PSF size and the apparent size of the galaxy. The set physical size of the galaxy, along with the choice of a constant distance, means that the apparent angular size of the galaxy is fixed and one need only vary the PSF to vary the resolution. Resolution ("Res") is defined in this analysis to be the ratio of the half light radius (R_{half}) in arcseconds and the PSF FWHM in arcseconds (Res=R_{half}/FWHM). By using R_{half} there is no need to fit the galaxy structure to measure radius, although note that any approximation of galaxy size with respect to PSF would suffice. Figure 3.1 summarizes the different levels of realism applied to an example TNG galaxy stellar mass map (top left panel). The top middle panel shows an example PSF similar to that in the MaNGA survey (2.48"), but given the small angular size of the galaxy (R_{half}=1.69") the resolution of the image is actually very low.

Second, noise is added to the mass map. As will be explained further in Section 3.3, the traditional asymmetry index involves the subtraction of a background sky term, in order to account for observational effects that contribute to asymmetry, but are not associated with the galaxy itself. This is akin to subtracting the sky from a photometric measurement. The subtraction of the background sky term has a significant effect on the traditional asymmetry index, due to its mathematical definition. Although this study focuses on stellar mass maps, rather than light, noise would still present in an observed stellar mass map in the form of measurement and post-processing uncertainties. Therefore, a random "noise" map must be created to add to the simulated galaxy mass map, to approximate an observational scenario where every pixel has some hypothetical uncertainty on the mass measurement. Signal-to-noise is measured from this noise map to quantify the significance of the contribution from uncertainty, with the goal of creating a variety of noise maps to span a large range of possible signal-to-noise values.

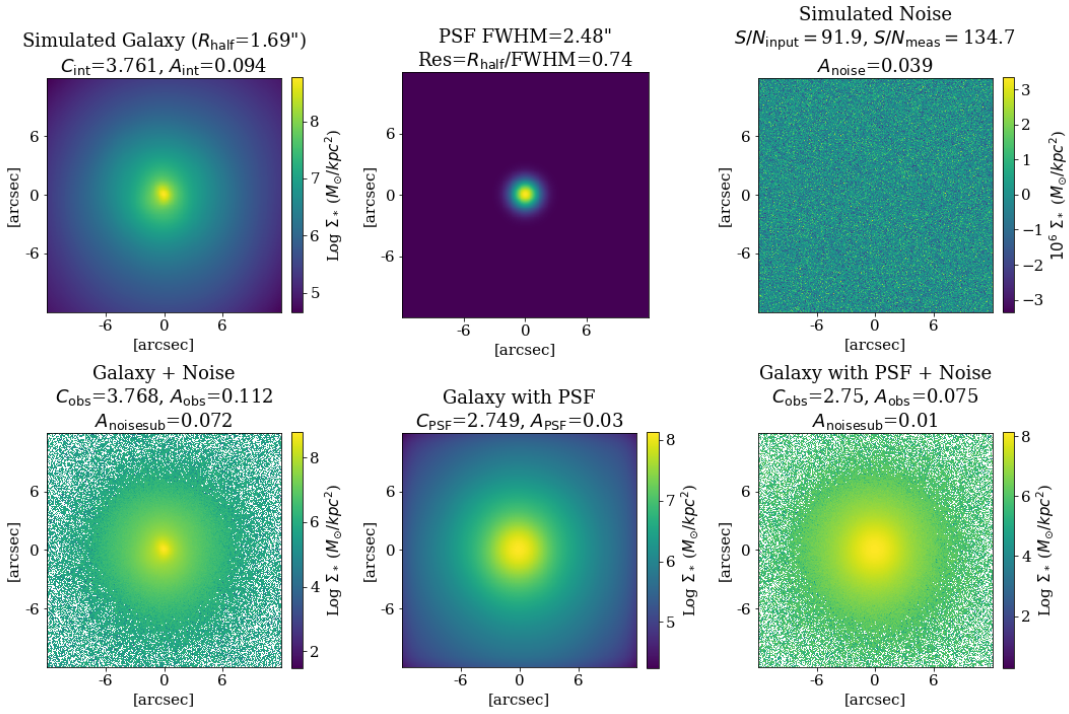

Figure 3.1: The steps through which realistic noise and resolution are applied to a simulated galaxy. Top-left: The stellar mass surface density of the simulated galaxy, from which intrinsic asymmetry and concentration are measured. Top-middle: A sample PSF applied to this galaxy, although values can range from 0.002"-7". Changing the PSF allows us to change the resolution to the simulated galaxies at a fixed distance. I have chosen to highlight this galaxy with a small angular size compared to the applied PSF, resulting in a small resolution value (smaller than has been examined in previous works), to highlight how significantly degrading the resolution changes the asymmetry and concentration. Top-right: Random noise generated from a Gaussian distribution, to be applied to the galaxy image. The desired (input) S/N is used to generate the width of the Gaussian distribution so that the measured S/N is of a similar (though not exactly the same) value. Bottom-left: The stellar mass surface density image of the galaxy with added noise. White values are where $\Sigma_\star$ is so small, adding negative noise results in a non-measurement. Bottom-middle: The image of the galaxy convolved with the PSF from the top-middle panel. Bottom-right: The image of the galaxy convolved with the PSF and with noise added, providing an image of the galaxy more similar to what would be seen with observations.

To generate a random noise map representing the hypothetical uncertainties on each pixel for the simulated stellar mass map, I first select a desired signal-to-noise ratio ranging from 0 to 1000. The median signal of the galaxy is then measured within a $1R_{\rm half}$ aperture. The median absolute deviation (MAD) is approximated within that aperture to be the median signal within that aperture divided by the desired signal-to-noise ratio. Given the noise map is created from a normal distribution, the MAD can be converted to a standard deviation by multiplying by the known scale factor $k = 1/(\Phi^{-1}(3/4)) = 1.4826$ (where Φ^{-1} is the inverse of the cumulative distribution, and 3/4 implies $\pm$MAD covers half the standard normal cumulative distribution function). Using the the standard deviation I construct a standard-normal distribution centred on zero; for each pixel I select a random value from this distribution to set the uncertainty of that pixel. This method ensures that the resulting signal-to-noise (the median value of the mass map within $1R_{\rm half}$ divided by the median value of the noise map within $1R_{\rm half}$) is approximately (though not exactly) equal to the desired signal-to-noise used to construct the noise map.

An example noise field is shown in the top right panel of Fig. 3.1. The lower panels of Figure 3.1 show the resulting mass maps when either the noise (left panel), the PSF (middle panel) or both (right panel) are included.

3.3 Concentration and asymmetry calculations

Non-parametric morphologies have long been used to quantify some metric of a galaxy's light distribution, in a way that can be automated on a large sample of galaxies. The focus on unique morphologies and the benefit of automation has made non-parametric morphologies a crucial tool in identifying merger galaxies in large galaxy surveys, by looking for outlier measurements to identify the highly-disturbed interacting galaxies. The "CAS" approach is one of the most commonly used for this purpose, measuring the concentration, asymmetry, and smoothness of a galaxy image (Conselice et al., 2000, 2003; Lotz et al., 2004). I focus on concentration, as it could be used to investigate the inflow of gas to the centre of the galaxy (and subsequent central starburst and metallicity dilution), and the asymmetry parameter, which could look for asymmetric features and gradients in $\Sigma_{\rm SFR}$ and gas-phase metallicity maps. Both non-parametric indices are computed using the `statmorph` package (Rodriguez-Gomez et al., 2019)[1], which automates the calculations described

[1] https://statmorph.readthedocs.io/en/latest/overview.html

below.

The concentration parameter (C) has been used for over half a century (see Morgan, 1959). Although there are a plethora of possible definitions of concentration, the most commonly used in the assessment of galaxy light distributions is that of Bershady et al. (2000) and Conselice (2003). These works define concentration as:

$$C = 5\log_{10}(r_{80}/r_{20}) \tag{3.1}$$

where r_{80} and r_{20} are the radii within which 80% and 20% of the galaxy's total flux (for this work, total stellar mass) is contained, respectively. The inner and outer radii are chosen specifically to mitigate the degradation in concentration that comes from low resolution (see Bershady et al. (2000) for details). For my analysis the intrinsic concentration ($C_{\rm int}$) is derived directly from the idealized simulation image. Once the image resolution is degraded by convolving with a PSF, the measured concentration is referred to as $C_{\rm Res}$; comparing this value to $C_{\rm int}$ demonstrates the impact of resolution on the true concentration. Finally, $C_{\rm obs}$ stands for the measured concentration once noise has been added to the image. Again, comparison of $C_{\rm obs}$ to $C_{\rm int}$ will quantify how much the intrinsic concentration of the simulated galaxy has been affected by realistic observational features.

Identifying the galaxy's centre is critical to the calculation of concentration, as well as many other non-parametric indices, including the second index of interest in this work asymmetry. Therefore concentration and asymmetry are often computed in conjunction, in an iterative approach that finds a centre that yields the minimum asymmetry value, then uses that centre to measure concentration as well. As the name implies, the asymmetry parameter quantifies how much of an image's light is not symmetric about an axis of rotation, calculated as the difference between an image and its 180°rotation (Conselice et al., 2000).

The intrinsic asymmetry ($A_{\rm int}$) is defined as:

$$A_{\rm int} \equiv \frac{\Sigma_{i,j} \mid I_{ij} - I_{ij}^{180} \mid}{\Sigma_{i,j} \mid I_{ij} \mid} \tag{3.2}$$

where $I_{i,j}$ is the flux contained within an individual pixel of the galaxy image, and $I_{i,j}^{180}$ is the pixel at that same i, j location once the image is rotated 180 degrees. These

values are computed within 1.5 times the Petrosian radius ($r_{\rm petro}$)[2]. For an idealized image, such as one generated from a simulation, $A_{\rm int}$ is a perfect representation of the galaxy's asymmetry (with no background noise).

However, in real images there are observational artefacts that can contribute to the asymmetry that are not intrinsic to the galaxy, such as sky noise and background gradients introduced by nearby bright sources. For either a real galaxy observation, or a simulated galaxy that has had noise added to it, the measured asymmetry is therefore a combination of the galaxy signal and the background noise:

$$A_{\rm obs} = \frac{\Sigma_{i,j} \mid (I + \text{noise})_{ij} - (I + \text{noise})^{180}_{ij} \mid}{\Sigma_{i,j} \mid (I + \text{noise})_{ij} \mid} \tag{3.3}$$

Therefore, in order to recover the intrinsic asymmetry, the noise asymmetry ($A_{\rm noise}$) needs to be quantified and removed from the observed asymmetry. This is analogous to the subtraction of background sky in the measurement to obtain galaxy photometry. In observations, $A_{\rm noise}$ is computed from a region offset from the galaxy; in simulations it can alternatively be computed from the noise (background) field generated in addition to the idealized image, i.e.:

$$A_{\rm noise} = \frac{\Sigma_{i,j} \mid \text{noise}_{ij} - \text{noise}^{180}_{ij} \mid}{\Sigma_{i,j} \mid \text{noise}_{ij} \mid} \tag{3.4}$$

The premise above is that subtracting the contribution to the measured asymmetry ($A_{\rm obs}$) from the background noise ($A_{\rm noise}$, a term that captures all background sources of asymmetry that must be removed), should approximate the intrinsic asymmetry. That is a corrected, noise-subtracted asymmetry $A_{\rm noisesub}$ can be defined as:

$$A_{\rm noisesub} \equiv A_{\rm obs} - A_{\rm noise} \tag{3.5}$$

with the assumption that $A_{\rm noisesub} \sim A_{\rm int}$.

However, due to the modulus present in the equations for $A_{\rm obs}$, $A_{\rm noise}$, and $A_{\rm int}$, it is not mathematically correct to assume that $A_{\rm int}$=$A_{\rm noisesub}$. Given the rule of modular subtraction ($\mid A \mid - \mid B \mid \leq \mid A - B \mid$), $A_{\rm noisesub}$ can only serve as a lower limit to the true value of $A_{\rm int}$. Indeed, due to the presence of the modulus in Equation 3.4, even a random noise field will have a non-zero asymmetry associated with it. The under-

[2]The Petrosian radius is the radius at which the mean surface brightness within that aperture is a fraction η of the mean isophotal brightness (Petrosian, 1976). η is typically set to 0.2, which we adopt here.

estimation of asymmetry through this noise correction method has been previously investigated in photometric studies, which recommend the asymmetry measurement only be made where $S/N > 100$. At lower S/N noise dominates the asymmetry (see Conselice et al. 2000). Whereas this regime is readily achievable in photometry, such a high S/N is unlikely to be reached in maps of galactic properties, and previous works on the asymmetry of galactic gas and dust have struggled with this as well (Bendo et al., 2007; Giese et al., 2016; Reynolds et al., 2020). Although stellar mass stellar mass maps do not suffer from a sky contribution, noise is still present in observed stellar mass maps in the form of uncertainties in the determination of the stellar mass itself, and these uncertainties are expected to far exceed the equivalent of a $S/N \sim 100$ criterion (e.g. Mendel et al., 2014; Sánchez et al., 2016a,b).

Figure 3.1 shows how asymmetry and concentration can be affected by resolution and noise, highlighting the impact of noise subtraction on the recovered asymmetry. In the example galaxy shown in Figure 3.1, the intrinsic concentration is measured to be $C_{\rm int}$=3.761 (top left panel). After degrading the resolution with Res=0.74 (the stellar half mass radius is smaller than the PSF that convolves the image), the concentration is significantly diminished to $C_{\rm obs}$=2.749 (lower middle panel). Conversely, if just noise is added to the image (no degraded resolution), the measured concentration is essentially unaffected, with a difference less than 0.1% from the intrinsic value. The combined effect of resolution and noise yields an observed concentration of $C_{\rm obs}$=2.75, i.e. a net decrease from the true value by ∼27 per cent. As will be shown for the full galaxy sample in the next section, observational changes in concentration can be traced solely to the value of resolution.

As for the impact of resolution and noise on asymmetry, the example galaxy in Figure 3.1 starts with an intrinsic asymmetry $A_{\rm int}$=0.094 (top left panel). The particular noise field generated for this example has an asymmetry (introduced by the use of the modulus in Equation 3.4) of $A_{\rm noise}$=0.039. Since the measured asymmetry in the noisy image for this example galaxy is $A_{\rm obs}$=0.112 (lower right panel), subtracting the noise asymmetry yields a corrected value of $A_{\rm noisesub}$ = 0.073. The noise-subtracted asymmetry is therefore, in this case, under-estimating the true asymmetry by a factor of ∼20%. The following section will compare the measured, corrected and intrinsic morphologies of the full simulated galaxy sample, and investigate whether further corrections could be made to improve them.

3.4 Correcting non-parametric morphologies for noise and resolution

I next assess the concentration and asymmetry of the sample of 1000 galaxies in the TNG simulation (a comparison with the Illustris simulation is given in Section 3.5). The impacts of noise (which in the case of observed mass maps is driven by uncertainty on the measurements) and resolution will be assessed separately, quantifying how well the intrinsic parameters can be recovered once these compounding observational effects are included.

3.4.1 Noise

Figure 3.2 demonstrates how adding random noise to the stellar mass map changes the observed asymmetry and concentration in the 1000 galaxies taken from the TNG simulation. Noise contribution has little impact on the observed concentration (left panel). This result is expected, since a randomly constructed noise field will contribute uniformly to the inner and outer apertures from which concentration is calculated. The only exception to this rule is galaxies with the lowest signal-to-noise ($S/N < 5$), where random clumping of pixels with high noise can shift the concentration measurement (hence why the scatter is also unbiased). Thus, when measuring the concentration of an image, one generally need not worry about any intrinsic bias created by the noise.

In contrast, adding noise to the image always leads to an over-estimate of the observed asymmetry (Equation 3.3) compared with its intrinsic value (right panel of Figure 3.2), although the change is greatest for galaxies with low signal-to-noise, when the noise dominates the image (see Conselice et al., 2000; Lotz et al., 2004; Giese et al., 2016). For $S/N > 100$ the difference rarely exceeds a 50% increase, but for $S/N < 100$ the asymmetry can increase anywhere between a factor of 2 to 10. To reiterate, because of the modulus within the asymmetry measurement even a random noise map will have a net-positive value.

The noise subtraction method has traditionally been used to account for the non-negligible addition of noise; however, as discussed in Section 3.3, it only works well for the $S/N > 100$ regime (when noise does not dominate the asymmetry). Figure 3.3 illustrates how subtracting the noise contribution to asymmetry decreases the scatter between the measured and intrinsic asymmetry. $A_{\rm noisesub}$ values for galaxies with $S/N > 100$ (the S/N cut suggested by Conselice et al. 2000) are within ± 0.05 of their intrinsic value (represented by the grey dashed lines). However, galaxies with

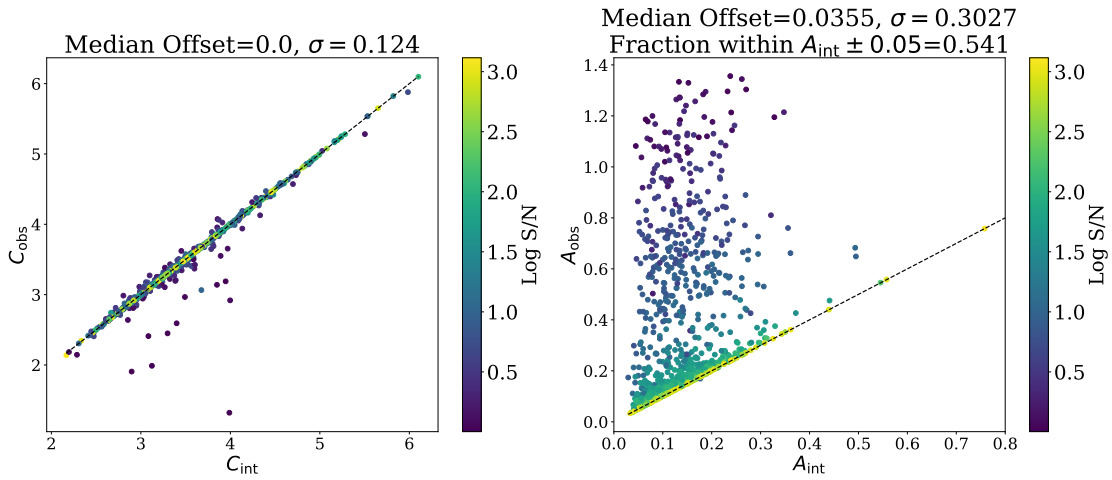

Figure 3.2: The observed concentration (left) and asymmetry (right) compared to intrinsic values (which have no random noise contribution). From the left panel it is clear that the addition of noise has no effect on concentration measurements (save catastrophic cases at the lowest signal-to-noise). Asymmetry, on the other hand, is always overestimated once noise is added, although the degree of that overestimation scales with inversely with S/N.

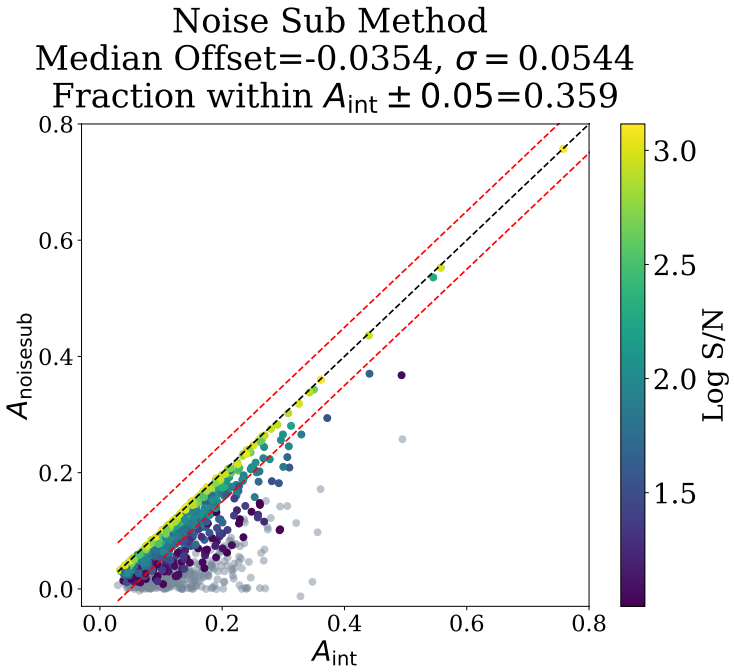

Figure 3.3: The standard noise subtraction method requires subtracting all of $A_{\rm noise}$ from $A_{\rm obs}$ to approximate the intrinsic asymmetry. The black dashed line represents the line of equality, with red dashed lines representing a 0.05 buffer from this line. Points are colour-coded by S/N, save for galaxies with $S/N < 10$, which are grey. By correcting for noise contribution to asymmetry the scatter between the measured and intrinsic asymmetry is lessened by a factor of 10, and 5% more galaxies have a good asymmetry measurement (within 0.05 of $A_{\rm int}$). However, the median offset using this correction is of a similar magnitude to doing no noise correction (see Figure 3.2), just in the opposite direction. The galaxies with asymmetries far less than $A_{\rm int} \pm 0.05$ are those with low S/N, in particular the galaxies with $S/N < 10$ have the greatest difference in asymmetry from noise.

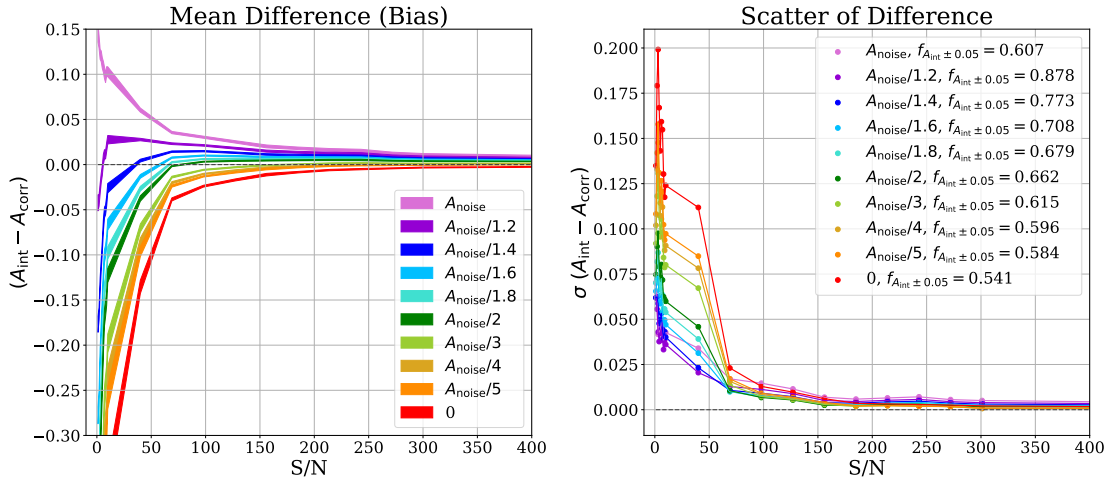

Figure 3.4: Left: The mean difference between the intrinsic asymmetry and corrected asymmetry for increasing signal-to-noise. Each curve represents subtracting a different fraction of the noise asymmetry, where red has no subtraction, and purple subtracts the entire $A_{\rm noise}$ value. The width of each line is the standard error on the mean. See Figure 3.7 for a comparison of these plots to my fit correction. Right: The standard deviation of the difference between intrinsic and corrected asymmetry in each signal-to-noise bin, for each correction method. Thus to recover the intrinsic asymmetry at $S/N < 100$, subtracting a fraction of $A_{\rm noise}$ does better than subtracting the total noise contribution to asymmetry. Subtracting $A_{\rm noise}/1.2$ recovers the most asymmetry values (within $A_{\rm int} \pm 0.05$) and has the smallest scatter in the difference at all S/N values.

$S/N < 100$ now have a preferentially underestimated asymmetry (creating a similar problem, although in the opposite direction, to the overestimation that occurs with no $A_{\rm noise}$ correction).

The presence of a bias in the asymmetry correction method is obviously problematic; despite being introduced as an improvement in the estimate of asymmetry of intermediate signal-to-noise galaxies (where background noise can have a non-negligible contribution), it actually introduces a new offset in the low S/N regime. However, given $A_{\rm obs}$ is an overestimation and $A_{\rm obs} - A_{\rm noise}$ is an underestimation of the true asymmetry, one could postulate that a noise correction that more accurately reproduces $A_{\rm int}$ lies somewhere in between. I propose that subtracting a fraction of $A_{\rm noise}$, rather than the entire value, could mitigate the over-correction. Subtracting multiple different fractions of $A_{\rm noise}$ from $A_{\rm obs}$ will determine what fraction of the noise needs to be corrected to reproduce $A_{\rm int}$.

Figure 3.4 exhibits how the difference between the intrinsic and noise corrected

asymmetry varies with S/N for multiple fractions of $A_{\rm noise}$ correction. Each coloured curve in Figure 3.4 represents a different fractional correction of $A_{\rm noise}$, with pink representing a full subtraction of $A_{\rm noise}$, and red representing no subtraction. Both subtracting the sky asymmetry and doing no subtraction only achieve reasonable accuracy within $A_{\rm int} \pm 0.05$ for a signal-to-noise greater than 100, when the curves begin to approach zero difference between the true and observed asymmetry. However, varying the fractional value of $A_{\rm noise}$ improves the recovery of the intrinsic asymmetry to lower signal-to-noise values. The best option between doing nothing and subtracting the total $A_{\rm noise}$ is actually to subtract $A_{\rm noise}/1.2$, which results in the greatest fraction of galaxies within 0.05 of $A_{\rm int}$ (excluding galaxies with $S/N < 10$ to ensure answers aren't skewed by the asymptotic nature of each curve). Correcting for $A_{\rm noise}/1.2$ also results in the smallest scatter in the difference for all S/N regimes. Figure 3.5 directly compares the measured and intrinsic asymmetry (as was completed in Figure 3.3 for traditional noise correction). Although the scatter in the difference between the two is only marginally better than regular $A_{\rm noise}$ correction, the median offset has diminished and over 20% more galaxies have reliable asymmetry measurements (within 0.05 of the intrinsic asymmetry). Therefore, when considering low S/N data using $A_{\rm obs} - A_{\rm noise}/1.2$ is the best way to approximate $A_{\rm int}$, and I will continue to investigate this as a candidate asymmetry measurement for the rest of the analysis (along with correcting for $A_{\rm noise}$, and doing no correction).

3.4.1.1 Fit to recover intrinsic asymmetry for all S/N

The two methods to correct for noise asymmetry described so far are approximations that work within a signal-to-noise limited system. However, if there exists some mathematical relationship between the intrinsic asymmetry, the observed asymmetry, and the signal-to-noise, one should be able to fit a relationship between two of those parameters to almost perfectly approximate the third. In order to explore this possibility, I assume a relationship between the intrinsic asymmetry, the observed asymmetry, and the signal-to-nose of the following form:

$$A_{\rm int} = (F_1(S/N) + 1)A_{\rm obs} + F_2(S/N)A_{\rm obs}^2 + F_3(S/N)A_{\rm obs}^3 \tag{3.6}$$

where F_3, F_2, and F_1 are each unique functions of signal-to-noise of the following form:

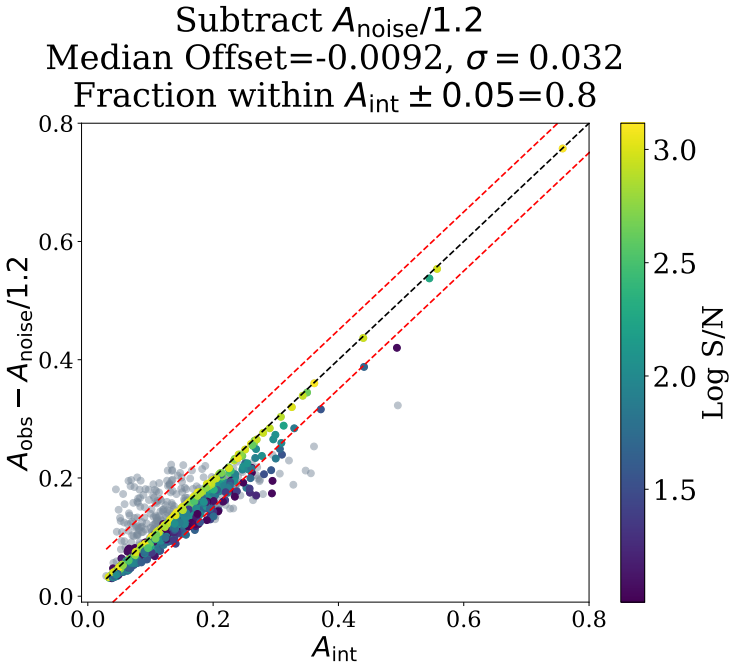

Figure 3.5: The asymmetry corrected for $A_{\rm noise}/1.2$ versus the intrinsic asymmetry. Points are colour-coded by S/N, except for galaxies with $S/N < 10$, which are grey. The scatter between the two is smaller than doing no noise correction, similar to the improvement from subtracting $A_{\rm noise}$ from the observed asymmetry (see Figure 3.3). However, the median offset is significantly less, and over 20% more of the simulated galaxies are within an accurate asymmetry measurement (within $A_{\rm int} \pm 0.05$). In fact, almost all galaxies with $S/N > 10$ are within 0.05 of $A_{\rm int}$, a much more forgiving S/N cut than the $S/N > 100$ cut necessary for the traditional $A_{\rm noise}$ correction.

$$F(S/N) = X_1(S/N)^{-1} + X_2(S/N)^{-2} + X_3(S/N)^{-3} \tag{3.7}$$

Equation 3.6 is designed so that as S/N goes to infinity, $A_{int} = A_{obs}$. As established in Figure 3.2, at the highest S/N the observed asymmetry is almost exactly equal to the intrinsic asymmetry, as the contribution from uncertainty is practically negligible. Thus I endeavour to replicate a relationship between $A_{\rm int}$, $A_{\rm obs}$, and S/N that aligns with the fact that as the uncertainty goes to zero (and S/N goes to infinity), $A_{\rm int}$ should equal $A_{\rm obs}$.

I elect to only fit data with $S/N < 500$. At $S/N > 500$, the difference between the observed and intrinsic asymmetry never exceeds 1% of $A_{\rm int}$, and it is therefore safe to assume that $A_{\rm int} \approx A_{\rm obs}$. Excluding high S/N data from the fit is better specialized to characterize the asymptotic change of asymmetry with S/N. Equation 3.6 is fit to the $A_{\rm obs}$ and S/N of the 788 TNG galaxies with $S/N < 500$, using the python package LM Fit[3], which minimises the root-mean-square difference between the intrinsic asymmetry and the observed asymmetry. The following fit is found to minimise the difference between $A_{\rm int}$ and $A_{\rm obs}$:

$$\begin{aligned}
&\textbf{S/N<500:}\ A_{\rm int} = (-(15.36 \pm 0.58)(S/N)^{-1} + (78.85 \pm 3.38)(S/N)^{-2} \\
&- (86.89 \pm 4.41)(S/N)^{-3} + 1)A_{\rm obs} + ((10.69 \pm 1.39)(S/N)^{-1} \\
&- (99.59 \pm 6.37)(S/N)^{-2} + (125.44 \pm 7.63)(S/N)^{-3})A_{\rm obs}^2 \\
&+ (-(0.91 \pm 0.83)(S/N)^{-1} + (31.98 \pm 3.19)(S/N)^{-2} \\
&- (45.82 \pm 3.43)(S/N)^{-3})A_{\rm obs}^3 \\
&\textbf{S/N>500:}\ A_{\rm int} = A_{\rm obs}
\end{aligned} \tag{3.8}$$

The coefficients in Equation 3.8 are specific to how the signal-to-noise ratio is measured, in particular using $R_{\rm half}$ to set the aperture from which that measurement is made. In practice one could repeat the fitting process laid out thus far using a different aperture radius (as would be necessary for different kinds of observations). This would significantly change the coefficients present in the final relationship between $A_{\rm int}$, $A_{\rm obs}$, and S/N. But the conceptualization of this fit, as well as its relative accuracy, would remain unchanged.

The goodness of this fit is evaluated by comparing the intrinsic asymmetry to

[3]https://dx.doi.org/10.5281/zenodo.11813

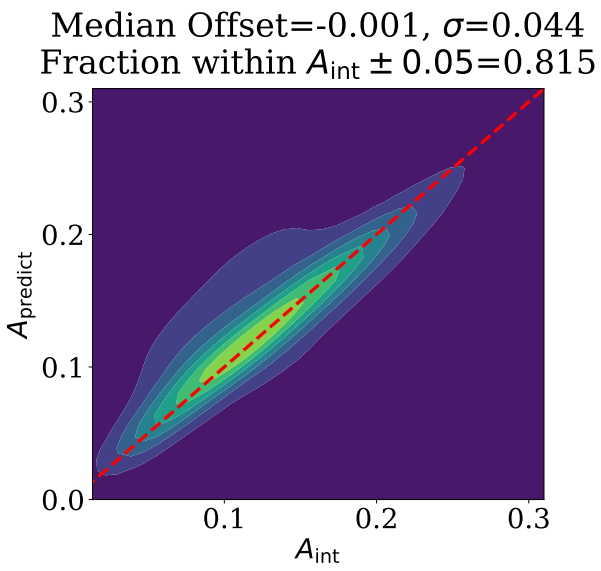

Figure 3.6: Density contours for the predicted asymmetry based on the fit relationship from Equation 3.8 versus the intrinsic asymmetry, the dashed red line representing where the two would be equal to each other. Applying a correction for the random noise based on a fit function significantly decreases the scatter of the difference between the predicted and intrinsic asymmetry, while also removing any bias in the predicted asymmetry. The scatter in the fit is dominated entirely by low S/N galaxies.

that predicted by Equation 3.8 in Figure 3.6 (see Section 3.5 for tests on independent samples). Both the median offset between the observed asymmetry and intrinsic asymmetry, and the scatter of this offset, is reduced by a factor of 10 after correcting asymmetry based on this fit. The majority of the scatter here comes from the lowest S/N (< 10) galaxies, where the accuracy of the fit is lowest. However, low S/N galaxies can both have over- or under-estimated asymmetry measurements (unlike the bias to one or the other when correcting based on $A_{\rm noise}$). The difficulty with fitting the low signal-to-noise data likely stems from the asymptotic relationship between the intrinsic and observed asymmetry at low signal-to-noise, thus a small change in the fit can lead to a more drastically incorrect prediction. Of the predicted asymmetries, including all S/N values, 81.5% are within 0.05 of $A_{\rm int}$ (what is considered a "good" asymmetry measurement). Thus the fit correction is a significant improvement on the 54.1% and 60.7% for doing no correction, and subtracting $A_{\rm noise}$, respectively. Subtraction of $A_{\rm noise}/1.2$ is still the best asymmetry prediction by a margin, recovering 87.8% of asymmetries within 0.05 of $A_{\rm int}$. Although the fit correction still has its own benefits over the $A_{\rm noise}/1.2$ correction, in particular when simultaneously correcting for resolution as is investigated in Section 3.4.2.1.

To determine the best method for measuring asymmetry I compare the results from Equation 3.8 to the traditional noise subtraction, the noise subtraction divided by 1.2, and doing no correction for noise asymmetry. Figure 3.7 examines how well each of these methods reproduce the intrinsic asymmetry in different signal-to-noise regimes. The traditional method of subtracting the noise asymmetry (the purple line) does poorly at low signal-to-noise, as expected based on the earlier discussions in this work. Excluding galaxies with $S/N < 100$ guarantees this bias in asymmetry is no more than 0.02, which given the range of possible asymmetry values (0 - 1) is relatively small. Even for low asymmetry galaxies where the bias has a greater percentage effect, because the bias is relatively constant after $S/N = 100$ you could still compare asymmetries within a sample of galaxies with this S/N cut. The signal-to-noise cut must be made though, otherwise the asymmetry of faint objects will appear systematically higher than brighter, nearby objects.

However, few galaxy properties (like those collected from an IFU observations) can achieve high enough signal-to-noise to recovery the majority of intrinsic asymmetry values with all of these correction methods. Although the signal-to-noise of the flux emission lines measured from spectra are excellent by design, other uncertainties that go into computing properties like stellar mass surface density can raise the statistical

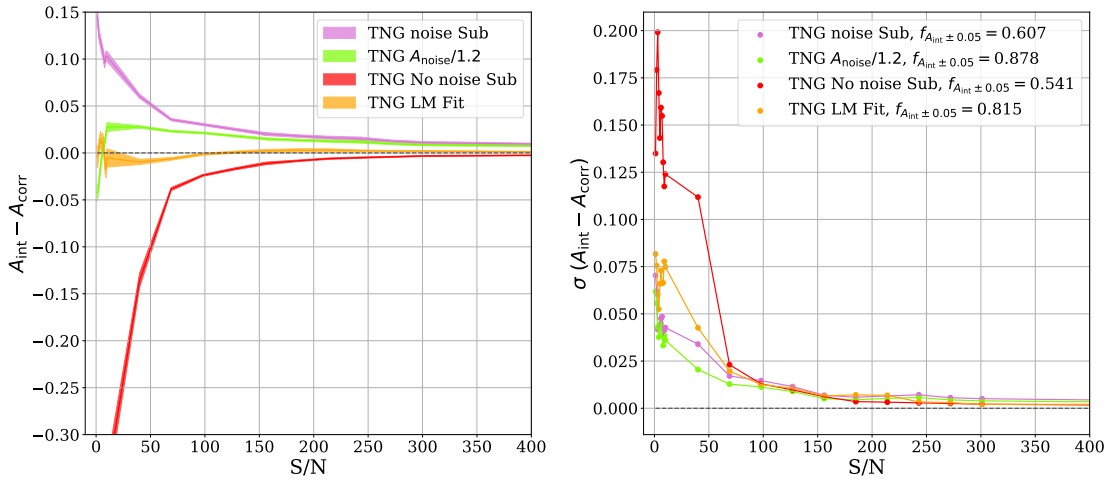

Figure 3.7: Left: The mean difference between the intrinsic and observed asymmetry for increasing signal-to-noise bins. The red line represents performing no correction for the sky asymmetry, the purple line represents correcting by A_{noise}, the green line for correcting by $A_{\text{noise}}/1.2$, and the orange line for applying the fit correction from Equation 3.8. The width of each line is the standard error on the mean. Right: The standard deviation of the difference in asymmetry for the four asymmetry correction methods. All methods that perform some kind of correction for noise contribution to asymmetry result in lower standard deviations than doing no noise subtraction. One should note that the standard deviation of the difference for the LM Fit method is comparable to the two noise subtraction methods except at low signal to noise. Here the scatter of the LM Fit method is slightly larger, although still relatively small and a significant improvement from doing no noise correction.

uncertainty of the pixel up to 0.1 dex or more. If one of the TNG stellar mass maps had an error of 0.1 dex on every pixel, the signal-to-noise of that stellar mass map (based on my calculation method) would be approximately 4. Thus to measure the asymmetry of spectral data products, the $A_{\rm noise}/1.2$ method is the better traditional noise correction compared to the $A_{\rm noisesub}$ method. The bias reaches less than 0.025 difference for S/N as low as 50, and no bias exists at $S/N > 100$. The asymmetry fit method, on the other hand, does better than all other asymmetry approximations at low S/N, with a difference between $A_{\rm int}$ and $A_{\rm obs}$ below 0.02 even at $S/N < 10$, making it the ideal asymmetry measurement for data products with large uncertainties. This method has the added benefit of also not requiring a measurement of $A_{\rm noise}$, so long as a global S/N value can be approximated accurately. The relationship between observed asymmetry, signal-to-noise, and intrinsic asymmetry is fit to this simulation for a particular subset of galaxies; Section 3.5 will evaluate how well this fit can be applied to other data sets by comparing to Illustris.

3.4.2 Spatial resolution

The resolution of an image can alter both the asymmetry and concentration measurements (e.g. Figure 3.1). Low resolution can smooth out asymmetric structures that would otherwise lead to a larger asymmetry measurement. Degrading the resolution of an image will also spread out the light distribution (or stellar mass distribution in this case), resulting in more light in the outer aperture compared to the inner aperture than in the original image. Thus, degrading the resolution will lead to a systematically lower concentration as well. Figure 3.8 shows both of these effects for the sample of TNG galaxies. In the left panel the asymmetry is systematically under-estimated as the resolution decreases, and the right panel shows a similar under-estimation of concentration with decreasing resolution. The effect of varying resolution when comparing asymmetry and concentration values has been discussed in detail in previous works (Bershady et al., 2000; Conselice et al., 2000; Lotz et al., 2004; Bendo et al., 2007; Giese et al., 2016).

3.4.2.1 Resolution corrected asymmetry

Just as asymmetry was corrected for noise based on a relationship between S/N and $A_{\rm obs}$ (Equation 3.6), a similar relationship must exist between $A_{\rm Res}$ and the resolution of the image that can recover $A_{\rm int}$. Although I define the resolution as the stellar half

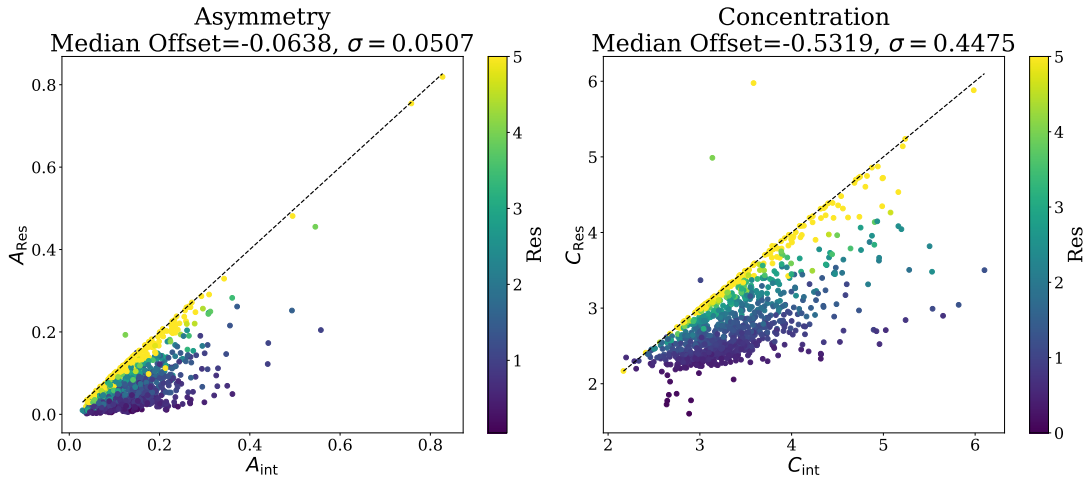

Figure 3.8: A demonstration of how degrading resolution changes the asymmetry (left) and the concentration (right) compared to their intrinsic values (where resolution is functionally infinite). Degrading the resolution systematically decreases both asymmetry and concentration, and the magnitude of this difference increases inversely with the value of resolution. Note that the points with the lowest resolution are furthest from the black dashed line representing $A_{\rm Res}$=$A_{\rm int}$. Given the bias in the asymmetry/concentration measurement is clearly dependent on the intrinsic asymmetry/concentration and resolution value, just as with S/N the resolution effects can be corrected for to recover the intrinsic index.

mass radius over the PSF FWHM (both in arcseconds), any approximation of the apparent galaxy size in respect to the PSF size would suffice here. Using the Res parameter instead of the PSF FWHM alone guarantees the correction will work for a variety of galaxy sizes and distances, rather than just working for a range of observational PSFs. Given that resolution and S/N have a similar effect on asymmetry, I assume a similar relationship between $A_{\rm int}$, $A_{\rm Res}$, and Res exists of the following form:

$$A_{\rm int} = (F_1({\rm Res}) + 1){\rm A_{Res}} + {\rm F_2(Res)A_{Res}^2} + {\rm F_3(Res)A_{Res}^3} \tag{3.9}$$

where $A_{\rm Res}$ is the observed asymmetry with degraded resolution (note that $A_{\rm Res}$ has no noise contribution) and F_3, F_2, and F_1 are each unique functions of this resolution parameter "Res" of the following form:

$$F({\rm Res}) = {\rm X_1(Res)^{-1} + X_2(Res)^{-2} + X_3(Res)^{-3}} \tag{3.10}$$

As with Equation 3.6, I design the relationship such that $A_{\rm int} = A_{\rm Res}$ as Res goes to infinity. As was completed with signal-to-noise in Section 3.4.1, I fit $A_{\rm Res}$ and Res to Equation 3.9 using LM Fit, resulting in the following relationship:

$$\begin{aligned} A_{\rm int} = {} & ((3.626 \pm 0.108){\rm Res^{-1}} + (0.0289 \pm 0.0714){\rm Res^{-2}} \\ & - (0.00680 \pm 0.00833){\rm Res^{-3}} + 1){\rm A_{Res}} + (-(15.53 \pm 1.46){\rm Res^{-1}} \\ & - (21.17 \pm 2.32){\rm Res^{-2}} + (0.036 \pm 0.454){\rm Res^{-3}}){\rm A_{Res}^2} \\ & + ((10.34 \pm 1.68){\rm Res^{-1}} + (77.4 \pm 11.5){\rm Res^{-2}} \\ & + (35.4 \pm 14.7){\rm Res^{-3}}){\rm A_{Res}^3} \end{aligned} \tag{3.11}$$

Figure 3.9 confirms that the asymmetry predicted by Equation 3.11 ($A_{\rm predict}$) accurately replicates $A_{\rm int}$ for the majority of the sample, with a median difference that equates to only a few percent of the measured asymmetry (for even the lowest asymmetry galaxies). Equation 3.11 could be used to correct for very high S/N observations, but in practicality resolution will need to be corrected for in conjunction with noise.

Figure 3.10 showcases how different resolution values would change the relationship between $A_{\rm int} - A_{\rm corr}$ and S/N for the no noise subtraction and $A_{\rm noise}/1.2$ subtraction correction methods. The original curve (with no PSF convolution) from Figure

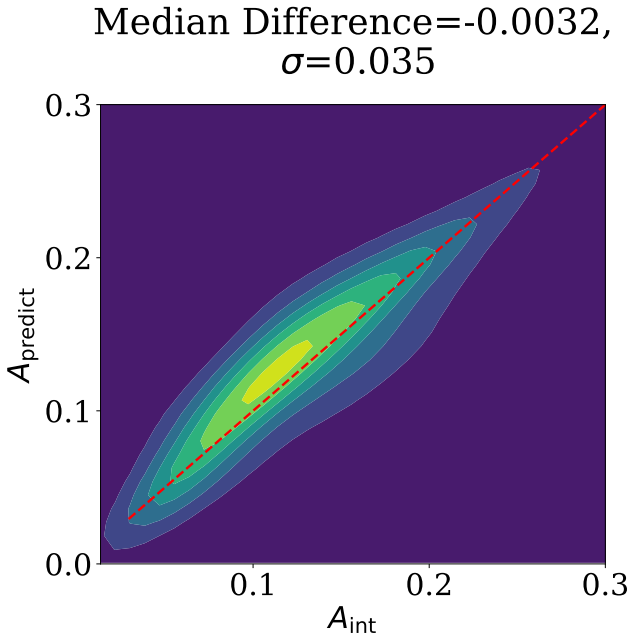

Figure 3.9: Density contours of the asymmetry predicted by Equation 3.11, plotted against the intrinsic asymmetry, with the red dashed line representing where the two would be equal. Note the median difference between these two values, even for the smallest asymmetries measurements, is only a few percent of the measured value. Thus the intrinsic asymmetry is recovered (within reason) for the majority of the galaxies in the sample.

3.7 is replicated here for reference. Although the impact in asymmetry is seen most strongly at low signal-to-noise, at $S/N > 100$ the change in asymmetry is dominated by the systematic decrease that comes from degrading resolution. The shift from decreasing resolution is also similar between the two correction methods, despite the $A_{\rm int} - A_{\rm corr}$ relationship differing between the two. The consistent upward shift of the curves above S/N=200 implies that there is some predictable change in asymmetry from PSF that is independent from signal-to-noise, and hence Equation 3.11 could be used to correct the asymmetry index irrespective of any choice of noise correction method. For $S/N < 200$, the effects of noise and resolution are more entangled (almost indistinguishable for $S/N < 100$) and need to be corrected for simultaneously.

To address the disparity between resolution changes in high and low S/N regimes, I recommend a piecewise correction to asymmetry. For $S/N > 200$ the asymmetry only needs to be corrected for resolution using Equation 3.11, given the change in asymmetry from noise is comparatively so small. $S/N < 200$ requires first correcting for noise using Equation 3.8. The resulting $A_{\rm corr}$ still has effects from resolution, so I use LM Fit determine the relationship between $A_{\rm corr}$, Res, and $A_{\rm int}$ assuming they follow the same relationship as Equation 3.9. If $A_{\rm corr}$ is the predicted asymmetry calculated from Equation 3.8 using $A_{\rm Res+Noise}$ and S/N, the following equation describes a combined noise and resolution correction for asymmetry:

$$
\begin{aligned}
&\textbf{S/N<200:}\ A_{\rm int} = ((1.930 \pm 0.118){\rm Res}^{-1} - (0.027 \pm 0.060){\rm Res}^{-2} \\
&- (0.012 \pm 0.007){\rm Res}^{-3} + 1)A_{\rm corr} + ((-15.209(\pm 1.260){\rm Res}^{-1} \\
&- (3.000 \pm 0.922){\rm Res}^{-2} + (0.307 \pm 0.127){\rm Res}^{-3})A_{\rm corr}^2 \\
&+ ((23.629 \pm 3.220){\rm Res}^{-1} + (11.098 \pm 3.000){\rm Res}^{-2} \\
&- (1.042 \pm 0.454){\rm Res}^{-3})A_{\rm corr}^3 \\
&\textbf{S/N>200:}\ A_{\rm int} = \text{Equation 3.11}
\end{aligned}
\tag{3.12}
$$

Figure 3.11 demonstrates how well Equation 3.12 recovers the intrinsic asymmetry. Comparing to the isolated noise (see Figure 3.6) and resolution (see Figure 3.9) corrections, the median offset when correcting for both simultaneously is larger by a factor of 10, with an increased scatter as well. A slightly worse fit is to be expected, considering resolution and noise change asymmetry in opposing ways. Given the effects of noise and resolution on asymmetry can cancel each other out, it makes it very difficult for a fit based on $A_{\rm Res+noise}$ to determine the individual change from

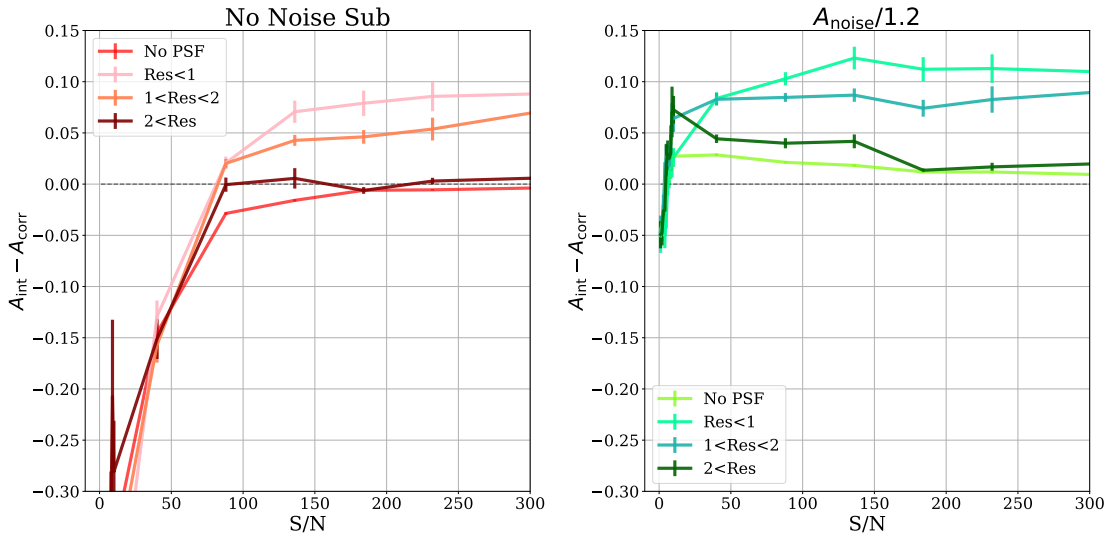

Figure 3.10: A demonstration of how applying a PSF (and thus degrading the resolution) changes two of the asymmetry approximation methods from Figure 3.7. Left panel: How resolution changes the difference in asymmetry when no correction for the noise asymmetry is performed. The curve from Figure 3.7 is replicated here, labelled "No PSF". The other three curves represent the relationship between $A_{\rm int} - A_{\rm corr}$ for different resolution bins. Applying a PSF to $A_{\rm obs}$ always shifts the curve up, since $A_{\rm obs}$ will systematically increase. This shift upward is greater for smaller resolutions. Right panel: The same investigation, but for the $A_{\rm noise}/1.2$ subtraction method. The curve from Figure 3.7 is replicated here, labelled "No PSF", where as the other three curves are separated into resolution bins. The same systemic shift upward is seen as in both methods. Not only that, but beyond $S/N = 200$ the change in asymmetry is almost entirely due to worsened resolution. The fact that both no noise subtraction and subtracting $A_{\rm noise}/1.2$ have similar changes from resolution beyond $S/N > 200$ implies that above that S/N, asymmetry only needs to be corrected for resolution effects.

resolution or noise alone. The overall broadening of the distribution of $A_{\rm predict}$ vs $A_{\rm int}$ stems from the dependence of the decrease in asymmetry from resolution effects on the intrinsic asymmetry: the absolute change in asymmetry from degrading resolution cannot be greater than its initial asymmetry value. Thus when the fit correction does poorly on small $A_{\rm int}$, resolution has a smaller effect than the noise contribution, which will drive an overestimation in $A_{\rm predict}$. When the fit does poorly on a large $A_{\rm int}$, the effects of resolution will dominate and lead to an underestimated $A_{\rm predict}$. Be that as it may, the broadening is driven entirely by galaxies with a combined low S/N and Res value (roughly $S/N < 20$ and Res< 1). For better measurements the combined fit does well enough that on average the combined correction is sufficient for the work herein. Future analysis could be devoted to improving the joint correction, using other advanced fitting techniques such as machine learning algorithms to disentangle the two effects for even the smallest S/N and Res values.

Figure 3.12 demonstrates how correcting for noise and PSF simultaneously with the LM Fit equations is superior to correcting them separately. Each panel represents a different noise correction method as presented in Section 3.4.1, with the original curves from Figure 3.7. When I degrade the resolution of the image and try to do the same correction (be it subtracting a fraction of the noise asymmetry or predicting asymmetry from Equation 3.8), the curves are shifted upwards due to the systematically lower asymmetry measurement once the resolution is degraded. For the "noise subtraction", "$A_{\rm noise}/1.2$", and "no noise subtraction", use Equation 3.11 to predict the intrinsic asymmetry form the noise corrected asymmetry and the Res value. Doing this brings us closer to the original curve, but there is still some disparity likely stemming from Equation 3.11 being constructed from asymmetries with no noise contribution and the slightly imperfect nature of these three noise correction methods. The curves are better recovered above $S/N = 100$ than below, supporting the conclusion that noise must be correctly accounted for to use Equation 3.11 on more realistic images.

The "LM Fit" method, on the other hand, uses Equation 3.12 to correct for resolution and noise simultaneously. In this case, the Noise+PSF corrected curve almost completely overlaps the original noise correction curve with no resolution effects. Although Figure 3.12 demonstrates that a resolution correction fit like Equation 3.11 can be applied to noise correction methods that do not require a fit, the most accurate way to account for both noise and resolution is to correct them with a fit function simultaneously (Equation 3.12).

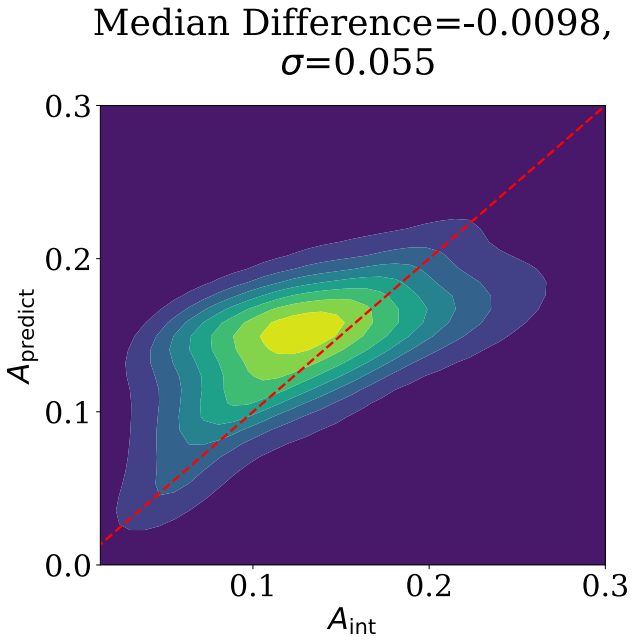

Figure 3.11: Density contours of the asymmetry predicted by Equation 3.12 to correct for resolution and noise, plotted against the intrinsic asymmetry. The red dashed line represents where the two values would be equal to each other. The median difference is only a small fraction of the intrinsic asymmetry, although it is larger than the corrections for noise (Figure 3.6) or resolution (Figure 3.9) alone. Correcting for noise and resolution simultaneously is inherently more difficult because both artefacts change asymmetry in opposite directions, making it difficult to distinguish which fraction of the change in asymmetry stems from noise or resolution. Most of the galaxies that constitute the outer contours have both a small signal-to-noise and resolution, demonstrating a weakness of the combined fit correction for the worst quality asymmetries. However, a median offset of 0.0098 is still good enough quality to make decent asymmetry measurements for the majority of the sample.

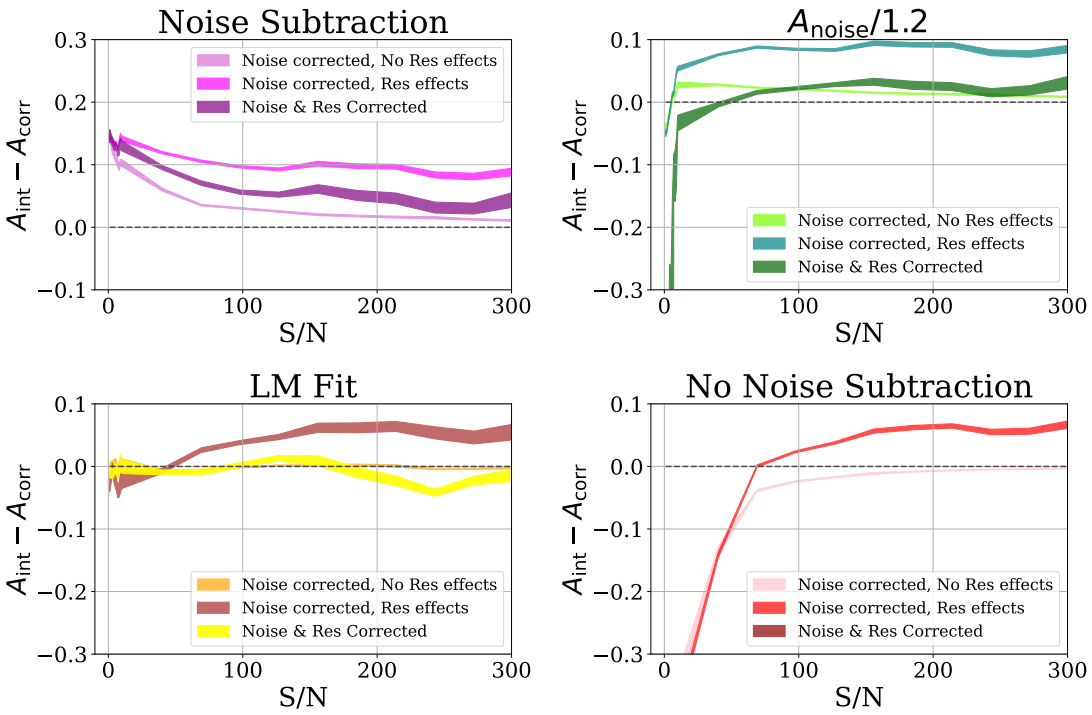

Figure 3.12: The difference between intrinsic asymmetry and the asymmetry measured for four different noise correction methods with no resolution effects (the same as in Figure 3.7), with resolution effects, and after resolution correction. Given noise and resolution affect asymmetry in ways that can cancel out, it is difficult to disentangle the two observational effects. Thus the resolution corrected curve approximates the curve with no PSF, but not exactly (particularly at low S/N). The LM Fit method reproduces the intrinsic asymmetry at low S/N most accurately from the four methods.

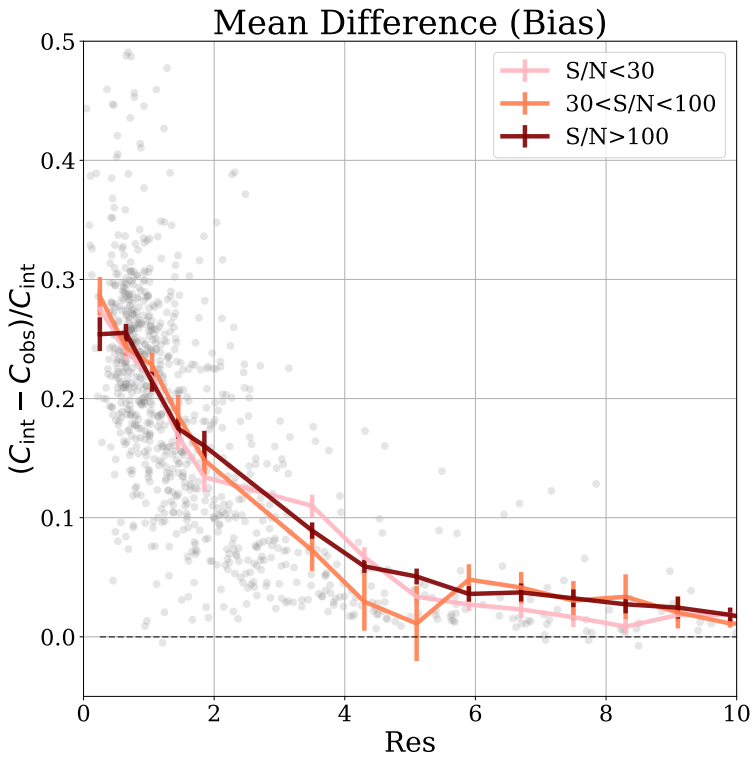

Figure 3.13: The mean fractional difference between intrinsic and observed concentration as a function of resolution for different S/N bins. The three curves overlap each other, indicating that a single resolution correction can be applied to concentrations of varying S/N. This logically follows the results from Figure 3.2, which demonstrated that noise has a negligible effect on the concentration measurement.

3.4.2.2 Resolution corrected concentration

Section 3.4.1 demonstrated that concentration is unaffected by noise. Figure 3.13 shows that the relationship between the fractional difference in concentration as a function of resolution is unchanged for different signal-to-noise bins. That is, a resolution value will have the same effect on concentration for both a high and low signal-to-noise galaxy. This uniformity is expected considering how little adding random noise changes the concentration. Therefore a function can be fit to this data to correct any concentration underestimation from resolution, without also needing to account for noise correction (unlike asymmetry). Section 3.5 will discuss the limitations of the LM Fit method further.

Just as with the asymmetry correction for noise, I postulate that the relationship between $C_{\rm int}$, $C_{\rm Res}$, and Res=$R_{\rm half}$/FWHM can be described by a single function

(Equation 3.13).

$$C_{\rm int} = (F_1({\rm Res}) + 1){\rm C}_{\rm Res} + {\rm F}_2({\rm Res}){\rm C}^2_{\rm Res} + {\rm F}_3({\rm Res}){\rm C}^3_{\rm Res} \tag{3.13}$$

Where F_3, F_2, and F_1 are of the same form as Equation 3.10. Once again I have constructed the relationship to ensure that $C_{\rm int} = C_{\rm Res}$ as the resolution goes to infinity. Utilising LM Fit reveals the best equation to express this relationship is:

$$\begin{aligned} C_{\rm int} = (&-(3.616 \pm 0.296){\rm Res}^{-1} - (1.467 \pm 0.268){\rm Res}^{-2} \\ &- (0.6106 \pm 0.0716){\rm Res}^{-3} + 1){\rm C}_{\rm Res} + ((2.159 \pm 0.164){\rm Res}^{-1} \\ &+ (0.996 \pm 0.225){\rm Res}^{-2} + (0.7367 \pm 0.0848){\rm Res}^{-3}){\rm C}^2_{\rm Res} \\ &+ (-(0.3090 \pm 0.0226){\rm Res}^{-1} - (0.0825 \pm 0.0432){\rm Res}^{-2} \\ &- (0.2197 \pm 0.0247){\rm Res}^{-3}){\rm C}^3_{\rm Res} \end{aligned} \tag{3.14}$$

This function predicts concentration values that are, on average, within 1% of the intrinsic concentration value (with a median difference of -0.033). Figure 3.14 further demonstrates that the predicted and intrinsic concentration are tightly correlated.

Thus, both asymmetry and concentration can be reliably corrected for Res values as low as 0.05. Such a correction is crucial to allow comparison of non-parametric morphology measurements for different resolutions, particularly if one wants to compare the morphologies of different observational data sets. The accuracy and convenience of a resolution correction is crucial in particular for asymmetry, given the more complex choices required to correct asymmetry for noise. The next section will evaluate the general applicability of the resolution and noise correction I have outlined thus far, by testing them on unseen TNG data and the Illustris simulation.

3.5 Comparison to unseen data

Section 3.4 demonstrated how by fitting the relationship between observed and measured asymmetry/concentration, it is possible to correct for most of the bias created by an observational effect such as noise/resolution. For asymmetry, this fitting method performs better than other background noise correction methods investigated in this work. In particular, the fitting method allows for correction of asymmetry measurements down to very low S/N. However, before such a fitting method can be used in practice its universality must be checked, or whether its form is appropriate only for the sample of TNG galaxies used thus far.

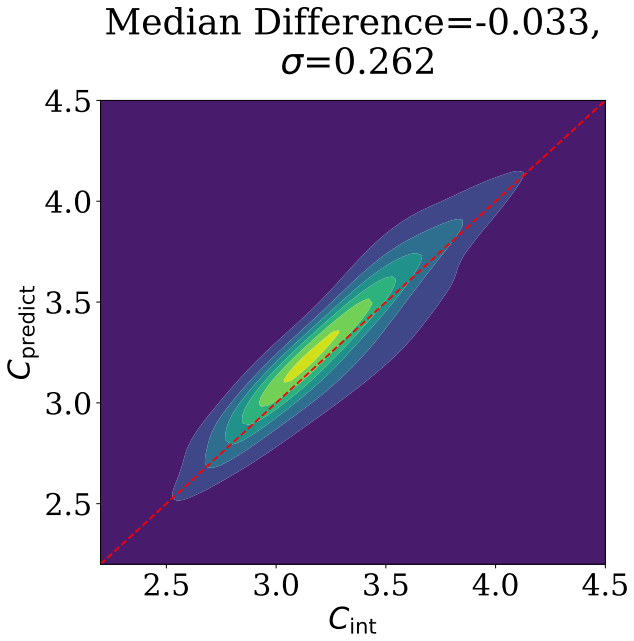

Figure 3.14: Density contours for the concentration predicted by Equation 3.14 versus the intrinsic concentration, with the red dashed line representing C_{predict}=C_{int} The small scatter about the line of equity demonstrates how effective the resolution correction is for this simulation. The median difference in concentration is less than 1% of the average measured concentration.

I first check that Equations 3.8, 3.11, 3.12, and 3.14 are not overfit to the training sample by applying those corrections to a set of test TNG galaxies not included in the initial 1000 galaxy set from which the fits were determined. I select 1000 new stellar mass maps from TNG galaxies, using the same quality cuts described in Section 3.2, but only selecting galaxies we have not used in the analysis yet. The 1000 galaxies are selected randomly, and thus the global properties (such as total stellar mass and stellar half mass radius) of the test set are comparable to the initial TNG sample. Noise is then added from the same range of input S/N values, and convolved with a PSF to achieve the same range of resolution values (refer back to Section 3.3 for details). I can then test to see how well Equations 3.8, 3.11, 3.12, and 3.14 recover the intrinsic asymmetry/concentration values for this new data set.

The top panel of Figure 3.15 presents the quality of the predicted asymmetry for these new galaxies: correcting for noise using Equation 3.8 (1st panel), for resolution using Equation 3.11 (2nd panel), and for resolution and noise using Equation 3.12 (3rd panel). There are 20 galaxies (2% of the sample) for which the asymmetry is predicted to be unrealistically high when correcting for noise and resolution together ($A_{\rm predict} > 1$); these are removed from the rest of the analysis so the statistics measured reflect the behaviour of the majority of the sample rather than a few outliers. The 4th panel shows how well Equation 3.14 corrects the concentration for resolution. The difference between the predicted and intrinsic values for this new sample are congruent with those seen in the training sample (compare to Figure 3.6 (median offset -0.001), Figure 3.9 (median offset -0.0032), Figure 3.11 (median offset -0.0098), and Figure 3.14 (median offset -0.033) respectively). Thus there is no evidence that the equations are overfit to the initial galaxy sample. With that confirmed, the robustness of the fit can now be investigated: i.e., are Equations 3.8, 3.11, 3.12, and 3.14 robust enough to be applied to other simulations, or ultimately, to observational data?

Assessing the accuracy of the fitting method is not possible on observational data, given the "intrinsic" asymmetry or concentration of an observed galaxy cannot be known. However, a different simulation suite can be used as a test case, to see how well the suggested fitting corrections work on an entirely different set of data. For this, I choose to test my fit on a sample of 1000 galaxies from the Illustris-1 simulation (Vogelsberger et al., 2014; Genel et al., 2014; Sijacki et al., 2015). Although simulated using the same code as Illustris, TNG has an updated galaxy formation model which is known to affect the morphologies of the galaxies (Rodriguez-Gomez et al., 2017, 2019). If the underlying physics in a simulation changes either the asymmetry and

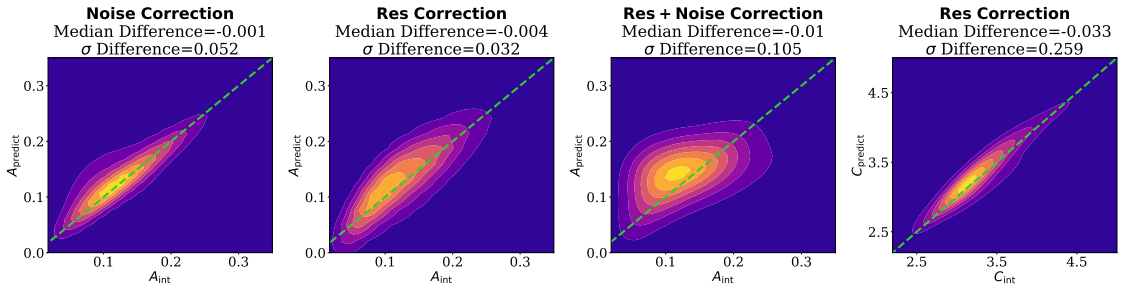

(a) Unseen TNG Galaxies

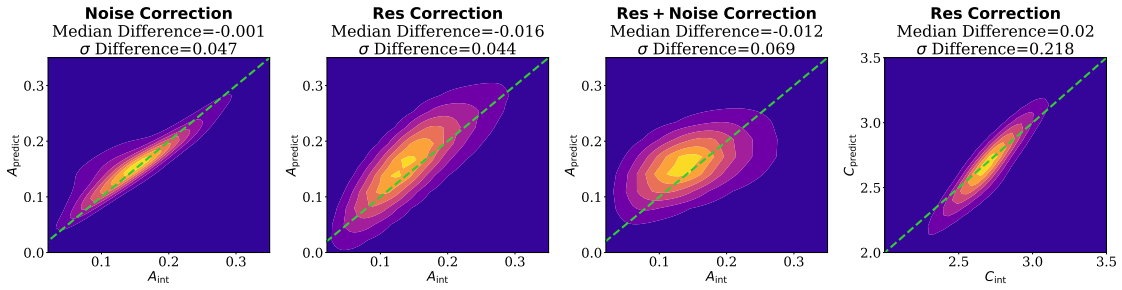

(b) Illustris Galaxies

Figure 3.15: *Top row:* Density contours of the intrinsic morphologies compared to values predicted by the fits presented in this work for a set of previously unseen TNG galaxies, with the dashed green line representing where the predicted values equal the intrinsic values. The first panel shows the asymmetry predicted after noise correction, the 2nd shows asymmetry predicted after resolution correction, the 3rd shows asymmetry corrected for both resolution and noise, and the fourth shows concentration predicted after resolution correction (no noise correction for concentration is necessary). *Bottom row:* Density contours of the intrinsic morphologies compared to values predicted by the fits presented in this work for a set of Illustris Galaxies, with the dashed green line representing where the predicted values equal the intrinsic values. The order of whether noise, resolution, or a combination of both is corrected for is the same as in the top row. For the combined noise and resolution correction (third column) galaxies with asymmetries predicted to be greater than 1 (far beyond the scope of $A_{\rm int}$) are removed from the analysis (20 in the unseen TNG and 4 in Illustris). For both data sets there is no clear bias in the predicted values, and the scatter on the predicted values reflects that seen in the training data (see Figures 3.6, 3.9, 3.11 and 3.14). For comparison the initial median offset for noise correction of asymmetry is -0.001, for resolution correction of asymmetry is -0.0032, for resolution and noise corrected asymmetry is -0.0098, and for resolution correction of concentration is -0.033. The combined noise and resolution correction does have a broader distribution than the other corrections, where galaxies with both a small S/N and Res value result in poorer asymmetry predictions. But the same effect is seen in the original TNG sample (see Figure 3.11). The replicability of the difference between the intrinsic and predicted indices with both Illustris and TNG implies that the corrections are viable for different galaxy samples.

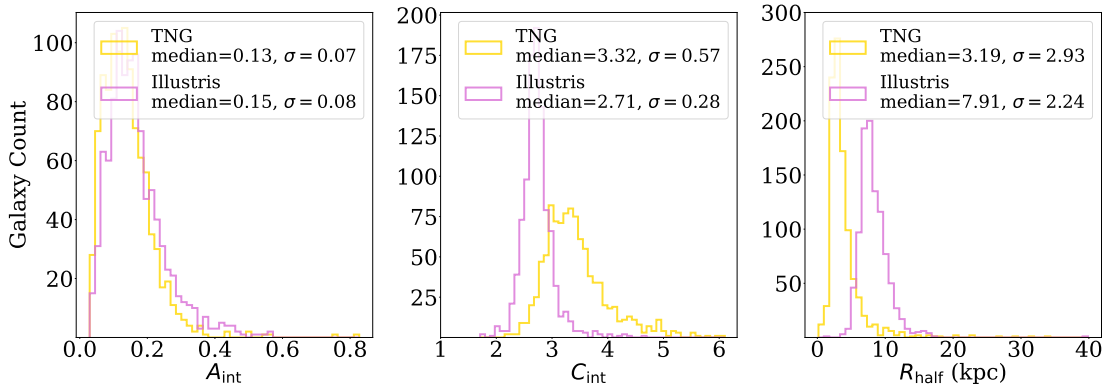

Figure 3.16: Distributions of intrinsic asymmetry (left), intrinsic concentration (middle) and stellar half mass radius (right) for the 1000 galaxies selected from TNG (yellow) and Illustris (pink) galaxies. Note that Illustris galaxies are on average larger and more highly concentrated, but have similar asymmetries as those in TNG. TNG has more accurate sizes for low mass galaxies (reflected in the smaller median R_{half} in TNG compared to Illustris), which likely leads to lower concentration values than were observed in Illustris.

concentration correction fits, then it is unlikely these same fits could be applied to other simulations or observations. More importantly, testing on a different data set will help further verify the signal-to-noise regimes in which the asymmetry fit correction is dependable.

The middle and right panels of Figure 3.16 show the differing distributions of asymmetry and concentration for the TNG and Illustris sub-samples used in this work, along with the stellar half mass radius of those galaxies. Although the asymmetry distributions are relatively similar, TNG has more highly concentrated galaxies than Illustris. Rodriguez-Gomez et al. (2019) noted this difference in concentration between TNG and Illustris, attributing it to the more accurate size of low-mass galaxies (see left panel of Figure 3.16) caused by the treatment of galactic winds and the enhanced quenching of high-mass galaxies from the new AGN and stellar feedback model. Given that the correction methods require input from both the observed concentration/asymmetry and the applied resolution/noise, the difference in distributions should not alter the viability of a comparison between the two samples.

The same noise addition (and range of S/N values) is then applied to Illustris as described in Section 3.2.1, such that the curves displayed in the left panel of Figure 3.7 can be replicated with Illustris, and compared to the same results acquired with TNG (see Figure 3.17). Doing no noise correction, subtracting $A_{\rm noise}$, and subtracting $A_{\rm noise}/1.2$ are shown to all work equally well for both Illustris and TNG in all signal-to-noise regimes. Not only that, but because the relationship between $A_{\rm int} - A_{\rm corr}$ and signal-to-noise is almost identical between TNG and Illustris for these three methods, those relationships could be used to predict the offset in asymmetry for any correction method used with data of a particular signal-to-noise. The bottom left hand panel of Figure 3.17 demonstrates how using Equation 3.8 to correct Illustris asymmetries for noise works just as well it did on TNG, despite the data being fit to minimize $A_{\rm int} - A_{\rm corr}$ for TNG alone. The bottom left panel of Figure 3.15 shows this more explicitly with the direct comparison of $A_{\rm predict}$ and $A_{\rm int}$, confirming that the median difference and scatter in the difference between the asymmetry predicted by Equation 3.8 and the intrinsic Illustris asymmetry is comparable to that seen in TNG (see Figure 3.6).

Next I test the effects of resolution on Illustris, and how well Equations 3.11, 3.12, and 3.14 correct for them. Given the overall larger size of Illustris galaxies (see the distribution of $R_{\rm half}$ in the left panel of Figure 3.16), I choose to select PSF FWHMs such that the Res values of Illustris match those in TNG (rather than applying the

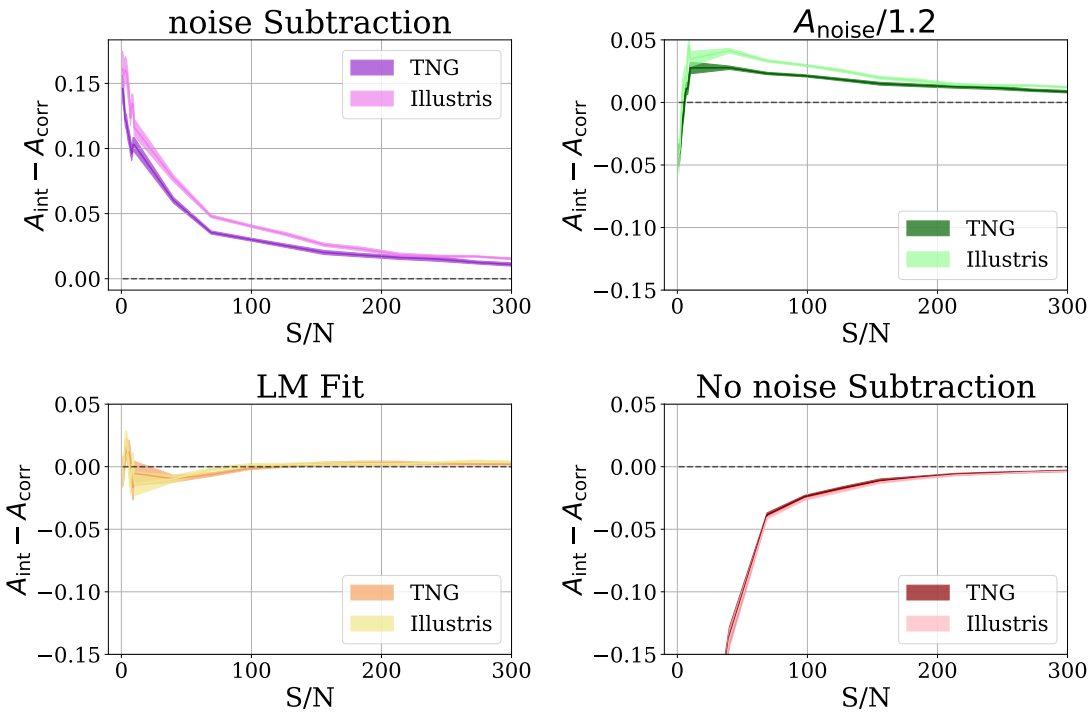

Figure 3.17: The mean difference between the intrinsic and corrected asymmetry as a function of signal-to-noise for subtracting $A_{\rm noise}$ (top left), subtracting $A_{\rm noise}/1.2$ (top right), predicting asymmetry from Equation 3.8 (bottom left), and doing no noise correction (bottom right) for both the TNG (the dark curve) and Illustris (the light curve) galaxy sets. All four correction methods match between the galaxy samples, implying that the relationship between the quality of correction and S/N is the same no matter which simulation is examined.

same range of PSFs to Illustris and TNG). If PSFs ranging from 0.002"-7" FWHM are applied to Illustris, they would have less effect on the overall resolution of Illustris galaxies than they did on TNG, given their greater size. Such a scenario would only test the PSF correction for comparatively "good" resolutions. Instead I use the Res values in TNG to compute a new range of PSF values to apply to Illustris (ranging from 0.002"-30" FWHM), which results in the same effective resolution of galaxy structure in the two simulations (note that this is distinct from the resolution of the simulation itself).

Equations 3.11 and 3.14 are used to correct for the changes to asymmetry / concentration on a Illustris galaxies with different resolutions. The bottom row of Figure 3.15 demonstrates how well the predicted asymmetry (2nd panel) and concentration (4th panel) reflect the intrinsic values. The median difference and scatter in difference for both asymmetry and concentration are comparable to that for the predicted values in TNG (compare to Figures 3.9 and 3.14). The distribution of $C_{\rm predict}$ vs. $C_{\rm int}$ looks narrower than that in TNG, stemming from the narrower range and overall smaller $C_{\rm int}$ values in Illustris (see Figure 3.16). The third panel demonstrates how a combined resolution and noise correction works on Illustris (Equation 3.12), where the median difference is similar to both that in the unseen TNG sample and the initial test sample (all are approximately off by 0.01, still well within a "good" asymmetry measurement).

The different physical models that shape TNG and Illustris galaxies do not alter the quality of the resolution and noise corrections described in this work. Thus, these corrections could feasibly be used on other data sets or even observations. The benefit of using simulations is that I control any changes between the intrinsic and observed data, and thus understand it completely. The same care needs to be taken to understand the difference between an observational data set and the simulation on which the fits are based. For example, I do not have to account for other observational effects that might add to (or detract from) the asymmetry outside of noise, such as neighbouring objects outside the field-of-view (when external flux leaks into the image of a galaxy). The correction methods also depend on how S/N and resolution are quantified; to use the fit coefficients provided in this work S/N and Res need to be measured similarly to what is laid out in this analysis. Although the work herein stands as a proof of concept, I caution those wishing to use a fit correction to take into account the unique features of their galaxy sample, and consider creating a fit on simulations meant to emulate that sample.

3.6 Implications for merger studies

There are a few studies that have attempted to measure non-parametric morphologies on data other than broad band light images, and how to account for the complex uncertainties in that scenario. Lanyon-Foster et al. (2012) characterize the morphology of stellar mass maps determined from Hubble Space Telescope imaging using CAS as well as other morphological measurements. The asymmetry of their stellar mass maps was on average larger than from the optical light image, which they attribute in part to random fluctuations in the mass-to-light ratio. The smallest asymmetries they measure for stellar mass maps are negative, implying that the background asymmetry they estimate from both regular background fluctuations and a generalized contribution from mass-to-light ratio fluctuations is larger than the asymmetry of the galaxy. Both of these findings are in agreement with the results of high uncertainties leading to falsely large asymmetries, and subtracting the total $A_{\rm noise}$ resulting in an over-corrected asymmetry.

Giese et al. (2016) is the only other paper to suggest a fitting method to correct asymmetry for noise, whilst measuring the asymmetries of extended HI gas disks from the Westerbork observations of neutral Hydrogen in Irregular and SPiral galaxies (WHISP) sample (van der Hulst et al., 2001). To account for the generally low S/N measurements of HI, Giese et al. (2016) use the Tilted Ring Fitting Code (TIRIFIC) model to approximate a correction in asymmetry based on the S/N. Using machine learning they are able to approximate the intrinsic asymmetry within 0.05 for most galaxies. Rather than creating a universal correction method, they fine-tune their correction to the WHISP sample to further their study. Indeed, the problem with creating a fit based on a simulated galaxy sample is the need to calibrate simulated galaxies to reflect the observations of interest. This is particularly relevant if one is interested in measuring the asymmetry of a galaxy property like surface mass density, or star formation rate density. In contrast, this work has investigated the universality of multiple different noise correction methods, and just as importantly, the signal-to-noise regimes for which those methods are viable. Using the work herein one can evaluate an approximate accuracy of asymmetry and concentration measurements for a data set and decide if any correction for bias in the measurements is necessary (and the most appropriate approach to correct for that bias).

Table 3.1: Summary of the validity of different asymmetry noise correction methods in various S/N regimes. For each method (no noise correction ("No corr"), subtract $A_{\rm noise}$ from the observed asymmetry ("Noise Sub"), subtract $A_{\rm noise}/1.2$ from the observed values ("$A_{\rm noise}/1.2$"), and corrected based on Equation 3.8 ("LM Fit")) we provide the mean difference and scatter in difference between the intrinsic asymmetry and the measured asymmetry. From this one can approximate the bias in asymmetry measurement for data with differing S/N regimes. The signal to noise must be measured as laid out in this analysis, using the median within an aperture of $1R_{\rm half}$ (an alternative radius with comparable size to $R_{\rm half}$ could be used as well).

S/N	No Corr Mean	No Corr σ	Noise Sub Mean	Noise Sub σ	$A_{\rm noise}/1.2$ Mean	$A_{\rm noise}/1.2$ σ	LM Fit Mean	LM Fit σ
S/N<5	-0.772	0.167	0.122	0.044	-0.027	0.043	0.009	0.066
5<S/N<10	-0.428	0.137	0.103	0.043	0.011	0.039	0.0	0.07
10<S/N<25	-0.349	0.124	0.103	0.043	0.028	0.036	-0.005	0.075
25<S/N<50	-0.135	0.112	0.06	0.034	0.028	0.02	-0.01	0.043
50<S/N<75	-0.039	0.023	0.035	0.017	0.023	0.013	-0.006	0.02
75<S/N<100	-0.024	0.013	0.03	0.015	0.021	0.011	-0.001	0.013
100<S/N<150	-0.017	0.01	0.025	0.011	0.018	0.009	0.001	0.011
150<S/N<200	-0.01	0.005	0.019	0.006	0.014	0.005	0.002	0.007
200<S/N<250	-0.006	0.003	0.016	0.007	0.012	0.005	0.003	0.005
250<S/N<300	-0.004	0.003	0.013	0.006	0.01	0.004	0.002	0.003
300<S/N<400	-0.003	0.002	0.011	0.005	0.009	0.004	0.002	0.002
400<S/N<600	-0.002	0.001	0.007	0.003	0.006	0.003	0.0	0.002
600<S/N<900	-0.001	0.001	0.005	0.002	0.004	0.002	-0.001	0.001
900<S/N<1200	-0.0	0.0	0.004	0.002	0.003	0.002	-0.0	0.0

The analysis within this work provides the opportunity to approximate both the bias in asymmetry, and the scatter in that bias, created by different amounts of noise in an image such that future works can check the quality of asymmetry measurements for the data set being used. Table 3.1 provides a simplified version of the results from Figure 3.7, supplying both the mean offset and the standard deviation of that offset for the four noise-correction methods discussed in this work. Using Table 3.1, one could check what the bias would be for a desired asymmetry correction method at the signal-to-noise of their particular set of observations, and determine which method would work best to both minimize the bias, as well as avoid varying biases within the same sample. As the community gets more creative with what kinds of observations and data products asymmetry is measured from, I hope this table can serve as a cautionary step as we explore this new regime of non-parametric morphologies.

It is paramount that when measuring asymmetry for a set of galaxies one can quantify the variability of an offset created by noise contribution. If one is working with high-quality photometry, or strong spectral lines, it is likely that the change in asymmetry from noise will be the same within that sample (no matter the noise-correction method chosen). However, comparisons of that data to lower-quality data sets becomes ill-advised, an issue which will only become more relevant as state-of-the-art non-parametric morphology measurements are compared to literature values. For low signal-to-noise data sets it is even unwise to compare asymmetries within the data set, given the bias created by a large noise/uncertainty can vary so drastically between asymmetry values. This is a particular issue for those measuring asymmetries in HI gas (e.g Holwerda et al., 2011; Giese et al., 2016; Reynolds et al., 2020). A recent work by Baes et al. (2020) explored the change in asymmetry in a range of wavelengths from the UV to the submm, as well as subsequent derived data products such as stellar mass, dust mass, and star formation rate. Although they saw trends reflective of understood physical models, without assessing the varying signal-to-noise levels of those observations it is not clear how much of those trends are driven by noise effects.

3.6.1 Example of effects of noise on merger asymmetries

The changes in asymmetry from noise contribution could lead to observing trends that do not exist, but they could also result in obscuring relationships as expected. My procedure of adding noise to simulations, and correcting for that noise with different methods, can be used to investigate the noise effects on an example science question:

does galaxy asymmetry increase as the result of galaxy-galaxy interactions?

Observational studies have reliably found that photometric asymmetry increases for galaxy pairs as the separation between the interacting pairs decreases (Hernández-Toledo et al., 2005; De Propris et al., 2007; Casteels et al., 2014). Asymmetric structures resulting from an interaction are tied to the tidal forces disturbing the galaxy morphology, therefore the correlation between pair separation and asymmetry should be apparent in both optical light and stellar mass maps. This serves as a good test case for how the heightened uncertainty of a mass measurement would effect the prominence of this trend.

To test how noise will impact asymmetry measurements of TNG stellar mass maps, I collect a new sample of interacting TNG galaxies on which the four different asymmetry measurements discussed can be applied. I select a sample of TNG galaxies at z = 0 with $10^9 \leq M_\star/M_\odot$ that are undergoing a major merger, i.e. they have a companion with a mass ratio greater than 0.1 that is closer than 100 kpc in 3D separation. I select 300 interacting galaxies from TNG, with the goal of having approximately (though not always exactly) 30 galaxies in each 10 kpc bin for 3D separations (r_{3D}) ranging from 0-100kpc.

I then apply 4 different S/N regimes to this data: $S/N < 40$, $40 < S/N < 80$, $80 < S/N < 120$, and $S/N > 120$, using the same methods described in Section 3.3. Figure 3.18 demonstrates how the relationship between asymmetry and pair separation varies between the intrinsic value (navy), the observed value (red), the observed corrected for $A_{\rm noise}$ (pink), the observed corrected for $A_{\rm noise}/1.2$ (green), and the asymmetry predicted from Equation 3.8 (the LM Fit method, yellow). If only these changes for small amounts of added noise ($80 < S/N < 120$ and $S/N > 120$) are examined, the observed asymmetry traces the intrinsic asymmetry's relationship to r_{3D} almost perfectly. Once in the intermediate signal-to-noise regime ($40 < S/N < 80$), the trend has diminished for observed asymmetry. This is because the magnitude of $A_{\rm noise}$ depends on $A_{\rm obs}$. Thus, at low r_{3D} values, where all galaxies have lower asymmetries compared to those in a later stage of interaction, the noise will have a greater impact on the observed asymmetry. As a result, galaxies at large separations will have an overestimated asymmetry, whereas the asymmetry of close galaxy pairs will be relatively unchanged by noise contribution.

Given the change in asymmetry from noise differs with the intrinsic asymmetry, for the three lower signal-to-noise regimes in Figure 3.18 some noise correction needs to be completed to capture the true relationship between asymmetry and pair separation.

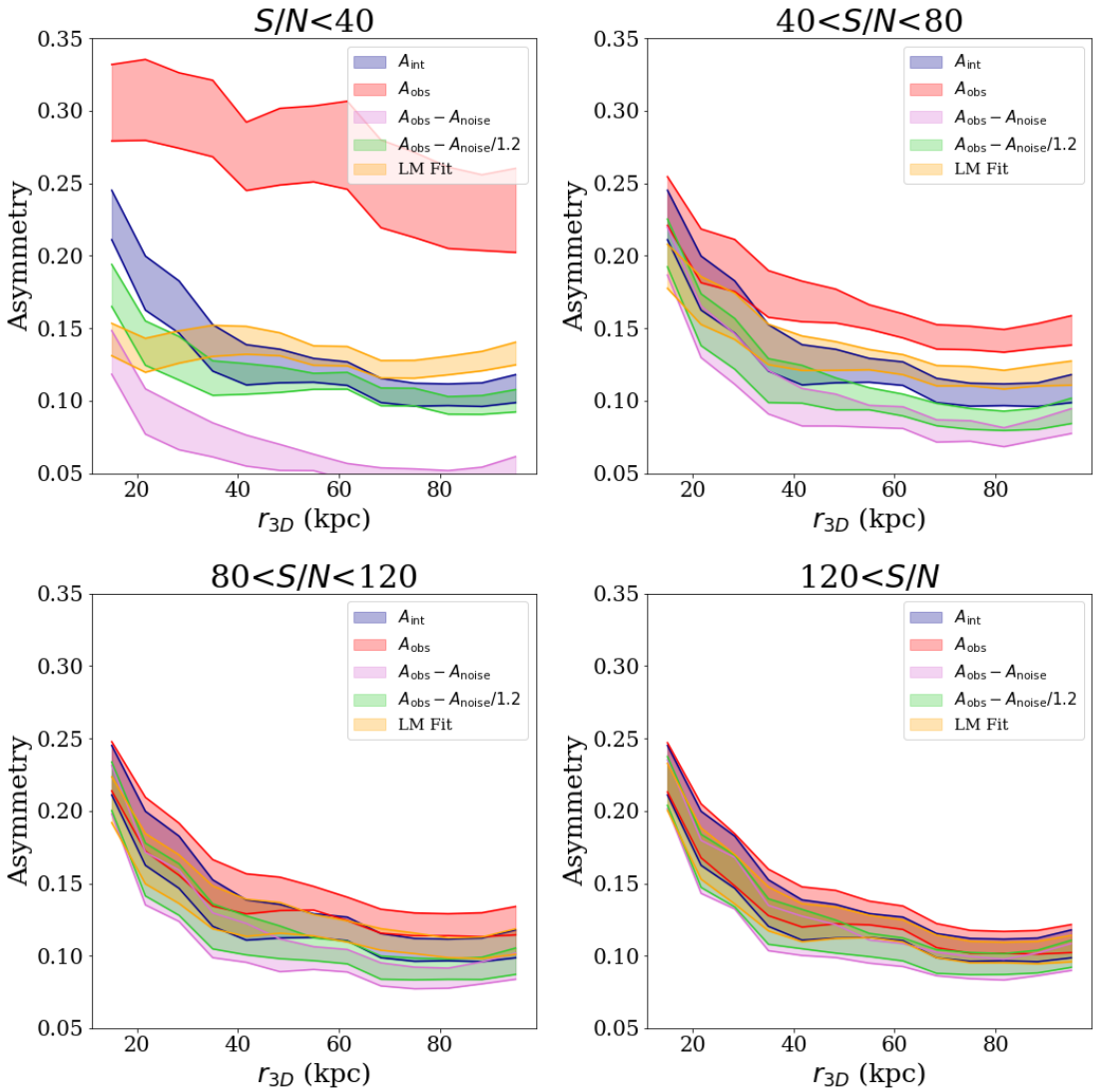

Figure 3.18: The asymmetry of interacting galaxies in TNG as a function of their 3D separation from the nearest companion (r_{3D}). The intrinsic asymmetry measurement (navy, identical in all panels), the observed asymmetry measurement (red), the observed asymmetry corrected for $A_{\rm noise}$ (pink), the observed asymmetry corrected for $A_{\rm noise}/1.2$ (green), and the asymmetry predicted by Equation 3.8 (yellow) are all included. The four panels represent four different signal-to-noise ranges applied to the same set of TNG galaxies, demonstrating how the trend between asymmetry and r_{3D} is obscured in observed asymmetry as signal-to-noise decreases. Ideally all curves would match the navy curve, but as the S/N regime decreases the different asymmetry measurements struggle to capture the true underlying trend between $A_{\rm int}$ and r_{3D}.

Below $S/N < 120$ the best traditional noise correction to recover the asymmetry trend at high r_{3D} is subtracting $A_{\rm noise}/1.2$ from $A_{\rm obs}$. One can also use the LM Fit method to correct for noise and achieve similar recovery, and this works well in the intermediate S/N regime. In the lowest signal-to-noise bin ($S/N < 40$), the relationship between asymmetry and r_{3D} has completely disappeared for the observed asymmetry. Correcting with the $A_{\rm noise}/1.2$ results in a trend closer to the intrinsic asymmetry, but it is still not as drastic a change in asymmetry between r_{3D} values as expected. The LM Fit method, though better at replicating the intrinsic asymmetry than the traditional $A_{\rm noise}$ correction, also doesn't capture the complete trend between asymmetry and pair separation due to the large scatter in the fit for $S/N < 50$. The degradation of this relationship with increased noise is an important example of how, even within a data set of relatively uniform signal-to-noise values, the effects of $A_{\rm noise}$ can still alter the final conclusions. Those endeavouring to use non-parametric morphologies in their analysis will need to consider what degree variations (or lack-there-of) in asymmetry will result from noise effects, and what kind of noise correction is required for their desired analysis.

3.7 Summary

Using stellar mass maps from the IllustrisTNG100-1 and Illustris-1 simulations, we investigated the impact of observational noise and resolution, and the accuracy of different methods to recover the intrinsic asymmetry and concentration parameters.

The traditional asymmetry metric is systematically biased by the presence of measurement uncertainties. The commonly used method of correcting for noise asymmetry contribution underestimates the asymmetry, particularly at $S/N < 100$, where the asymmetry can be overestimated anywhere from a factor of 2 to 10 (see Figure 3.2 and 3.3). An alternative correction method, which subtracts $A_{\rm noise}/1.2$ from the observed asymmetry reduces this systematic bias, reaching less than 0.05 difference by $S/N \sim 25$ (Figure 3.4). In addition to traditional noise correction, I also fit the relationship between the observed asymmetry and the signal-to-noise to predict the intrinsic asymmetry (see Equation 3.8), removing the bias in asymmetry created by noise as low as $S/N \sim 5$ (Figure 3.9).

Degraded resolution also changes the asymmetry (and concentration) measurement from its intrinsic value. A fit relationship is determined between observed asymmetry or concentration and resolution (Res=$R_{\rm half}$/FWHM) to correct for this

bias (see Equations 3.11 and 3.14, respectively) that accurately replicates the intrinsic values (Figures 3.9 and 3.14). Real asymmetries will need to be corrected for both resolution and noise, and although Equation 3.12 does not correct asymmetry as well as when just resolution needs to be accounted for (compare Figure 3.11 to Figure 3.9), it still brings the majority of asymmetry measurements within $A_{\rm int} \pm 0.05$.

The noise and resolution corrections are tested on a sample of previously unseen TNG galaxies in Section 3.5, confirming the corrections are not overfit to their training data. The same corrections are also tested on a sample of Illustris galaxies, and appear to work just as well despite the different physical models implemented in Illustris. Figure 3.15 summarizes the robustness of noise and resolution correction procedures, confirming also that correcting for both resolution and noise is the most tenuous result.

Tables 3.1 provides an important summary of the biases created by different corrections for S/N values to help future works ascertain the best method for their intended study. Concluding this work I have provided various examples to non-parametric morphology studies to demonstrate how the choice of asymmetry noise correction can alter results. My own hypothetical investigation into the relationship between asymmetry and galaxy interactions (see Figure 3.18) illustrates how different S/N regimes and asymmetry corrections can muddle previously confirmed results.

As resolved, multiwavelength galaxy surveys grow in size and accessibility, it is tempting to apply well-established metrics like asymmetry and concentration to a variety of observations. Although there is a procedure through which non-parametric morphology measurements could be calculated for IFS data, be it MaNGA ΔO/H maps from Chapter 2 or the star formation efficiency maps to be discussed in Chapter 4, the application of these metrics would require substantial checks to create a proper fit as described in this chapter. Such an analysis is beyond the scope of this thesis, but provides an excellent opportunity for future resolved merger studies.

Chapter 4

Resolved molecular gas and star formation properties of mergers with ALMaQUEST

Chapter 2 grappled with the complexity of studying the resolved properties of large merger sets, and Chapter 3 introduced methodologies that can ease that analysis but are complicated in application. Such obstacles have rarely arisen in studies of the resolved molecular gas properties of mergers: primarily because those studies have been limited to examining one or a small handful of mergers. Only recently have observations of resolved molecular gas properties of galaxies been collected for large samples to complement large optical IFS surveys, allowing for the combined exploration of Σ_{H_2} and Σ_{SFR} maps of non-interacting galaxies. In this chapter I present the largest study of Σ_{H_2} and Σ_{SFR} for a set of merger galaxies, using a combination of archival data and new observations.

The goal of this work is to understand what drives resolved enhancements in star formation seen in mergers (noted in Chapter 2): an enhanced amount of molecular gas to fuel star formation, or an enhanced rate at which gas is converted into stars. Section 4.1 will review how molecular gas is derived from observations (in particular those paired with IFS), as well as some recent results from $\Sigma_{H_2}/\Sigma_{SFR}$ observations concerning what drives resolved changes in star formation. In Section 4.2 I introduce new observations of mergers taken with the ALMA telescope as a continuation of the ALMaQUEST survey, selected by myself along with co-authors Hsi-An Pan, Lihwai Lin, and Sara Ellison. Within this section I will outline how ALMA data was reduced by myself and Hsi-An Pan (Section 4.2.2), as well as additional data products used from the MaNGA survey (Section 4.2.3). The main results concerning the resolved properties of merging galaxies are discussed in Section 4.3, followed by an examination of whether gas fraction or SFE plays a more prominent role in driving merger-induced

star formation (Section 4.3.2). Before final remarks I will confirm my results are consistent even if different methods of measuring Σ_{SFR} and Σ_{H_2} are employed (Section 4.4).

4.1 Observing molecular gas in other galaxies

Most galactic star formation occurs in giant molecular clouds, which are predominantly composed of molecular (H_2) hydrogen gas (Solomon & Sage, 1988; Leroy et al., 2008; Kennicutt & Evans, 2012). H_2 in the ISM of galaxies beyond our own is in practice difficult to observe. The H_2 molecule has widely spaced rotational levels, and thus radiates inefficiently for most of the cool ISM and especially for molecular clouds (Temperatures ∼10K, Heyer & Dame 2015). Instead observations of molecular hydrogen gas are often tied to galactic dust, given H_2 requires dust to form within galaxies. Dust grains consist of elements heavier than Hydrogen and Helium, in particular solid carbon and silicates which coagulate into grains that can be as small as a few molecules across or as large as 0.1 microns (Draine, 2003; Carroll & Ostlie, 2007). Dust's ability to interact with light (scattering, absorbing, polarizing, re-emitting), regulate local heating/cooling, and regulate molecule formation make it an important constituent of the star formation process (Draine, 2003). Dust grains provide a sink for the binding energy that must be released for HI to form H_2, rather than relying on random collisions of atomic hydrogen to form the molecule. Excess energy from the collision of two hydrogen atoms is absorbed by the dust grain, radiating heat and ejecting H_2 from the site. Thus the distribution of dust and H_2 are tightly linked, and measuring the amount of dust can be used as an alternative for direct H_2 measurements.

Though there are a handful of methods to measure the dust distribution in a molecular cloud, one of the most viable for extragalactic studies is molecular line emission. ^{12}CO and its isotopomers (^{13}CO or C^{18}O) correlate with dust extinction in nearby molecular clouds (and thus also correlates with H_2 column density) (Dickman, 1978; Frerking et al., 1982; Goldsmith et al., 1997). The rotational transition $J = 1 \rightarrow 0$ of ^{12}CO at 115 GHz has high atmospheric transmission such that it is perfect for ground based observations, and at the ground state probes the coldest ISM at temperatures ranging from 5 - 22 K (Heyer & Dame, 2015). ^{12}CO can suffer from problems of optical depth, where overlapping clouds result in high H_2 density but underluminous ^{12}CO intensity (Bolatto et al., 2013). ^{13}CO or C^{18}O are far less

abundant and thus suffer less from optical depth problems, but as a result are much harder to observe (Danielson et al., 2013). The remainder of this work will focus on ^{12}CO as the main proxy for measuring molecular gas.

H_2 column density can be approximated from ^{12}CO luminosity by assuming a conversion factor between the two (α_{CO}). This conversion factor can depend heavily on the local properties of the ISM and the global properties of the host galaxy (Bolatto et al., 2013). Many studies have suggested that starburst galaxies should use a smaller conversion factor (Downes & Solomon, 1998; Bryant & Scoville, 1999; Papadopoulos et al., 2012; Sargent et al., 2014). Others have determined that the position in the galaxy (Sandstrom et al., 2013; Leroy et al., 2017) or the metallicity of the ISM (Narayanan et al., 2012; Accurso et al., 2017) can alter α_{CO}. Evaluations of α_{CO} have only been possible through large samples of both integrated and resolved molecular gas properties, where the variations between galaxies can be investigated.

Recent multiwavelength galaxy surveys, such as EDGE-CALIFA (Bolatto et al., 2017) and ALMaQUEST (Lin et al., 2020), have combined ^{12}CO observations with IFS data to dissect relations between Σ_{H_2}, Σ_{SFR}, and $\Sigma_\star$ on a kpc-scale. EDGE-CALIFA has investigated gradients in SFE and other processes that can regulate star formation (Utomo et al., 2017; Colombo et al., 2018; Barrera-Ballesteros et al., 2021). ALMaQUEST has thoroughly probed the interdependencies of the resolved star-forming main sequence (rSFMS), resolved Kennicutt-Schmidt (rKS), and resolved molecular gas main sequence (rMGMS) (Lin et al. 2019; Ellison et al. 2021a; Baker et al. 2022). ALMaQUEST has also revealed that even though the global star formation rate in a galaxy is primarily driven by the amount of molecular gas, the scatter in the resolved star formation is mostly driven by local changes in SFE (Ellison et al., 2020b). An ALMaQUEST study of starbursts found heightened SFE also drove the central starbursts like those noted in Chapter 2, both for isolated galaxies and 3 merger starbursts (Ellison et al., 2020a). Further investigation of the interplay between star formation and molecular gas has been done on the scale of molecular clouds with the Physics at High Angular resolution in Nearby Galaxies (PHANGS)-ALMA survey (Leroy et al., 2021). With resolution on the order of ∼100pc, PHANGS-ALMA found greater scatter in all three scaling relations compared to lower-resolution studies, revealing significant variation in star formation and molecular gas content even within similar morphological environments (Pessa et al., 2021; Querejeta et al., 2021).

Although EDGE-CALIFA, the largest survey of this kind, does have a small number of mergers that may be responsible for changes in SFR and depletion times

(Bolatto et al., 2017; Utomo et al., 2017; Chown et al., 2019), none of the surveys with both IFS and molecular gas data have a sufficient number of mergers to make a dedicated study of interaction-induced physics. A handful of detailed case-studies of the resolved star formation efficiency of pre-merger galaxies have been completed, revealing significant diversity of depletion time on a resolved scale (Tomičić et al., 2018; Bemis & Wilson, 2019). A study dedicated to a diverse sample of merging and post-merger galaxies is required to better understand the most extreme variations in star formation and gas properties. Consequently, a follow-up program to ALMaQUEST was designed to observe maps of ^{12}CO emission with the Atacama Large Millimetre Array (ALMA) for galaxy mergers selected from MaNGA, incorporating a variety of interaction stages. As a co-P.I. on this proposal, I helped select merger candidates from the MaNGA data available at the time. Although very similar to merger selection described in Chapter 2, the following section will review that selection process before outlining further cuts to select proper ALMA observation candidates.

4.2 ALMaQUEST merger set

4.2.1 Sample selection

The sample of merging galaxies is collected from the MaNGA data release 15 (DR15), which was the most recent publicly available release at the time of our observations and for the duration of this project. I visually classify post-merger and interacting galaxies from the ∼4800 galaxies in DR15 using the Sloan Digital Sky Survey (SDSS) Sky Server *gri*-images (r-band half-light surface brightness limit of 23.0 mag arcsec^{-2}; Strauss et al. 2002). Post-merger galaxies are distinguished by clear morphological disturbances indicating a recent interaction, such as tidal tails or shells, but with no obvious companion. Galaxies in an interacting pair are identified with similar indicators, with the addition of a clear visual connection to a second disturbed galaxy (such as tidal bridges).

Beyond the visually selected sample, I also identify a group of spectroscopic pairs, where a visible connection between a galaxy and a possible companion is unclear, but spatial and redshift information reveal the two galaxies may be interacting. Spectroscopic pairs are selected using the Patton et al. (2016) catalogue, which provides the closest companion for each galaxy in SDSS data release 7 (DR7), with a companion boundary at projected separation $r_p = 1$ Mpc and a maximum difference in velocity between the two of Δv = 1000 km/s. I assume any MaNGA galaxies with a projected

separation less than 2" from the Patton et al. (2016) galaxy position are the same object. Spectroscopic pairs are limited to those with a mass ratio between 0.1 and 10 (meaning the smaller of the pair is more than 10% the mass of the larger), and only include galaxies whose companion is within $r_p < 100$ kpc and Δ v <500 km/s. For simplicity, the rest of this work will not distinguish visually and spectroscopically selected pairs; referring exclusively to "pairs". The combination of the pair and post-merger galaxies yields a total sample of 903 galaxies in DR15 which are hence referred to as the parent merger sample, from which I can select a subsample for ALMA observations.

To select candidate mergers for ALMA observations I first exclude all mergers with declination greater than 20°, leaving only those with positions that overlap with ALMA's observational range. From the initial parent merger sample only 143 galaxies meet this criterion. I next select mergers for which the target CO line S/N can be achieved in less than 5 hours, to ensure as many merger observations as possible within a competitive proposal (see Section 4.2.2 for more details). What remains is a sample of 6 post-mergers and 14 pairs, which are observed as part of an ALMA Cycle 7 program (2019.1.00260.S, P.I.: Hsi-An Pan). I also make use of eleven galaxies from the ALMaQUEST survey that show clear signs of an interaction within the classification scheme: 8 post-mergers and 3 pairs (Lin et al., 2020; Ellison et al., 2020a). The SDSS *gri*-images for the entire ALMaQUEST-merger suite are provided in Appendix A.2 (Figures A.22 - A.25). The final sample of 14 post-merger and 17 pair galaxies is summarized in Table 4.1. Included in the table are key global properties from the MaNGA PIPE3D Value Added Catalogue (VAC) including total stellar mass ($M_\star$), total star formation rate (SFR), and redshift (z). Also included are offsets from the global star-forming main sequence ΔSFR, where $\Delta\mathrm{SFR} = \log \mathrm{SFR}_{\mathrm{galaxy}} - \log \mathrm{SFR}_{\mathrm{control}}$. Just as in Chapter 2, $\mathrm{SFR}_{\mathrm{control}}$ is the median SFR value of galaxies within 2σ of a fit to the star-forming main sequence (controls are also matched within 0.1 dex in $M_\star$ and 0.005 in z). Merger properties are listed as well, including r_p, Δv, and mass ratio. Post-merger galaxies have empty r_p, Δv, and mass ratio values since there is no companion with which to compare. Pair galaxies that were visually identified do not have measured Δv and mass ratio values, since there is no spectroscopic information from their companion.

The merger sample covers a broad range of $M_\star$ and SFR. Figure 4.1 compares these properties for the post-merger (orange circles) and pair (triangles) galaxies with respect to the rest of MaNGA, shown as grey hexbins. Pairs are colour-coded by the

Table 4.1: Summary of global properties of post-merger and pair galaxies observed with ALMA, with post-mergers first (no r_p values), followed by pairs ordered by r_p. Key global properties derived from the MaNGA VAC are included ($M_\star$, SFR, ΔSFR, z), as well as merger properties such as r_p, Δv, and mass ratio (the mass of the galaxy divided by that of its companion). Post-mergers have empty columns for merger properties, which require information about a companion galaxy. Pair galaxies that were visually identified only have r_p values, since spectroscopic information is not available for the companion.

plate-ifu	$\log M_\star$	log SFR	Δ SFR	z	r_p	Δ v	Mass Ratio
	$\log M_\odot$	$\log M_\odot/yr$	dex		kpc	km/s	
9195-3702	11.14	1.10	0.62	0.064	-	-	-
9194-3702	11.06	0.97	0.52	0.075	-	-	-
8083-9101	11.14	0.59	0.11	0.038	-	-	-
8952-12701	10.73	−0.38	−0.23	0.029	-	-	-
8084-3702	10.23	0.43	0.60	0.022	-	-	-
8156-3701	10.52	0.87	0.66	0.053	-	-	-
8081-9101	10.60	0.32	0.23	0.028	-	-	-
8615-3703	10.19	0.40	0.45	0.018	-	-	-
9512-3704	10.70	0.14	−0.03	0.055	-	-	-
7977-12705	10.85	0.47	0.26	0.027	-	-	-
8623-1902	10.17	−1.00	−0.84	0.025	-	-	-
8616-12702	10.76	−0.24	−0.40	0.031	-	-	-
9195-3703	10.39	0.47	0.42	0.027	-	-	-
8615-1901	9.68	−0.08	0.51	0.020	-	-	-
8153-12702	9.90	−0.74	−0.45	0.038	0.46	-	-
7975-6104	11.01	0.61	0.17	0.079	7.04	-	-
8241-12705	10.40	0.00	−0.05	0.027	8.23	80.0	3.14
8082-9102	10.74	0.73	0.53	0.037	12.24	-	-
7977-9102	10.93	0.83	0.41	0.063	13.78	-	-
9195-9101	10.74	0.39	0.16	0.057	15.36	-	-
8616-9101	11.10	0.75	0.28	0.092	19.89	276.0	4.19
8078-12703	10.81	0.14	−0.02	0.028	20.20	102.0	-
7968-12705	11.30	−1.41	−1.37	0.086	20.45	13.0	0.80
8078-6104	10.41	0.23	0.16	0.044	26.15	109.0	0.42
8085-12701	10.43	0.59	0.61	0.030	29.51	-	-
8085-6101	11.07	−0.73	−1.09	0.052	31.48	-	-
8083-12703	10.46	0.32	0.24	0.025	45.24	60.6	-
8082-12704	11.42	0.77	0.05	0.132	51.28	-	-
8085-3704	10.72	0.66	0.43	0.037	58.73	37.0	0.89
8450-6102	10.43	0.64	0.54	0.042	75.35	102.0	1.81
8728-3701	10.64	−0.37	−0.49	0.028	89.75	113.0	1.96

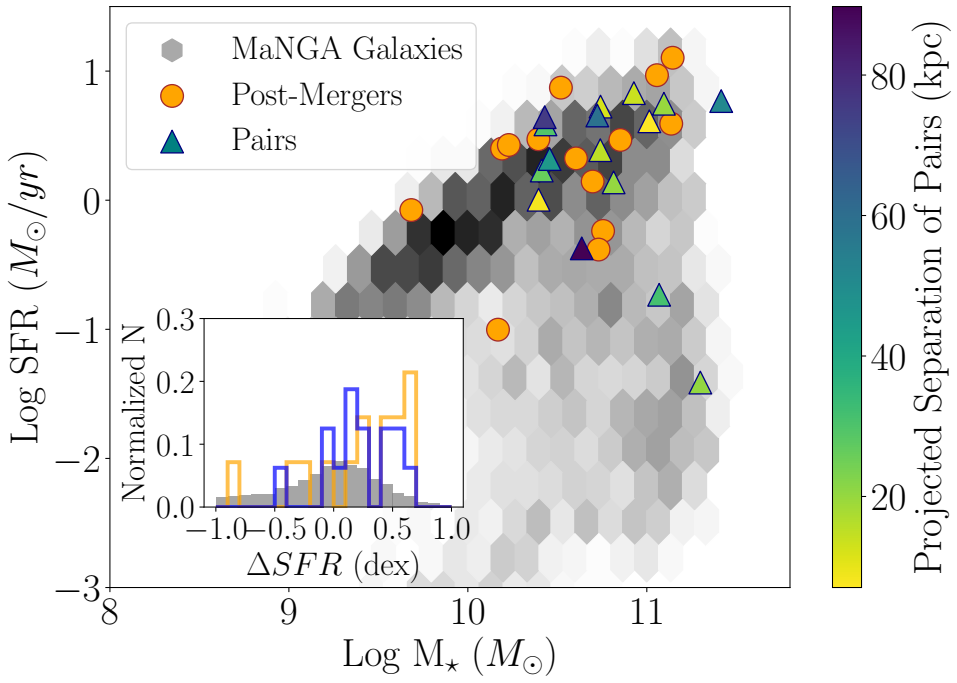

Figure 4.1: Position of the post-merger (orange circles) and pair (triangles) galaxies on the global star-forming main sequence defined by the rest of the MaNGA survey (grey hexbin). Pair galaxies are colour-coded by the projected separation from their closest companion (in kpc). Galaxies that were excluded due to a lack of viable CO spaxels are excluded from this diagram (see Table 4.2 and Section 4.2.2 for details). An inset histogram shows the distribution in ΔSFR for post-mergers (orange) and pair (blue) galaxies with respect to MaNGA (grey). Although this merger sample probes more highly star-forming galaxies than a random population, it still covers a broad range of ΔSFR values.

projected separation from their closest companion. These galaxies are representative of a typical merger sample, containing galaxies with both greatly elevated and comparatively low SFRs. The inset histogram of Figure 4.1 shows the distribution of the offset from the star-forming main sequence ΔSFR of the post-merger (orange) and pair (blue) galaxies with respect to the rest of MaNGA (grey). Although the pair and post-merger samples have on average larger ΔSFR values than non-interacting galaxies, both still cover a broad range of ΔSFR values to reflect the overall variety of behaviours seen in larger galaxy merger studies and to probe any corresponding diversity in the molecular gas properties of those mergers. Note that there may be some selection bias in the sample, given some post-mergers come from the ALMaQUEST starburst sample of Ellison et al. (2020a), and the rest still need to have enough gas for detectable ^{12}CO as described in the following section.

4.2.2 ALMA observations

Observations of ^{12}CO $J = 1 \rightarrow 0$ (CO hereafter), rest frame 115 GHz, were completed for 6 post-merger and 14 pair galaxies as part of Cycle 7 ALMA program 2019.1.00260.S (P.I.: Hsi-An Pan). The remaining 11 mergers were already available from the original ALMaQUEST sample (Lin et al., 2020). Cycle 7 observations were designed to replicate the methodology used in the original ALMaQUEST survey, the details of which can be found in the survey paper by Lin et al. (2020). A summary of those techniques is provided below.

Observations were carried out using the Band 3 receiver, taken in the C43-2 configuration to achieve a synthesized beam full-width half maximum (FWHM) of 2.5" in order to match the effective resolution of the MaNGA survey (Law et al., 2015). The ALMA field of view in the chosen configuration is ∼50", which is sufficient to cover the MaNGA footprint for all target galaxies. The spectral set up includes one high resolution spectral window targeting the CO emission (∼10 km/s), and three low-resolution spectral windows around the target line to detect the continuum (∼90 km/s). To reach a CO S/N greater than 3 for 50% of spaxels with Hα $S/N > 3$, the on-target integration time varied between 0.1-3.3 hours. The same methodology is used for the main ALMaQUEST sample, ensuring consistent data quality between ALMaQUEST data and that acquired in Cycle 7 (Lin et al., 2017, 2020).

Data were calibrated using the ALMA data reduction software Common Astronomy Software Applications (CASA, McMullin et al. 2007) using version 5.4 for all but

3 galaxies (which were observed in earlier cycles and thus used CASA version 4.5), along with the standard ALMA reduction pipeline. In ALMA's Band 3 the systematic flux uncertainty inherent with calibration is roughly 5-10% (Diaz Trigo et al., 2019). Continua were subtracted in the visibility domain for a handful of galaxies both in the original ALMaQUEST and the Cycle 7 galaxies. Once the continuum was subtracted, the task CLEAN was used to clean data down to 1σ and produce spectral line data cubes with a Briggs weighting (robust parameter=0.5), resulting in a native effective beam size ranging from 1.6" - 2.8" depending on the target. The data were then re-imaged with a user-specified spaxel size (0.5") and a restoring beamsize (2.5" $\times$ 2.5") to match the MaNGA image grid (prior) and spatial resolution (latter). The final cubes have channel widths of 11 km/s and $\sigma_{\rm rms}$ $\sim$0.2-2 mJy/beam. I applied the CASA task IMMOMENTS to these datacubes to determine moment 0 (integrated intensity) maps. IMMOMENTS can also generate moment 1 (intensity-weighted velocity) and moment 2 (intensity-weighted velocity dispersion) maps, but those are not relevant to the analysis of this work and are saved for future projects. Moment 0 maps are constructed by integrating the CO emission from a set velocity range without any clipping in signal. Table 4.2 lists the number of spaxels in each galaxy where the CO line emission from the moment 0 map has $S/N > 3$. Four of the merger galaxies observed as part of Cycle 7 (8615-1901, 8153-12702, 7968-12705, 8085-6101, all four early-type galaxies) have less than ten spaxels with CO $S/N > 3$, and are thus excluded from any further analysis that looks at individual galaxies (rather than spaxels).

The CO luminosity per spaxel determined from the moment 0 map is converted to molecular gas surface density $\Sigma_{\rm H_2}$ ($\rm M_\odot/kpc^2$) using a constant conversion factor of $\alpha_{\rm CO}$=4.35 ($\rm M_\odot(K\ km/s\ pc^2)^{-1}$) (Bolatto et al., 2013). All $\Sigma_{\rm H_2}$ values are then inclination corrected using the b/a axial ratios from the NASA Sloan Atlas (NSA) catalogue, themselves determined from single Sérsic fits. Three example $\Sigma_{\rm H_2}$ maps are provided in Figure 4.2, with the rest of the $\Sigma_{\rm H_2}$ maps from the sample provided in Appendix A.2.

There has been extensive research into the viability of a constant conversion factor, and many suggest using a metallicity dependent (Accurso et al., 2017; Sun et al., 2020) or metallicity and line intensity dependent (Narayanan et al., 2012) conversion instead. $\rm H_2$ is mostly self-shielded from the UV-radiation of nearby massive stars (as observed in Milky Way clouds, Abgrall et al. 1992), but CO is only mildly self-shield and thus depends on dust-shield to avoid photodissociation (van Dishoeck & Black,

Table 4.2: Spaxel counts for each galaxy merger that meet the various star-forming and CO S/N cuts, along with the overlap between these regions. Galaxies with less than 10 spaxels of CO+SF(Hα+D4000) overlap are excluded for plots of individual galaxies.

plate-ifu	SF	SF (Hα)	CO $S/N > 3$ (Hα+D4000)	CO+SF (Hα)	CO+SF (Hα+D4000)
	# Spaxels	# Spaxels	# Spaxels	# Overlap	# Overlap
9195-3702	0	53	204	0	5
9194-3702	0	811	379	0	328
8083-9101	331	1163	322	60	186
8952-12701	21	37	354	18	28
8084-3702	240	1007	552	150	531
8156-3701	778	941	279	279	279
8081-9101	321	600	436	255	335
8615-3703	324	997	538	276	519
9512-3704	168	552	136	33	40
7977-12705	981	1472	538	197	201
8623-1902	4	175	257	2	87
8616-12702	469	1113	258	78	104
9195-3703	225	833	504	110	460
8615-1901	461	588	2	2	2
8153-12702	333	1119	0	0	0
7975-6104	209	588	391	209	320
8241-12705	847	1678	592	381	508
8082-9102	554	1197	668	422	591
7977-9102	524	1129	380	287	354
9195-9101	678	1797	722	455	675
8616-9101	112	1044	363	84	249
8078-12703	1208	2597	1128	444	796
7968-12705	0	93	8	0	0
8078-6104	197	1039	433	153	431
8085-12701	2293	2601	458	456	458
8085-6101	0	0	2	0	0
8083-12703	822	2201	1264	641	1171
8082-12704	3	1617	451	3	244
8085-3704	319	727	608	299	552
8450-6102	1162	1550	536	503	536
8728-3701	0	31	156	0	0

1988). Regions of lower metallicity will also have lower dust-to-gas ratios such that CO is more easily photodissociated into C^+ and O, but the amount of H_2 remains the same (Bolatto et al., 1999). However, the requirements needed to determine accurate metallicity measurements would limit the spaxel count significantly, given the sparse overlap between high S/N star-forming spaxels and CO measurements (see Table 4.2), as will be discussed further in Section 4.2.3.1. To minimize the loss of spaxels I choose to use a constant conversion factor. Section 4.4.1 explores the difference in Σ_{H_2} measurements when a metallicity dependent α_{CO} is used (for spaxels where that is possible), and confirms that key conclusions from this work cannot result from inaccuracies of conversion factor.

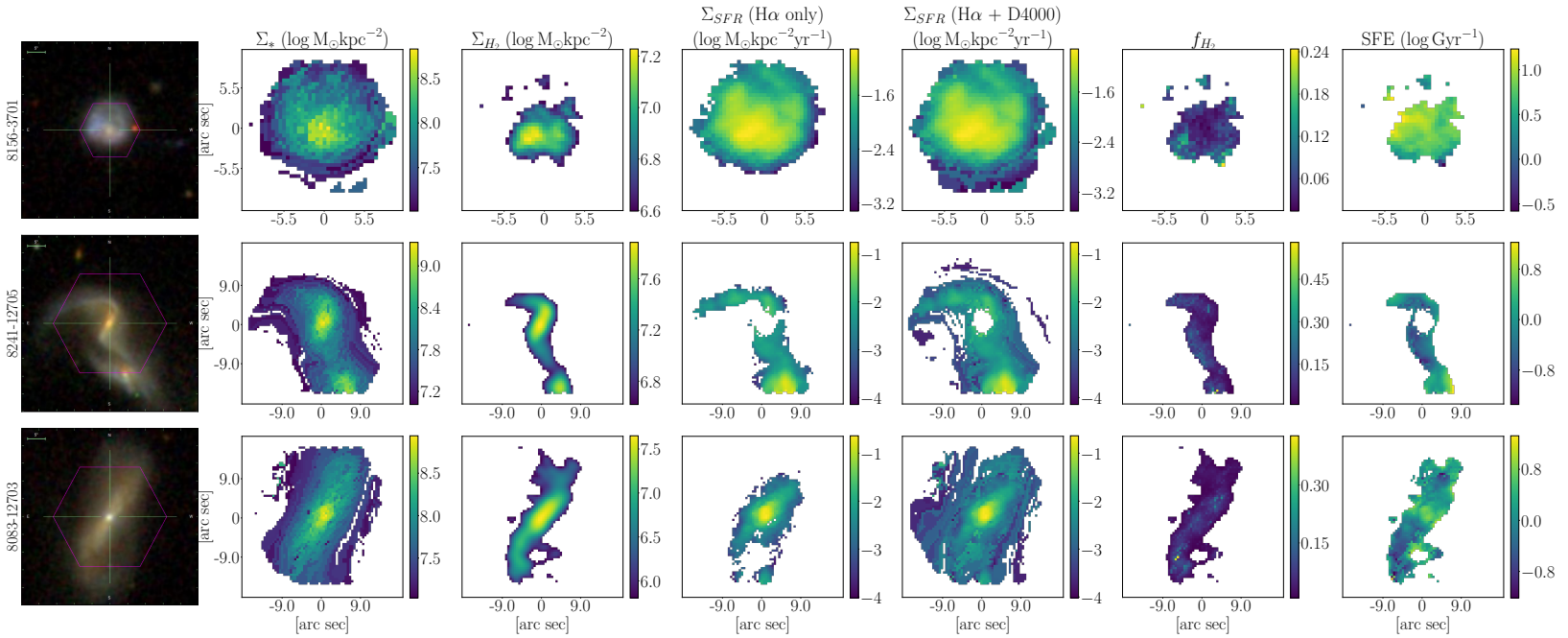

Figure 4.2: Data product maps for three of the galaxies in the ALMaQUEST merger sample (see Appendix A.2 for the remaining 28 galaxies in the sample), a post-merger (top), a visual pair (middle), and a spectroscopic pair with the companion out of frame (bottom). From left to right: the SDSS *gri*-image, inclination corrected stellar mass surface density (from PIPE3D), inclination corrected molecular gas surface density (computed from CO luminosity), inclination corrected star formation rate surface density (computed from Hα luminosity), inclination corrected star formation rate surface density (computed from Hα luminosity and sSFR-D4000 relation), molecular gas fraction ($\Sigma_{\rm H_2}/\Sigma_\star$), and star formation efficiency ($\Sigma_{\rm SFR}/\Sigma_{\rm H_2}$). Note the significant increase in spaxel count when both Hα and D4000 $\Sigma_{\rm SFR}$ are used. The central gap still present in the combined $\Sigma_{\rm SFR}$ map for 8241-12705 (second row, fifth column) is the result of D4000 exceeding 1.4 in those spaxels. Including D4000-$\Sigma_{\rm SFR}$ measurements optimizes the overlap between $\Sigma_{\rm H_2}$ and $\Sigma_{\rm SFR}$ for this analysis.

4.2.3 Additional MaNGA dataproducts

The work presented here primarily uses MaNGA data products from the PIPE3D spectral fitting pipeline, described in detail in Sánchez et al. (2016b,a) and in Chapter, 2 Section 2.1.1. Similar techniques are used here and a brief overview is provided for reference. Along with global values provided by the PIPE3D VAC mentioned previously, I also make extensive use of the PIPE3D stellar mass surface density ($\Sigma_\star$) and emission line fluxes. I correct all emission line fluxes for dust using a Milky Way dust extinction curve (Cardelli et al., 1989), assuming an intrinsic Hα/Hβ ratio of 2.85. Star formation rate surface densities ($\Sigma_{\rm SFR}$) are determined from the dust corrected Hα luminosity using the Kennicutt et al. (1994) relation and assuming a Salpeter initial mass function (Salpeter, 1955). Both $\Sigma_\star$ and $\Sigma_{\rm SFR}$ are inclination corrected using the b/a axial ratios (derived from single Sérsic fits) provided in the NSA catalogue. The same b/a ratio is used to compute an inclination corrected galactocentric radius from the V-band centre of the MaNGA map. I also take advantage of the 4000Å break strength (D4000) provided by PIPE3D, as it serves a crucial role in expanding star formation rate measurements described in the next section.

4.2.3.1 Star formation rates - D4000 vs Hα

The work presented here requires that both SFRs and molecular gas surface densities are measured in a given spaxel. Ideally SFRs would be determined from Hα and only the $\Sigma_{\rm SFR}$ values of star-forming spaxels defined by the Kauffmann et al. (2003) designation on a Baldwin, Phillips & Terlevich diagram (BPT; Baldwin et al. 1981) would be considered. Along with a Kauffmann et al. (2003) star-forming cut, I also impose a $S/N > 3$ cut for the flux of each diagnostic emission line, as well as requiring an Hα equivalent width (EW)>6Å limit to ensure Hα flux stems from a young stellar population. Of the 13,046 spaxels with CO detections of $S/N > 3$, only 44.5% pass all of these star-forming criteria. Table 4.2 provides for each galaxy the total count of spaxels that pass the star-forming criteria cut for Hα, that have CO $S/N > 3$, and that pass both criteria.

To maximize the number of spaxels with both CO and SFR measurements, I approximate $\Sigma_{\rm SFR}$ for spaxels that are not star-forming (based on my BPT and EW criteria) using the relationship between sSFR and D4000 found for both global (Brinchmann et al., 2004) and local (Spindler et al., 2018; Wang et al., 2019; Bluck et al., 2020a) scales. I adopt an empirical approach similar to that in Bluck et al. (2020a),

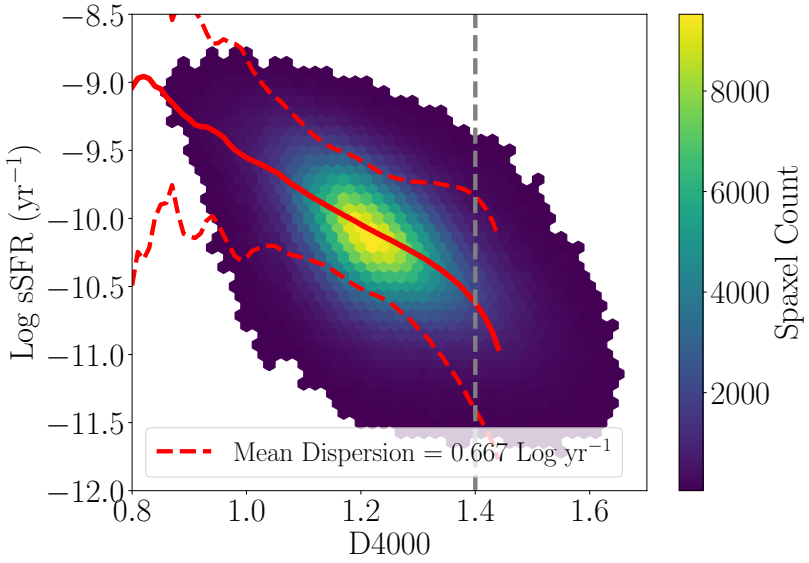

Figure 4.3: The sSFR-D4000 distribution for all star-forming spaxels in MaNGA (shown as a density hexbin). The median sSFR value in each D4000 bin is shown as red line out to D4000=1.45; this value is used to approximate $\Sigma_{\rm SFR}$ based on D4000 for spaxels that do not meet are star-forming criteria. The standard deviation of sSFR within each bin is shown as a red dashed line. The median sSFR value steeply changes at high D4000, leading to vary different sSFR values in relatively close D4000 bins. I therefore only use the D4000-sSFR calibration when D4000<1.4 (vertical dashed line).

who tested the validity of this approximation in the MaNGA PIPE3D data products. For bins of D4000 a median sSFR value is computed based on all star-forming spaxels (using the previous criteria). For any spaxel that does not meet the star-forming criteria, either due to low signal-to-noise or AGN contamination based on the BPT cut, I assign the median sSFR from the closest D4000 bin, and convert that to $\Sigma_{\rm SFR}$ by multiplying sSFR and $\Sigma_{\star}$. Figure 4.3 displays the complete sSFR-D4000 distribution for star-forming spaxels in MaNGA along with a red line showing the median sSFR value, up to D4000=1.45, used to approximate $\Sigma_{\rm SFR}$ when a spaxel is not star forming.

Spaxels with D4000>1.45 are generally quenched and therefore the sSFR-D4000 relation is no longer viable (Bluck et al., 2020a). As can be seen from Figure 4.3, the D4000-sSFR relation turns steeply downwards at D4000>1.4. Therefore $\Sigma_{\rm SFR}$ is only estimated from D4000 when D4000<1.4, which represents a slightly stricter cut than that used in Bluck et al. (2020a). Table 4.2 provides the increased spaxel

count when both Hα- and D4000-$\Sigma_{\rm SFR}$ values are employed. Of the 13,046 spaxels with CO $S/N > 3$, now 78.8% of spaxels have measurable $\Sigma_{\rm SFR}$, almost doubled from the 44.5% of the previous criteria. 9195-3702 and 8450-6102, despite having a considerable number of spaxels with CO $S/N > 3$, still have less than 10 spaxels of overlap between good CO and $\Sigma_{\rm SFR}$ measurements. These two galaxies are thus excluded from individual galaxy analysis later in this work, along with the other four galaxies previously mentioned. Thus there are 25 galaxies that can be studied on an individual basis, and the remainder of the work described in this chapter is limited to these 25. Multiple tests are performed to check how using D4000 approximated $\Sigma_{\rm SFR}$ might impact the final results, the details of which are included in Section 4.4.2. Adopting this method of measuring $\Sigma_{\rm SFR}$ sacrifices accuracy for completeness in my analysis; to assess how this will impact my results I repeat key parts of my analysis using only H$\alpha-\Sigma_{\rm SFR}$ (for galaxies where that is possible). Unless specified otherwise, for the rest of this work, $\Sigma_{\rm SFR}$ and any derived products use the combined Hα+D4000 $\Sigma_{\rm SFR}$ values for both the merger and isolated sample.

Figure 4.2 summarizes the various data products from MaNGA and ALMA used within this work for three galaxies from the merger sample: a post-merger galaxy (top), an interacting pair (middle), and a spectroscopic pair (bottom). Also included are maps of Hα-$\Sigma_{\rm SFR}$ and the combined Hα+D4000-$\Sigma_{\rm SFR}$ map. The middle galaxy is a clear case where a significant number of spaxels can be recovered using the combined $\Sigma_{\rm SFR}$ values. In particular, a significant fraction of spaxels in the outskirts of the galaxy are recovered to maximize the spatial coverage of the analysis. Although the middle galaxy demonstrates how the combined Hα+D4000-$\Sigma_{\rm SFR}$ method recovers lower $\Sigma_{\rm SFR}$ values, the method also recovers AGN dominated spaxels (see 9195-3703 in Appendix A.2). Thus the main limitation of this analysis becomes the CO signal-to-noise, and the overlap between CO and $\Sigma_{\rm SFR}$.

4.3 Results: resolved scaling relations

The stellar mass surface density ($\Sigma_\star$), SFR surface density ($\Sigma_{\rm SFR}$), and molecular gas surface density ($\Sigma_{\rm H_2}$) are all interconnected in three well established resolved relations: the resolved Kennicutt-Schmidt relation and the resolved molecular gas main sequence, which together drive the resolved star-forming main sequence (Lin et al., 2019; Ellison et al., 2021a; Baker et al., 2022). I investigate these three scaling relations both for merger populations, and for individual galaxies in the merger

sample.

Figure 4.4 compares the resolved scaling relations for post-merger (orange) and pair (blue) galaxies with respect to the relatively isolated galaxies in the rest of ALMaQUEST (grey). Histograms of the $\Sigma_{\rm SFR}$, $\Sigma_{\rm H_2}$, and $\Sigma_\star$ are provided for context as well. Note that the grey histogram does not represent a control spaxel population matched in relevant properties (as will be discussed in Section 4.3.1), rather all spaxels where $\Sigma_{\rm SFR}$ can be measured for ALMaQUEST. Given the selection of the original ALMaQUEST sample, including a sample of starburst galaxies, the non-interacting spaxels may be biased to high $\Sigma_{\rm SFR}$. This is likely why the median $\Sigma_{\rm SFR}$ for non-interacting galaxies (shown as a dashed line in the $\Sigma_{\rm SFR}$ histogram) is slightly larger than the median $\Sigma_{\rm SFR}$ of the pair sample. I complete Kolmogorov-Smirnov (KS) tests between all three samples to ascertain whether the pair or post-merger $\Sigma_{\rm SFR}/\Sigma_{\rm H_2}/\Sigma_\star$values could be drawn randomly from the non-interacting spaxel sample. The probability of this hypothesis is approximately zero for all three properties ($P_{KS} \approx 0$). The pair sample has a tail towards lower $\Sigma_{\rm H_2}$, which seems to be driven by two individual galaxies with uniquely low $\Sigma_\star$ and $\Sigma_{\rm H_2}$ values (8078-6104 and 8083-12703). The post-merger sample also has a tail towards large $\Sigma_{\rm SFR}$, $\Sigma_{\rm H_2}$, and $\Sigma_\star$ values, which manifests at the upper end of each scaling relation. Along with the clear lack of post-merger spaxels with $\Sigma_{\rm H_2} < 6.5 \log {\rm M_\odot/kpc^2}$, it is clear that the post-merger sample probes regions of heightened SFR and molecular gas properties.

There is significant diversity on a galaxy-per-galaxy basis to consider, as has been seen in other studies (Vulcani et al. 2019; Ellison et al. 2021a; Pessa et al. 2021, Brown et al. in prep). Figure 4.5 shows the rSFMS for each post-merger and pair galaxy. The star-forming spaxels are colour-coded by radius, while the D4000-$\Sigma_{\rm SFR}$ are a plain yellow if they did not meet the S/N cuts or brown if they are AGN based on the Kauffmann et al. (2003) criteria. The non-interacting ALMaQUEST spaxels are shown as a grey histogram for comparison (including both Hα-$\Sigma_{\rm SFR}$ and D4000-$\Sigma_{\rm SFR}$). Examining galaxies as individuals reveals a clear divergence from the spaxels in non-interacting galaxies, as well as a diversity of behaviour within post-merger and pair classifications. Many mergers show a large population of spaxels above the star-forming main sequence, as is expected if mergers trigger star formation, such as 8156-3701 (1st row, 5th column), 8615-3703 (2nd row, 2nd column), and 8085-12701 (5th row, 1st column). Note that three post-mergers (8084-3702, 8156-3701, 8615-3703) and one pair (8450-6102) were selected from the starburst sample as part of the original ALMaQUEST (ALMA program 2018.1.00541.S, PI: Ellison), which could

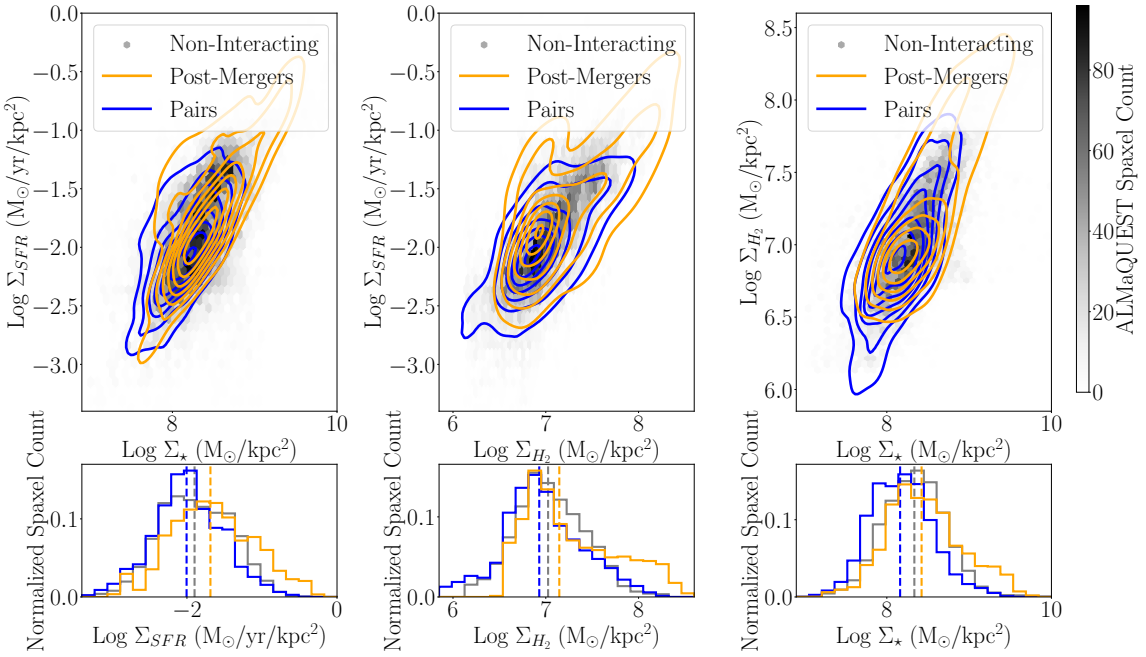

Figure 4.4: Resolved scaling relations for non-interacting ALMaQUEST galaxies (grey histogram), pairs (blue contours), and post-mergers (orange contours). The rSFMS is shown on the left, the rKS is shown in the middle, and the rMGMS is show on the right. All measurements required a CO $S/N > 3$, along with the quality criteria to measure $\Sigma_{\rm SFR}$ with either Hα or D4000 methods as described in Subsection 4.2.3.1. These cuts result in 22782 isolated spaxels, 7990 pair spaxels, and 4012 post-merger spaxels. Below each histogram distributions of $\Sigma_{\rm SFR}$, $\Sigma_{\rm H_2}$, and $\Sigma_\star$are included, separated into non-interacting, post-merger, and pair populations. The median value of each distribution is shown as a horizontal dashed line. Note that the non-interacting ALMaQUEST sample is biased towards higher $\Sigma_{\rm SFR}$ values resulting from the population of starbursts in the original ALMaQUEST sample (see Subsection 4.3.1 for clarification on how this differs from offset parameter controls). A KS-test reveals that all three populations are distinct from each other in $\Sigma_{\rm SFR}$, $\Sigma_{\rm H_2}$, and $\Sigma_\star$. The pair sample has a small offset to lower $\Sigma_{\rm SFR}$, $\Sigma_{\rm H_2}$, and $\Sigma_\star$, which is driven by two pair galaxies with uniquely low $\Sigma_\star$ and $\Sigma_{\rm H_2}$ values (8078-6104 and 8083-12703). Overall, all three populations cover a similar range of surface densities.

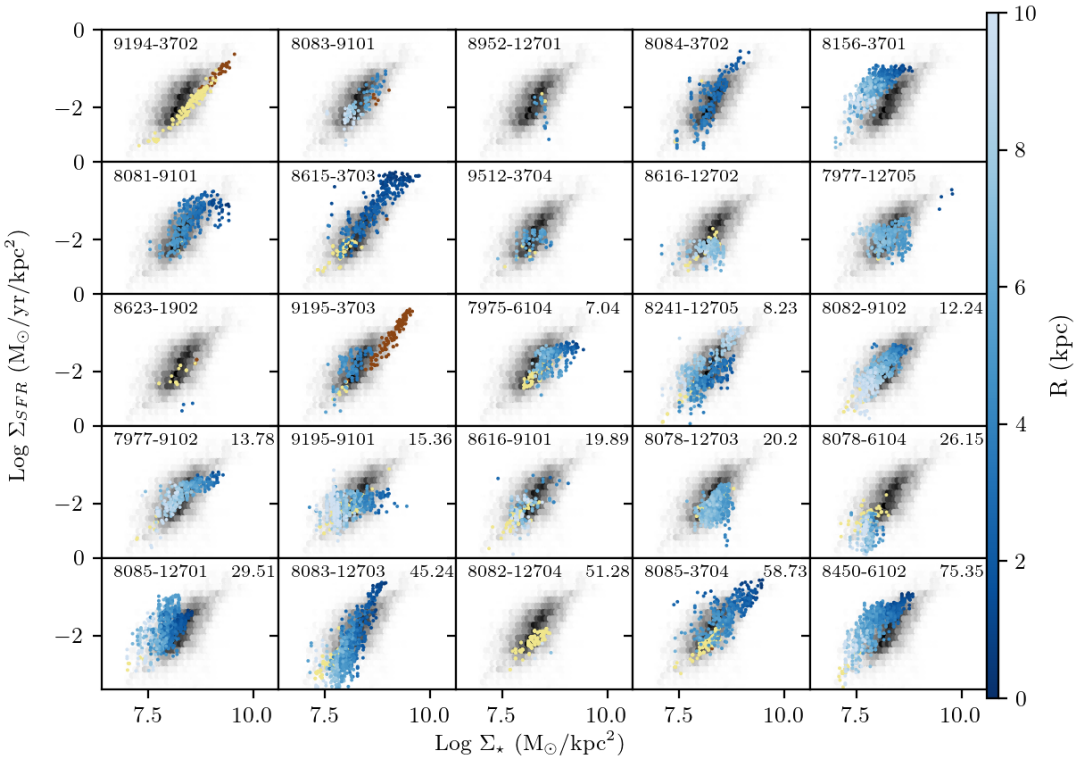

Figure 4.5: Resolved star-forming main sequence for all merger galaxies, with the MaNGA plate-ifu of the galaxy in the left corner and r_p (kpc) in the right corner (left blank for post-mergers). Star-forming spaxels are colour-coded by radius, and spaxels with $\Sigma_{\rm SFR}$ determined by D4000 are yellow (low Hα S/N) or brown (AGN contamination). The non-interacting galaxies in ALMaQUEST are shown as a grey histogram, for reference (including both Hα-$\Sigma_{\rm SFR}$ and D4000-$\Sigma_{\rm SFR}$). Note that there is a diversity of star formation behaviour in the merger sample. Some post-mergers and pairs are significantly offset from the rest of ALMaQUEST. Those that exhibit suppressed star formation (such as 8241-12705, 7975-6104, and 8078-6104) can be derived from both Hα- and D4000- $\Sigma_{\rm SFR}$ values, confirming the validity of the combined $\Sigma_{\rm SFR}$ method.

bias the merger sample towards strongly star-forming galaxies. Yet many spaxels and at times entire mergers are also below the star-forming main sequence, such as 9194-3702 (1st row, 1st column), 7975-6104 (3rd row, 3rd column), and 8078-12703 (4th row, 4th column). In particular, both galaxies with concentrations of "AGN" spaxels as defined by the BPT diagram tend to lie below the non-interacting rSFMS (see 9194-3702 (1st row, 1st column) and 9195-3703 (3rd row, 2nd column)), as has been observed previously with global quantities (Ellison et al., 2016; Leslie et al., 2016; McPartland et al., 2019). This range of enhanced and suppressed star formation rates drives much of the overall scatter of this sample on the global star-forming main sequence (refer back to Figure 4.1).

Mergers exhibit diverse behaviour in the rKS as well, as shown in in Figure 4.6. Many post-mergers and pairs have overall greater scatter in the rKS than the non-interacting sample (see 8615-3703 (2nd row, 2nd column), 8085-12701 (5th row, 1st column), 8083-12703 (5th row, 2nd column)), looking "puffier"; a similar effect as was seen in Ellison et al. (2021a). The increased scatter could represent smaller regions of enhanced SFE in a merger that, on average, has a low or normal global SFE. Note that although D4000-$\Sigma_{\rm SFR}$ values tend to be lower on the rKS, many still overlap with Hα-$\Sigma_{\rm SFR}$ spaxels. Spaxels that are classified as "AGN" by a BPT diagram (brown in the figure) tend to exist at larger $\Sigma_{\rm H_2}$ and $\Sigma_{\rm SFR}$ values, reflecting their central location in the galaxy and the overall radial dependence of the rKS (smaller radii predominantly fill the upper end of the rKS). However, AGN spaxels at large $\Sigma_{\rm H_2}$ could also support a scenario where the infall of molecular gas fuels a central AGN. The two largest AGN spaxel populations belonging to post-mergers appears to support such a scenario, although two galaxies alone are not enough to determine if one scenario is more likely than another. Such a query can be further investigated by looking for enhancements in the molecular gas main sequence at high $\Sigma_{\rm H_2}$ values.

Figure 4.7 appears to confirm that variations in the rMGMS are the least drastic of the three relations, as was found for non-interacting galaxies by Ellison et al. (2021a). Interestingly, the AGN spaxels (shown in brown) are not offset to below the rMGMS, as would be implied by the comparatively low gas fractions found for AGN spaxels with MaNGA (Sánchez et al., 2018) and EDGE-CALIFA (Ellison et al., 2021c). Rather the AGN spaxels in the merger sample are comparable to star-forming isolated spaxels, or even enhanced in the case of 9194-3702 (1st row, 1st column) and 9195-3703 (3rd row, 2nd column). What seems to be an inconsistency may stem from the unique nature of the merger stage. Rather than capture central gas depletion

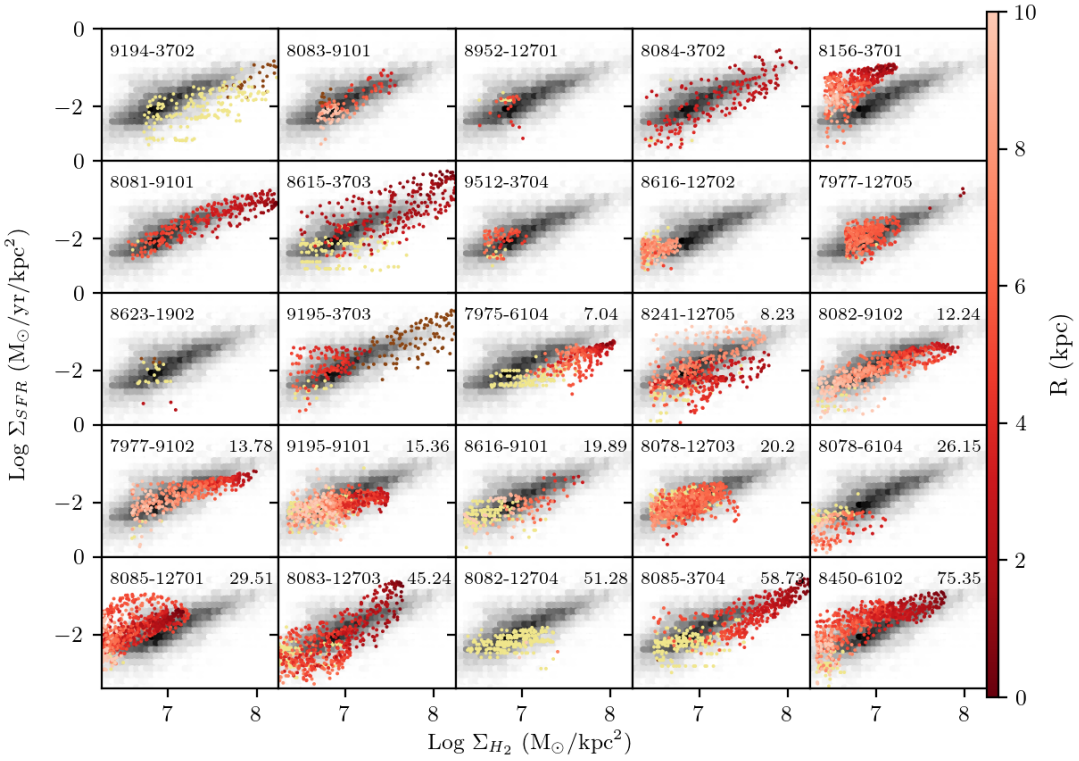

Figure 4.6: Resolved Kennicutt-Schmidt relation for all merger galaxies, with the MaNGA plate-ifu of the galaxy in the left corner and r_p (kpc) in the right corner (left blank for post-mergers). Star-forming spaxels are red and colour-coded by radius, and spaxels with $\Sigma_{\rm SFR}$ determined by D4000 are yellow (low Hα S/N) or brown (AGN contamination). The non-interacting galaxies in ALMaQUEST are shown as a grey histogram, for reference, (including both Hα-$\Sigma_{\rm SFR}$ and D4000-$\Sigma_{\rm SFR}$). Examining mergers on an individual basis reveals many mergers that are offset, both above and below, the non-interacting rKS.

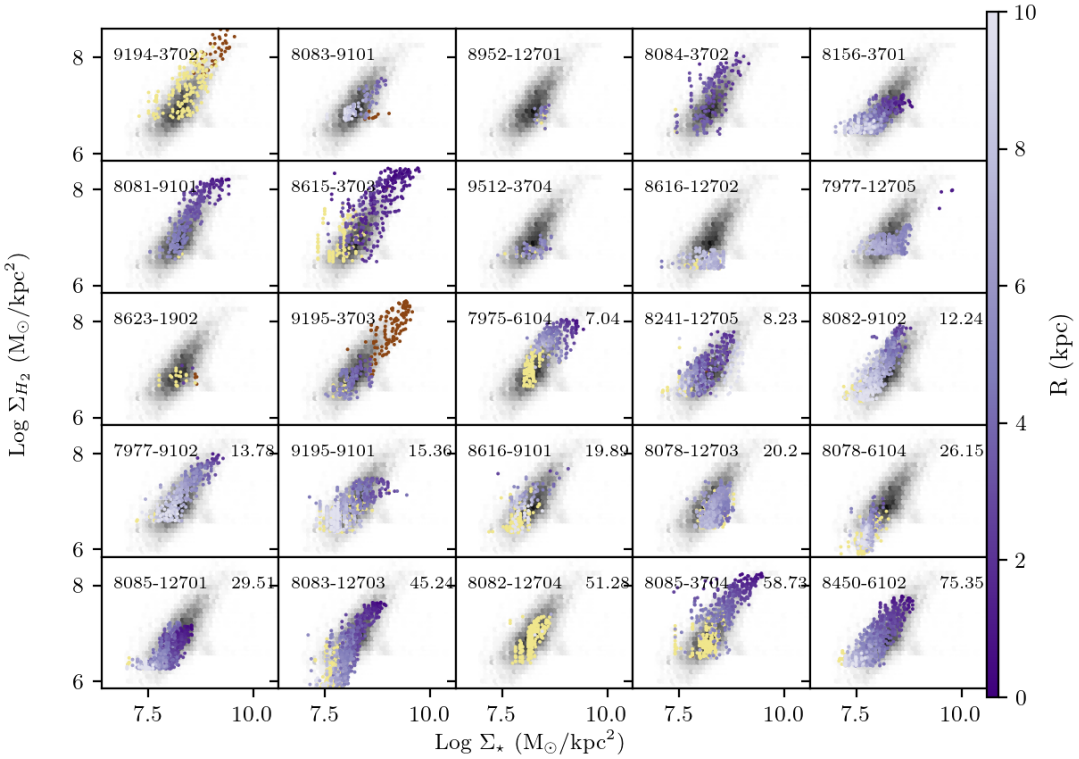

Figure 4.7: Resolved molecular gas main sequence for all merger galaxies, with the MaNGA plate-ifu of the galaxy in the left corner and r_p (kpc) in the right corner (left blank for post-mergers). Star-forming spaxels are colour-coded purple by radius, and spaxels with $\Sigma_{\rm SFR}$ determined by D4000 are yellow (low Hα S/N) or brown (AGN contamination). The non-interacting galaxies in ALMaQUEST are shown as a grey histogram, for reference. Many merging galaxies have tails at the high mass end of the molecular gas main sequence, at times for AGN spaxels as well (supporting a paradigm where mergers fuel AGN).

triggered by an AGN, as in the isolated galaxies of Ellison et al. (2021c), mergers may have more recently funnelled molecular gas to the galaxy's centre that has yet to be consumed by the AGN. The following section will investigate what drives a galaxy merger to be offset from the resolved scaling relations by comparing spaxel offsets from scaling relations.

4.3.1 Spaxel offsets from resolved relations

Following Ellison et al. (2020a), I compute offsets from the rKS, rSFMS, and rMGMS to quantify how an individual spaxel may deviate from the average spaxel behaviour. All offsets are computed as the log difference between a spaxel value and the median value of a set of control spaxels that defines the average behaviour, i.e. $\Delta X = \log X - < \log X_{\rm control} >_{\rm median}$. For example, similar to Chapter 2 I define an offset from the SFMS as $\Delta\Sigma_{\rm SFR}$, with positive $\Delta\Sigma_{\rm SFR}$ values corresponding to enhanced star formation compared to the control sample. The sample of control spaxels is collected from all DR15 MaNGA spaxels from non-merging galaxies (as classified in Subsection 4.2.1) with b/a>0.34 (excluding galaxies with inclination greater than 70°) and that are star-forming based on my cuts for the Hα-$\Sigma_{\rm SFR}$ measurements described in Section 4.2.3.1. All MaNGA $\Sigma_{\rm SFR}$ values are included, not just ALMaQUEST, such that the requirement for CO detections in ALMaQUEST spaxels does not bias the control spaxel set to higher $\Sigma_{\rm SFR}$. Note that D4000-$\Sigma_{\rm SFR}$ values are excluded from the control sample, given I want to know the difference from the star-forming population that defines the resolved star-forming main sequence. The majority of spaxels on the rSFMS for which accurate D4000-$\Sigma_{\rm SFR}$ can be measured tend to not meet the star-forming criteria due to low S/N in BPT diagnostic emission lines, rather than being classified as AGN or composite spaxels. Including D4000-$\Sigma_{\rm SFR}$ in the control would lead to slightly lower $\Delta\Sigma_{\rm SFR}$ values as a result of the contribution from low S/N spaxels. I test whether the inclusion of D4000-$\Sigma_{\rm SFR}$ in the control would alter any major conclusions of this work in Appendix A.3. From the set of star-forming controls I select a subset that is matched within 0.1 dex $\Sigma_\star$, 0.1 R/R$_e$ (where R is the inclination corrected galactocentric radius, and the effective radius R$_e$ is the r-band half-light radius from the NSA catalogue), and 0.1 dex M$_\star$ of the merger spaxel. The median of this control set defines "regular" star-forming behaviour. Similar offsets can be determined for the other scaling relations.

An offset from the resolved KS is referred to as ΔSFE; a value above the KS

would have a larger star formation rate given the molecular gas in a spaxel, i.e. an enhancement in the efficiency at which gas is converted to stars. Rather than rely on S/N and BPT cuts to define star-forming spaxels, as was achieved with $\Delta\Sigma_{\rm SFR}$, I instead make use of the $\Delta\Sigma_{\rm SFR}$ value to construct the star-forming rKS. The control sample is also limited to galaxies in ALMaQUEST, rather than all of DR15, given $\Sigma_{\rm H_2}$ is required to compute ΔSFE. Thus the control sample is selected from non-interacting ALMaQUEST galaxies with b/a>0.34, with the additional cut of $-0.5 < \Delta\Sigma_{\rm SFR} < 0.5$ to select star-forming spaxels. A subset of the control is found by matching to the merger spaxel within 0.1 dex $\Sigma_{\rm H_2}$, 0.1 R/R$_e$, and 0.1 dex M$_\star$.

Using the same control spaxel sample as for ΔSFE, I determine offsets from the rMGMS, referred to as $\Delta f_{\rm H_2}$. The control spaxels are again taken from non-interacting ALMaQUEST galaxies and matched within 0.1 dex $\Sigma_{\rm H_2}$, 0.1 R/R$_e$, and 0.1 dex M$_\star$. Unlike the other two offset metrics, $\Delta f_{\rm H_2}$ can be computed for any spaxels with CO $S/N > 3$. Since there is no dependence on whether $\Sigma_{\rm SFR}$ is measurable, or if measured $\Sigma_{\rm SFR}$ values overlap with good CO measurements, maps of $\Delta f_{\rm H_2}$ tend to be more complete than the other two offsets. Maps of offset parameters for the merger sample are provided in Appendix A.4.

One key difference between Ellison et al. (2020a), who first introduced these offset methods, and the methods used here is I do not match control spaxels by metallicity. Limiting this analysis to spaxels with valid metallicity measurements drastically diminishes the total spaxel count, as described in detail in Section 4.2.2, limiting the spatial coverage of some galaxies and removing three from viable examination entirely. Nonetheless, I have repeated the analysis described in this section with a metallicity control (similar to that used in Ellison et al. 2020a), and find little change in my key results for those galaxies on which this check can be performed (i.e., those with large CO+SFR(Hα) overlap). Further discussion of this can be found in Section 4.4.1.

4.3.2 What drives enhanced star formation?

Maps of spaxel offsets from resolved scaling relations ($\Delta\Sigma_{\rm SFR}$, ΔSFE, and $\Delta f_{\rm H_2}$, as described in Subsection 4.3.1) can be used to discern whether changes in SFE or $f_{\rm H_2}$ drive enhancements in star formation rate. Figure 4.8 shows the offset maps for an example post-merger galaxy (maps for the entire sample are provided in Appendix A.4) for which I can attempt to discern whether star formation is driven by enhanced SFE or

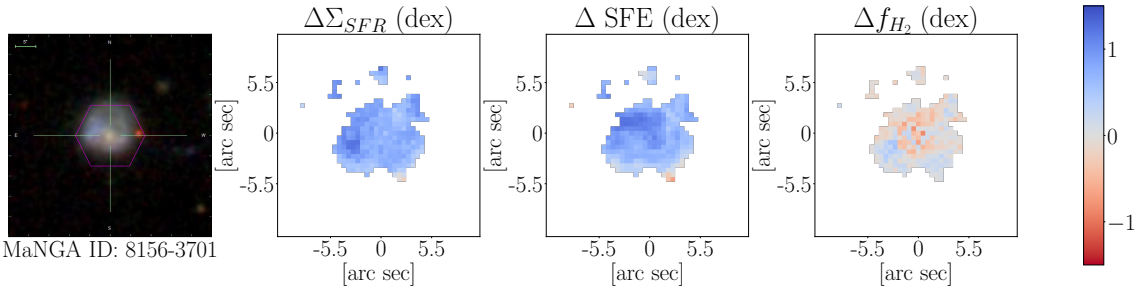

Figure 4.8: Maps of the offset parameters for an example post-merger galaxy. 1st column: the SDSS *gri*-image of the galaxy, for reference. 2nd column: $\Delta\Sigma_{\rm SFR}$ distribution, with blue representing an enhancement in star formation. 3rd column: ΔSFE distribution, with blue representing enhanced star formation efficiency. 4th column: $\Delta f_{\rm H_2}$ distribution, with blue representing enhanced gas fraction in a spaxel. The correlation between a uniform enhancement in $\Sigma_{\rm SFR}$ and SFE, along with the patchy deficits of molecular gas, imply that the star formation in this galaxy is driven by an enhanced efficiency at which gas is converted to stars.

enhanced $f_{\rm H_2}$. Star formation in this post-merger is generally enhanced ($\Delta\Sigma_{\rm SFR} > 0$), as is expected given the average spatial enhancement of post-mergers (see Thorp et al. 2019). That enhancement corresponds to a global enhancement in star formation efficiency (positive ΔSFE). Interestingly, this post-merger mostly has a deficit in molecular gas (negative $\Delta f_{\rm H_2}$), with some smaller regions of surplus gas. Figure 4.8 thus implies that the boost of star formation in this post-merger in particular is predominantly driven by an enhanced efficiency at which gas is converted to stars, not an enhanced amount of gas to fuel that star formation.

The offset maps alone reveal some interesting behaviour. Many pair galaxies, for example, have large $\Delta f_{\rm H_2}$ values along spiral arms (see 9195-9101, 7977-9102, and 8241-12705 in Appendix A.4). Some pair galaxies have central enhancements in $\Sigma_{\rm H_2}$ that correspond to a central burst of star formation, such as 9195-3703 and 8078-6104. These two galaxies support a scenario where inflow of molecular gas fuels merger-triggered central star formation. Post-merger galaxies 8615-3703 and 8084-3702 have an excess of molecular gas across the galaxy's surface, rather than a central concentration. Yet that is not a universal scenario; within this sample, 8156-3701 has one of the strongest enhancements in SFR, but has suppressed $\Sigma_{\rm H_2}$ across the galaxy.

Although the distribution of these offset parameters can reveal interesting results for individual galaxy behaviour, it is difficult to extract general trends for merging and post-merger galaxies from visual examination alone. In particular it is difficult to parse whether enhanced SFE or enhanced $\Sigma_{\rm H_2}$ drives any merger-triggered star

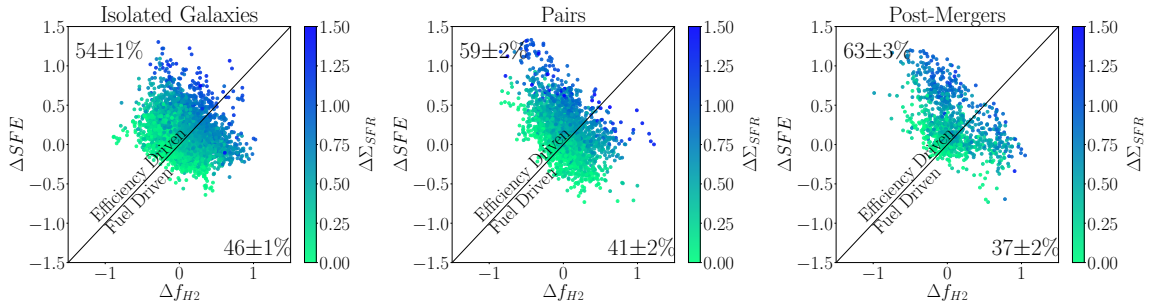

Figure 4.9: ΔSFE versus $\Delta f_{\rm H_2}$ for all spaxels that have $\Delta\Sigma_{\rm SFR}>0$, separated into spaxels which belong to isolated galaxies (left), pair galaxies (middle), and post-merger galaxies (right). Spaxels are colour-coded by $\Delta\Sigma_{\rm SFR}$. The line of equality is shown to delineate the efficiency-driven regime (where ΔSFE$>\Delta f_{\rm H_2}$) and the fuel-driven regime (where ΔSFE$<\Delta f_{\rm H_2}$). The percentage of isolated/pair/post-merger spaxels in each regime is overplotted on the figure, with the uncertainty in the percentage being propagated error of the number of spaxels above/below the line divided by the total number of spaxels. Based on these percentages there is a slight bias towards efficiency-driven star formation in post-mergers and pairs (though more so in the former), but other than that the amount of efficiency and fuelled spaxels with enhanced star formation is relatively even.

formation. To discern which mechanism is likely more influential over star formation enhancements, I implement an analysis that includes all three offset parameters in a single diagram as pioneered by Ellison et al. (2020a) using ALMaQUEST and Moreno et al. (2021) using simulations.

Figure 4.9 shows the offsets in star formation efficiency versus the offsets in molecular gas, for all spaxels with enhanced star formation ($\Delta\Sigma_{\rm SFR}> 0$). Galaxies are separated into three categories: the non-interacting set from ALMaQUEST, pair galaxies, and post-merger galaxies. Figure 4.9 includes a line of equality that is used to distinguish an "efficiency-driven" and "fuel-driven" regime, i.e. where one offset is greater than the other. If a spaxel lies above this line of equality, then ΔSFE $>\Delta f_{\rm H_2}$; if $\Delta\Sigma_{\rm SFR}>0$ this would imply enhanced efficiency is prompting the enhanced star formation, more so than the gas fraction. All three galaxy populations have a relatively equal percentage of spaxels in the efficiency-driven and fuel-driven regime, implying that enhanced star formation is equally driven by enhanced fuel and SFE when all spaxels are examined together. There is a slight bias towards efficiency-driven star formation for the post-merger spaxels, with 63.3% of spaxels in the efficiency-driven regime. Although, the original ALMaQUEST sample includes 11 galaxies that were deliberately selected to be starbursts (Ellison et al., 2020a). Three of these starbursts

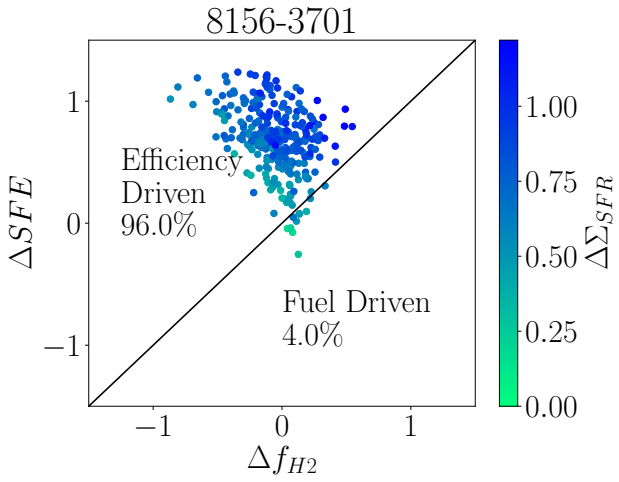

Figure 4.10: ΔSFE versus $\Delta f_{\rm H_2}$ for all spaxels with $\Delta\Sigma_{\rm SFR}$>0 in an example post-merger galaxy (MaNGA plate-ifu = 8156-3701). In this galaxy almost all spaxels are in the efficiency-driven regime, as might be expected from examining the distribution of offset parameters in Figure 4.8.

are in the post-merger sample, one is in the pairs sample, and 12 are in the isolated sample. Since Ellison et al. (2020a) showed that starbursts tend to be dominated by high SFEs, the isolated sample in Figure 4.9 is not statistically representative of a normal galaxy distribution.

Figure 4.9 might lead us to believe that enhancements in both SFE and $f_{\rm H_2}$ are equally important for driving SFR enhancements in both post-mergers and pairs. However, the previous subsection found that ensemble spaxel distributions showed considerable diversity when plotted on a galaxy-by-galaxy basis. I investigate whether the same is true for distributions of offset properties. Figure 4.10 replicates the combined offset diagram from Figure 4.9, but for a single post-merger galaxy (the same one that is shown in Figure 4.8). 96% of spaxels with $\Delta\Sigma_{\rm SFR}> 0$ in this galaxy are in the efficiency-driven regime, confirming that the star formation in this galaxy is driven by enhanced SFE as is evident from visually inspecting Figure 4.8. Figure 4.10 highlights that whilst the ensemble of spaxels across all galaxies might have a relatively even split between those whose star formation is enhanced by SFE or gas fraction (Figure 4.9), individual galaxies may be strongly driven by one process or the other.

Offset diagrams like that in Figure 4.10 are provided for all mergers that have more than 20 spaxels where $\Delta\Sigma_{\rm SFR}> 0$ in Figure 4.11, including the percentage of

spaxels in the fuel/efficiency-driven regimes. There are cases of both post-merger and pair galaxies that are indisputably driven by a single mechanism, such as 9194-3702 (fuel-driven) or 8085-12701 (efficiency-driven), but for the majority the dominant star formation driver is less clear. In order to classify the dominance of fuel or efficiency in driving star formation enhancements on a galaxy-by-galaxy basis, I quantify the percentage of spaxels in the fuel/efficiency-driven regime of these offset diagrams. If more than 60% of a galaxy's $\Delta\Sigma_{\rm SFR}>0$ spaxels are in the fuel-driven regime (i.e., $\Delta f_{\rm H_2}>\Delta$SFE), then I classify the galaxy as "fuel-driven". If less than 40% of a galaxy's $\Delta\Sigma_{\rm SFR}>0$ spaxels are in the fuel-driven regime, then I classify the galaxy as "efficiency-driven". If the percentage of spaxels in the fuel-driven regime is between 40% and 60%, the enhanced amounts of gas and enhanced SFE are approximately equally contributing to the enhanced star formation. Note that this method of classification gives equal weight to all spaxels, regardless of the strength of star formation in each spaxel. By doing so this analysis focuses on what mechanism drives star formation for most regions in a galaxy, not necessarily the mechanism that drives "the most" star formation.

The fraction of fuel-driven spaxels for every merger is listed in Table 4.3. I calculate this fraction for both the combined $\Sigma_{\rm SFR}$ values and for the Hα-$\Sigma_{\rm SFR}$ only, although some mergers do not have enough Hα-$\Sigma_{\rm SFR}$ spaxels to meet this criteria. For galaxies that have enough Hα-$\Sigma_{\rm SFR}$ spaxels to measure the fuel-driven fraction, adding D4000-$\Sigma_{\rm SFR}$ to the analysis does not change the classification of the galaxy as fuel or efficiency-driven (except for 8616-9101). Interestingly, those galaxies that require the inclusion of D4000-$\Sigma_{\rm SFR}$ for a proper analysis tend to have large fractions of fuel-driven spaxels, i.e. the star formation is driven by an excess of fuel. All four recovered galaxies miss our Hα-$\Sigma_{\rm SFR}$ criteria based on low signal-to-noise, implying that the star formation in these galaxies is truly low (and thus a small or negative ΔSFE is to be expected). Further discussion on how D4000-$\Sigma_{\rm SFR}$ impacts the fraction of fuel-driven spaxels is included in Section 4.4.2, where the inclusion of D4000-$\Sigma_{\rm SFR}$ does not drastically change my results. For both $\Sigma_{\rm SFR}$ measurement methods there is a relatively similar number of fuel- and efficiency-driven galaxies, with slightly fewer galaxies driven by neither mechanism. It is also possible that variations in the fraction of fuel-driven spaxels could be driven by inaccuracies resulting from using a constant $\alpha_{\rm CO}$ conversion factor. I investigate the error in $\Sigma_{\rm H_2}$ from using a constant conversion factor, and its impact on the fraction of fuel-driven spaxels, in Section 4.4.1, and find my results are robust to variations in $\alpha_{\rm CO}$.

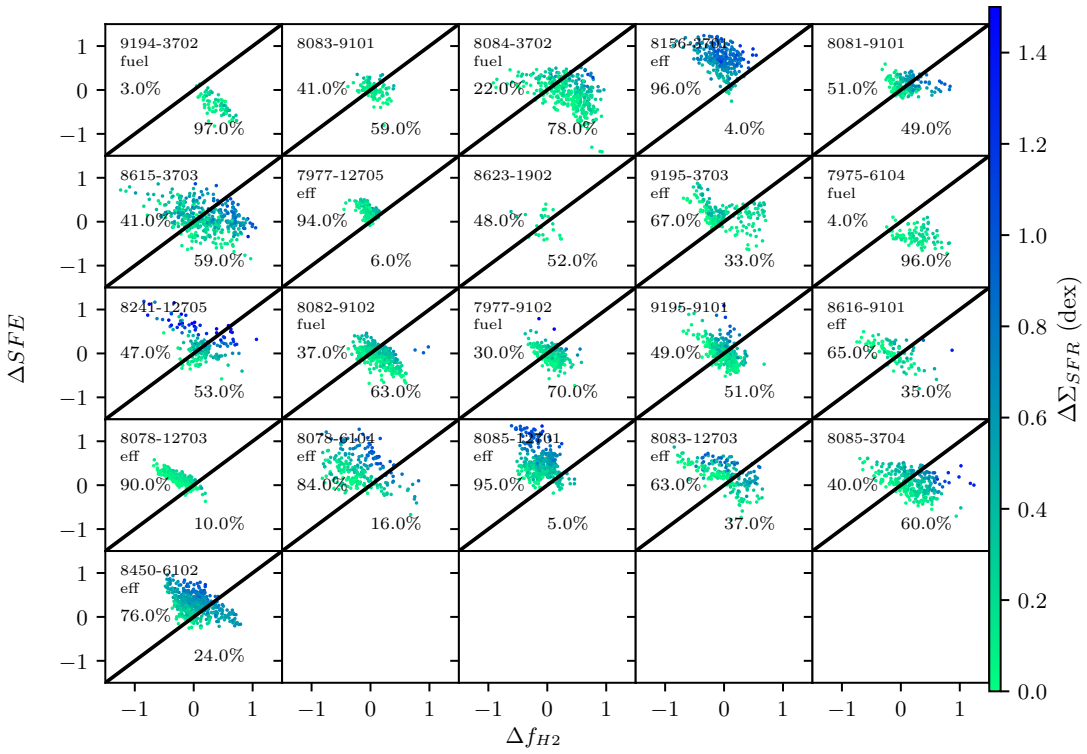

Figure 4.11: ΔSFE versus $\Delta f_{\mathrm{H_2}}$ for all spaxels with $\Delta\Sigma_{\mathrm{SFR}}>0$ in each galaxy merger with more than 20 spaxels with $\Delta\Sigma_{\mathrm{SFR}}>0$, the plate-ifu number of each galaxy is provided in the left corner of every plot. Spaxels are colour-coded by $\Delta\Sigma_{\mathrm{SFR}}$. The percentage of spaxels above and below the line of equality are provided as well, which help discern whether the star formation in a galaxy is predominantly driven by enhanced SFE or enhanced $f_{\mathrm{H_2}}$. Galaxies that are predominantly efficiency-driven (< 40% below the line) and fuel-driven (> 60% above the line) are labelled for reference. For some galaxies there is clearly a dominant mechanism driving star formation, but many galaxies have contributions from both efficiency and fuel-driven SFR enhancements.

Table 4.3: The fraction of $\Delta\Sigma_{SFR}>0$ spaxels in the fuel-driven regime (i.e., $\Delta f_{H_2}>\Delta$SFE) for each merger with more than 20 $\Delta\Sigma_{SFR}>0$ spaxels. The fraction of fuel-driven spaxels is computed using the combined Hα+D4000 Σ_{SFR}, as well as just the Hα star formation rates (with appropriate cuts). Note some galaxies do not have fractions computed for Hα, because they do not have more than 20 spaxels that meet my star-forming cuts. Fractions greater than 0.6, what I consider a fuel-driven merger, are coloured blue. Fractions less than 0.4, what I consider an efficiency-driven merger, are coloured red. Those between 0.4 and 0.6 are left black, since both mechanisms contribute relatively equally.

plate-ifu	Fraction of Fuel-driven Spaxels	Fraction of Fuel-Driven Spaxels (Hα only)
9195-3702	-	-
9194-3702	0.97	-
8083-9101	0.59	0.50
8952-12701	-	-
8084-3702	0.78	0.75
8156-3701	0.04	0.04
8081-9101	0.50	0.53
8615-3703	0.60	0.64
9512-3704	-	-
7977-12705	0.06	0.06
8623-1902	0.52	-
8616-12702	-	-
9195-3703	0.33	0.05
7975-6104	0.97	0.97
8241-12705	0.52	0.52
8082-9102	0.64	0.62
7977-9102	0.69	0.68
9195-9101	0.51	0.55
8616-9101	0.34	0.60
8078-12703	0.10	0.14
8078-6104	0.16	0.21
8085-12701	0.05	0.05
8083-12703	0.38	0.39
8082-12704	-	-
8085-3704	0.60	0.67
8450-6102	0.24	0.24

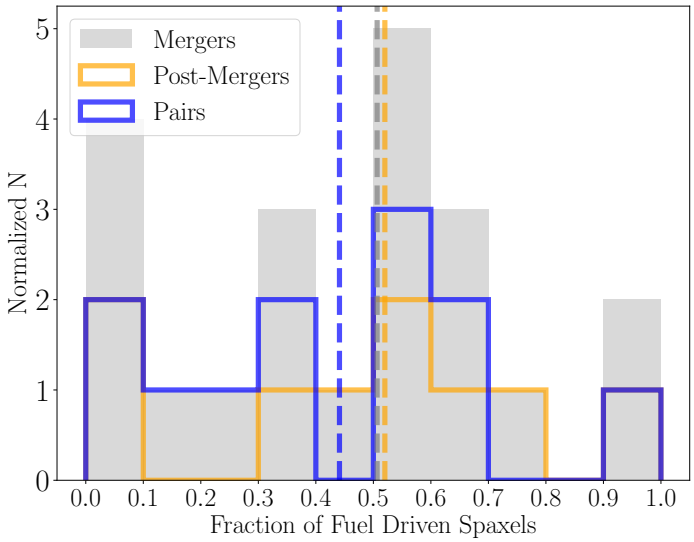

Figure 4.12: Distributions of the fraction of fuel-driven spaxels for the merger sample (grey), along with the pair (blue) and post-merger (orange) sub-samples. The median of each distribution is shown with a vertical dashed line: 0.51 for the entire merger sample, 0.44 for pairs, and 0.52 for post-mergers. The median value of each sub-smaple being so similar, and so close to 0.5, confirms that there are an equal number of fuel- and efficiency-driven mergers.

Figure 4.12 displays the distribution of the fraction of fuel-driven spaxels, both for the merger sample as a whole (grey) and the pair (blue) and post-merger (orange) subsamples. Both the post-merger and pair sample show relatively equal distribution in fuel fraction implying a diversity of star formation drivers throughout the interaction process. There is an intriguing excess of extremely low fuel fractions (below 0.1), compared to the more uniform distribution above a fuel fraction of 0.5, implying that "efficiency-driven" mergers have $\Delta\mathrm{SFE}>\Delta f_{\mathrm{H_2}}$ in most spaxels. However, given only 3 post-mergers are below a fuel fraction of 0.4, this could be the result of small number statistics.

Both observations (Ellison et al., 2013b; Patton et al., 2013; Knapen et al., 2015) and simulations (Cox et al., 2008; Torrey et al., 2012; Moreno et al., 2019; Patton et al., 2020) have demonstrated that merger-induced star formation peaks at coalescence. Despite the diversity demonstrated in Table 4.3, it is interesting to note that 2 of the 3 post-mergers with a global $\Delta\mathrm{SFR} > 0.5$ dex are fuel-driven enhancements (9194-3702, 8084-3702). One might wonder, then, if there is some correlation between the fraction of fuel-driven spaxels and the interaction stage, with the largest fraction of fuel-driven spaxels occurring at coalescence when the star formation is strongest. The higher percentage of efficiency-driven galaxies in the pair sample (50% as opposed to 33% in the post-mergers) would agree with a scenario where efficiency-driven star formation becomes less important towards coalescence. Such a correlation would fit with the hypothesis that merger-induced star formation stems from non-axisymmetric structures causing a loss of angular momentum for gas, which then funnels into the centre of the galaxy towards the end of an interaction.

Figure 4.13 is a visual representation of Table 4.3, showing the fraction of fuel-driven spaxels as a function of projected separation between pairs, with each point colour-coded by global offset from the star-forming main sequence. The post-mergers are shown with a projected separation as arbitrary values below zero, in the grey bar. Figure 4.13 reveals no clear correlation with the fraction of fuel-driven spaxels and the projected separation (Pearson's correlation coefficient$=-0.355$). Thus there is no evidence from this sample that the merger stage is strongly linked to whether enhanced star formation is driven by elevated fuel or efficiency. It is important to note that projected separation is not a perfect representation of merger stage due to both uncertainty on whether a galaxy has already completed one or more pericentric passages, as well as projection effects. Morphological signs can serve as an additional indicator for interaction stage given galaxies are most disturbed at first

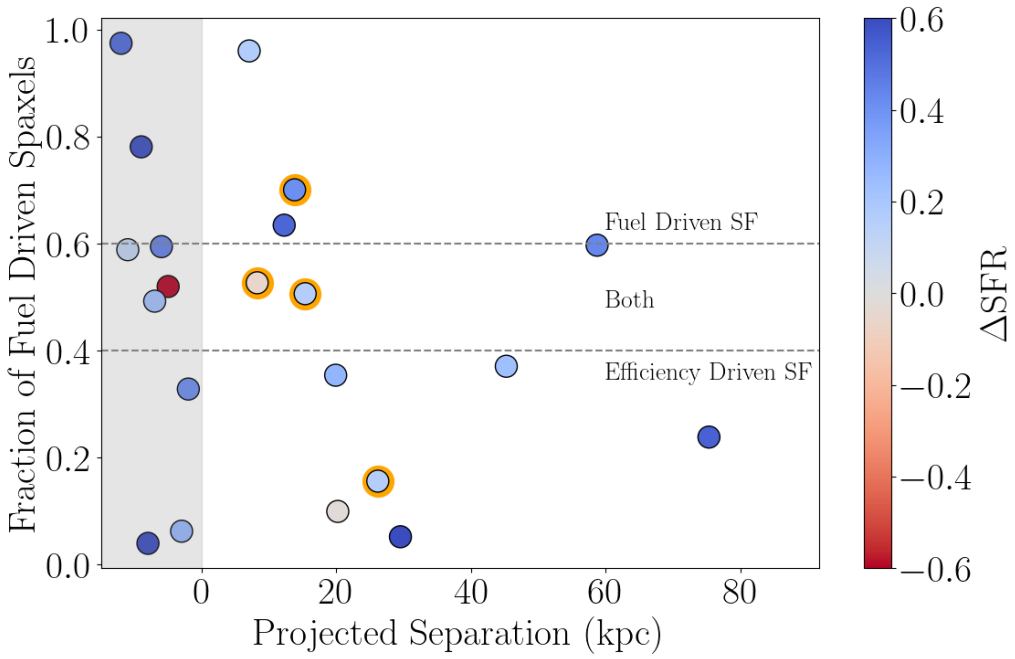

Figure 4.13: Fraction of fuel-driven spaxels as a function of projected separation in kpc, with post-mergers in the grey region (since projected separation cannot be measured without a companion). All points are colour-coded by the galaxy's global offset from the star-forming main sequence, ΔSFR (bluer points have globally enhanced SFR, red points have globally suppressed SFR, compared with the global SFMS). Note that galaxies with negative ΔSFR can still have regions of enhanced star formation, which is used to compute a fuel fraction. Pairs that have tidal arms connecting the two galaxies are highlighted with orange. Neither projected separation, nor this secondary morphology characteristic, show any trend with the fraction of fuel-driven spaxels.

passage and right before coalescence (Lotz et al., 2004, 2008; Hambleton et al., 2011). Unfortunately most of my mergers have some degree of visual disturbance (see images in Appendix A.2), making it difficult to directly link morphology to a distinct interaction stage (outside of pre- and post-coalescence). I attempt to account for this by highlighting pair galaxies which are connected to their companion by a tidal arm on Figure 4.13, as a more concrete indicator that first passage has already occurred. Even with this additional category, no trend with merger stage and fraction of fuel-driven spaxels arises, further affirming that interaction stage plays a secondary role influencing how star formation is enhanced.

Figure 4.13 encapsulates one of the main conclusions of this paper: interacting

galaxies show a broad diversity of the relative contributions of fuel and efficiency, with no obvious dependence on the merger stage I adopted. This sample suggests that the properties of the galaxies themselves (e.g. gas fractions, morphologies) as well as the details of the interaction (orbit and mass ratio) play a larger role in how star formation is enhanced. I have checked to see if the fraction of fuel-driven spaxels correlates with $M_\star$, M_{H_2}, f_{H_2}, SFR, and ΔSFR, and found only M_{H_2} and f_{H_2} have a Pearson's correlation coefficient greater than 0.6[1]. However, a correlation between the fraction of spaxels driven by enhanced amounts of molecular gas and large gas fractions is not a particularly noteworthy result. More likely it is the combined properties of the galaxy and its companion that drive the diversity of star formation properties observed. Recent simulations have found that mass ratio and orbital geometry can both impact how star formation is powered in mergers (Moreno et al., 2021). It is possible that, with a larger sample, more pronounced correlations with merger stage or integrated galaxy property would emerge, but for this sample such trends are not obvious.

4.3.2.1 What drives resolved changes in star formation?

This chapter has shown that, for both pair and post-merger galaxies, either enhanced SFE or enhanced f_{H_2} can drive the subsequent star formation enhancement that results from an interaction. The merger sample is split evenly between galaxies whose star formation driven by SFE, by f_{H_2}, and those equally driven by both. An underlying issue yet to be addressed is how the mechanism that powers star formation relates to the spatial variations in star formation.

Figure 4.14 displays radial profiles of $\Delta\Sigma_{SFR}$ for the merger sample separated into distinct categories of efficiency-driven, fuel-driven, or driven by both based on the fraction of fuel-driven spaxels in Table 4.3 (profiles are additionally colour-coded by the exact fuel fraction computed). Creating radial profiles of offsets in Σ_{SFR} allows for investigation of whether the fuel fraction I have computed can help explain the diversity of merger radial profiles seen with previous MaNGA studies (i.e., Thorp et al. 2019; Pan et al. 2019; Steffen et al. 2021). A more detailed analysis of merger radial profiles for different ALMaQUEST data products will be included in Pan et al. (in prep); what is discussed here is simply to assess how the global fuel fraction might relate to variations in Σ_{SFR} already noted by previous works.

[1] note that f_{H_2} and M_{H_2} are themselves correlated, with a Pearson's correlation coefficient of 0.69

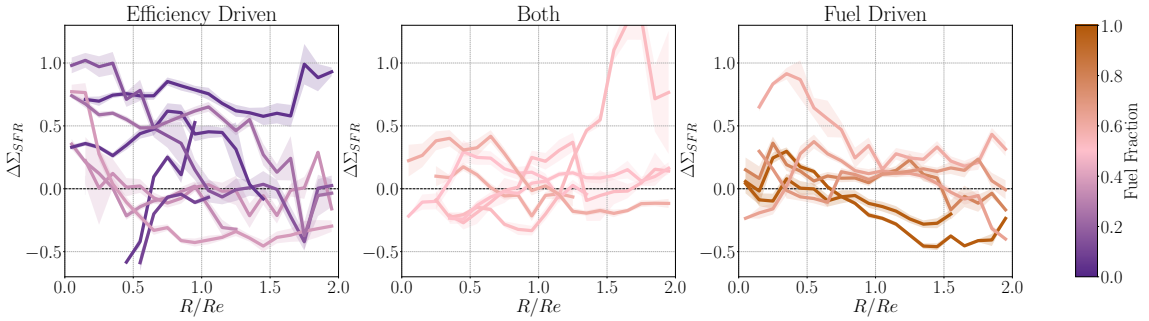

Figure 4.14: Radial profiles of the median $\Delta\Sigma_{\rm SFR}$ in bins of effective radius for post-merger and pair galaxies included in my analyses, separated into groups of "Efficiency-Driven", "Both", and "Fuel-Driven" based on the fuel fraction value (the second column of Table 4.3). Each profile is also colour-coded by the fuel fraction. Radial profiles are plotted as a function of the effective radius, with the solid line representing the median in a bin of 0.1 R_e, and the faded width of the line representing the error on the mean. Efficiency-driven mergers tend to have the strongest and most extended enhancements in star formation, whereas fuel-driven mergers are more likely to have centrally concentrated bursts of star formation, likely due to an inflow of gas.

The efficiency-driven and fuel-driven radial profiles in Figure 4.14 have clearly distinct behaviour. Fuel-driven mergers tend to have greater $\Delta\Sigma_{\rm SFR}$ at small radii, although that does not always lead to a suppression of star formation in the outskirts. Efficiency-driven mergers have both greater peaks in $\Delta\Sigma_{\rm SFR}$ (5 out of 9 surpass 0.5 dex enhancement at one point) and a greater diversity in profile behaviour. Profiles for the efficiency-driven mergers can both increase $\Delta\Sigma_{\rm SFR}$ with radius, decrease $\Delta\Sigma_{\rm SFR}$ with radius, or have consistent $\Delta\Sigma_{\rm SFR}$ out to $2R_e$. Thus it is likely a diversity of fuel fraction values could explain some of the diversity of post-merger profiles noted in Thorp et al. (2019). Interestingly, the fuel-driven mergers show similar profiles to the starburst $\Delta\Sigma_{\rm SFR}$ profiles found in Ellison et al. (2020a), despite non-interacting starbursts being primarily driven by enhanced SFE. It is possible that mergers provide one route to a starburst by funnelling gas to a centralized starburst, and the resulting SFR enhancement profile is indistinguishable from secular starbursts. Efficiency-driven mergers, on the other hand, are more likely to have stronger and continuous SFR enhancements that distinguish them from isolated galaxies of a similar ΔSFR. In the case of the later, the strongest bursts of star formation cannot be driven by enhanced gas reservoirs alone.

There are still issues with applying a single "fuel-driven" prescription to what is clearly quite variable on the resolved scale. Simulations of the resolved gas properties of mergers have demonstrated that mergers with overall suppressed star formation can still have appreciable amounts of centralized cold-dense gas (Moreno et al., 2021). Such a phenomenon is also evident in the handful of fuel-driven mergers that have suppressed star formation beyond $1R_e$, despite centralized boosts in star formation. It is possible that, even though a merger is primarily fuel or efficiency-driven, there are regions that deviate from this norm. After all, the mergers that are driven by "both" are lacking any trend in radial profile unlike the other two categories. It is clearly worthwhile to explore how the dominant mechanism might vary within a galaxy.

I attempt to pinpoint spatial variations in the dominant star-forming mechanism by examining the difference between ΔSFE and $\Delta f_{\rm H_2}$. The difference between two offset parameters provides a rough approximation of which offset is dominant in an individual spaxel by simply quantifying which is larger. The difference between ΔSFE and $\Delta f_{\rm H_2}$ is a bit like a fuel fraction for each spaxel, although note that the number attributed to each has no physical meaning beyond comparing offset values. Maps of $\Delta{\rm SFE}-\Delta f_{\rm H_2}$ are constructed to demonstrate which mechanism is more important within a certain region of a galaxy. Every spaxel in each map must have positive

$\Delta\Sigma_{\rm SFR}$, ΔSFE, and $\Delta f_{\rm H_2}$, to avoid interpreting the contribution of suppressed SFE or $f_{\rm H_2}$.

Figure 4.15 displays maps of ΔSFE$-\Delta f_{\rm H_2}$ for three example galaxies, in conjunction with the ΔSFE vs. $\Delta f_{\rm H_2}$ diagram colour-coded by ΔSFE$-\Delta f_{\rm H_2}$. Note how the magnitude of ΔSFE$-\Delta f_{\rm H_2}$ scales with distance from the line of equality, where the contribution from SFE and $f_{\rm H_2}$ is equal. Regions where ΔSFE is greater are shown in purple, and regions where $\Delta f_{\rm H_2}$ is greater are shown in brown. Three galaxies that are predominantly efficiency or fuel-driven are specifically chosen to demonstrate how this clear-cut classification may break down on a spaxel-per-spaxel basis.

Figure 4.15 demonstrates that, even within a given galaxy, the dominant driver of enhanced star formation can vary spatially. The first row of Figure 4.15 shows a post-merger galaxy with a global fuel fraction of 0.33, indicating that SFE is the dominant driver of enhanced star formation. However, a more complicated picture emerges when examining the spatially resolved map of ΔSFE$-\Delta f_{\rm H_2}$ in the right column. Although the extended spiral arms are indeed dominated by enhanced SFE, the core is dominated by enhanced gas fractions. Similar results were found for the Antennae merging galaxies, which had central enhancements in dense gas along with lowered SFE (Bemis & Wilson, 2019). By examining maps of ΔSFE$-\Delta f_{\rm H_2}$ for all mergers (included in Appendix A.4, column five), most of the merger sample follows a similar trend of $\Delta f_{\rm H_2}$ dominating the central regions of the galaxy.

To quantify whether $\Delta f_{\rm H_2}$ is more important in the centre of a merging galaxy, a gradient in ΔSFE$-\Delta f_{\rm H_2}$ is computed for each merger, subtracting the median ΔSFE$-\Delta f_{\rm H_2}$ within 1R$_e$ from the median where R>1 R$_e$. All but two mergers have a positive gradient (i.e., $\Delta f_{\rm H_2}$ is more important in the centres than the outskirts), confirming that, similar to previous case studies, $\Delta f_{\rm H_2}$ plays a key role in triggering central bursts of star formation. Positive gradients are found both within efficiency-driven and fuel-driven mergers, with no correlation to the global fraction of fuel-driven spaxels (Pearson's correlation coefficient=$-$0.19). Efficiency-driven mergers have mostly efficiency-driven spaxels (positive values in ΔSFE$-\Delta f_{\rm H_2}$ maps) with fuel-driven central starbursts; but given there are more spaxels at large radii than small, those efficiency-driven spaxels dominate the percentage of star-forming regions overall. The two mergers with negative gradients, 8156-3701 and 8081-9101, are not unique in their global galaxy properties, but have distinct $\Delta\Sigma_{\rm SFR}$ profiles. 8156-3701 (a post-merger with fuel fraction=0.04) has $\Delta\Sigma_{\rm SFR} > 0.5$ out to two effective radii, powered by predominantly ΔSFE. In contrast, 8081-9101 (a post-merger fuel

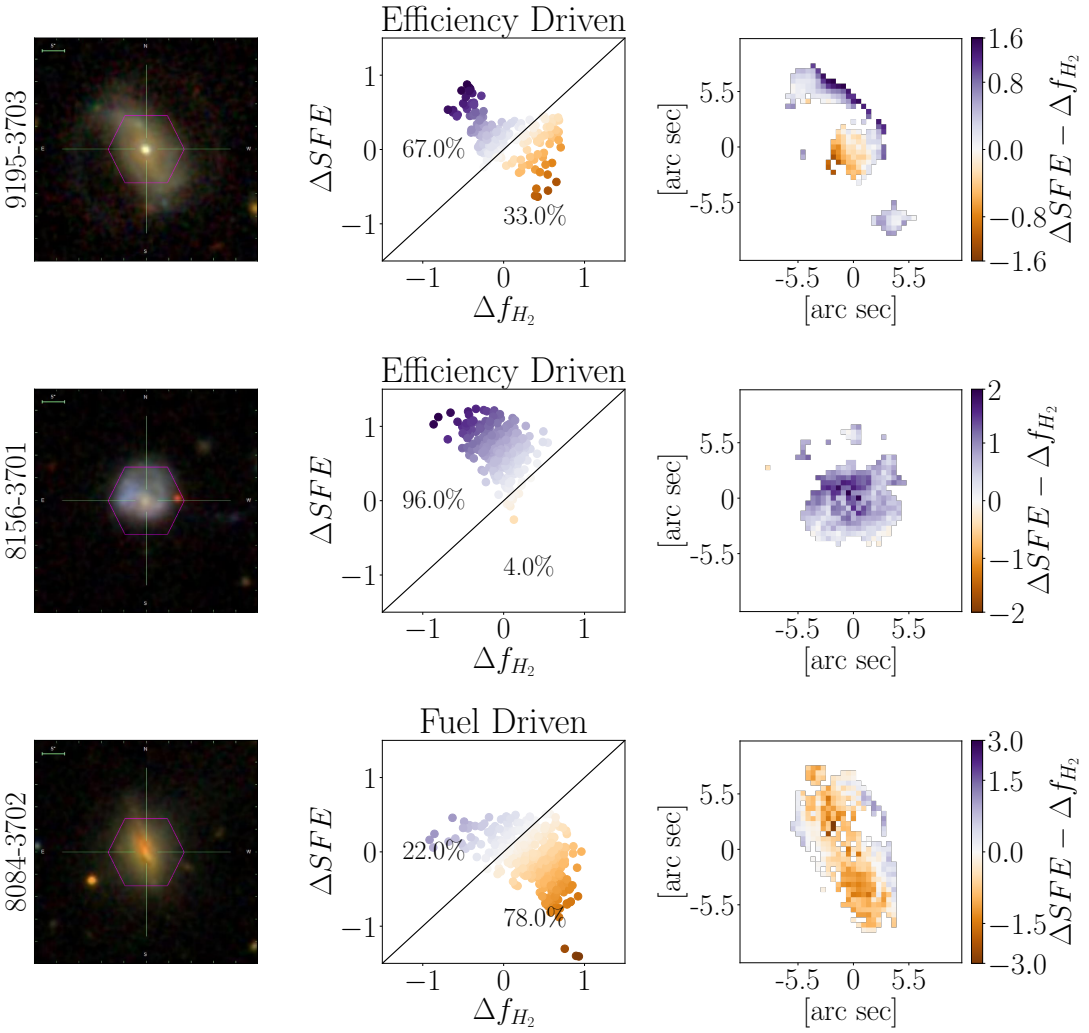

Figure 4.15: *1st column: gri*-image of the merger galaxy. *2nd column:* ΔSFE versus $\Delta f_{\mathrm{H_2}}$ for all spaxels where $\Delta\Sigma_{\mathrm{SFR}}>0$, colour-coded by ΔSFE$-\Delta f_{\mathrm{H_2}}$. *3rd column:* spatially resolved map of ΔSFE$-\Delta f_{\mathrm{H_2}}$for spaxels where all three offset parameters are positive. The colour bars change slightly for each merger, which have different spans of ΔSFE$-\Delta f_{\mathrm{H_2}}$, but zero is always white. Note that ΔSFE-$\Delta f_{\mathrm{H_2}}$ scales with distance from the line of equality shown in the 2nd column. Within each galaxy there is distinct variability in the importance of ΔSFE and $\Delta f_{\mathrm{H_2}}$, particularly between the centre and outskirts of the galaxy.

fraction=0.5) has brief deficits in star formation at the centre and edge of the galaxy, but enhancements ∼0.25 dex for the majority of the galaxy. Although no substantial result can be derived from two galaxies alone, it is interesting that mergers without central fuel enhancements display two of the most chaotic $\Delta\Sigma_{\rm SFR}$ profiles. However, on average, this sample confirms that central bursts of star formation in mergers require centralized enhancements in gas fraction.

Clearly the consistency of positive gradients in $\Delta{\rm SFE}-\Delta f_{\rm H_2}$ does not negate further variations between galaxies, as can be seen in the examples from Figure 4.15 alone. The middle row of Figure 4.15 shows a post-merger with a negative gradient in $\Delta{\rm SFE}-\Delta f_{\rm H_2}$. Although star formation in this merger is clearly driven by enhanced SFE (it has a fuel fraction of 0.04), $f_{\rm H_2}$ plays a slightly more important role in the outskirts than in the centre (though ΔSFE is always greater). But even galaxies with a positive gradient, as expected, can have local variations from the norm. The last row of Figure 4.15 shows a fuel-driven post-merger (fuel fraction 0.78) with a positive $\Delta{\rm SFE}-\Delta f_{\rm H_2}$ gradient. However, regions where $\Delta{\rm SFE}-\Delta f_{\rm H_2} < 0$ persist out to large radii as well, following a central extended structure within the galaxy. In this case fuel-driven star formation is not limited to the centre of the galaxy (though ΔSFE becomes more important at large radii as well). Such variations are similar to those found in studies of isolated galaxies, where the slope and offset of the rSFMS, rKS, and rMGMS can vary significantly depending on the local galaxy environment (particularly for spiral arms, Pessa et al. 2021). In summary, there is not only considerable diversity from galaxy-to-galaxy in terms of the relative importance of fuel and efficiency, but even within a given galaxy, different regions show considerable variation.

4.4 Impact of varying techniques to compute $\Sigma_{\rm H_2}$ and $\Sigma_{\rm SFR}$

4.4.1 Metallicity dependent $\alpha_{\rm CO}$

Throughout this work I elect to use a constant $\alpha_{\rm CO}$ rather than a metallicity dependent one. This is highly beneficial to my analysis in that spaxels that do not meet the requirements to measure accurate gas-phase metallicities (requiring high signal-to-noise in multiple emission lines) can be used. As a result the $\Sigma_{\rm H_2}$ measurements will be imperfect, leading to the possibility that variations ΔSFE and $\Delta f_{\rm H_2}$ (both of which require $\Sigma_{\rm H_2}$) could be the result of inaccuracies in $\alpha_{\rm CO}$. Depending on the degree of that inaccuracy this could sully the final conclusions concerning the role enhanced efficiency and fuel play in increasing star formation activity.

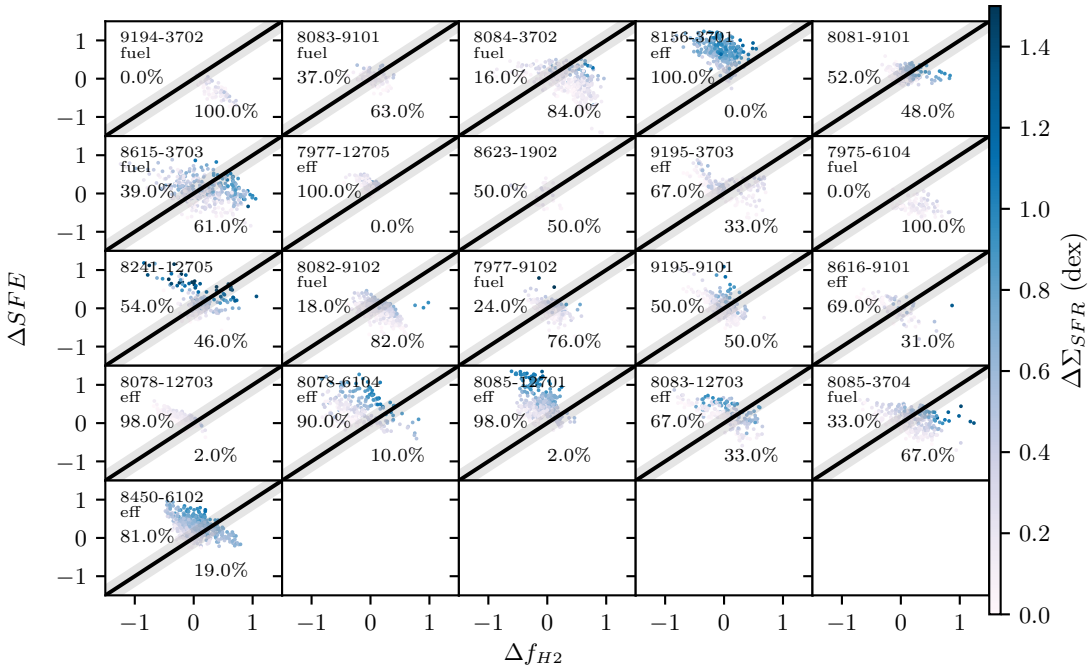

Figure 4.16: A replication of Figure 4.11, but now with a grey line indicating the 0.248 dex error on both offset parameters from using a constant $\alpha_{\rm CO}$. Spaxels within this grey region are not considered when calculating the fraction of fuel-driven spaxels. This biases the distribution of fuel fractions to the extreme ends (very high or very low), as spaxels further away from the line become more important in the calculation.

Though I cannot compute a metallicity dependent α_{CO} ($\alpha_{CO,\,met}$ from here on) for every spaxel, I can characterize the change in Σ_{H_2} for spaxels where $\alpha_{CO,\,met}$ is measurable. I compute a $\alpha_{CO,\,met}$ for all spaxels that are star-forming based on the criteria described in Subsection 4.2.3.1, for which I can also measure the gas phase metallicity using the O3N2 calibration of Pettini & Pagel (2004). I set $\alpha_{CO,\,met} = 4.35 \times Z'^{-1.6}(M_\odot(\text{K km/s pc}^2)^{-1})$ where Z' is the metallicity normalized to solar metallicity ($Z' = 10^{PP04_{O3N2}-8.69}$) (Sun et al., 2020). The median difference between Σ_{H_2} and to be -0.068 dex, with a standard deviation of 0.124 dex. To be conservative I can say that Δf_{H_2} and ΔSFE both have an uncertainty of 2σ on the difference in Σ_{H_2}, or 0.248 dex. Figure 4.16 is a replication of Figure 4.11, with a grey bar representing 0.248 dex of uncertainty; points within this range could change from fuel to efficiency-driven, or vice versa, if one switched from a constant to a metallicity dependent α_{CO}. Thus spaxels within this grey bar are excluded from calculations of the fuel fraction to achieve a value that is independent of variations in α_{CO}. By excluding borderline spaxels, most galaxies tend to be more "fuel" or "efficiency" driven.

Figure 4.17 directly compares the original fuel fraction, using a constant α_{CO}, to this new one that incorporates error from not using $\alpha_{CO,\,met}$. Ideally all points would be along the line of equality, confirming that the fraction of fuel-driven spaxels does not change. Instead galaxies that are fuel-driven become more fuel-driven, rising above the line of equality, and galaxies that are efficiency-driven become more efficiency-driven. As a result very few galaxies change whether they are considered "efficiency" or "fuel" driven. I highlight regions where both the new and old fuel fractions agree on the dominant mechanism: where efficiency dominates (red), fuel fraction dominates (blue), or both equally influence star formation(grey). Only two mergers change which mechanism dominates: both are mergers where efficiency and fuel are equally important with a constant α_{CO}, but then change to fuel-driven. This shift is not the result of a significant change in fuel fraction, rather the two mergers were already at the border between categories. As discussed in the main analysis, these categories of "efficiency" and "fuel" driven are less robust than the continuously changing fuel fraction measurement.

In summary, the measured fuel fraction changes little when uncertainties in α_{CO} are considered. Moreover, results concerning ΔSFE being more important to star formation than Δf_{H_2} (or vice versa) are unlikely to stem from local variations in conversion factor. Rather they characterize the true relationship between star formation

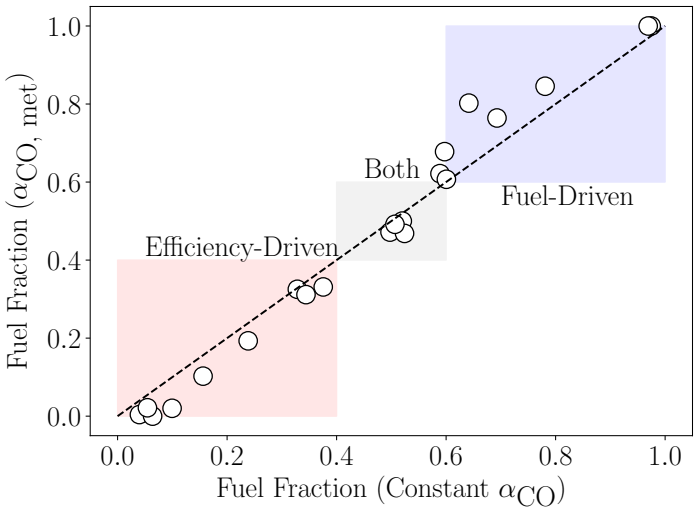

Figure 4.17: The fuel fraction determined from Figure 4.16, considering uncertainties from not using $\alpha_{CO,\ met}$, plot against the original fuel fraction determined from Figure 4.11. Note that efficiency-driven mergers move below the line of equality (black dashed line), and fuel-driven mergers move above the line; thus the dominant star-forming mechanism only appears more dominant when uncertainties in α_{CO} are considered. I have highlighted regions that indicate the dominant mechanism has not changed (ideally where all points would lie): where both fractions imply star formation is efficiency-driven (red), where both fractions imply star formation is fuel-driven (blue), and where both fractions imply star formation is driven by both (grey). Only two mergers change category (from "both" to "fuel-driven"), and both galaxies were already at the border between these two categories.

and molecular gas in a merger event.

4.4.2 Estimating Σ_{SFR} with D4000

The SFRs presented herein include those that have been calibrated from D4000. This Section will demonstrate that the main conclusions of this chapter are not significantly affected by the inclusion of SFRs computed in this way. Figure 4.18 shows the distribution of sSFR versus D4000 for all star-forming spaxels in MaNGA, based on the star forming criteria described in Subsection 4.2.3.1, with contours representing the density of the distribution of hexbins colour-coded by the median $\Delta\Sigma_{SFR}$ value in that bin. The asymptotic nature of the sSFR-D4000 relation as D4000 approaches 1.45 can lead to drastic difference in approximated Σ_{SFR} for spaxels with very similar D4000 values. Therefore, only spaxels with D4000>1.4 are used for SFR calculations.

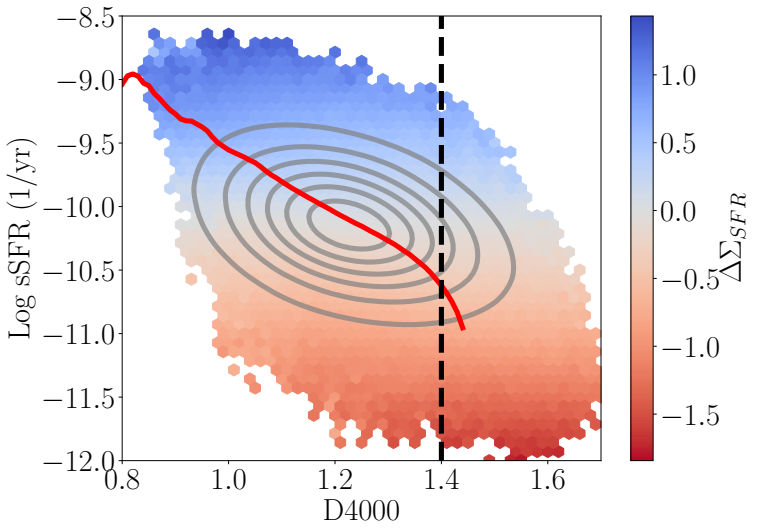

Figure 4.18: sSFR versus D4000 for all star-forming spaxels in MaNGA. Density contours of this distribution are shown in grey, over a hexbin distribution colour-coded by the median $\Delta\Sigma_{\rm SFR}$ value in each bin. The median sSFR value in a D4000 bin is shown in red: these points are used to approximate $\Sigma_{\rm SFR}$ for spaxels that do not meet my star-forming criteria. Spaxels with D4000>1.4 are excluded, given the asymptotic nature of the sSFR-D4000 at high D4000. Note that there is significant scatter in this relation, which correlates with $\Delta\Sigma_{\rm SFR}$.

There is a non-negligible scatter in the sSFR-D4000 relation that is strongly correlated with $\Delta\Sigma_{\rm SFR}$. This is to be expected; by definition a spaxel with high sSFR given the D4000 index would have a higher $\Sigma_{\rm SFR}$ given its $\Sigma_\star$. The red line is a median sSFR in a bin so it makes sense that scatter significantly above the line would corresponds to large, positive $\Delta\Sigma_{\rm SFR}$. Thus by approximating $\Sigma_{\rm SFR}$ from the median sSFR, the offset of the star formation from regular behaviour (both enhancements and deficits) will always be underestimated. That bias works in favour of this analysis given it looks for strong offsets in $\Sigma_{\rm SFR}$. Thus for D4000-$\Sigma_{\rm SFR}$ values, any enhancement or suppression in star formation is a lower limit on the true offset; the same can be said for enhancements and deficits in SFE.

When D4000-$\Sigma_{\rm SFR}$ is used the absolute value of $\Delta\Sigma_{\rm SFR}$ and ΔSFE will be underestimated, but $\Delta f_{\rm H_2}$ (which does not depend on a $\Sigma_{\rm SFR}$ measurement) will not be changed. The dependence of ΔSFE on $\Sigma_{\rm SFR}$ is crucial when comparing ΔSFE and $\Delta f_{\rm H_2}$ to determine which mechanism drives enhanced star formation. When using a D4000-$\Sigma_{\rm SFR}$ the value of ΔSFE is a lower limit, so $\Delta{\rm SFE}>\Delta f_{\rm H_2}$ will be consistent even if D4000-$\Sigma_{\rm SFR}$ is less accurate than Hα-$\Sigma_{\rm SFR}$. However if $\Delta{\rm SFE}<\Delta f_{\rm H_2}$, ΔSFE could be underestimated and the statement might not be true if accurate measurements of Hα-$\Sigma_{\rm SFR}$ were possible. Therefore, galaxies with a large fraction of fuel-driven spaxels (i.e., $\Delta{\rm SFE}<\Delta f_{\rm H_2}$) might have a smaller fraction if this study was not dependent on D4000-$\Sigma_{\rm SFR}$ measurements.

To check how this bias might alter my results, I calculate the fraction of fuel-driven spaxels both with the combined Hα+D4000 $\Sigma_{\rm SFR}$ values, as well as those which only have Hα-$\Sigma_{\rm SFR}$. Four galaxies do not have at least 20 spaxels with viable Hα-$\Sigma_{\rm SFR}$, so cannot be part of the test. Both fractions are included in Table 4.3 and discussed in the text, with additional comparison provided here. Figure 4.19 directly compares the fuel fraction determined from only Hα spaxels to the fuel fraction when both Hα and D4000 spaxels are included. Ideally these two values would be equal and all galaxies would lie on the line of equality, but as expected there is some difference between the two. Difference between the two fuel fractions can be acceptable so long as it does not change which mechanism predominantly drives star formation. To better demonstrate this distinction I highlight regions where both fractions agree: that star formation is efficiency drive (red), fuel-driven (blue), or both (grey). Only one galaxy is outside these acceptable regions: 8616-9101, which is efficiency-driven when both Hα and D4000 spaxels are included, but fuel-driven when only Hα spaxels are considered. 8616-9101 is an interesting case given spaxels that D4000-$\Sigma_{\rm SFR}$ are

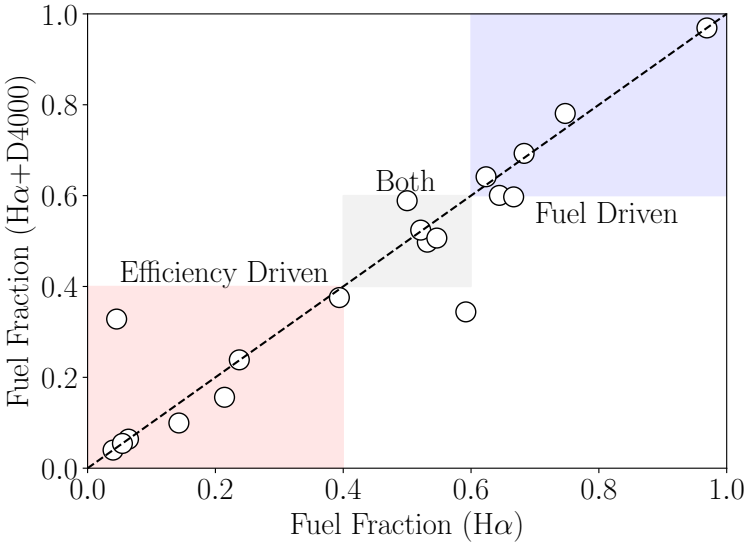

Figure 4.19: The fuel fraction determined from only Hα spaxels compared to the fuel fraction when both Hα and D4000 spaxels are included. Ideally all galaxies would lie on the line of equality, implying that the inclusion of D4000 spaxels does not drastically change my results. But realistically there is scatter about the line of equality as more spaxels are included in the analysis. Difference between the two fuel fractions is alright, so long as it does not change which mechanism predominantly drives star formation. I have highlighted regions that ideally the points should lie within: where both fractions imply star formation is efficiency-driven (red), where both fractions imply star formation is fuel-driven (blue), and where both fractions imply star formation is driven by both (grey). Only one point lies outside these acceptable regions: 8616-9101, which is efficiency-driven when both Hα and D4000 spaxels are included, but fuel-driven when only Hα spaxels are considered.

expected to underestimate ΔSFE and bias towards large fuel fractions, but in this case including D4000 spaxels leads to a smaller fuel fraction. Considering only one galaxy changes dominant mechanism, this assures that the main results of this work are not dependent on the inclusion of D4000-$\Sigma_{\rm SFR}$ values.

4.5 Summary

This chapter presented MaNGA+ALMA CO observations of 31 merging galaxies from the ALMaQUEST merger sample in order to study whether interaction-induced star formation is driven primarily by enhancements in SFE or gas fraction. The sample includes 14 post-merger galaxies and 17 pairs with projected separations up to 90 kpc. The rSFMS, rKS, and rMGMS of the merger galaxies are compared to relatively isolated galaxies in the ALMaQUEST survey. Although the ensemble of spaxels in the post-mergers, pairs and isolated galaxies have similar scaling relations (Figure 4.4), significant variation can be seen when examining the resolved relations for individual mergers (see Figures 4.5, 4.6, and 4.7).

In order to better understand the spatial variations in each merger, I construct maps of offsets from these resolved relations ($\Delta\Sigma_{\rm SFR}$, ΔSFE, and $\Delta f_{\rm H_2}$). By directly comparing ΔSFE and $\Delta f_{\rm H_2}$ for all spaxels with enhanced star formation, I can identify whether the star formation is driven by an large gas reservoir, or an enhanced efficiency at which gas is converted into stars. I find that when all spaxels in all galaxies are considered together, $f_{\rm H_2}$ and SFE contribute equally to enhanced star formation (Figure 4.9).

However, the approximately equal importance of fuel and efficiency across the entire sample is misleading. When examining galaxies on an individual basis, a different picture emerges. Some mergers are clearly dominated by either efficiency or fuel-driven star formation, with all points lying in one regime of Figure 4.11. About a third of the merger sample is predominantly efficiency-driven, a third is fuel-driven, and a third is driven equally by both. I investigate whether the dominant star formation mechanism might be correlated with global galaxy properties (SFR, $\rm M_\star$, $\rm M_{H_2}$, $f_{\rm H_2}$, ΔSFR), and find only an unsurprising correlation with fuel-driven star formation and large gas fractions.

The driving star formation mechanism does not depend on the stage of an interaction either. The percentage of fuel-driven post-mergers is somewhat more than the percentage of fuel-driven pair galaxies. But fuel fraction does not correlate with

other indicators of interaction stage, such as projected separation and tidal connections (Figure 4.13). The progression of the interaction does not lead to clear evolution in the fuel fraction, which implies the unique properties of the progenitors are more influential on which mechanisms powers enhancements in star formation.

Section 4.3.2.1 investigates how the dominant star-forming mechanism leads to variations on a spatial scale. Radial profiles of $\Delta\Sigma_{\rm SFR}$ for the merger sample are shown in Figure 4.14, separated into three categories based on fuel fraction. "Fuel-driven" mergers (with fuel fractions > 0.6) have relatively distinct $\Delta\Sigma_{\rm SFR}$ profiles compared to "efficiency-driven" mergers (fuel fraction < 0.4), which often have stronger and more extended $\Delta\Sigma_{\rm SFR}$ enhancements. Thus a range of fuel fractions in mergers could explain the diversity of star formation offset profiles seen in Chapter 2 as well as in other merger studies (Thorp et al., 2019; Pan et al., 2019; Steffen et al., 2021).

The range of $\Delta\Sigma_{\rm SFR}$ profiles in these three categories implies more internal variation within a galaxy than a single fuel fraction can capture. Figure 4.15 demonstrates this variation in the dominant mechanism within a galaxy by presenting 2D maps of ΔSFE$-\Delta f_{\rm H_2}$, indicating which offset parameter is largest in each spaxel. Even galaxies that are driven predominantly by a single mechanism on a global scale can exhibit internal deviations from the dominant mechanism. For example, both efficiency and fuel-driven mergers tend to have $\Delta f_{\rm H_2}>\Delta$SFE in their centre, confirming that enhanced amounts of molecular gas are crucial to merger-induced central starbursts, even if the rest of the galaxy has efficiency-driven star formation.

The work presented here is the first to investigate the resolved molecular gas and star formation properties for a relatively large set of mergers spanning a wide range of sSFRs and stages of interaction, with the explicit goal of understanding how gas and star formation evolve with an interaction. This work adds to the growing evidence that, despite following overall scaling relationships, galaxies are diverse in their details. Moreover, I have shown that in addition to diversity on a global scale (i.e. some mergers have their star formation driven by fuel, others by efficiency), there is significant internal variation on kpc-scales concerning what powers star formation.

Chapter 5

Conclusions

This thesis presents a multifaceted analysis of galaxy mergers, revealing how major interactions impact star formation, metallicity, molecular gas, and star formation efficiency on a kpc-scale. Utilizing the largest IFS merger sample to date exposes a range of merger properties; throughout my analysis I propose innovative approaches to try to comprehend this diversity. This chapter provides an overview of the main conclusions presented in this thesis, as well as what they mean for future resolved merger studies.

5.1 Diversity of resolved star formation and metallicity properties of mergers

The growth of IFS galactic surveys has paved the way for statistical analysis of the kpc-scale impact of galaxy interactions. Within the CALIFA survey, there are ∼100 galaxy mergers that have relatively flat gas-phase metallicity gradients compared to non-interacting CALIFA galaxies, implying gaseous inflows homogenize the galaxy's metallicity (Sánchez et al., 2014). However, the metallicity measured in a central aperture was found to be similar to that in non-interacting galaxies, despite the much stronger central starburst (Barrera-Ballesteros et al., 2015). Instead CALIFA mergers had lower metallicity in an outer aperture, and regular star formation. Merger studies using the MaNGA survey found different results, with both galaxies at apocentre passage and coalescence exhibiting enhanced star formation at large radii (Thorp et al., 2019; Pan et al., 2019). These works were completed when the MaNGA survey was only partially complete, using a sample of ∼50 post-mergers and ∼200 interacting pairs. The greater sample size compared to CALIFA allows MaNGA studies to investigate how different merger properties impact $\Sigma_{\rm SFR}$. For example, mass ratio

can impact both the strength of the central starburst, and the possible presence of enhanced star formation at large radii (Steffen et al., 2021).

Chapter 2 examines merger radial profiles using MaNGA data, much as was completed in Thorp et al. (2019); Pan et al. (2019); Steffen et al. (2021), but with two key differences. First, this chapter is the first merger study to use the complete MaNGA dataset, resulting in a merger sample 8 times larger than that in previous publications. Secondly, my work investigates gas-phase metallicity profiles along with $\Sigma_{\rm SFR}$, analysis which had previously only been done with the much smaller CALIFA survey.

My work examines radial profiles of $\Delta\Sigma_{\rm SFR}$ and ΔO/H for 400 post-mergers and 1523 interacting pairs. Such as was found for isolated galaxies (Ellison et al., 2018a; Liu et al., 2018; Medling et al., 2018; Wang et al., 2019), the strength of the central starburst in post-mergers and pairs depends on the global ΔSFR. However, even within constrained bins of ΔSFR there is significant variability in merger $\Delta\Sigma_{\rm SFR}$ and ΔO/H profiles. Although a spaxel with enhanced star formation ($+\Delta\Sigma_{\rm SFR}$) is more likely to have diluted metallicity ($-\Delta$O/H), such is not true for all spaxels. For example, plenty of post-merger with $\Delta\Sigma_{\rm SFR} \leq 0$ at most radii (as is expected for their low ΔSFR values) can still have ΔO/H ≤ 0 continuously across the galaxy.

The larger size of my merger sample allows for a deeper investigation of how different properties impact merger parameters, which is particularly important for galaxy pairs where various factors of an interaction can impact changes in star formation, including but not limited to interaction stage (often quantified by the separation between pairs, i.e., Patton et al. 2020), orbital parameters (Di Matteo et al., 2007; D'Onghia et al., 2010; Moreno et al., 2015), mass ratio between constituents (Cox et al., 2006, 2008; Lotz et al., 2010b), and gas fraction of the interacting disk (Bournaud et al., 2011; Perez et al., 2011; Scudder et al., 2015; Fensch et al., 2017). Although on average galaxy pairs in my sample with smaller projected separation have stronger central starbursts than those further apart, there are still many pairs with large r_p that have just as strong a central enhancement as those very close to each other. This, in conjunction with the lack of correlation between r_p and extended star formation, motivates the examination of other interaction parameters.

When we examine radial profiles of $\Delta\Sigma_{\rm SFR}$ binned by mass ratio, we find that galaxies of equal mass or smaller than their companion have the strongest central starbursts. This has been noted in previous resolved pair studies (Steffen et al., 2021) and simulations (Moreno et al., 2015, 2021). My work uniquely confirms that this result is consistent for galaxies on and above the SFMS, meaning a boost in

the central star formation activity occurs regardless of how globally enhanced star formation becomes. As predicted by Moreno et al. (2015, 2021), we find galaxies with the smallest mass ratios have suppressed star formation at large radii. Unlike those results, we find galaxies with the largest mass ratio ($\mu > 4$) can also have outer $\Sigma_{\rm SFR}$ deficits. Interestingly, these galaxies also have metallicity dilutions in their outskirts, once again highlighting that dilutions in metallicity do not always correspond to $\Sigma_{\rm SFR}$ enhancements.

Results from this chapter expose just how diverse the resolved properties of mergers can be, and thus the difficulty in discerning how different interaction characteristics impact these properties. Although the range of $\Delta\Sigma_{\rm SFR}$ and ΔO/H behaviour is an interesting result in its own right, there is hope that future studies could begin to decipher which galaxy/interaction properties are most important to shaping $\Delta\Sigma_{\rm SFR}$ and ΔO/H profiles. Recent MaNGA studies have utilized Random Forest regression models to extricate the dependencies of multiple inter-connected quantities, revealing what parameters predominantly drive galaxy quenching (Bluck et al., 2020b, 2022) or scatter in the rSFMS for isolated galaxies (Ellison et al., 2020b; Baker et al., 2022). Techniques like these will be crucial to disentangle what merger properties predominantly drives resolved star formation and metallicity properties, when so many factors are at play.

Synergy with galaxy simulations will also be crucial at this step, since many properties of a galaxy interaction are unobservable based on current techniques or unavailable in current merger surveys. For example, Moreno et al. (2021) is able to examine the resolved star-forming and gas properties of interacting galaxies with various orbital parameters, revealing that the dependence of the central starburst strength on μ stems from the larger galaxy in an interaction having lowered central SFEs (not necessarily a lack of inflowing molecular gas). The amount of resolved changes that occur also depends heavily on orbital parameters, with near-retrograde orbits exhibiting milder changes to radial profiles as the interaction progresses whereas near-polar orbits have far more drastic changes in radial structure. Although some global studies have attempted to discern how spin orbit orientation impact merger-induced star formation (e.g., Mesa et al. 2014), no follow-up of the resolved star-forming properties of such mergers has been completed. Even if such a study was accomplished, simulations have demonstrated that the full interaction history can have a major impact on resolved properties, such as whether at first pericentric passage the two galaxy discs interpenetrate one another, and that information will never be observable (Moreno

et al., 2015, 2021). Synergy between observations and simulations will be necessary to account for the shortcomings of both, and help us construct a complete picture of the merging process.

5.2 Recovering accurate asymmetry and concentration measurements for observations of varying quality

To address some of the difficulty analyzing resolved spectroscopic data, as discussed in Chapter 2, I propose the use of non-parametric morphology measurements as an alternative analysis tool. In Chapter 3 I test the validity of non-parametric indices asymmetry and concentration on IFS quality data, by measuring both indices on simulated galaxies before and after adding layers of observational realism. By doing so I offer realistic limitations to asymmetry and concentration use, and design procedures through which these metrics could be applied to marginal astronomical data.

Specifically, I used stellar mass maps from the IllustrisTNG100-1 and Illustris-1 simulation to test whether the intrinsic values of concentration and asymmetry (measured directly from the simulation stellar mass particle maps) are recovered after the application of measurement uncertainty and PSF (impacting resolution). I degrade simulated stellar mass maps to a wide range of S/N and PSF values, such that I can discern where the calculation of these metrics breaks down.

Asymmetry measurements require some correction for noise contribution, otherwise the measured asymmetry will be overestimated from a factor of 2 to 10 (see Figure 3.2). The most commonly used method of correcting for noise contribution to asymmetry underestimates the final asymmetry, and is particularly bad at $S/N < 100$, as pointed out in Figure 3.3 and in previous works (Conselice et al., 2000). The S/N dependence of accurate asymmetry measurements has posed a significant problem to studies that have applied asymmetry measurements outside of photometric data (in particular, to observations of galactic gas and dust, Bendo et al. 2007; Giese et al. 2016; Reynolds et al. 2020). I recommend an alternative correction method of subtracting $A_{\rm noise}/1.2$ from the observed asymmetry, which reduces the systematic bias and achieves asymmetry differences less than 0.05 by $S/N \sim 25$. I also provide an alternative correction using a fit to observed asymmetry and signal-to-noise (see Equation 3.8), which removes the bias in asymmetry created by noise as low as $S/N \sim 5$. Accuracy of correction to this degree would be necessary for a MaNGA stellar mass surface density map, which by my calculations used in this procedure

would have a $S/N \sim 5$.

Although concentration is not effected by measurement noise, degrading the resolution of an image impacts both concentration and asymmetry measurements. I create a fit relationship between the observed asymmetry/concentration and resolution (see Equations 3.11 and 3.14, respectively) that can accurately replicate the intrinsic values. I also discuss how asymmetry can be simultaneously corrected for resolution and noise, both with more traditional noise correction techniques and a fit that accounts for both S/N and resolution.

I confirm that the noise and resolution corrections work equally well on an unseen set of TNG galaxies (confirming they are not overfit to the training data) and a set of Illustris galaxies (confirming these corrections can be applied to different physical models). Figure 3.15 provides a detailed summary of these tests. The suggested asymmetry and concentration corrections work well between different simulated datasets, but their application to observed data will be less trivial. Contemporary studies have demonstrated just how crucial applying observational realism to simulations is to compare results to the real world (Bottrell et al., 2017a,b; Huertas-Company et al., 2019; Bottrell et al., 2019b; Zanisi et al., 2020; Ferreira et al., 2020). This work does not provide a blanket procedure that could be applied to observed data, but rather a procedure to check what kind of correction is necessary, and how to go about constructing a fit correction to asymmetry and concentration.

5.3 What powers merger-induced star formation?

Though studies of the resolved star formation properties have sky-rocketed over the last decade, there is a significant lack of corresponding studies of the resolved molecular gas properties of galaxy mergers. This has left one key question unanswered: is merger-triggered star formation facilitated by an abundance of molecular gas fuel or enhanced star formation efficiencies? Until recently such analysis was limited to case-studies, which revealed significant diversity of SFE on a resolved scale (Tomičić et al., 2018; Bemis & Wilson, 2019). In Chapter 4, I present the largest study of resolved star formation and molecular gas properties in galaxy mergers, providing insights into what drives resolved changes in star formation for a variety of merger stages.

I introduce spatially resolved measurements of CO emission collected with ALMA for 20 merging galaxies (either pairs or post-mergers) selected from the MaNGA

survey. Eleven additional merging galaxies are selected from the ALMaQUEST survey, resulting in a set of 31 mergers at various stages of interaction and covering a broad range of star formation rates (SFR). I use this sample to investigate galaxy-to-galaxy variations in the resolved Kennicutt-Schmidt relation, (rKS: Σ_{H_2} vs. Σ_{SFR}), the resolved molecular gas main sequence (rMGMS: $\Sigma_\star$ vs. Σ_{H_2}), and the resolved star-forming main sequence (rSFMS: $\Sigma_\star$ vs. Σ_{SFR}). Post-mergers, pairs, and isolated galaxies have considerable overlap in all three relations, although on a galaxy-to-galaxy basis there is significant variation.

I quantify offsets from these resolved relations to determine if star formation rate, molecular gas fraction, and/or star formation efficiency (SFE) is enhanced in different regions of an individual galaxy. By comparing offsets in all three parameters I am able to discern whether gas fraction or SFE powers an enhanced Σ_{SFR}. When all spaxels are considered together (grouped as either non-interacting, pair, or post-merger), f_{H_2} and SFE appear to contribute equally to enhanced Σ_{SFR}. When examining individual galaxies a new picture emerges; some are clearly dominated by either fuel or efficiency-driven star formation, while others are driven by a combination of both. In fact the merger sample is relatively evenly split by fuel-driven, efficiency-driven, and evenly driven star formation.

The primary star formation mechanism does not depend on the stage of galaxy interaction, besides there being a slightly larger percentage of fuel-driven post-mergers than pairs. Figure 4.13 demonstrates how projected separation between pairs has no impact on the measured fraction of fuel-driven spaxels, implying the unique properties of merger progenitors are more influential on the star formation mechanisms. The fuel fraction can impact $\Delta\Sigma_{SFR}$ profiles; efficiency-driven mergers are more likely to have strong and continuous star formation enhancements, whereas fuel-driven mergers have centrally concentrated boosts in $\Delta\Sigma_{SFR}$ that fall off with radius. Therefore, whether a merger is fuel or efficiency-driven could explain the significant diversity of $\Delta\Sigma_{SFR}$ profiles noted in Chapter 2.

Even though I assign each merger an overall fuel fraction measurement, that does not mean different mechanisms could not be at play within a galaxy. For each merger I create maps of the difference between ΔSFE and Δf_{H_2} , indicating within each spaxel which has a higher value (full maps are provided in Appendix A.4). Even galaxies that are predominantly driven by a single mechanism on a global scale demonstrate significant internal variations. In fact, most mergers regardless of global fuel fraction have $\Delta f_{H_2} > \Delta$SFE in the centre. This supports a model where the

inflow of molecular gas creates the central starbursts so commonly seen in mergers. Efficiency-driven regimes are often concentrated in spiral arms and tidal tails. Higher-resolution studies of molecular gas and star formation have found that spiral arms have different slopes in resolve scaling relations, which agrees with this result (Pessa et al., 2021). Most extragalactic surveys of gas and star formation with high enough resolution to delineate spiral arm features, like the PHANGS survey, have not focused on investigating mergers in particular. My results from ALMaQUEST motivate a 100pc - scale study of merger gas and star formation, to discern whether the variations in the dominate star forming mechanism are unique to mergers or stem from secular environmental structures like spiral arms and bars.

5.4 Future work

As I have discussed, there are multiple follow-up projects motivated from the main results of this thesis. Chapter 2 demonstrated the diversity of $\Delta\Sigma_{\rm SFR}$ and ΔO/H profiles for mergers, and the application of non-linear regression with an artificial neural network as has been used in previous resolved studies could begin to disentangle what drives this variation. Chapter 3 presents a route through which accurate asymmetry and concentration measurements could be made for a variety of data sets. This study has motivated more scrupulous comparisons between the asymmetry of HI and H_2 observations in the Virgo Environment Traced in CO (VERTICO) survey (Roberts et al. in prep), and the asymmetry correction I proposed are being used for a set of galaxy and quasar host observations with the Hyper Suprime-Cam (HSC) on the Subaru telescope (Tang, private communication).

Most of my future work will stem from results in Chapter 4. Indeed, that work focused almost entirely on what drove *enhanced* star formation in mergers, but left analysis of $\Delta\Sigma_{\rm SFR} < 0$ dex spaxels untouched. I will next investigate what drives suppressed star formation in galaxy mergers: a deficit in molecular gas, or a lowered star formation efficiency. Many mergers in the ALMaQUEST sample that had fuel-driven central starbursts had a deficit in star formation at large radii. One could easily postulate that a lack of gas is the cause of that suppression, as the majority of the gas reservoir is funnelled into a central starburst. However many galaxies have heightened SFEs at large radii to fuel star formation despite the modest gas supply (see Figure 4.15 as an example). Thus, there is still much to investigate concerning the source of diminished star formation in these chaotic systems. With a complete

picture of what drives both suppressed and enhanced star formation in mergers, I can then discern if any trends are unique to the merger stage or if similar results are found for the non-interacting ALMaQUEST sample.

There is also the question of how AGN might impact the dominant star-forming driver in a galaxy. Observations have regularly confirmed that mergers can trigger AGN, although they are not necessarily the only phenomena that can do so (Alonso et al., 2007; Satyapal et al., 2014; Goulding et al., 2018; Ellison et al., 2019). The combined effects of a nuclear starburst and AGN feedback could be a significant route through which galaxies transition from the blue, star-forming population to a "red-and-dead" passive population (often referred to as "quenching", Di Matteo et al. 2005; Hopkins et al. 2008; Somerville et al. 2008; Quai et al. 2021).

There is significant observational evidence indicating a connection between AGN and galaxy quenching. Galaxies that host AGN, as identified with both optical and radio data, tend to have lower global star formation rates compared to the average star-forming galaxy (Ellison et al., 2016; Sánchez et al., 2018). The quenched galaxy fraction also correlates with bulge strength (Bluck et al., 2014, 2020a) and black hole mass (Terrazas et al., 2016, 2017; Piotrowska et al., 2022), further linking black hole growth and quenching. Yet global studies of low redshift galaxies have demonstrated that AGN hosts have similar or higher molecular (Saintonge et al., 2017; Shangguan et al., 2020) and total (Vito et al., 2014; Shangguan et al., 2018) gas mass compared to galaxies without AGN. If AGN are strongly correlated with quenching, why then do we not observe the expected impact on the gas reservoir?

Spatially resolved studies have revealed that this contradiction may result from the scale of AGN feedback, which is only a few kpc (Karouzos et al., 2016; Kang & Woo, 2018). After all, observational evidence suggests quenching may occur from the inside out based on $\Sigma_{\rm SFR}$ profiles (Ellison et al., 2018a; Sánchez et al., 2018; Medling et al., 2018). Recent IFS studies have revealed that although AGN can exist in galaxies with regular global gas fractions, the presence of an AGN leads to lowered gas fractions in the centre of the galaxy (Sánchez et al., 2018; Ellison et al., 2021c). Contrary to that result, the only merger in Chapter 4 that hosts an AGN (9195-3703) has elevated gas fractions in the centre of the galaxy. Figure 5.1 shows the rMGMS for the merger AGN host (left) compared to a non-interacting galaxy from ALMaQUEST that hosts an AGN. The spaxels associated with AGN emission (red) for the non-interacting galaxy are shifted far below the rMGMS (shown in grey), whereas the post-merger AGN spaxels are either on or boosted above the rMGMS, indicating heightened $f_{\rm H_2}$

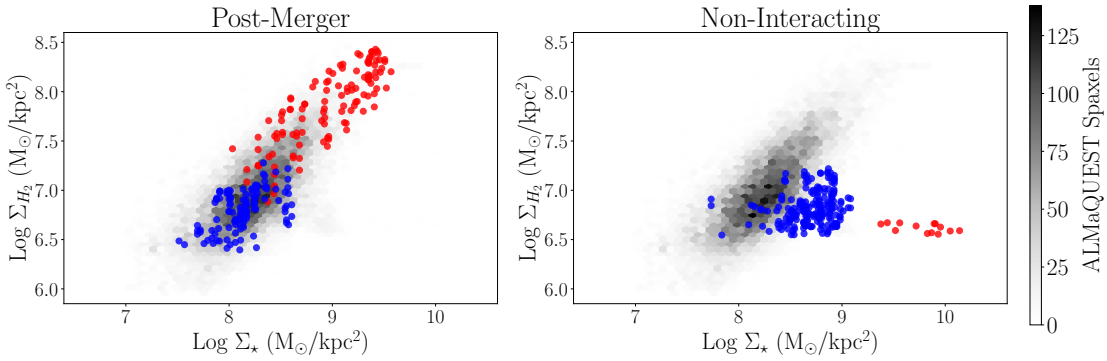

Figure 5.1: Molecular gas surface density versus stellar mass surface density for star-forming(blue) and AGN(red) pixels in a post-merger and a non-interacting galaxy taken from the archival data of ALMaQUEST. The resolved molecular gas main sequence for isolated ALMaQUEST galaxies is shown in grey. The non-interacting galaxy has suppressed gas fractions in the AGN pixels, as has been seen with other resolved molecular gas studies. However, in the post-merger, the gas fractions in AGN pixels range from regular to enhanced. This implies the relationship between an AGN and nuclear molecular gas is different in this post-merger than would be expected from a non-interacting system.

in the nuclear region.

There has yet to be any study confirming if AGN in mergers also cause nuclear gas depletion, or if merger induced inflows keep gas fractions high despite AGN feedback. I submitted an ALMA cycle 9 proposal to expand ALMaQUEST with a set of galaxy mergers that contain an AGN to investigate how AGN impact local gas reservoirs. My proposal was accepted with priority grade C. In cycle 9, 1769 proposals were submitted requesting over 27,900 hours on the 12-m array, compared to the 4300 hours available (an oversubscription factor of 6.5). That my proposal was one of few to be accepted given the oversubscription demonstrates just how important an investigation into the resolved effects of AGN and mergers combined is to our overall understanding of the evolution of star formation.

Large, resolved mergers studies are still a relatively new frontier, and there remains a critical necessity to create multiwavelength follow-ups to IFS studies. Nevertheless, we are at the precipice of understanding the resolved impact of mergers for a broad range of galactic properties. But the more we uncover, the more diversity of merger behaviour we find, which clouds our understanding of what properties are important to resolved changes. As we seek more observations to better understand the role of mergers in galactic evolution, we must continue to innovate new approaches to

analyzing large resolved studies.

Bibliography

Abazajian K. N., et al., 2009, The Astrophysical Journal Supplement Series, 182, 543

Abdurro'uf et al., 2022, The Astrophysical Journal Supplement Series, 259, 35

Abgrall H., Le Bourlot J., Pineau Des Forets G., Roueff E., Flower D. R., Heck L., 1992, Astronomy and Astrophysics, 253, 525

Abraham R., Bergh S. v. d., Nair P., 2003, The Astrophysical Journal, 588, 218

Accurso G., et al., 2017, Monthly Notices of the Royal Astronomical Society, 470, 4750

Ackermann S., Schawinski K., Zhang C., Weigel A. K., Dennis Turp M., 2018, Monthly Notices of the Royal Astronomical Society, 479, 415

Agostino C. J., Salim S., 2019, The Astrophysical Journal, 876, 12

Allen J. T., et al., 2015, Monthly Notices of the Royal Astronomical Society, 446, 1567

Alonso-Herrero A., Rosales-Ortega F. F., Sánchez S. F., Kennicutt R. C., Pereira-Santaella M., Díaz I., 2012, Monthly Notices of the Royal Astronomical Society: Letters, 425, L46

Alonso M. S., Tissera P. B., Coldwell G., Lambas D. G., 2004, Monthly Notices of the Royal Astronomical Society, 352, 1081

Alonso M. S., Lambas D. G., Tissera P., Coldwell G., 2007, Monthly Notices of the Royal Astronomical Society, 375, 1017

Alonso S., Mesa V., Padilla N., Lambas D. G., 2012, Astronomy & Astrophysics, 539, A46

Arp H., 1966, Astrophysical Journal Supplement Series, 14, 1

Baes M., et al., 2020, Astronomy & Astrophysics, 641, A119

Baker W. M., Maiolino R., Bluck A. F. L., Lin L., Ellison S. L., Belfiore F., Pan H.-A., Thorp M., 2022, Monthly Notices of the Royal Astronomical Society, 510, 3622

Baldwin J. A., Phillips M. M., Terlevich R., 1981, Publications of the Astronomical Society of the Pacific, 93, 5

Banerji M., et al., 2010, Monthly Notices of the Royal Astronomical Society, 406, 342

Barnes J. E., 1988, Astrophysical Journal, 331, 699

Barnes J. E., Hernquist L. E., 1991, The Astrophysical Journal, 370, L65

Barnes J. E., Hernquist L., 1992, Nature, 360, 715

Barnes J. E., Hernquist L., 1996, Astrophysical Journal, 471, 115

Barrera-Ballesteros J. K., et al., 2015, Astronomy & Astrophysics, 579, A45

Barrera-Ballesteros J. K., et al., 2016, Monthly Notices of the Royal Astronomical Society, 463, 2513

Barrera-Ballesteros J. K., Sánchez S. F., Heckman T., Blanc G. A., Team T. M., 2017, The Astrophysical Journal, 844, 80

Barrera-Ballesteros J. K., et al., 2018, The Astrophysical Journal, 852, 74

Barrera-Ballesteros J. K., et al., 2020, Monthly Notices of the Royal Astronomical Society, 492, 2651

Barrera-Ballesteros J. K., et al., 2021, Monthly Notices of the Royal Astronomical Society, 18, 1

Barton Gillespie E. B., Geller M. J., Kenyon S. J., 2003b, The Astrophysical Journal, 582, 668

Barton Gillespie E., Geller M. J., Kenyon S. J., 2003a, The Astrophysical Journal, 582, 668

Barton E. J., Geller M. J., Kenyon S. J., 2000, The Astrophysical Journal, 530, 660

Baugh C. M., Cole S., Frenk C. S., 1996, Monthly Notices of the Royal Astronomical Society, 283, 1361

Belfiore F., et al., 2016, Monthly Notices of the Royal Astronomical Society, 461, 3111

Belfiore F., et al., 2017, Monthly Notices of the Royal Astronomical Society, 469, 151

Belfiore F., et al., 2018, Monthly Notices of the Royal Astronomical Society, 477, 3014

Bell E. F., 2008, The Astrophysical Journal, 682, 355

Bell E. F., et al., 2004, The Astrophysical Journal, 608, 752

Bell E. F., Monachesi A., Harmsen B., De Jong R. S., Bailin J., Radburn-Smith D. J., D'souza R., Holwerda B. W., 2017, The Astrophysical Journal Letters, 837

Bemis A., Wilson C. D., 2019, The Astronomical Journal, 157, 18

Bendo G. J., et al., 2007, Monthly Notices of the Royal Astronomical Society, 380, 1313

Bershady M. A., Jangren A., Conselice C. J., 2000, The Astronomical Journal, 119, 2645

Bershady M. A., Verheijen M. A. W., Swaters R. A., Andersen D. R., Westfall K. B., Martinsson T., 2010, The Astrophysical Journal, 716, 198

Bertola F., Capaccioli M., 1975, The Astrophysical Journal, 200, 439

Bickley R., Bottrell C., Hani M. H., Ellison S. L., Teimoorinia H., Moo Yi K., Wilkinson S., 2021, Monthly Notices of the Royal Astronomical Society, 504, 372

Bickley R. W., Ellison S. L., Patton D. R., Bottrell C., Gwyn S., Hudson M. J., 2022, Monthly Notices of the Royal Astronomical Society, 514, 3294

Bigiel F., Leroy A., Walter F., Brinks E., De Blok W. J. G., Madore B., Thornley M. D., 2008, The Astronomical Journal, 136, 2846

Blanc G. A., et al., 2013, The Astronomical Journal, 145, 138

Blanton M. R., Kazin E., Muna D., Weaver B. A., Price-Whelan A., 2011, The Astronomical Journal, 142, 31

Bloom J. V., et al., 2017, Monthly Notices of the Royal Astronomical Society, 465, 123

Bluck A. F. L., Mendel J. T., Ellison S. L., Moreno J., Simard L., Patton D. R., Starkenburg E., 2014, Monthly Notices of the Royal Astronomical Society, 441, 599

Bluck A. F. L., et al., 2019, Monthly Notices of the Royal Astronomical Society, 485, 666

Bluck A., Maiolino R., Sánchez S., Ellison S., Thorp M., Piotrowska J., Teimoorinia H., Bundy K., 2020a, Monthly Notices of the Royal Astronomical Society, 492, 96

Bluck A. F., et al., 2020b, Monthly Notices of the Royal Astronomical Society, 499, 230

Bluck A. F. L., Maiolino R., Brownson S., Conselice C. J., Ellison S. L., Piotrowska J. M., Thorp M. D., 2022, Astronomy & Astrophysics, 659, A160

Blumenthal G. R., Faber S. M., Primack J. R., Rees M. J., 1984, Nature, 311, 517

Bolatto A. D., Jackson J. M., Ingalls J. G., 1999, The Astrophysical Journal, 513, 275

Bolatto A. D., Wolfire M., Leroy A. K., 2013, Annual Review of Astronomy and Astrophysics, 51, 207

Bolatto A. D., et al., 2017, The Astrophysical Journal, 846, 159

Bolton A. S., et al., 2012, The Astronomical Journal, 144, 144

Bothwell M. S., Maiolino R., Kennicutt R., Cresci G., Mannucci F., Marconi A., Cicone C., 2013, Monthly Notices of the Royal Astronomical Society, 433, 1425

Bothwell M. S., Maiolino R., Cicone C., Peng Y., Wagg J., 2016, Astronomy & Astrophysics, 595, 48

Bottrell C., Torrey P., Simard L., Ellison S. L., 2017a, Monthly Notices of the Royal Astronomical Society, 467, 2879

Bottrell C., Torrey P., Simard L., Ellison S. L., 2017b, Monthly Notices of the Royal Astronomical Society, 467, 1033–1066

Bottrell C., Simard L., Mendel J. T., Ellison S. L., 2019a, Monthly Notices of the Royal Astronomical Society, 486, 390

Bottrell C., et al., 2019b, Monthly Notices of the Royal Astronomical Society, 490, 5390

Bournaud F., Jog C. J., Combes F., 2005, Astronomy & Astrophysics, 437, 69

Bournaud F., et al., 2011, The Astrophysical Journal, 730, 4

Bower R. G., Lucey J. R., Ellis R. S., 1992, Monthly Notices of the Royal Astronomical Society, 254, 601

Boylan-Kolchin M., Springel V., White S. D., Jenkins A., Lemson G., 2009, Monthly Notices of the Royal Astronomical Society, 398, 1150

Braine J., Combes F., 1993, Astronomy & Astrophysics, 269, 7

Brinchmann J., Charlot S., White S. D. M., Tremonti C., Kauffmann G., Heckman T., Brinkmann J., 2004, Monthly Notices of the Royal Astronomical Society, 351, 1151

Brodie J. P., et al., 2014, The Astrophysical Journal, 796, 52

Brooks A. M., Governato F., Booth C. M., Willman B., Gardner J. P., Wadsley J., Stinson G., Quinn T., 2007, The Astrophysical Journal, 655, L17

Bryant P. M., Scoville N. Z., 1999, The Astronomical Journal, 117, 2632

Bundy K., et al., 2015, The Astrophysical Journal, 798, 7

Bustamante S., Sparre M., Springel V., Grand R. J., 2018, Monthly Notices of the Royal Astronomical Society, 479, 3381

Calura F., Pipino A., Chiappini C., Matteucci F., Maiolino R., 2009, Astronomy & Astrophysics, 504, 373

Calzetti D., 2013, in Falcón-Barroso J., Knapen J. H., eds, , Secular Evolution of Galaxies. p. 419

Cano-Díaz M., et al., 2016, The Astrophysical Journal, 821, L26

Cano-Díaz M., Ávila-Reese V., Sánchez S. F., Hernández-Toledo H. M., Rodríguez-Puebla A., Boquien M., Ibarra-Medel H., 2019, Monthly Notices of the Royal Astronomical Society, 488, 3929

Capelo P. R., Volonteri M., Dotti M., Bellovary J. M., Mayer L., Governato F., 2015, Monthly Notices of the Royal Astronomical Society, 447, 2123

Cappellari M., et al., 2011, Monthly Notices of the Royal Astronomical Society, 413, 813

Cardelli J. A., Clayton G. C., Mathis J. S., 1989, The Astrophysical Journal, 345, 245

Carroll B. W., Ostlie D. A., 2007, An Introduction to Modern Astrophysics, 2 edn. Pearson: Addison Wesley, San Francisco

Casasola V., Bettoni D., Galletta G., 2004, Astronomy & Astrophysics, 422, 941

Casteels K. R. V., et al., 2014, Monthly Notices of the Royal Astronomical Society, 445, 1157

Cattaneo A., Blaizot J., Devriendt J., Guiderdoni B., 2005, Monthly Notices of the Royal Astronomical Society, 364, 407

Ceverino D., Dekel A., Tweed D., Primack J., 2015, Monthly Notices of the Royal Astronomical Society, 447, 3291

Chabrier G., 2003, Publications of the Astronomical Society of the Pacific, 115, 763

Chandrasekhar S., 1943, Astrophysical Journal, 97, 225

Cheng T. Y., et al., 2020, Monthly Notices of the Royal Astronomical Society, 493, 4209

Chiosi C., Carraro G., 2002, Monthly Notices of the Royal Astronomical Society, 335, 335

Chisholm J., Tremonti C., Leitherer C., 2018, Monthly Notices of the Royal Astronomical Society, 481, 1690

Chown R., et al., 2019, Monthly Notices of the Royal Astronomical Society, 484, 5192

Cisternas M., et al., 2011, The Astrophysical Journal, 726, 57

Clements D. L., Sutherland . W. J., Mcmahon R. G., Saunders W., 1996, Monthly Notices of the Royal Astonomical Society, 279, 477

Cole S., Lacey C. G., Baugh C. M., Frenk C. S., 2000, Monthly Notices of the Royal Astronomical Society, 391, 168

Colombo D., et al., 2018, Monthly Notices of the Royal Astronomical Society, 475, 1791

Combes F., Prugniel P., Rampazzo R., Sulentic J., 1994, Astronomy and Astrophysics, 281, 725

Conselice C. J., 2003, Astrophysical Journal Supplement Series, 147, 1

Conselice C. J., 2006, The Astrophysical Journal, 638, 686

Conselice C. J., 2014, Annual Review of Astronomy and Astrophysics, 52, 291

Conselice C. J., Bershady M. A., Jangren A., 2000, The Astrophysical Journal, 529, 886

Conselice C. J., Bershady M. A., Dickinson M., Papovich C., 2003, The Astronomical Journal, 126, 1183

Conselice C. J., Yang C., Bluck A. F. L., 2009, Monthly Notices of the Royal Astronomical Society, 394, 1956

Cook R. H. W., Cortese L., Catinella B., Robotham A., 2020, Monthly Notices of the Royal Astronomical Society, 493, 5596

Cooper M. C., Tremonti C. A., Newman J. A., Zabludoff A. I., 2008, Monthly Notices of the Royal Astronomical Society, 390, 245

Cox T. J., Jonsson P., Primack J. R., Somerville R. S., 2006, Monthly Notices of the Royal Astronomical Society, 373, 1013

Cox T. J., Jonsson P., Somerville R. S., Primack J. R., Dekel A., 2008, Monthly Notices of the Royal Astronomical Society, 384, 386

Cresci G., Mannucci F., Curti M., 2019, Astronomy & Astrophysics, 627, 10

Croom S. M., et al., 2012, Monthly Notices of the Royal Astronomical Society, pp no–no

Croom S. M., et al., 2021, MNRAS, 505, 991

Curti M., Mannucci F., Cresci G., Maiolino R., 2020, Monthly Notices of the Royal Astronomical Society, 491, 944

D'Eugenio F., Colless M., Groves B., Bian F., Barone T. M., 2018, Monthly Notices of the Royal Astronomical Society, 479, 1807

D'Onghia E., Vogelsberger M., Faucher-Giguere C.-A., Hernquist L., 2010, The Astrophysical Journal, 725, 353

Daddi E., et al., 2007, The Astrophysical Journal, 670, 156

Dalcanton J. J., 2007, The Astrophysical Journal, 658, 941

Danielson A. L., et al., 2013, Monthly Notices of the Royal Astronomical Society, 436, 2793

Darg D. W., et al., 2010, Monthly Notices of the Royal Astronomical Society, 401, 1043

Davé R., Rafieferantsoa M. H., Thompson R. J., Hopkins P. F., 2017, Monthly Notices of the Royal Astronomical Society, 467, 115

Davis T. A., et al., 2014, Monthly Notices of the Royal Astronomical Society, 444, 3427

De La Calleja J., Fuentes O., 2004, Monthly Notices of the Royal Astronomical Society, 349, 87

De Los Reyes M. A., et al., 2015, The Astronomical Journal, 149, 79

De Propris R., Liske J., Driver S. P., Allen P. D., Cross N. J. G., 2005, The Astronomical Journal, 130, 1516

De Propris R., Conselice C. J., Liske J., Driver S. P., Patton D. R., Graham A. W., Allen P. D., 2007, The Astrophysical Journal, 666, 212

De Rossi M. E., Bower R. G., Font A. S., Schaye J., Theuns T., 2017, Monthly Notices of the Royal Astronomical Society, 472, 3354

De Vaucouleurs G., 1959, Handbuch der Physik, 53, 275

Dey A., et al., 2019, The Astronomical Journal, 157, 168

Di Matteo T., Springel V., Hernquist L., 2005, Nature, 433, 604

Di Matteo P., Combes F., Melchior A. L., Semelin B., 2007, Astronomy & Astrophysics, 468, 61

Di Matteo P., Bournaud F., Martig M., Combes F., Melchior A. L., Semelin B., 2008, Astronomy & Astrophysics, 492, 31

Diaz Trigo M., Carpenter J., Maude L., Miura R., Plunkett A., 2019, ALMA Cycle 7 Proposer's Guide, 2019, doi:10.5281/zenodo.4511962

Dickman R. L., 1978, The Astrophysical Journal Supplement Series, 37, 407

Domínguez Sánchez H., et al., 2019, Monthly Notices of the Royal Astronomical Society, 484, 93

Downes D., Solomon P. M., 1998, The Astrophysical Journal, 507, 615

Draine B. T., 2003, Annual Review of Astronomy and Astrophysics, 41, 241

Dressler A., 1980, The Astrophysical Journal, 236, 351

Driver S. P., et al., 2006, Monthly Notices of the Royal Astronomical Society, 368, 414

Drory N., Bender R., Feulner G., Hopp U., Maraston C., Snigula J., Hill G. J., 2004, The Astrophysical Journal, 608, 742

Elbaz D., et al., 2007, Astronomy & Astrophysics, 468, 33

Ellison S. L., Patton D. R., Simard L., McConnachie A. W., 2008a, The Astronomical Journal, 135, 1877

Ellison S. L., Patton D. R., Simard L., McConnachie A. W., 2008b, The Astrophysical Journal, 672, L107

Ellison S. L., Patton D. R., Simard L., McConnachie A. W., Baldry I. K., Mendel J. T., 2010, Monthly Notices of the Royal Astronomical Society, 407, 1514

Ellison S. L., Patton D. R., Mendel J. T., Scudder J. M., 2011, Monthly Notices of the Royal Astronomical Society, 418, 2043

Ellison S. L., Mendel J. T., Patton D. R., Scudder J. M., 2013a, Monthly Notices of the Royal Astronomical Society, 435, 3627

Ellison S. L., Mendel J. T., Patton D. R., Scudder J. M., 2013b, Monthly Notices of the Royal Astronomical Society, 435, 3627

Ellison S. L., Fertig D., Rosenberg J. L., Nair P., Simard L., Torrey P., Patton D. R., 2015, Monthly Notices of the Royal Astronomical Society, 448, 221

Ellison S. L., Teimoorinia H., Rosario D. J., Mendel J. T., 2016, MNRAS, 458, 34

Ellison S. L., Sánchez S. F., Ibarra-Medel H., Antonio B., Mendel J. T., Barrera-Ballesteros J., 2018a, Monthly Notices of the Royal Astronomical Society, 474, 2039

Ellison S. L., Catinella B., Cortese L., 2018b, Monthly Notices of the Royal Astronomical Society, 478, 3447

Ellison S. L., Viswanathan A., Patton D. R., Bottrell C., McConnachie A. W., Gwyn S., Cuillandre J.-C., 2019, Monthly Notices of the Royal Astronomical Society, 487, 2491

Ellison S. L., Thorp M. D., Pan H.-A., Lin L., Scudder J. M., Bluck A. F. L., Sánchez S. F., Sargent M., 2020a, Monthly Notices of the Royal Astronomical Society, 492, 6027

Ellison S., et al., 2020b, Monthly Notices of the Royal Astronomical Society, 493, L39

Ellison S. L., Lin L., Thorp M. D., Pan H.-A., Scudder J. M., Sánchez S. F., Bluck A. F. L., Maiolino R., 2021a, Monthly Notices of the Royal Astronomical Society, 501, 4777

Ellison S. L., Lin L., Thorp M. D., Pan H.-A., Sánchez S. F., Bluck A. F. L., Belfiore F., 2021b, Monthly Notices of the Royal Astronomical Society: Letters, 502, L6

Ellison S. L., et al., 2021c, Monthly Notices of the Royal Astronomical Society, 505, L46

Elmegreen D. M., Elmegreen B. G., 1982, Monthly Notices of the Royal Astronomical Society, 201, 1021

Elmegreen B. G., Elmegreen D. M., Montenegro L., 1992, The Astrophysical Journal Supplement Series, 79, 37

Evans I. N., 1986, The Astrophysical Journal, 309, 544

Faber S. M., et al., 2007, The Astrophysical Journal, 665, 265

Farrah D., et al., 2001, Monthly Notices of the Royal Astronomical Society, 326, 1333

Feng S., Shen S.-Y., Yuan F.-T., Riffel R. A., Pan K., 2020, The Astrophysical Journal Letters, 892, L20

Fensch J., et al., 2017, Monthly Notices of the Royal Astronomical Society, 465, 1934

Ferreira L., Conselice C. J., Duncan K., Cheng T.-Y., Griffiths A., Whitney A., 2020, Astrophysical Journal, 895, 115

Flores Velázquez J. A., et al., 2021, Monthly Notices of the Royal Astronomical Society, 501, 4812

Forbes J., Krumholz M., Burkert A., 2012, The Astrophysical Journal, 754, 48

Frerking M. A., Langer W. D., Wilson R. W., 1982, The Astrophysical Journal, 262, 590

Fu H., et al., 2018, Astrophysical Journal, 856, 93

Gabor J. M., et al., 2009, The Astrophysical Journal, 691, 705

Gallagher M. J., et al., 2018, The Astrophysical Journal, 858, 90

Gao Y., et al., 2018, The Astrophysical Journal, 868, 14

Gao F., et al., 2020, Astronomy & Astrophysics, 637, A94

Garnett D. R., 2002, The Astrophysical Journal, 581, 1019

Garnett D. R., Shields G. A., 1987, The Astrophysical Journal, 317, 82

Genel S., et al., 2014, Monthly Notices of the Royal Astronomical Society, 445, 175

Gensior J., Kruijssen J. M. D., Keller B. W., 2020, Monthly Notices of the Royal Astronomical Society, 495, 199

Giese N., van der Hulst T., Serra P., Oosterloo T., 2016, Monthly Notices of the Royal Astronomical Society, 461, 1656

Gil de Paz A., Madore B. F., 2002, The Astronomical Journal, 123, 1864

Goldsmith P. F., Bergin E. A., Lis D., 1997, The Astrophysical Journal, 491, 615

González Delgado R. M., et al., 2014, The Astrophysical Journal Letters, 791, L16

González Delgado R. M., et al., 2016, Astronomy & Astrophysics, 590

Gordon K. D., Clayton G. C., Misselt K. A., Landolt A. U., Wolff M. J., 2003, The Astrophysical Journal, 594, 279

Goulding A. D., et al., 2018, Publications of the Astronomical Society of Japan, 70, 37

Greif T. H., Glover S. C. O., Bromm V., Klessen R. S., 2009, Monthly Notices of the Royal Astronomical Society, 392, 1381

Grogin N. A., et al., 2005, The Astrophysical Journal, 627, L97

Gunn J. E., et al., 2006, The Astronomical Journal, 131, 2332

Hambleton K. M., Gibson B. K., Brook C. B., Stinson G. S., Conselice C. J., Bailin J., Couchman H., Wadsley J., 2011, Monthly Notices of the Royal Astronomical Society, 418, 801

Hani M. H., Sparre M., Ellison S. L., Torrey P., Vogelsberger M., 2018, Monthly Notices of the Royal Astronomical Society, 475, 1160

Hani M. H., Gosain H., Ellison S. L., Patton D. R., Torrey P., 2020, Monthly Notices of the Royal Astronomical Society, 493, 3716

Hao C.-N., Kennicutt R. C., Johnson B. D., Calzetti D., Dale D. A., Moustakas J., 2011, The Astrophysical Journal, 741, 124

Hernández-Toledo H. M., Avila-Reese V., Conselice C. J., Puerari I., 2005, The Astronomical Journal, 129, 682

Hernquist L., 1989, Nature, 340, 687

Heyer M., Dame T. M., 2015, Annual Review of Astronomy and Astrophysics, 53, 583

Ho I.-T., et al., 2017, The Astrophysical Journal, 846, 39

Holwerda B. W., Pirzkal N., De Blok W. J. G., Bouchard A., Blyth S.-L., Van Der Heyden K. J., Elson E. C., 2011, Monthly Notices of the Royal Astronomical Society, 416, 2401

Holwerda B. W., et al., 2013, The Astrophysical Journal, 781, 12

Hopkins P. F., Quataert E., 2011, Monthly Notices of the Royal Astronomical Society, 415, 1027

Hopkins P. F., Hernquist L., Cox T. J., Di Matteo T., Robertson B., Springel V., 2006, Astrophysical Journal Supplement Series, 163, 1

Hopkins P. F., Bundy K., Hernquist L., Ellis R. S., 2007, The Astrophysical Journal, 659, 976

Hopkins P. F., Hernquist L., Cox T. J., Younger J. D., Besla G., 2008, The Astrophysical Journal, 688, 757

Hopkins P. F., et al., 2009, Monthly Notices of the Royal Astronomical Society, 397, 802

Hopkins P. F., et al., 2010, The Astrophysical Journal, 715, 202

Hopkins P. F., Cox T. J., Hernquist L., Narayanan D., Hayward C. C., Murray N., 2013, Monthly Notices of the Royal Astronomical Society, 430, 1901

Hsieh B. C., et al., 2017, The Astrophysical Journal, 851, L24

Hubble E., 1926, The Astrophysical Journal, 64, 321

Hubble E. P., 1936, Realm of the Nebulae. Yale University Press, New Haven

Huchtmeier W. K., Petrosian A., Krishna G., McLean B., Kunth D., 2008, Astronomy & Astrophysics, 492, 367

Huertas-Company M., et al., 2009, Astronomy & Astrophysics, 497, 743

Huertas-Company M., et al., 2015, The Astrophysical Journal Supplement Series, 221, 8

Huertas-Company M., et al., 2019, Monthly Notices of the Royal Astronomical Society, 489, 1859

Hwang H.-C., et al., 2018, The Astrophysical Journal, 872, 144

Illingworth G., 1977, The Astrophysical Journal, 218, 43

Iono D., Yun M. S., Mihos J. C., 2004, The Astrophysical Journal, 616, 199

Isbell J. W., Xue R., Fu H., 2018, The Astrophysical Journal Letters, 869, L37

Jian H.-Y., Lin L., Chiueh T., 2012, The Astrophysical Journal, 754, 26

Jiménez-Donaire M. J., et al., 2019, The Astrophysical Journal, 880, 127

Johansson P. H., Naab T., Ostriker J. P., 2012, The Astrophysical Journal, 754, 115

Kang D., Woo J.-H., 2018, The Astrophysical Journal, 864, 124

Karouzos M., Woo J.-H., Bae H.-J., 2016, The Astrophysical Journal, 819, 148

Kauffmann G., et al., 2003, Monthly Notices of the Royal Astronomical Society, 346, 1055

Keller B. W., Wadsley J., Benincasa S. M., Couchman H. M. P., 2014, Monthly Notices of the Royal Astronomical Society, 442, 3013

Kennicutt R. C., 1983, The Astrophysical Journal, 272, 54

Kennicutt R. C., 1989, The Astrophysical Journal, 344, 685

Kennicutt R. C., 1998a, Annual Review of Astronomy and Astrophysics, 36, 189

Kennicutt R. C., 1998b, The Astrophysical Journal, 498, 541

Kennicutt R. C., Evans N. J., 2012, Annual Review of Astronomy and Astrophysics, 50, 531

Kennicutt R. C., Keel W. C., Van Der Hulst J. M., Hummel E., Roettiger K. A., 1987, The Astronomical Journal, 93, 1011

Kennicutt R. C., Tamblyn P., Congdon C. W., 1994, Astrophysical Journal, 435, 22

Kennicutt R. C., et al., 2009, The Astrophysical Journal, 703, 1672

Kewley L. J., Dopita M. A., 2002, The Astrophysical Journal Supplement Series, 142, 35

Kewley L. J., Ellison S. L., 2008, Astrophysical Journal, 681, 1183

Kewley L. J., Dopita M. A., Sutherland R. S., Heisler C. A., Trevena J 2001, The Astronomical Journal, 556, 121

Kewley L. J., Geller M. J., Barton E. J., 2006a, The Astronomical Journal, 131, 2004

Kewley L. J., Groves B., Kauffmann G., Heckman T., 2006b, Monthly Notices of the Royal Astronomical Society, 372, 961

Kewley L. J., Rupke D., Jabran Zahid H., Geller M. J., Barton E. J., 2010, The Astrophysical Journal, 721, L48

Kinman T. D., Davidson K., 1981, The Astrophysical Journal, 243, 127

Knapen J. H., James P. A., 2009, The Astrophysical Journal, 698, 1437

Knapen J. H., Cisternas M., Querejeta M., 2015, Monthly Notices of the Royal Astronomical Society, 454, 1742

Kobulnicky H. A., Kewley L. J., 2004, The Astrophysical Journal, 617, 240

Kormendy J., Bender R., 2011, The Astrophysical Journal Supplement Series, 198, 2

Kroupa P., 2002, SCIENCE, 295, 82

Kuntschner H., et al., 2010, Monthly Notices of the Royal Astronomical Society, 408, 97

Lackner C. N., Gunn J. E., 2012, Monthly Notices of the Royal Astronomical Society, 421, 2277

Lagos C. d. P., et al., 2016, Monthly Notices of the Royal Astronomical Society, 459, 2632

Lambas D. G., Tissera P. B., Alonso M. S., Coldwell G., 2003, Monthly Notices of the Royal Astronomical Society, 346, 1189

Lambas D. G., Alonso S., Mesa V., O'Mill A. L., 2012, Astronomy & Astrophysics, 539, A45

Lanyon-Foster M. M., Conselice C. J., Merrifield M. R., 2012, Monthly Notices of the Royal Astronomical Society, 424, 1852

Lara-López M. A., Bongiovanni A., Cepa J., Pérez García A. M., Sánchez-Portal M., Castañeda H. O., Fernández Lorenzo M., Pović M., 2010, Astronomy and Astrophysics, 519, A31

Lara-López M. A., et al., 2013, Monthly Notices of the Royal Astronomical Society, 434, 451

Larson R. B., 1974, Monthly Notices of the Royal Astronomical Society, 169, 229

Larson R. B., Tinsley B. M., 1978, The Astrophysical Journal, 219, 46

Larson K. L., et al., 2016, The Astrophysical Journal, 825, 128

Law D. R., et al., 2015, The Astronomical Journal, 150, 19

Law D. R., et al., 2016, The Astronomical Journal, 152, 83

Law D. R., et al., 2021, The Astronomical Journal, 161, 52

Leitherer C., Ferguson H. C., Heckman T. M., Lowenthal J. D., 1995, The Astrophysical Journal, 454, L19

Lequeux J., Peimbert M., Rayo J. F., Serrano A., Torres-Peimbert S., 1979, Astronomy and Astrophysics, 80, 155

Leroy A. K., Walter F., Brinks E., Bigiel F., De Blok W. J. G., Madore B., Thornley M. D., 2008, The Astronomical Journal, 136, 2782

Leroy A. K., et al., 2013, The Astronomical Journal, 146, 19

Leroy A. K., et al., 2017, The Astrophysical Journal, 846, 71

Leroy A. K., et al., 2021, The Astrophysical Journal Supplement Series, 257, 61

Leslie S. K., Kewley L. J., Sanders D. B., Lee N., 2016, Monthly Notices of the Royal Astronomical Society, 455, 82

Leslie S. K., et al., 2020, The Astrophysical Journal, 899, 58

Lin L., et al., 2004, The Astrophysical Journal, 617, L9

Lin L., et al., 2017, The Astrophysical Journal, 851, 18

Lin L., et al., 2019, Astrophysical Journal Letters, 884

Lin L., et al., 2020, The Astrophysical Journal, 903, 19

Lintott C., et al., 2011, Monthly Notices of the Royal Astronomical Society, 410, 166

Liu Q., Wang E., Lin Z., Gao Y., Liu H., Berhane Teklu B., Kong X., 2018, The Astrophysical Journal, 857, 17

López-Cobá C., et al., 2020, The Astronomical Journal, 159, 167

Lotz J. M., Primack J., Madau P., 2004, The Astronomical Journal, 128, 163

Lotz J. M., Madau P., Giavalisco M., Primack J., Ferguson H. C., 2006, The Astrophysical Journal, 636, 592

Lotz J. M., Jonsson P., Cox T., Primack J. R., 2008, Monthly Notices of the Royal Astronomical Society, 391, 1137

Lotz J. M., Jonsson P., Cox T. J., Primack J. R., 2010a, Monthly Notices of the Royal Astronomical Society, 404, 575

Lotz J. M., Jonsson P., Cox T. J., Primack J. R., 2010b, Monthly Notices of the Royal Astronomical Society, 404, 590

Ma C.-P., Greene J. E., McConnell N., Janish R., Blakeslee J. P., Thomas J., Murphy J. D., 2014, The Astrophysical Journal, 795, 158

Maiolino R., Mannucci F., 2019, The Astronomy & Astrophysics Review, 27, 3

Maiolino R., et al., 2008, Astronomy & Astrophysics, 488, 463

Malin D. F., Carter D., 1983, The Astrophysical Journal, 274, 534

Mannucci F., Cresci G., Maiolino R., Marconi A., Gnerucci A., 2010, Monthly Notices of the Royal Astronomical Society, 408, 2115

Marian V., et al., 2019, The Astrophysical Journal, 882, 141

Marinacci F., et al., 2018, Monthly Notices of the Royal Astronomical Society, 480, 5113

Marino R. A., et al., 2013a, Astronomy & Astrophysics, 559, A114

Marino A. F., Milone A. P., Lind K., 2013b, The Astrophysical Journal, 768, 27

Martig M., Bournaud F., Teyssier R., Dekel A., 2009, The Astrophysical Journal, 707, 250

Massey P., 1998, in Gilmore G., Howell D., eds, The Stellar Initial Mass Function (38th Herstmonceux Conference). p. 17, http://articles.adsabs.harvard.edu/pdf/1998ASPC..142...17M

McMullin J. P., Waters B., Schiebel D., Young W., Golap K., 2007, in Astronomical Data Analysis Software and Systems XVI. p. 127, http://casa.nrao.edu

McPartland C., Sanders D. B., Kewley L. J., Leslie S. K., 2019, Monthly Notices of the Royal Astronomical Society: Letters, 482, L129

Mcgaugh S. S., 1991, The Astrophysical Journal, 380, 140

Medling A. M., et al., 2018, Monthly Notices of the Royal Astronomical Society, 475, 5194

Meert A., Vikram V., Bernardi M., 2015, Monthly Notices of the Royal Astronomical Society, 446, 3943

Mendel J. T., Simard L., Ellison S. L., Patton D. R., 2013, Monthly Notices of the Royal Astronomical Society, 429, 2212

Mendel J. T., Simard L., Palmer M., Ellison S. L., Patton D. R., 2014, The Astrophysical Journal Supplement Series, 210, 21

Mesa V., Duplancic F., Alonso S., Coldwell G., Lambas D. G., 2014, Monthly Notices of the Royal Astronomical Society, 438, 1784

Michel-Dansac L., Lambas D. G., Alonso M. S., Tissera P., 2008, Monthly Notices of the Royal Astronomical Society, 386, 82

Michiyama T., et al., 2016, Publications of the Astronomical Society of Japan, 68

Mihos J. C., Dubinski J., 1998, The Astrophysical Journal, 494, 183

Mihos J. C., Hernquist L., 1994, The Astrophysical Journal, 437, L47

Mihos J. C., Hernquist L., 1996, The Astrophysical Journal, 464, 641

Montuori M., Di Matteo P., Lehnert M. D., Combes F., Semelin B., 2010, Astronomy and Astrophysics, 518, A56

Moreno J., Torrey P., Ellison S. L., Patton D. R., Bluck A. F., Bansal G., Hernquist L., 2015, Monthly Notices of the Royal Astronomical Society, 448, 1107

Moreno J., et al., 2019, Monthly Notices of the Royal Astronomical Society, 485, 1320

Moreno J., et al., 2021, Monthly Notices of the Royal Astronomical Society, 503, 3113

Morgan W. W., 1959, Publications of the Astronomical Society of the Pacific, 71, 394

Morselli L., Popesso P., Erfanianfar G., Concas A., 2017, Astronomy and Astrophysics, 597, A97

Mouhcine M., Gibson B. K., Renda A., Kawata D., 2008, Astronomy & Astrophysics, 486, 711

Muzzin A., et al., 2013, The Astrophysical Journal, 777, 18

Naiman J. P., et al., 2018, Monthly Notices of the Royal Astronomical Society, 477, 1206

Narayanan D., Krumholz M. R., Ostriker E. C., Hernquist L., 2012, Monthly Notices of the Royal Astronomical Society, 421, 3127

Nelson D., et al., 2018, Monthly Notices of the Royal Astronomical Society, 475, 624

Nelson D., et al., 2019, Computational Astrophysics and Cosmology, 6, 2

Nikolic B., Cullen H., Alexander P., 2004, Monthly Notices of the Royal Astronomical Society, 355, 874

Noeske K. G., et al., 2007a, The Astrophysical Journal, 660, L43

Noeske K. G., et al., 2007b, The Astrophysical Journal, 660, L47

Oemler A. J., 1974, The Astrophysical Journal, 194, 1

Osterbrock D. E., Ferland G. J., 2006, Astrophysics of Gaseous Nebulae and Active Galactic Nuclei, 2 edn. University Science Books

Pagel B. E. J., Edmunds M. G., 1981, Annual Review of Astronomy and Astrophysics, 19, 77

Pakmor R., Bauer A., Springel V., 2011, Monthly Notices of the Royal Astronomical Society, 418, 1392

Pakmor R., Springel V., Bauer A., Mocz P., Munoz D. J., Ohlmann S. T., Schaal K., Zhu C., 2016, Monthly Notices of the Royal Astronomical Society, 455, 1134

Pan H.-A., et al., 2018a, The Astrophysical Journal, 854, 159

Pan H.-A., et al., 2018b, The Astrophysical Journal, 868, 132

Pan H.-A., et al., 2019, The Astrophysical Journal, 881, 119

Pannella M., et al., 2009, The Astrophysical Journal, 698, L116

Papadopoulos P. P., van der Werf P. P., Xilouris E. M., Isaak K. G., Gao Y., Mühle S., 2012, Monthly Notices of the Royal Astronomical Society, 426, 2601

Patton D. R., Ellison S. L., Simard L., McConnachie A. W., Mendel J. T., 2011, Monthly Notices of the Royal Astronomical Society, 412, 591

Patton D. R., Torrey P., Ellison S. L., Mendel J. T., Scudder J. M., 2013, Monthly Notices of the Royal Astronomical Society: Letters, 433, 59

Patton D. R., Qamar F. D., Ellison S. L., Bluck A. F. L., Simard L., Mendel J. T., Moreno J., Torrey P., 2016, Monthly Notices of the Royal Astronomical Society, 461, 2589

Patton D. R., et al., 2020, Monthly Notices of the Royal Astronomical Society, 494, 4969

Pawlik M. M., Wild V., Walcher C. J., Johansson P. H., Villforth C., Rowlands K., Mendez-Abreu J., Hewlett T., 2016, Monthly Notices of the Royal Astronomical Society, 456, 3032

Pearson W. J., Wang L., Trayford J. W., Petrillo C. E., Van Der Tak F. F. S., 2019a, Astronomy & Astrophysics, 626, 49

Pearson W. J., Wang L., Trayford J. W., Petrillo C. E., Van Der Tak F. F. S., 2019b, Astronomy & Astrophysics, 626, 18

Peeples M. S., Pogge R. W., Stanek K. Z., 2008, The Astrophysical Journal, 685, 904

Peeples M. S., Pogge R. W., Stanek K. Z., 2009, The Astrophysical Journal, 695, 259

Pei Y. C., 1992, The Astrophysical Journal, 395, 130

Peimbert M., Peimbert A., Delgado-Inglada G., 2017, Publications of the Astronomical Society of the Pacific, 129, 082001

Pérez-Montero E., Contini T., 2009, Monthly Notices of the Royal Astronomical Society, 398, 949

Perez J., Michel-Dansac L., Tissera P., 2011, Monthly Notices of the Royal Astronomical Society, 417, 580

Pessa I., et al., 2021, Astronomy & Astrophysics, 650, A134

Petrosian V., 1976, The Astrophysical Journal, 210, L53

Pettini M., Pagel B. E. J., 2004, Monthly Notices of the Royal Astronomical Society, 348, L59

Pillepich A., et al., 2018a, Monthly Notices of the Royal Astronomical Society, 473, 4077

Pillepich A., et al., 2018b, Monthly Notices of the Royal Astronomical Society, 475, 648

Pilyugin L. S., Grebel E. K., Mattsson L., 2012, Monthly Notices of the Royal Astronomical Society, 424, 2316

Piotrowska J. M., Bluck A. F., Maiolino R., Peng Y., 2022, Monthly Notices of the Royal Astronomical Society, 512, 1052

Pozzetti L., et al., 2010, Astronomy & Astrophysics, 523, A13

Quai S., Hani M. H., Ellison S. L., Patton D. R., Woo J., 2021, Monthly Notices of the Royal Astronomical Society, 504, 1888

Querejeta M., et al., 2019, Astronomy & Astrophysics, 625, A19

Querejeta M., et al., 2021, Astronomy & Astrophysics, 656, A133

Rennehan D., Babul A., Hopkins P. F., Davé R., Moa B., 2019, Monthly Notices of the Royal Astronomical Society, 483, 3810

Renzini A., Peng Y.-j., 2015, The Astrophysical Journal, 801, L29

Reynolds T. N., Westmeier T., Staveley-Smith L., Chauhan G., Lagos C. D. P., 2020, Monthly Notices of the Royal Astronomical Society, 499, 3233

Rich J. A., Torrey P., Kewley L. J., Dopita M. A., Rupke D. S. N., 2012, The Astrophysical Journal, 753, 5

Rich J. A., Kewley L. J., Dopita M. A., 2014, The Astrophysical Journal, 781, L12

Rich J. A., Kewley L. J., Dopita M. A., 2015, The Astrophysical Journal Supplement Series, 221, 28

Rodriguez-Gomez V., et al., 2015, Monthly Notices of the Royal Astronomical Society, 449, 49

Rodriguez-Gomez V., et al., 2017, Monthly Notices of the Royal Astronomical Society, 467, 3083

Rodriguez-Gomez V., et al., 2019, Monthly Notices of the Royal Astronomical Society, 483, 4140

Rodríguez-Montero F., Davé R., Wild V., Anglés-Alcázar D., Narayanan D., 2019, Monthly Notices of the Royal Astronomical Society, 490, 2139

Rosales-Ortega F. F., Sánchez S. F., Iglesias-Páramo J., Díaz A. I., Vílchez J. M., Bland-Hawthorn J., Husemann B., Mast D., 2012, The Astrophysical Journal Letters, 756, L31

Rowlands K., et al., 2018, Monthly Notices of the Royal Astronomical Society, 480, 2544

Rupke D., 2018, Galaxies, 6, 138

Rupke D. S. N., Kewley L. J., Barnes J. E., 2010, The Astrophysical Journal, 710, L156

Sabater J., Best P. N., Heckman T. M., 2015, Monthly Notices of the Royal Astronomical Society, 447, 110

Saintonge A., et al., 2012, The Astrophysical Journal, 758, 73

Saintonge A., et al., 2017, The Astrophysical Journal Supplement Series, 233, 22

Salim S., Lee J. C., Ly C., Brinchmann J., Davé R., Dickinson M., Salzer J. J., Charlot S., 2014, The Astrophysical Journal, 797, 126

Salpeter E. E., 1955, The Astrophysical Journal, 121, 161

Sánchez S. F., 2020, Annual Review of Astronomy and Astrophysics, 58, 99

Sánchez Almeida J., Sánchez-Menguiano L., 2019, The Astrophysical Journal Letters, 878, L6

Sánchez-Menguiano L., et al., 2016, Astronomy & Astrophysics, 587, A70

Sánchez S. F., García-Lorenzo B., Jahnke K., Mediavilla E., González-Serrano J. I., Christensen L., Wisotzki L., 2006, New Astronomy Reviews, 49, 501

Sánchez S. F., et al., 2012, Astronomy & Astrophysics, 538, A8

Sánchez S. F., et al., 2013, Astronomy & Astrophysics, 554, A58

Sánchez S. F., et al., 2014, Astronomy & Astrophysics, 563, A49

Sánchez S. F., et al., 2016a, Revista Mexicana de Astronomia y Astrofisica, 52, 21

Sánchez S. F., et al., 2016b, Revista Mexicana de Astronomia y Astrofisica, 52, 171

Sánchez S. F., et al., 2018, Revista Mexicana de Astronomia y Astrofisica, 54, 217

Sánchez S. F., et al., 2019, Monthly Notices of the Royal Astronomical Society, 484, 3042

Sánchez S. F., et al., 2022, The Astrophysical Journal Supplement Series, 262, 36

Sanders D. B., Soifer B. T., Elias J. H., Madore B. F., Matthews K., Neugebauer G., Scoville N. Z., 1988, The Astrophysical Journal, 325, 74

Sanders R. L., Shapley A. E., Zhang K., Yan R., 2017, The Astrophysical Journal, 850, 136

Sandstrom K. M., et al., 2013, The Astrophysical Journal, 777

Sargent M. T., et al., 2014, Astrophysical Journal, 793, 19

Satyapal S., Ellison S. L., Mcalpine W., Hickox R. C., Patton D. R., Mendel J. T., 2014, Monthly Notices of the Royal Astronomical Society, 441, 1297

Sauvage M., Thuan T. X., 1992, The Astrophysical Journal, 396, L69

Scalo J. M., 1986, Fundamentals of Cosmic Physics, 11, 1

Schaller G., Schaerer D., Meynet G., Maeder a., 1992, Astronomy and Astrophysics Supplement Series (ISSN 0365-0138), 96

Schawinski K., et al., 2014, Monthly Notices of the Royal Astronomical Society, 440, 889

Schmidt M., 1959, The Astrophysical Journal, 129, 243

Schreiber C., et al., 2015, Astronomy & Astrophysics, 575, A74

Schruba A., et al., 2011, The Astronomical Journal, 142, 37

Schweizer F., 1980, The Astrophysical Journal, 237, 303

Schweizer F., 1982, The Astrophysical Journal, 252, 455

Scudder J. M., Ellison S. L., Torrey P., Patton D. R., Mendel J. T., 2012, Monthly Notices of the Royal Astronomical Society, 426, 549

Scudder J. M., Ellison S. L., Momjian E., Rosenberg J. L., Torrey P., Patton D. R., Fertig D., Mendel J. T., 2015, Monthly Notices of the Royal Astronomical Society, 449, 3719

Segers M. C., Crain R. A., Schaye J., Bower R. G., Furlong M., Schaller M., Theuns T., 2016, Monthly Notices of the Royal Astronomical Society, 456, 1235

Sérsic J. L., 1963, Boletin de la Asociacion Argentina de Astronomia La Plata Argentina, 6, 4

Shangguan J., Ho L. C., Xie Y., 2018, The Astrophysical Journal, 854, 158

Shangguan J., Ho L. C., Bauer F. E., Wang R., Treister E., 2020, The Astrophysical Journal, 899, 112

Shields G. A., 1990, Annual Review of Astronomy and Astrophysics, 28, 525

Sijacki D., Vogelsberger M., Genel S., Springel V., Torrey P., Snyder G. F., Nelson D., Hernquist L., 2015, Monthly Notices of the Royal Astronomical Society, 452, 575

Simard L., Mendel J. T., Patton D. R., Ellison S. L., McConnachie A. W., 2011, The Astrophysical Journal Supplement Series, 196, 11

Simmons B. D., et al., 2017, Monthly Notices of the Royal Astronomical Society, 464, 4420

Smee S. A., et al., 2013, The Astronomical Journal, 146, 32

Solomon P. M., Sage L. J., 1988, The Astrophysical Journal, 334, 613

Somerville R. S., Davé R., 2015, Annu. Rev. Astron. Astrophys, 53, 51

Somerville R. S., Hopkins P. F., Cox T. J., Robertson B. E., Hernquist L., 2008, Monthly Notices of the Royal Astronomical Society, 391, 481

Spindler A., et al., 2018, Monthly Notices of the Royal Astronomical Society, 476, 580

Spolaor M., Kobayashi C., Forbes D. A., Couch W. J., Hau G. K. T., 2010, Monthly Notices of the Royal Astronomical Society, 408, 272

Springel V., 2000, Monthly Notices of the Royal Astronomical Society, 312, 859

Springel V., 2010, Monthly Notices of the Royal Astronomical Society, 401, 791

Springel V., Hernquist L., 2005, The Astrophysical Journal, 622, L9

Springel V., et al., 2005, Nature, 435, 629

Springel V., et al., 2018, Monthly Notices of the Royal Astronomical Society, 475, 676

Stasińska G., Cid Fernandes R., Mateus A., Sodré L., Asari N. V., 2006, Monthly Notices of the Royal Astronomical Society, 371, 972

Stasińska G., Asari N. V., Cid Fernandes R., Gomes J. M., Schlickmann M., Mateus A., Schoenell W., Sodré L., 2008, Monthly Notices of the Royal Astronomical Society: Letters, 391, L29

Stasinska G., et al., 2012, in EAS Publications Series.

Steffen J. L., Fu H., Comerford J. M., Dai Y. S., Feng S., Gross A. C., Xue R., 2021, The Astrophysical Journal, 909, 120

Strateva I., et al., 2001, The Astronomical Journal, 122, 1861

Strauss M. A., Weinberg D. H., Lupton R. H., Narayanan V. K., 2002, The Astronomical Journal, 124, 1810

Sun J., et al., 2020, The Astrophysical Journal, 892, 28

Tacchella S., et al., 2015, Science, 348, 314

Tacconi L. J., et al., 2018, The Astrophysical Journal, 853, 179

Terrazas B. A., Bell E. F., Henriques B. M. B., White S. D. M., Cattaneo A., Woo J., 2016, The Astrophysical Journal, 830, L12

Terrazas B. A., Bell E. F., Woo J., Henriques B. M. B., 2017, The Astrophysical Journal, 844, 170

The Astropy Collaboration A., et al., 2013, Astronomy & Astrophysics, 558, 9

The Astropy Collaboration A., et al., 2018, The Astronomical Journal, Volume 156, Issue 3, article id. 123, 19 pp. (2018)., 156

Thorp M., Ellison S., Simard L., Sánchez S., Antonio B., 2019, Monthly Notices of the Royal Astronomical Society: Letters, 482, L55

Tim De Zeeuw P., et al., 2002, Monthly Notices of the Royal Astronomical Society, 329, 513

Tissera P. B., Lambas D. G., Abade M. G., 1997, Monthly Notices of the Royal Astronomical Society, 286, 384

Tomičić N., et al., 2018, The Astrophysical Journal Letters, 869, L38

Tonnesen S., Cen R., 2012, Monthly Notices of the Royal Astronomical Society, 425, 2313

Toomre A., 1977, in Tinsley B. M., Larson R. B., Gehret D. C., eds, Evolution of Galaxies and Stellar Populations. p. 401, http://articles.adsabs.harvard.edu/pdf/1977egsp.conf..401T

Toomre A., Toomre J., 1972, The Astrophysical Journal, 178, 623

Torrey P., Cox T. J., Kewley L., Hernquist L., 2012, The Astrophysical Journal, 746, 108

Torrey P., et al., 2018, Monthly Notices of the Royal Astronomical Society, 477, 16

Tremonti C. A., et al., 2004, The Astrophysical Journal, 613, 898

Tumlinson J., et al., 2011, Science, 334, 948

Usero A., et al., 2015, The Astronomical Journal, 150, 115

Utomo D., et al., 2017, The Astrophysical Journal, 849, 16

Veilleux S., Osterbrock D. E., 1987, The Astrophysical Journal Supplement Series, 63, 295

Veilleux S., Cecil G., Bland-Hawthorn J., 2005, Annual Review of Astronomy and Astrophysics, 43, 769

Vincenzo F., Belfiore F., Maiolino R., Matteucci F., Ventura P., 2016, Monthly Notices of the Royal Astronomical Society, 458, 3466

Violino G., Ellison S. L., Sargent M., Coppin K. E. K., Scudder J. M., Mendel T. J., Saintonge A., 2018, Monthly Notices of the Royal Astronomical Society, 476, 2591

Vito F., et al., 2014, Monthly Notices of the Royal Astronomical Society, 441, 1059

Vogelsberger M., et al., 2014, Nature, 509, 177

Von Der Linden A., Best P. N., Kauffmann G., White S. D. M., 2007, Monthly Notices of the Royal Astronomical Society, 379, 867

Vulcani B., et al., 2019, Monthly Notices of the Royal Astronomical Society, 488, 1597

Wake D. A., et al., 2017, The Astronomical Journal, 154, 86

Walmsley M., Ferguson A. M., Mann R. G., Lintott C. J., 2019, Monthly Notices of the Royal Astronomical Society, 483, 2968

Walmsley M., et al., 2021, Monthly Notices of the Royal Astronomical Society, 509, 3966

Walterbos R. A. M., Greenawalt B., 1996, The Astrophysical Journal, 460, 696

Wang E., Lilly S. J., Pezzulli G., Matthee J., 2019, The Astrophysical Journal, 877, 132

Weinberger R., et al., 2017, Monthly Notices of the Royal Astronomical Society, 465, 3291

Weiner B. J., et al., 2009, The Astrophysical Journal, 692, 187

White S. D. M., 1978, Monthly Notices of the Royal Astronomical Society, 184, 185

White S. D. M., 1979, Monthly Notices of the Royal Astronomical Society, 189, 831

White S. D., Rees M. J., 1978, Monthly Notices of the Royal Astronomical Society, 183, 341

Wild V., et al., 2014, Astronomy & Astrophysics, 567, A132

Wilkinson S., Ellison S. L., Bottrell C., Bickley R. W., Gwyn S., Cuillandre J.-C., Wild V., 2022, Accepted for publication in MNRAS

Willett K. W., et al., 2017, Monthly Notices of the Royal Astronomical Society, 464, 4176

Wong K. C., et al., 2011, The Astrophysical Journal, 728, 119

Wong T., et al., 2013, The Astrophysical Journal Letters, 777

Woo J., Dekel A., Faber S. M., Koo D. C., 2015, Monthly Notices of the Royal Astronomical Society, 448, 237

Woods D. F., Geller M. J., 2007, The Astronomical Journal, 134, 527

Woods D. F., Geller M. J., Kurtz M. J., Westra E., Fabricant D. G., Dell'Antonio I., 2010, The Astronomical Journal, 139, 1857

Worthey G., 1994, The Astrophysical Journal Supplement Series, 95, 107

Wuyts S., et al., 2011, The Astrophysical Journal, 742, 96

Yan R., et al., 2016, The Astronomical Journal, 152, 197

Yang C.-C., Krumholz M., 2012, The Astrophysical Journal, 758, 48

Yang C., Gruendl R. A., Chu Y., Mac Low M., Fukui Y., 2007, The Astrophysical Journal, 671, 374

York D. G., et al., 2000, The Astronomical Journal, 120, 1579

Yuan F., Takeuchi T. T., Matsuoka Y., Buat V., Burgarella D., Iglesias-Páramo J., 2012, Astronomy & Astrophysics, 548, A117

Zahid H. J., Kewley L. J., Bresolin F., 2011, The Astrophysical Journal, 730, 137

Zanisi L., et al., 2020, Monthly Notices of the Royal Astronomical Society, 492, 1671

Zaritsky D., Kennicutt R. C. J., Huchra J. P., 1994, The Astrophysical Journal, 420, 87

Zuo P., Xu C. K., Yun M. S., Lisenfeld U., Li D., Cao C., 2018, The Astrophysical Journal Supplement Series, 237, 2

de Vaucouleurs G., 1948, Annales d'Astrophysique, 11, 247

van Dishoeck E. F., Black J. H., 1988, The Astrophysical Journal, 334, 771

van den Bergh S., 1998, Galaxy Morphology and Classification

van der Hulst J. M., van Albada T. S., Sancisi R., 2001, in Hibbard J. E., Rupen M., van Gorkom J. H., eds, Astronomical Society of the Pacific Conference Series Vol. 240, Gas and Galaxy Evolution. p. 451

Appendix A

Additional Information

A.1 MaNGA DR17 merger sample

Below are SDSS *gri*-images of all post-merger, visual pair, and spectroscopic pair galaxies selected from MaNGA DR17 for analysis in Chapter 2. Figures A.1-A.5 show the post-merger sample, all of which were visually classified. Figures A.5-A.21 show the pair sample. The IFU footprint on each galaxy is shown in magenta, providing reference for galaxy coverage. Each image is 50" wide, and some mergers have asymmetric structures that extend beyond this field of view. Visual classification was completed using the SDSS SkyServer navigation tool, which provides an adjustable field of view utilized to see the complete galaxy.

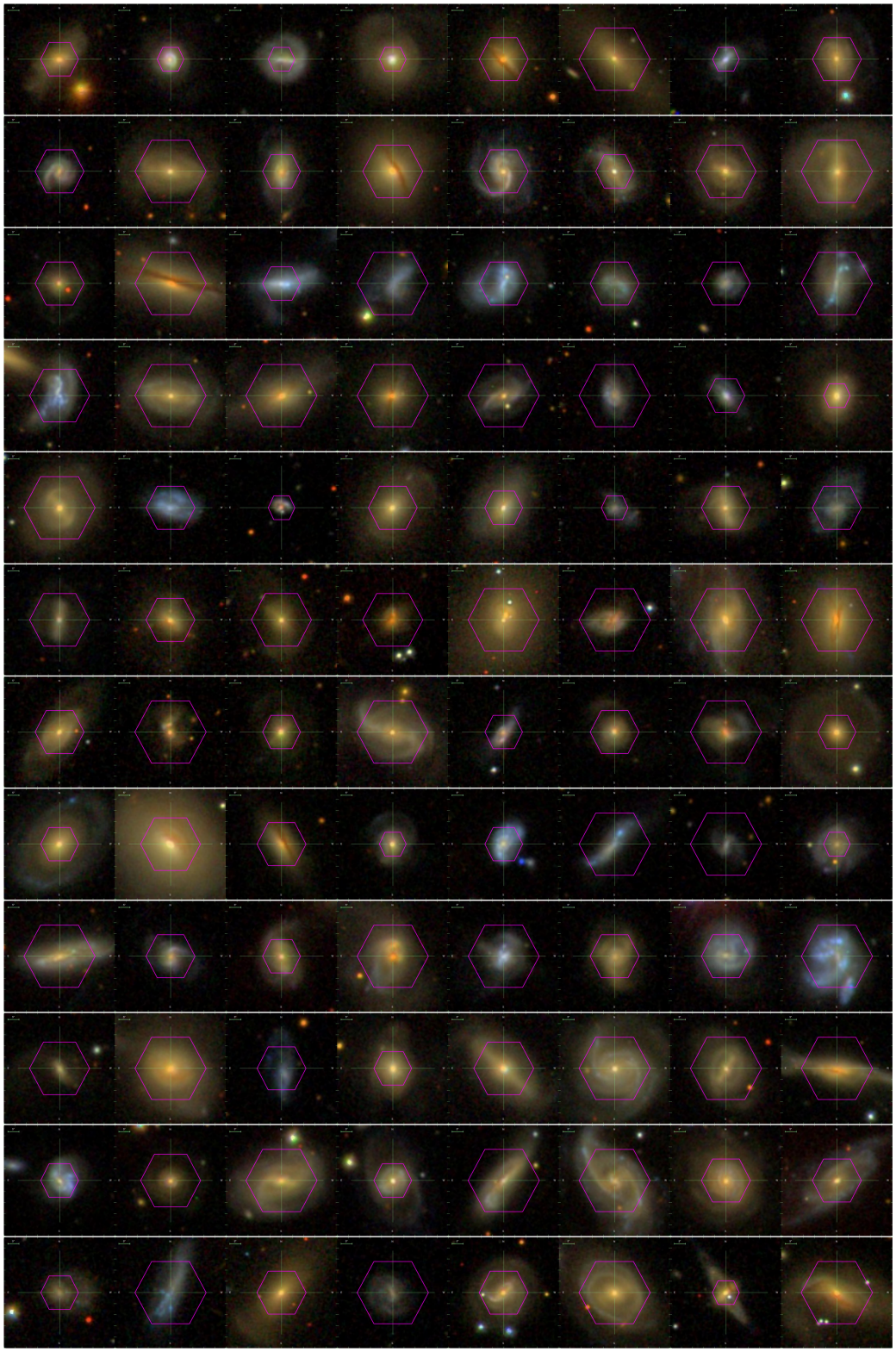

Figure A.1

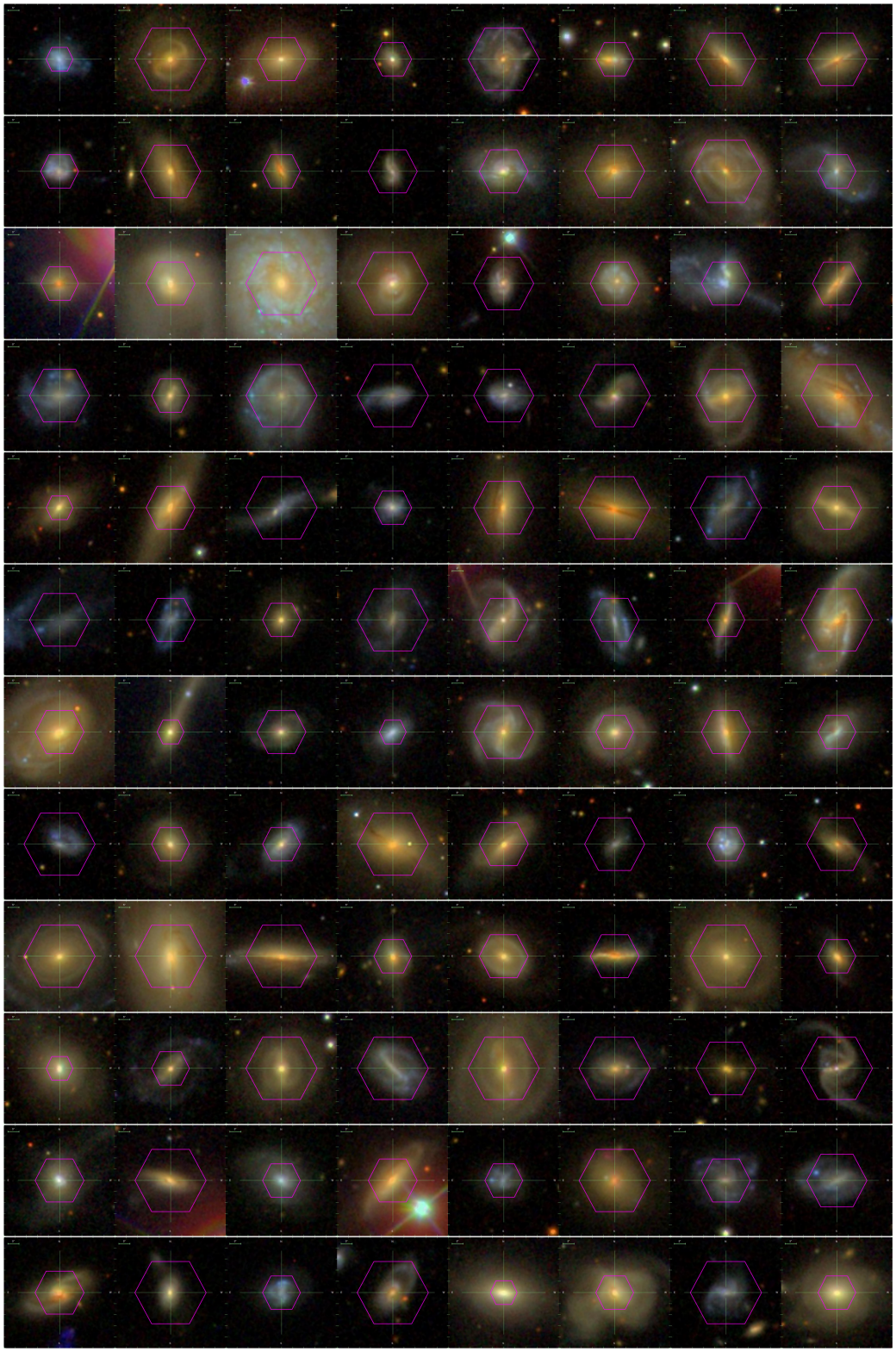

Figure A.2

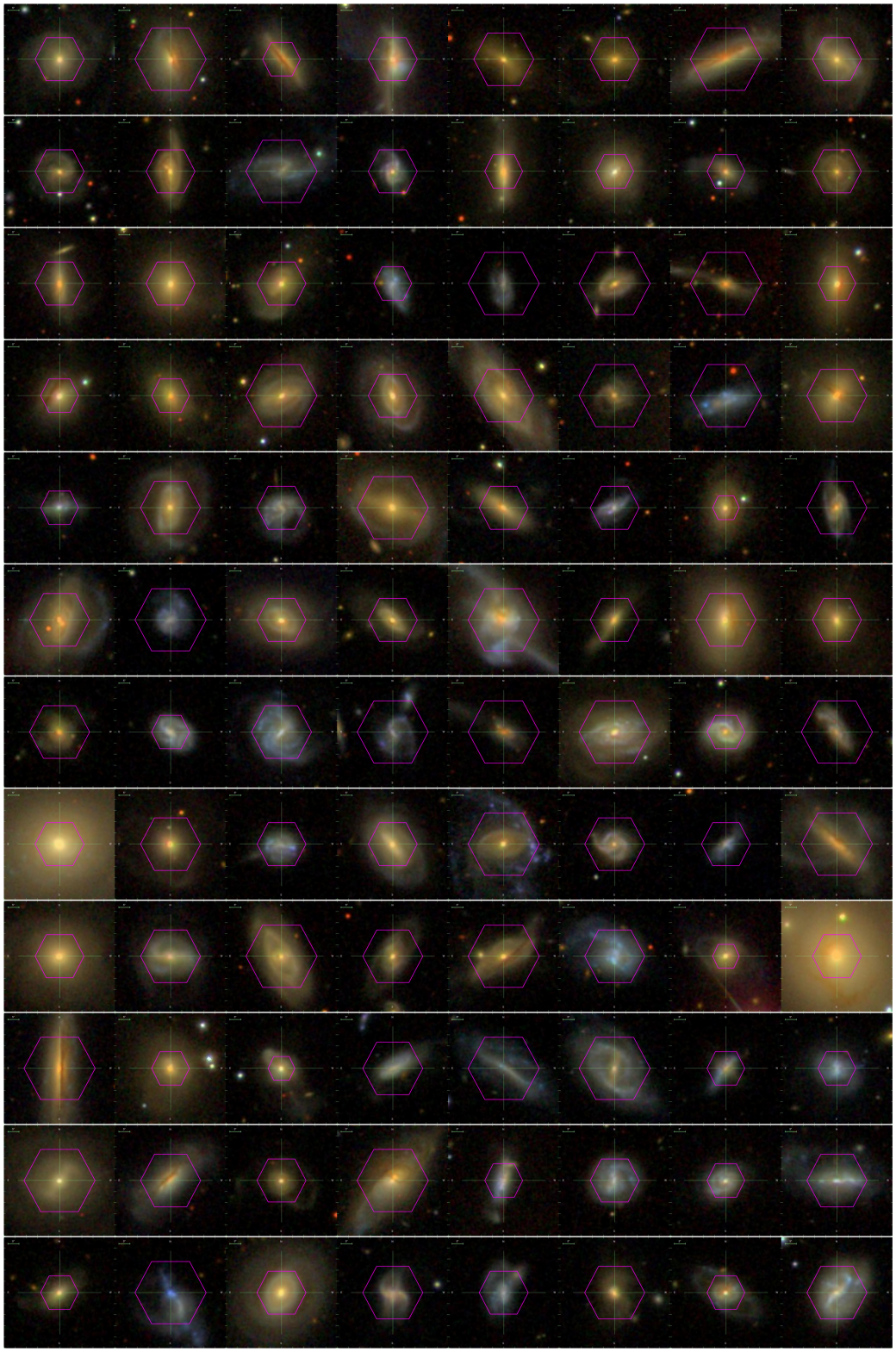

Figure A.3

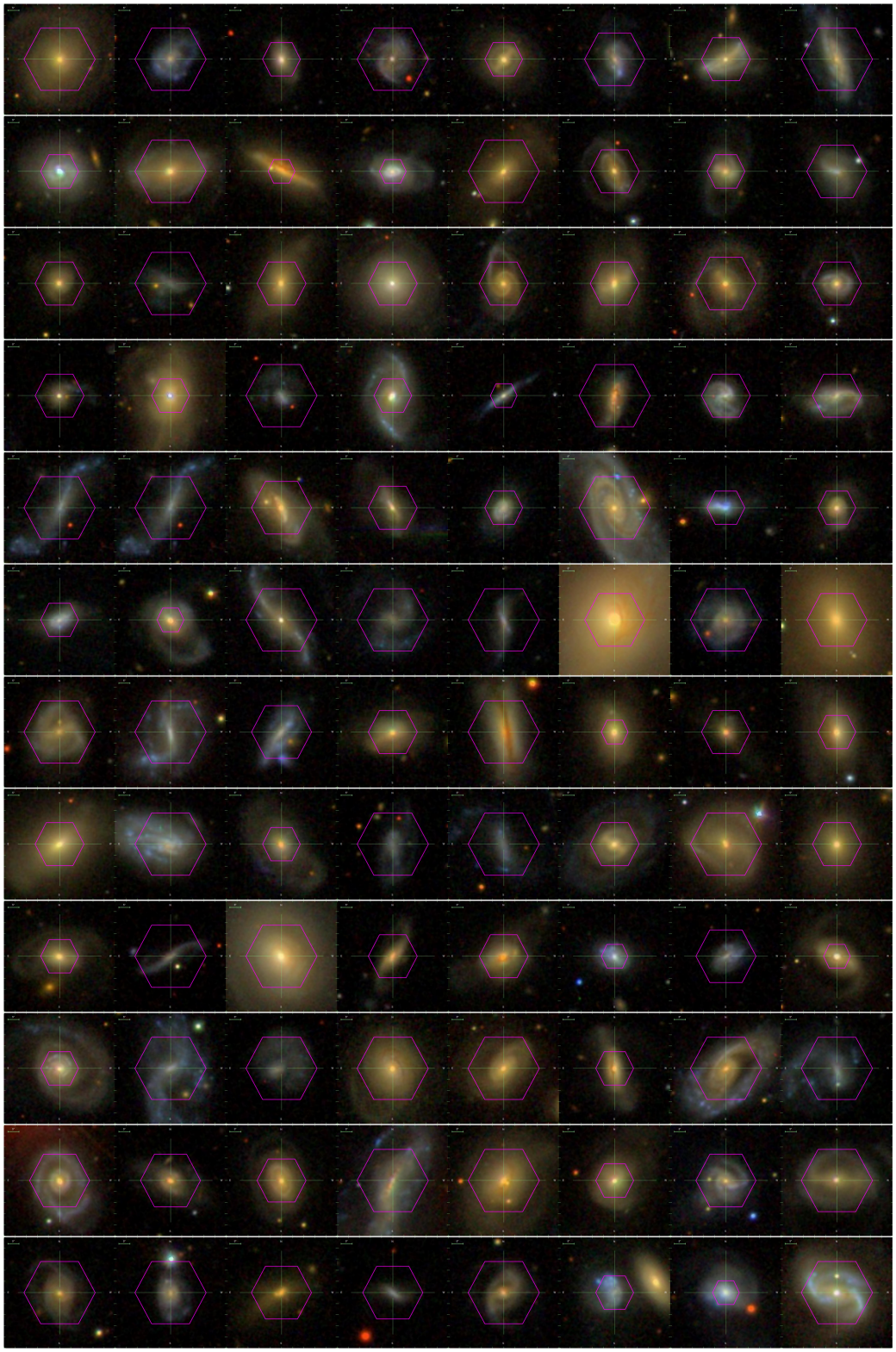

Figure A.4

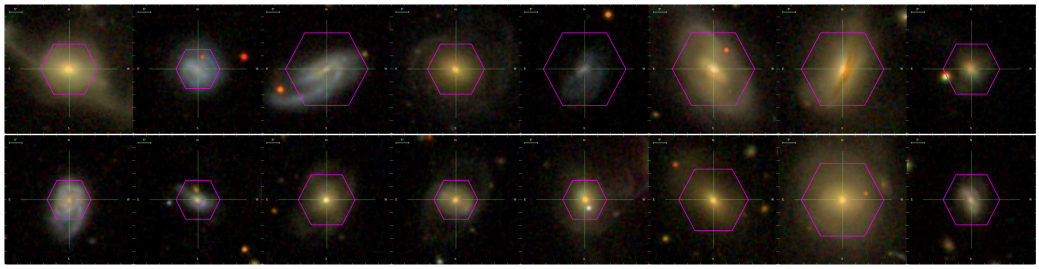

Figure A.5

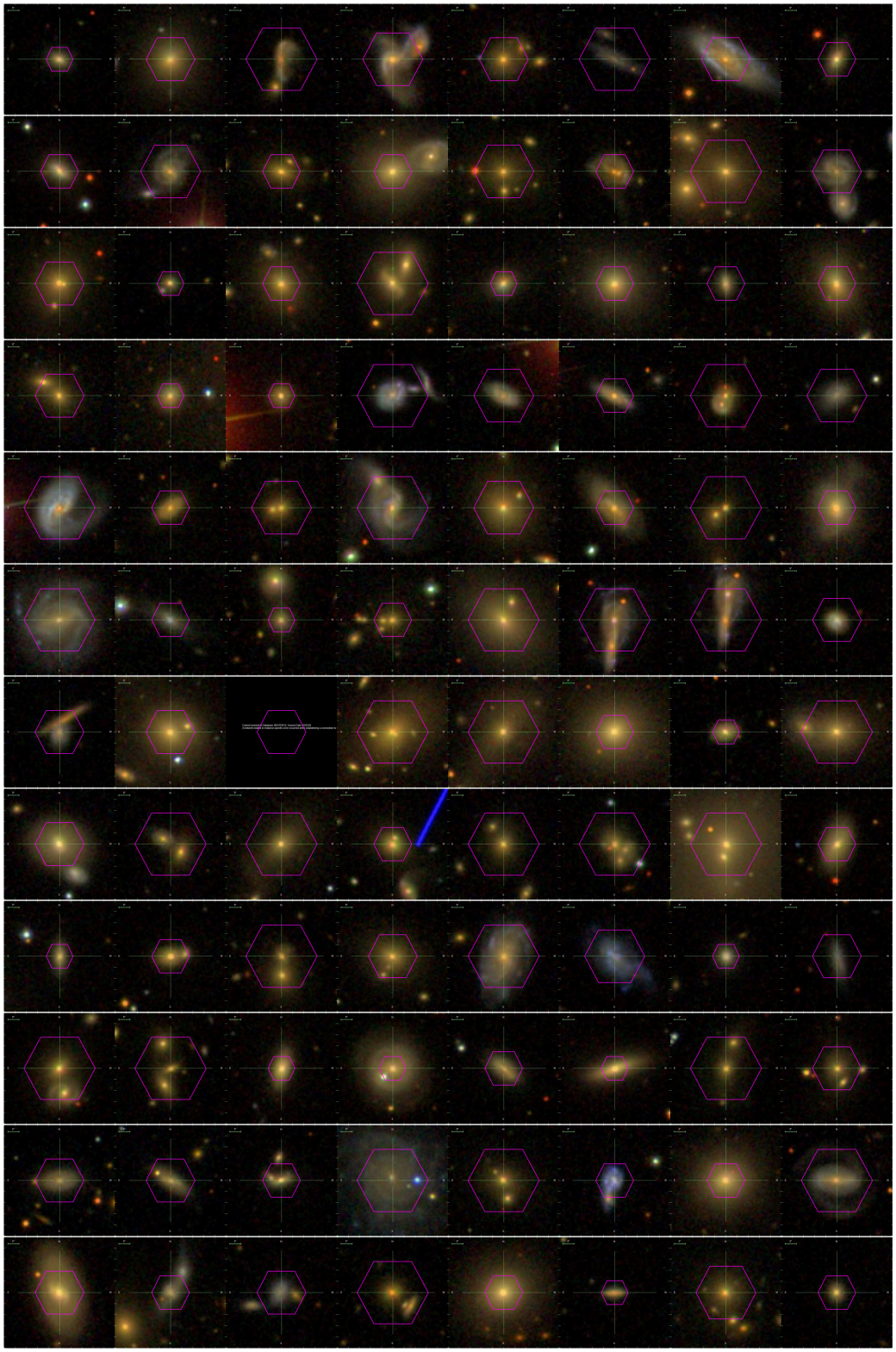

Figure A.6

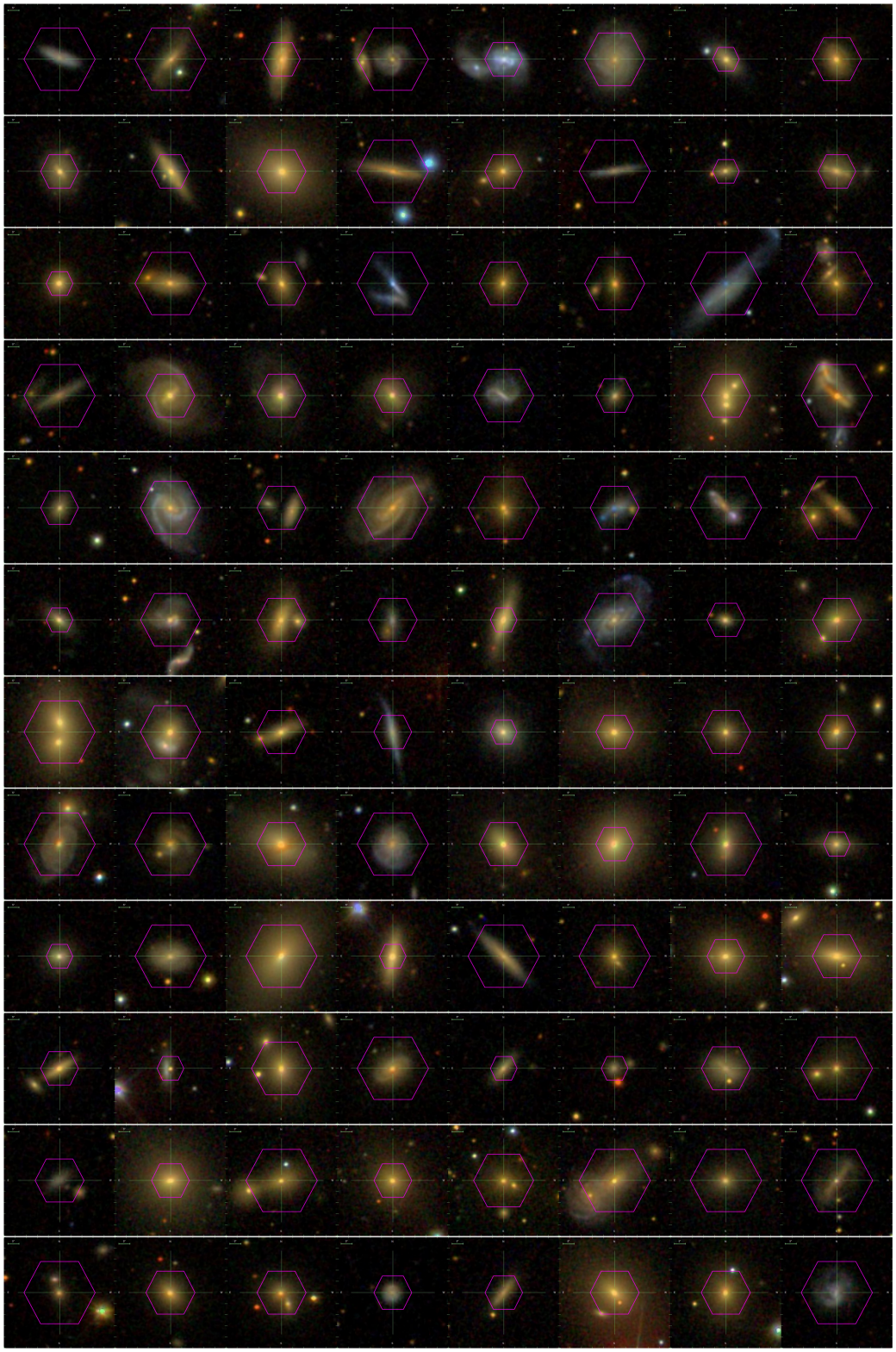

Figure A.7

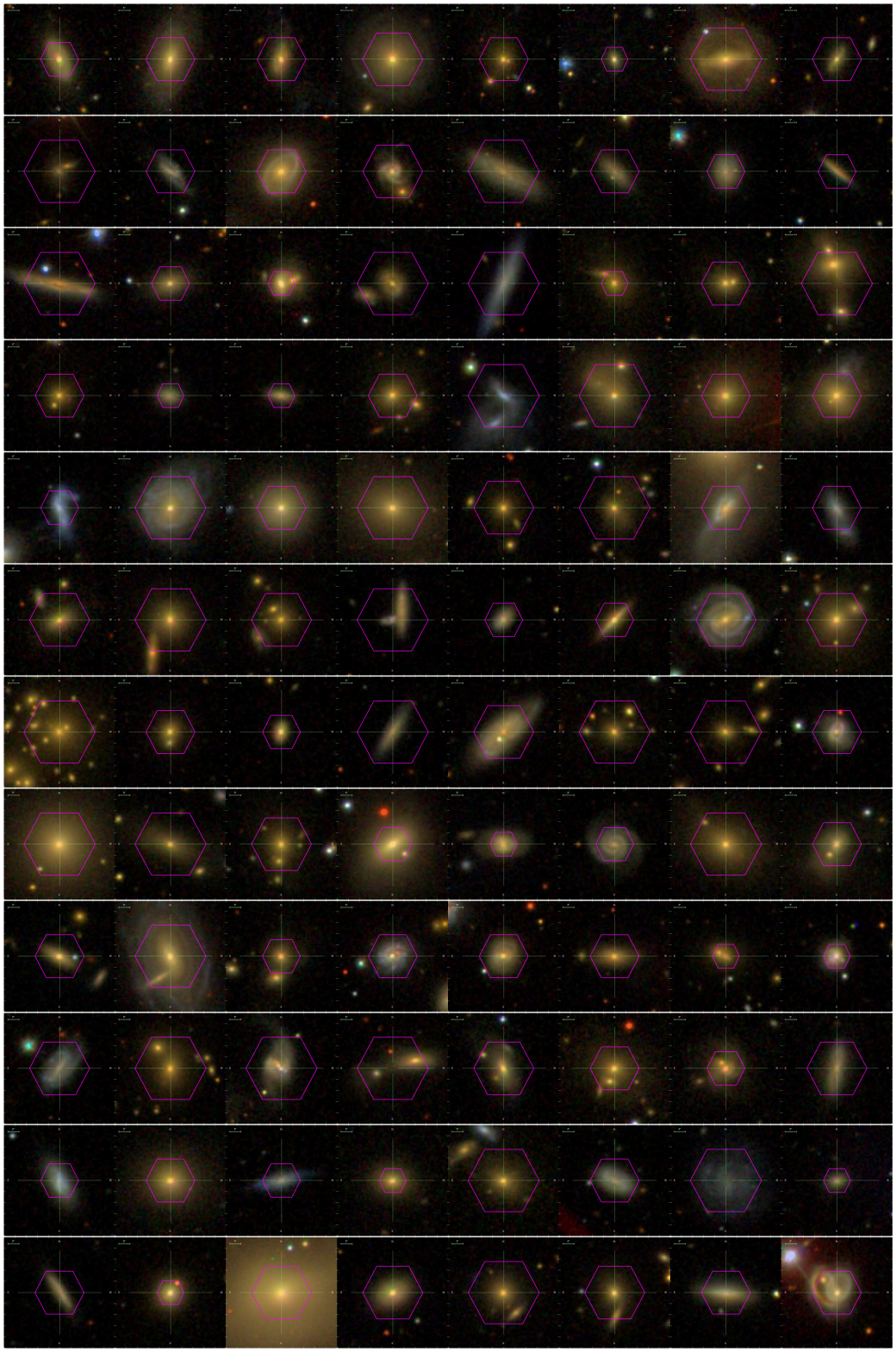

Figure A.8

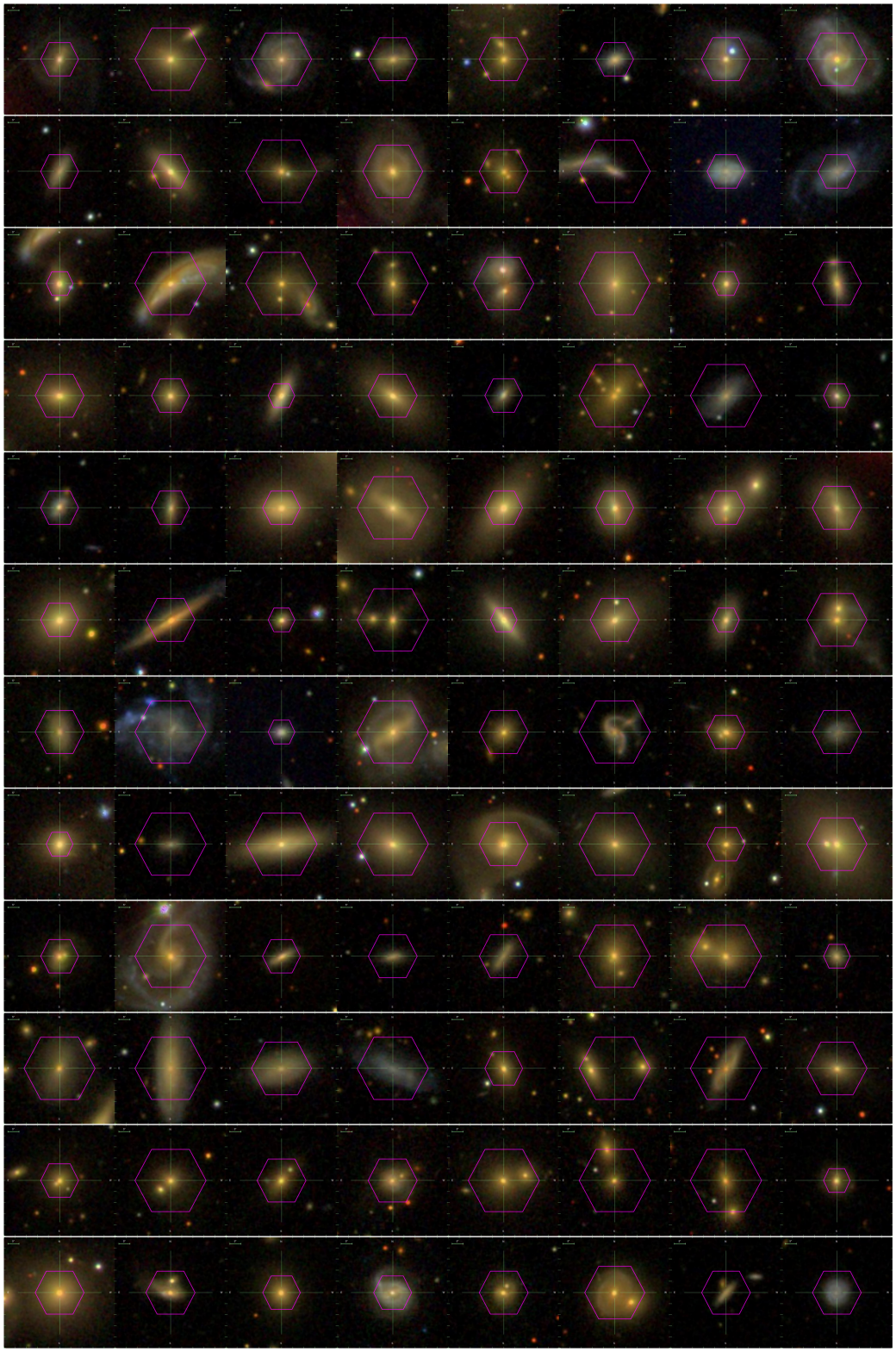

Figure A.9

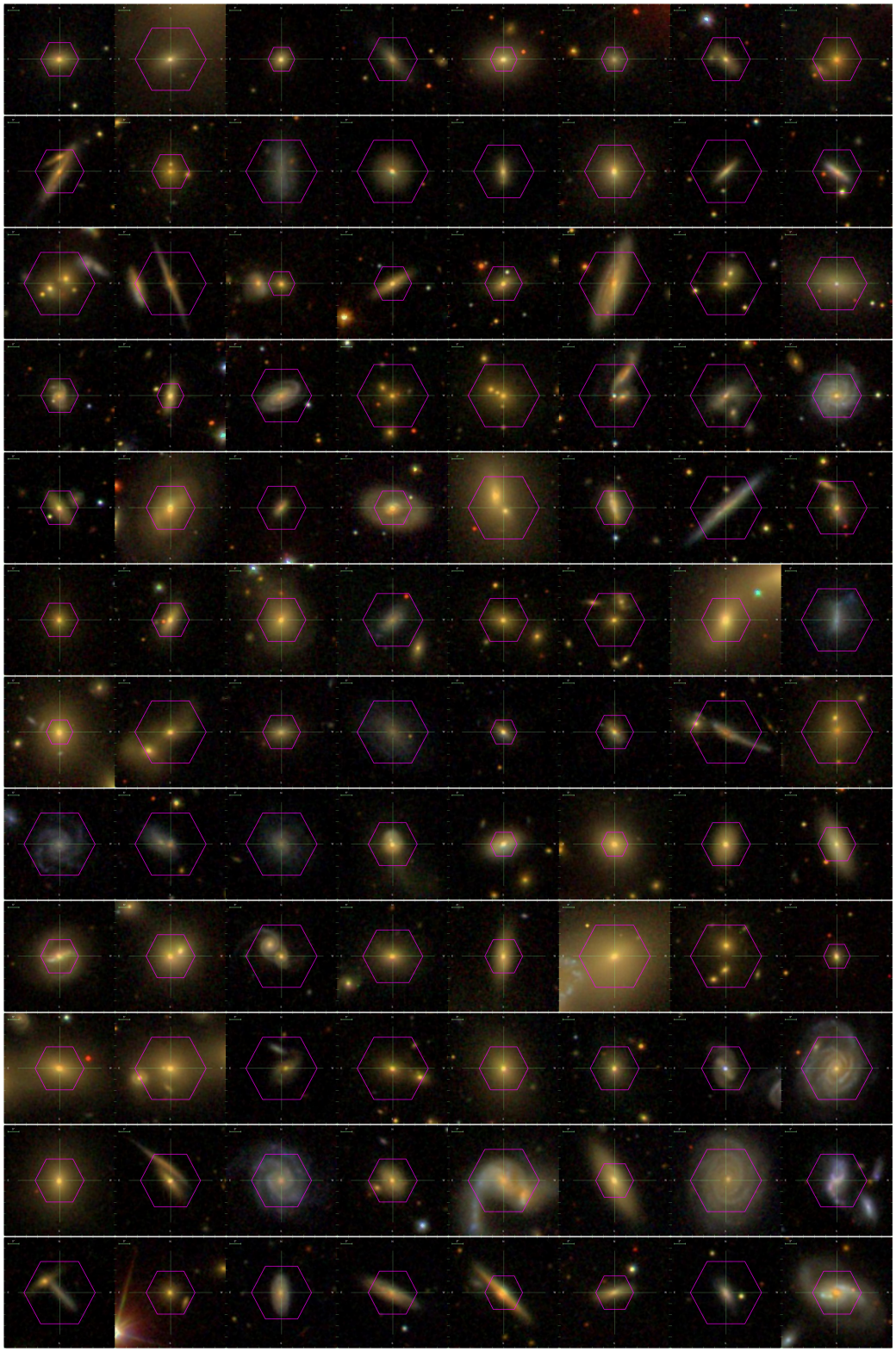

Figure A.10

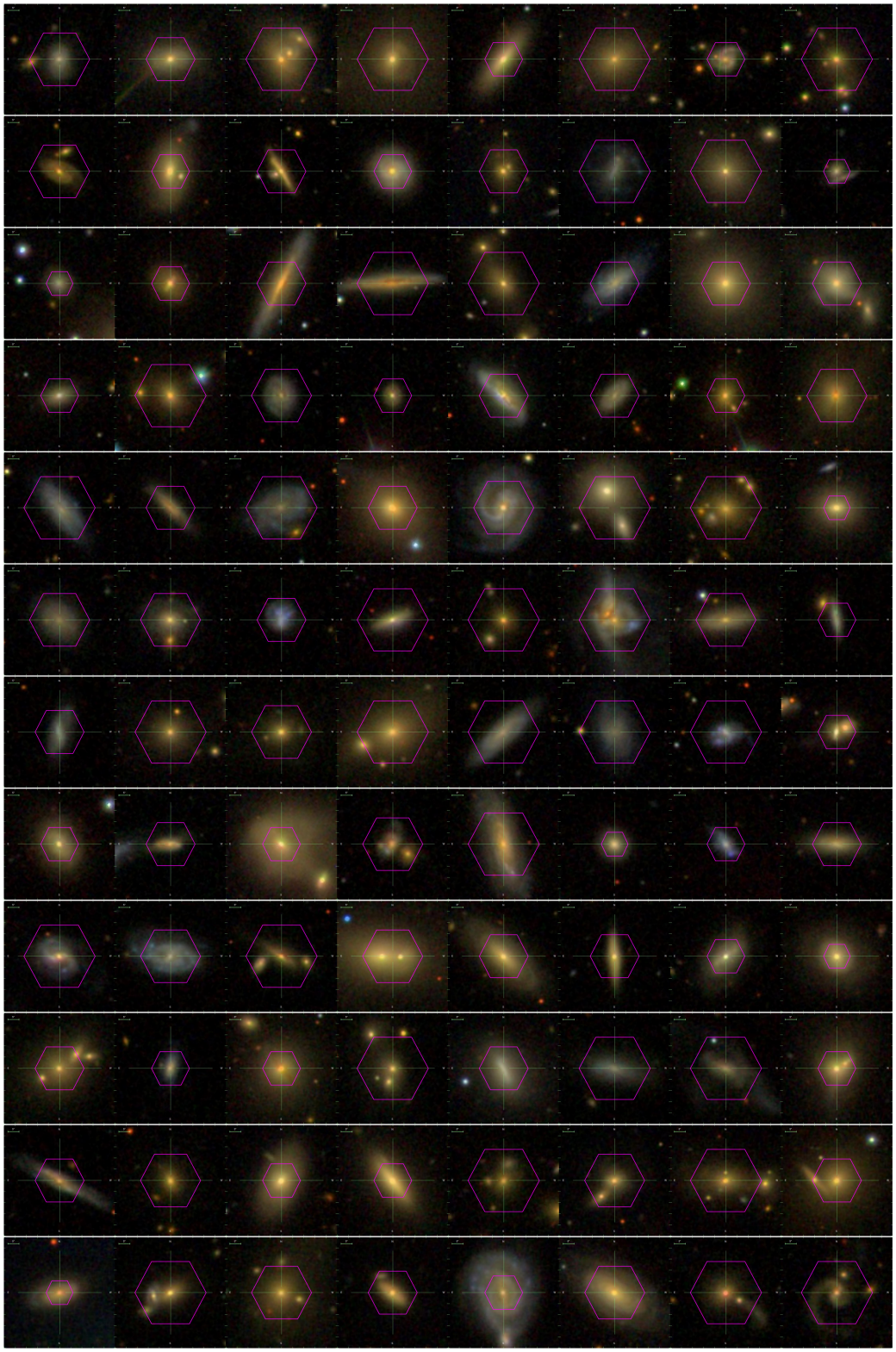

Figure A.11

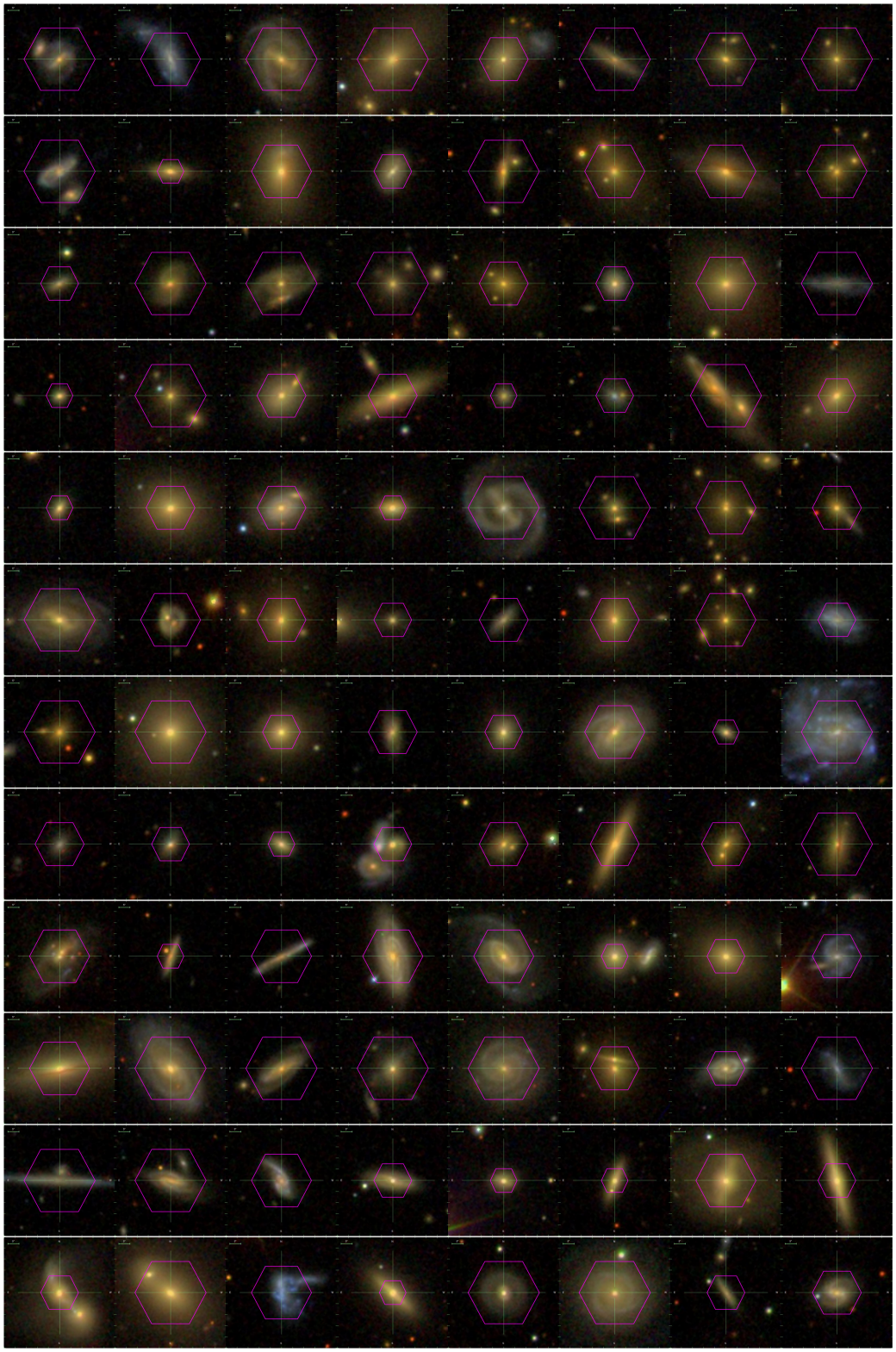

Figure A.12

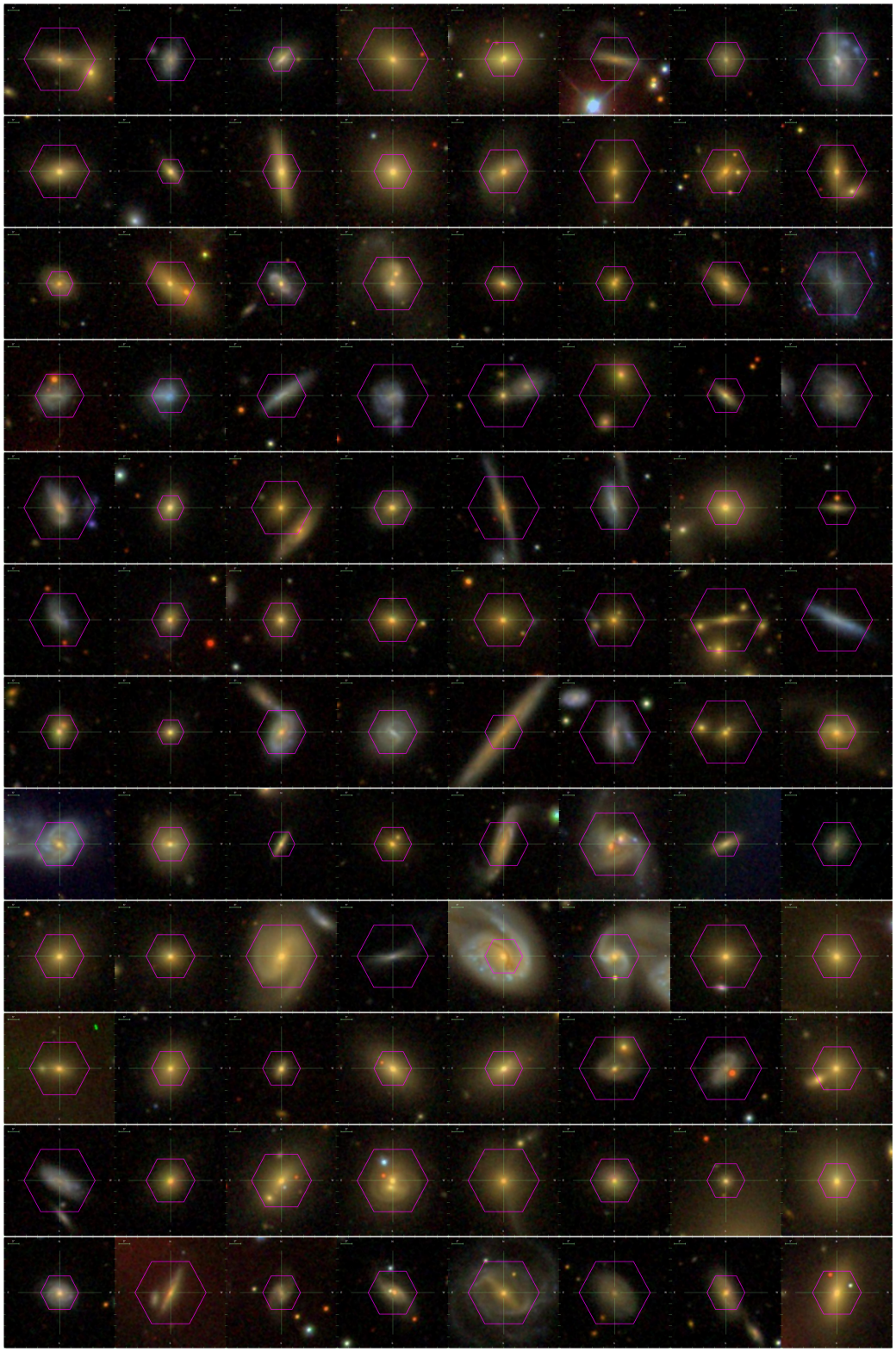

Figure A.13

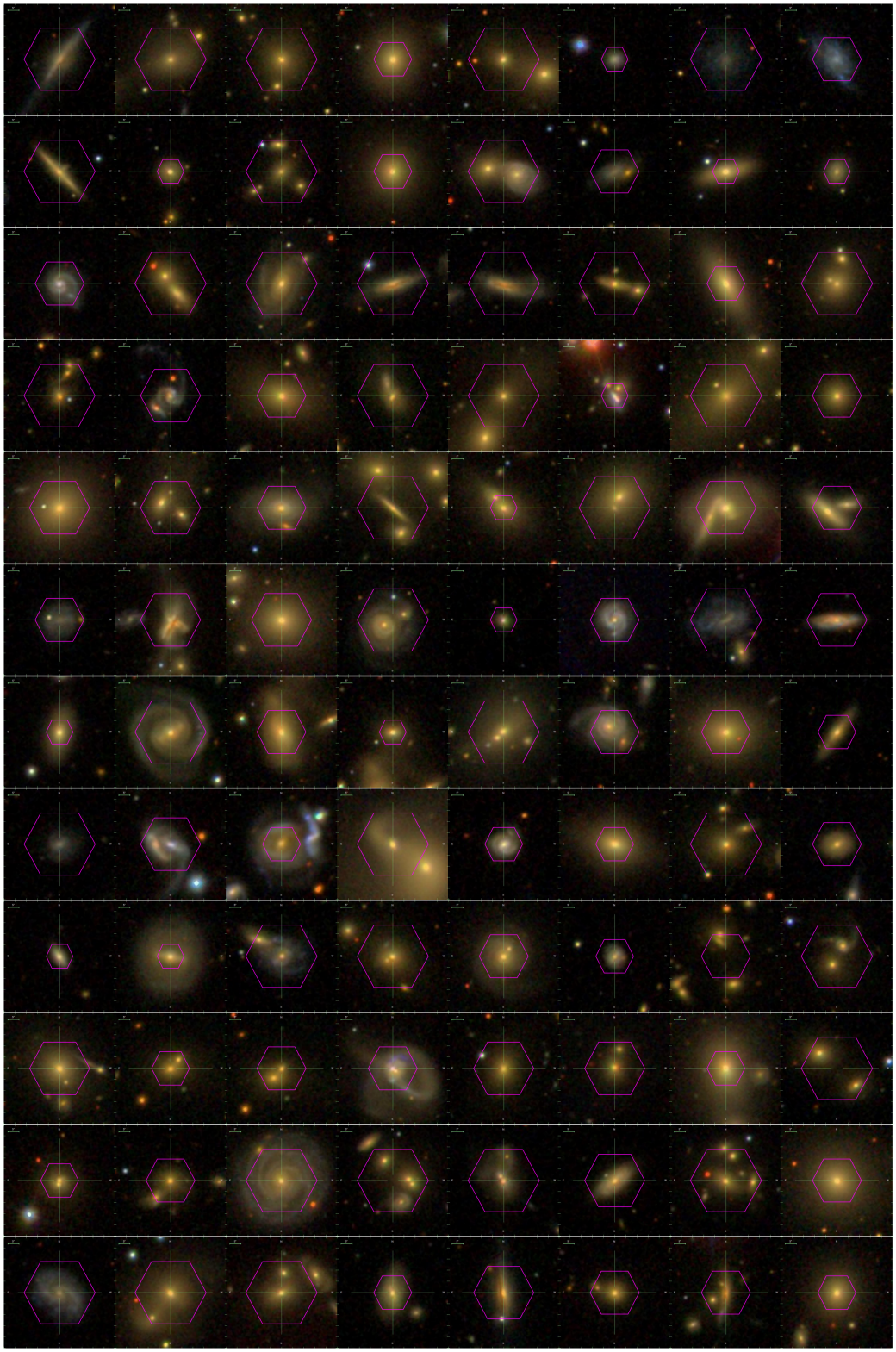

Figure A.14

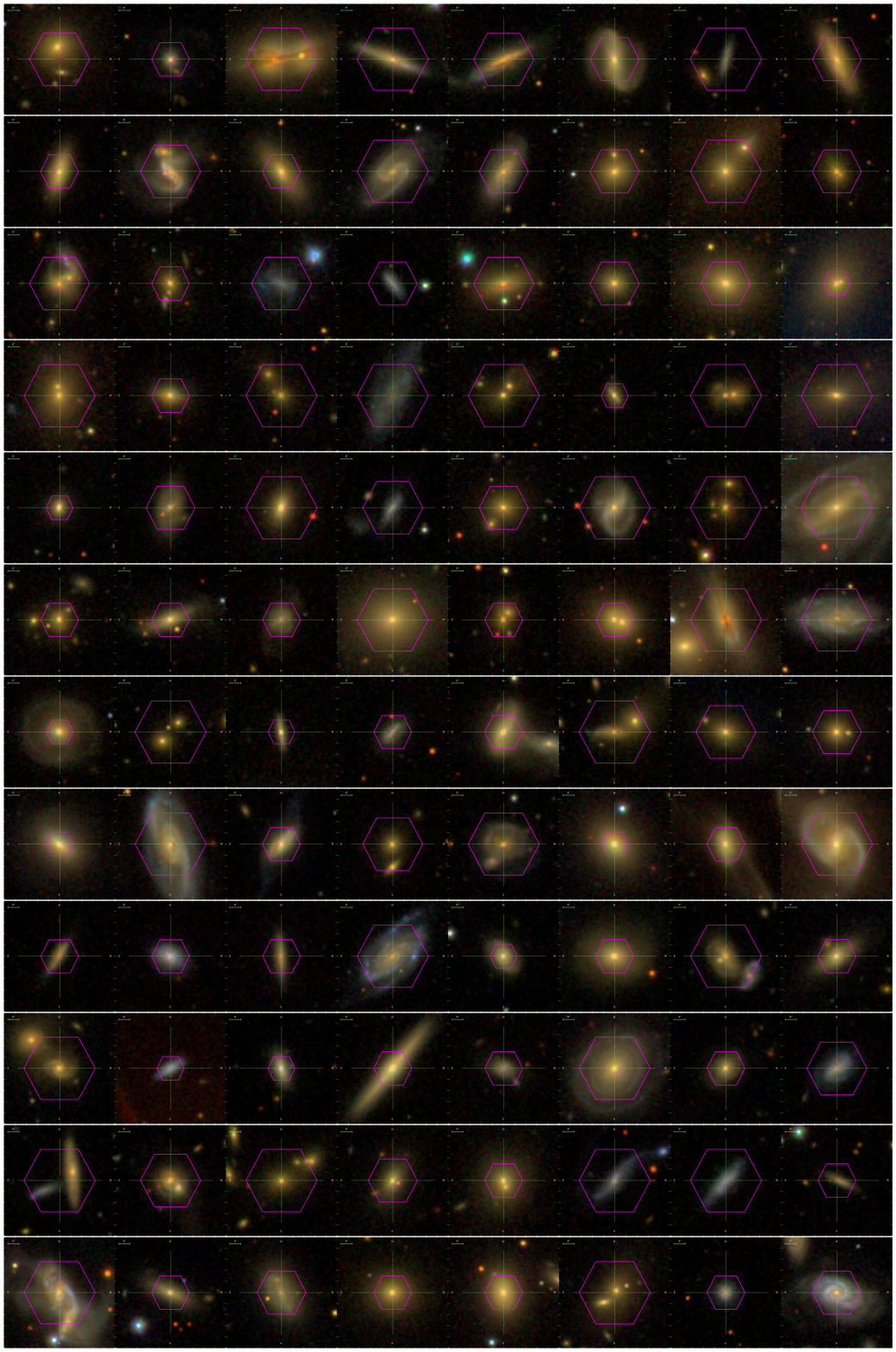

Figure A.15

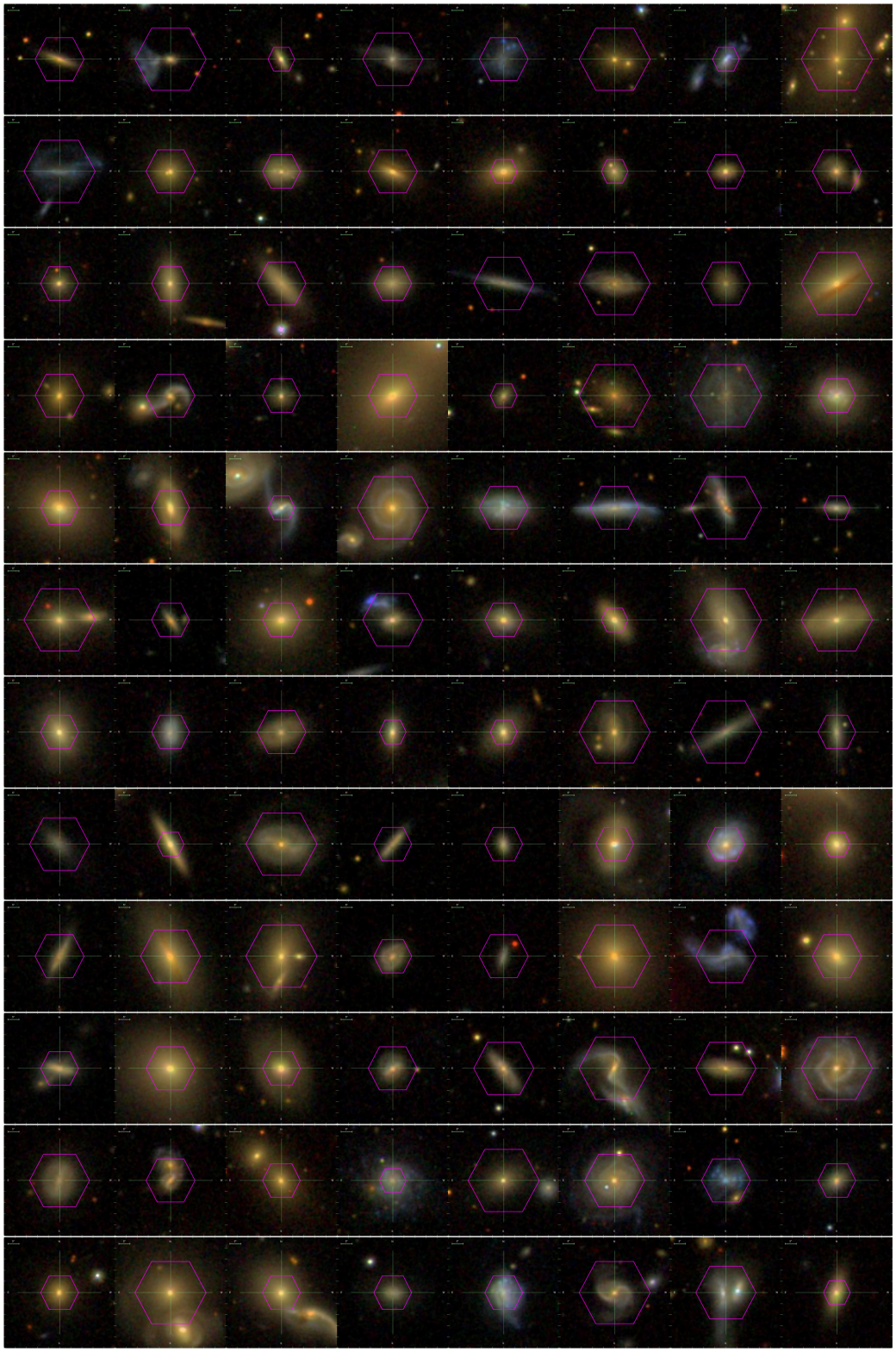

Figure A.16

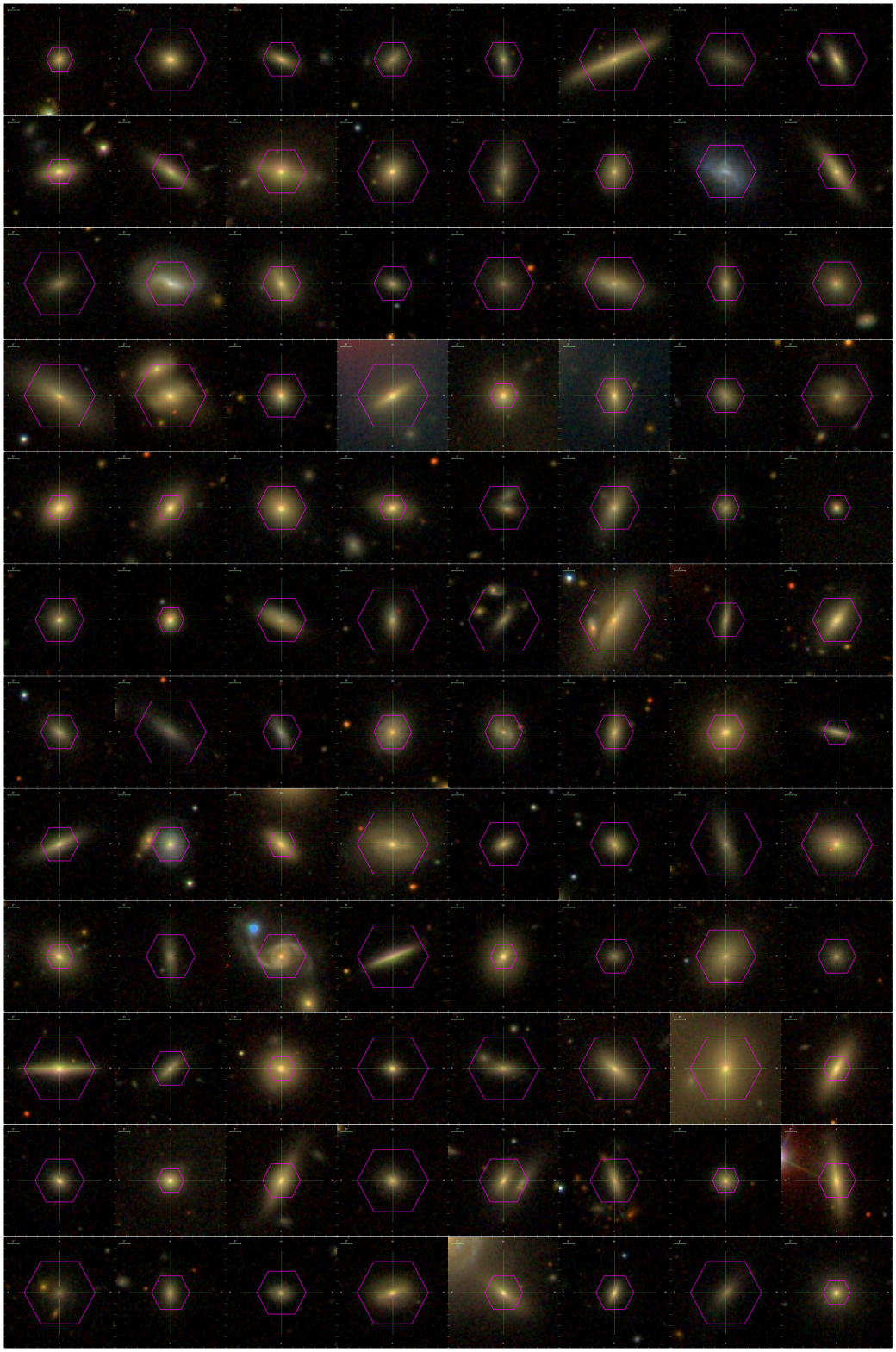

Figure A.17

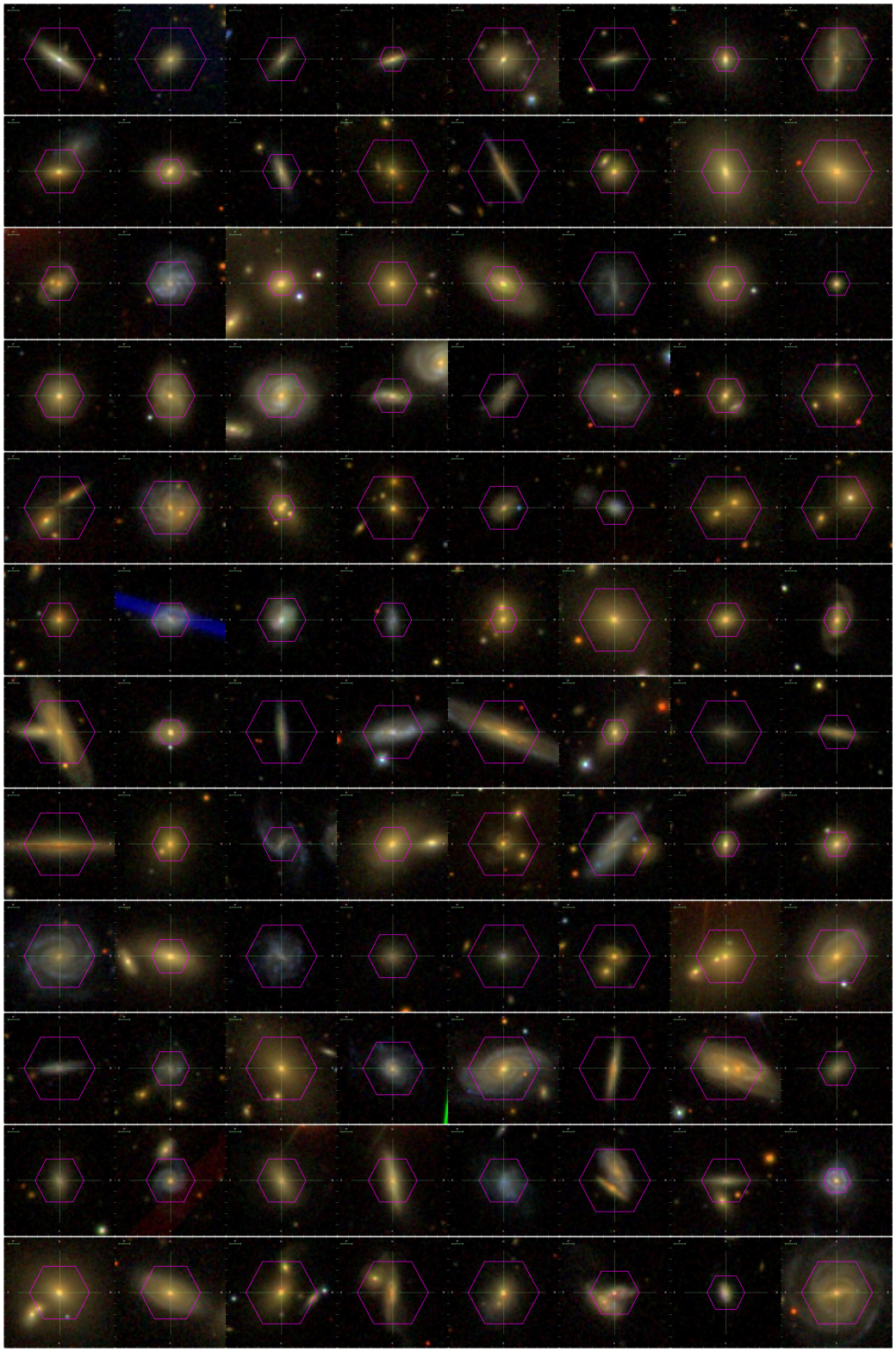

Figure A.18

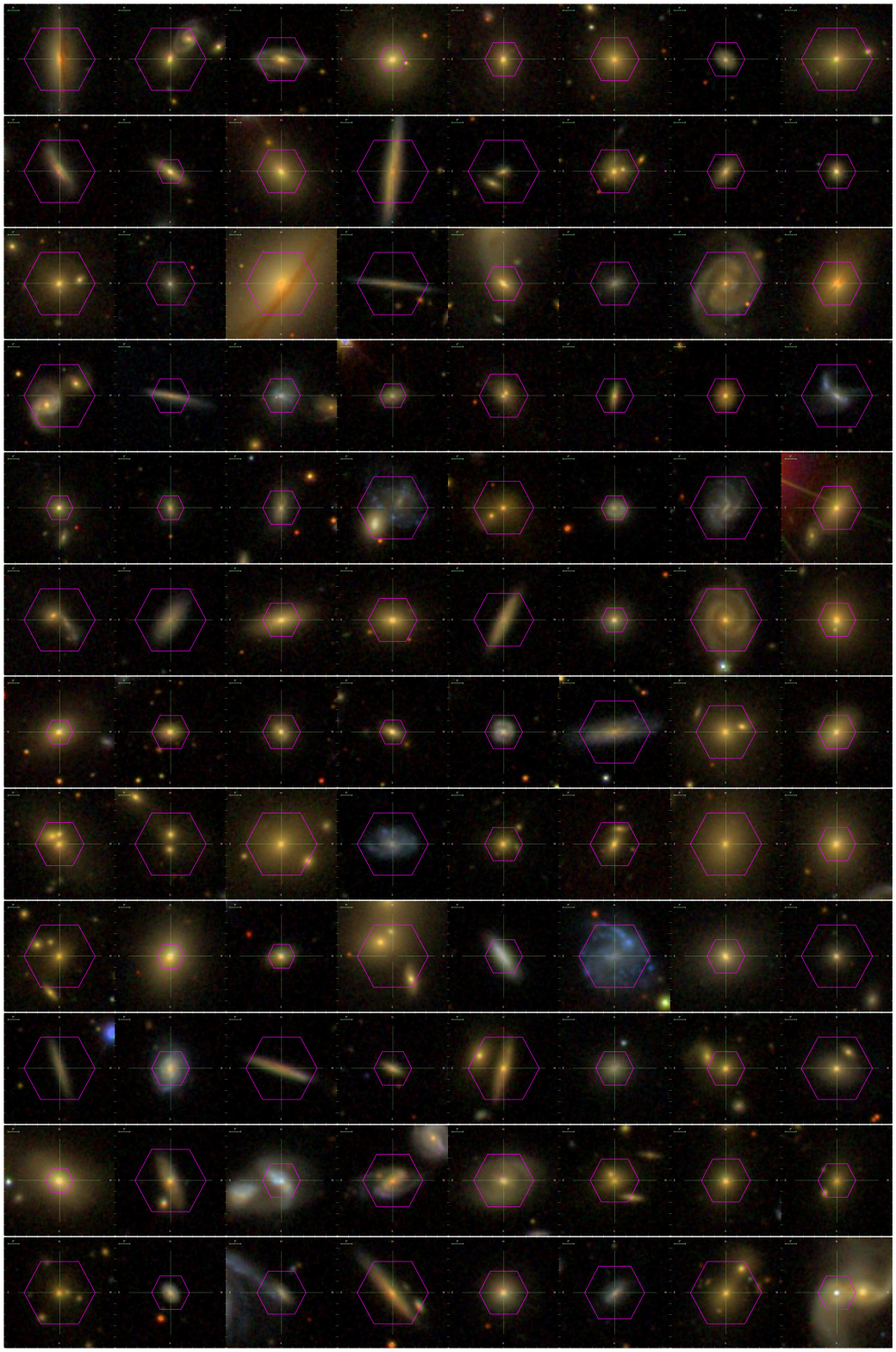

Figure A.19

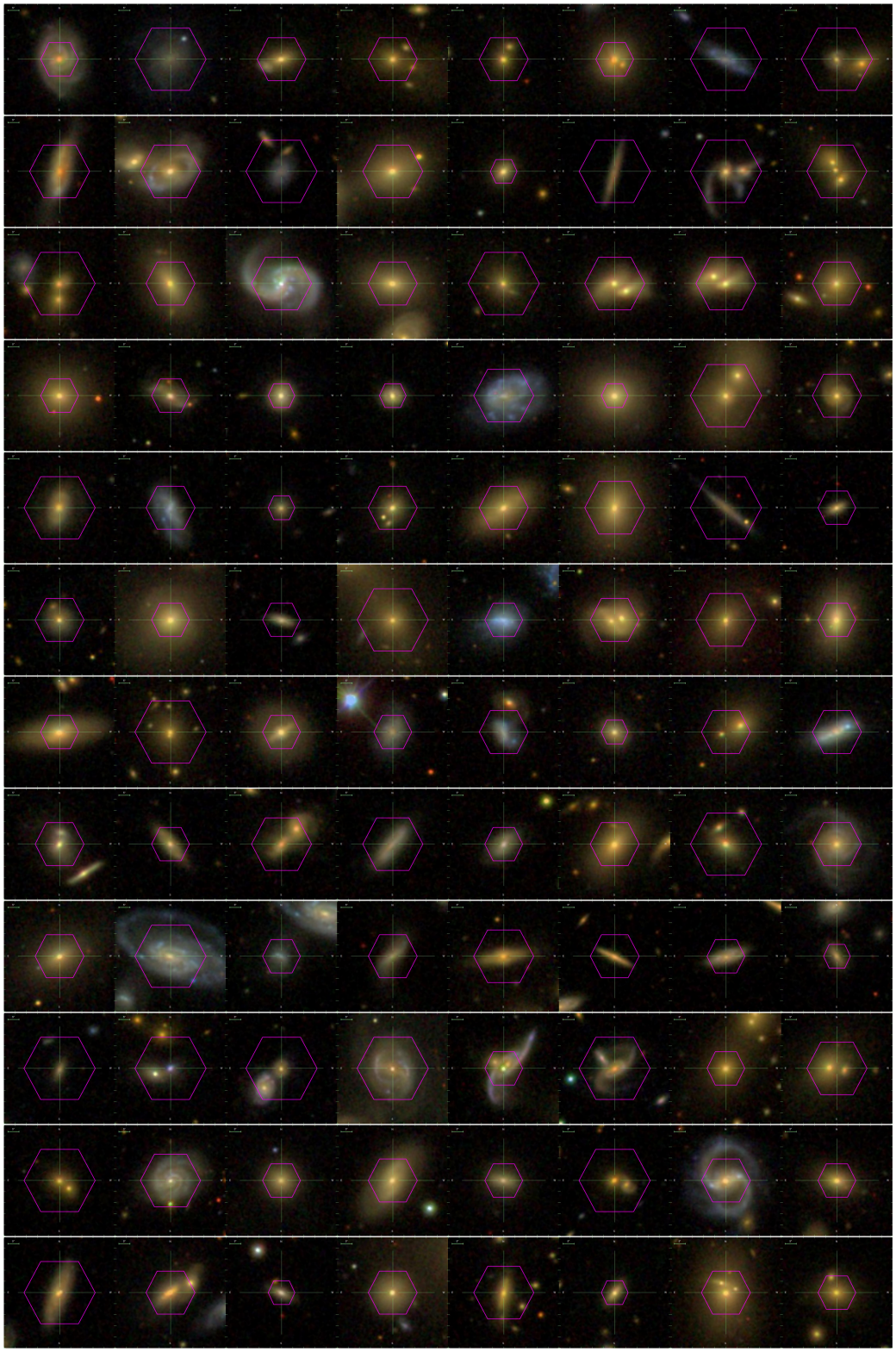

Figure A.20

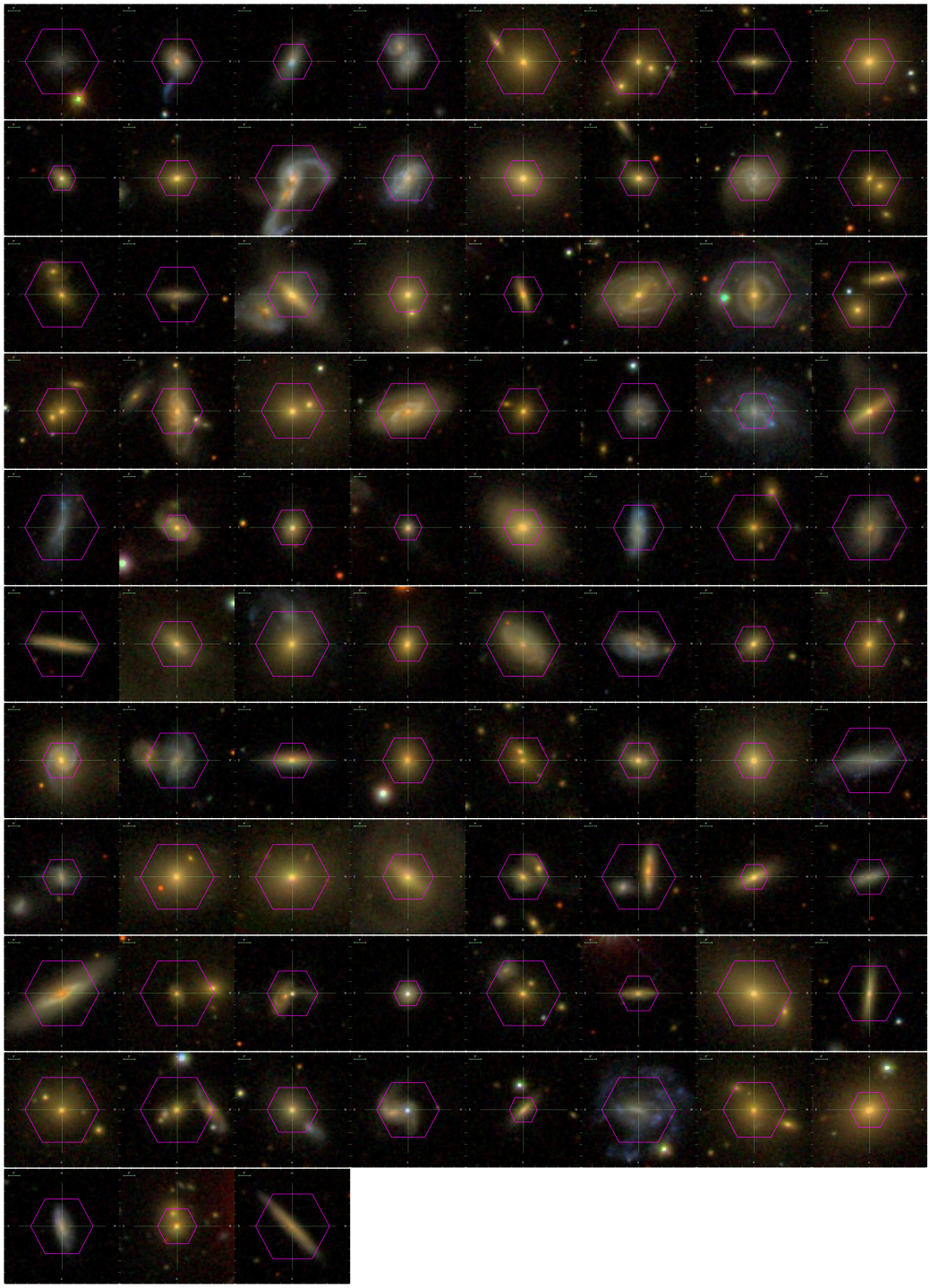

Figure A.21

A.2 ALMaQUEST - merger dataproducts

Included in figures A.22-A.26 are data product maps for the ALMaQUEST merger set. Post-mergers are shown first, followed by pairs in order of increasing pair separation. All 31 mergers are included, even the 6 galaxies with insufficient overlap between CO $S/N > 3$ and Hα+D4000 $\Sigma_{\rm SFR}$ measurements that are excluded from individual galaxy analysis. Data products include, from left to right: the SDSS *gri*-image, inclination corrected stellar mass surface density (from PIPE3D), inclination corrected molecular gas surface density (computed from CO luminosity), inclination corrected star formation rate surface density (computed from Hα luminosity), inclination corrected star formation rate surface density (computed from Hα luminosity and sSFR-D4000 fit), molecular gas fraction ($\Sigma_{\rm H_2}/\Sigma_\star$), and star formation efficiency ($\Sigma_{\rm SFR}/\Sigma_{\rm H_2}$).

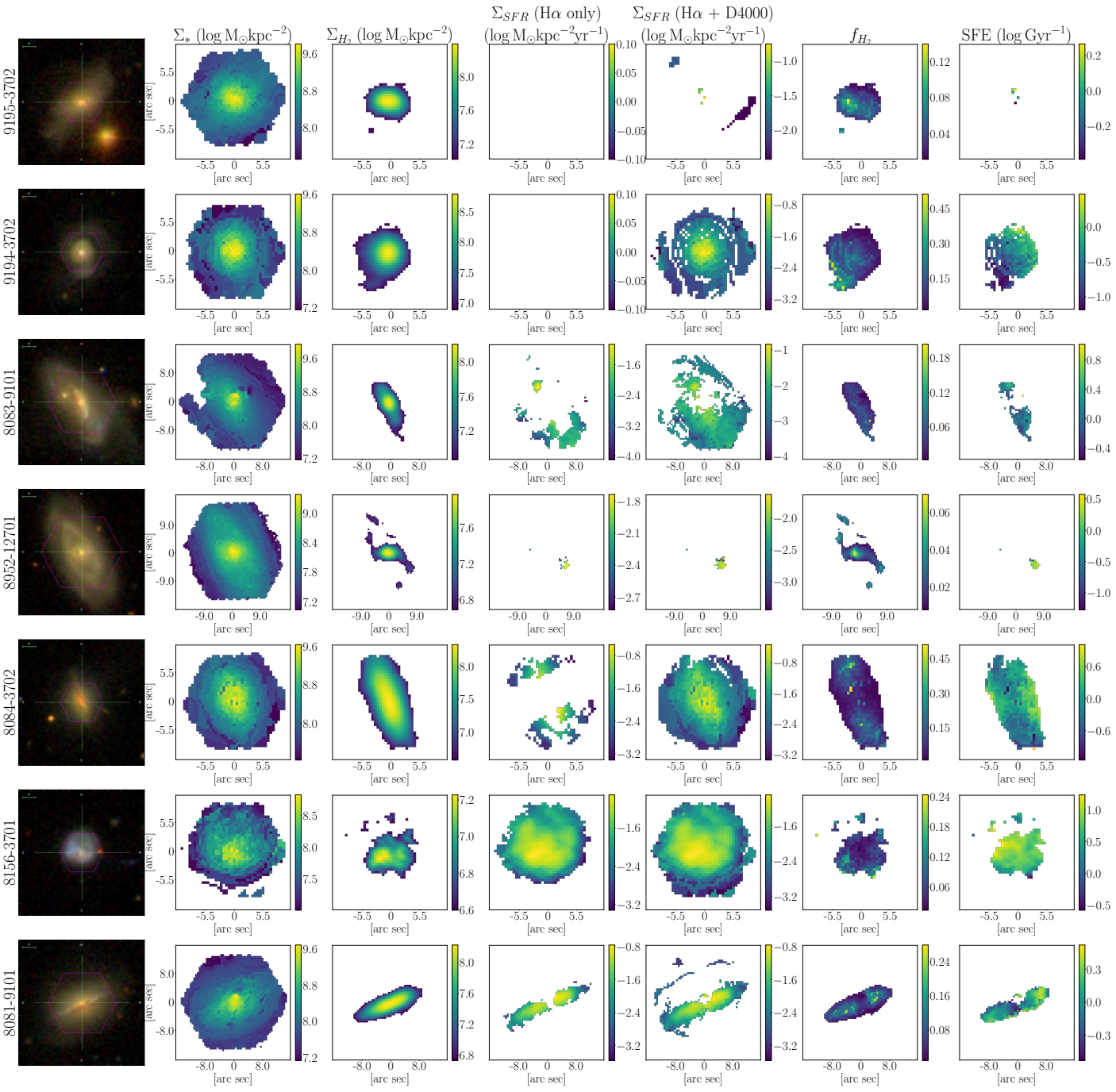
9195-3702
9194-3702
8083-9101
8952-12701
8084-3702
8156-3701
8081-9101
Σ_* (log M$_\odot$kpc^{-2})
Σ_{H_2} (log M$_\odot$kpc^{-2})
Σ_{SFR} (Hα only) (log M$_\odot$kpc^{-2}yr^{-1})
Σ_{SFR} (Hα + D4000) (log M$_\odot$kpc^{-2}yr^{-1})
f_{H_2}
SFE (log Gyr^{-1})
[arc sec]

Figure A.22

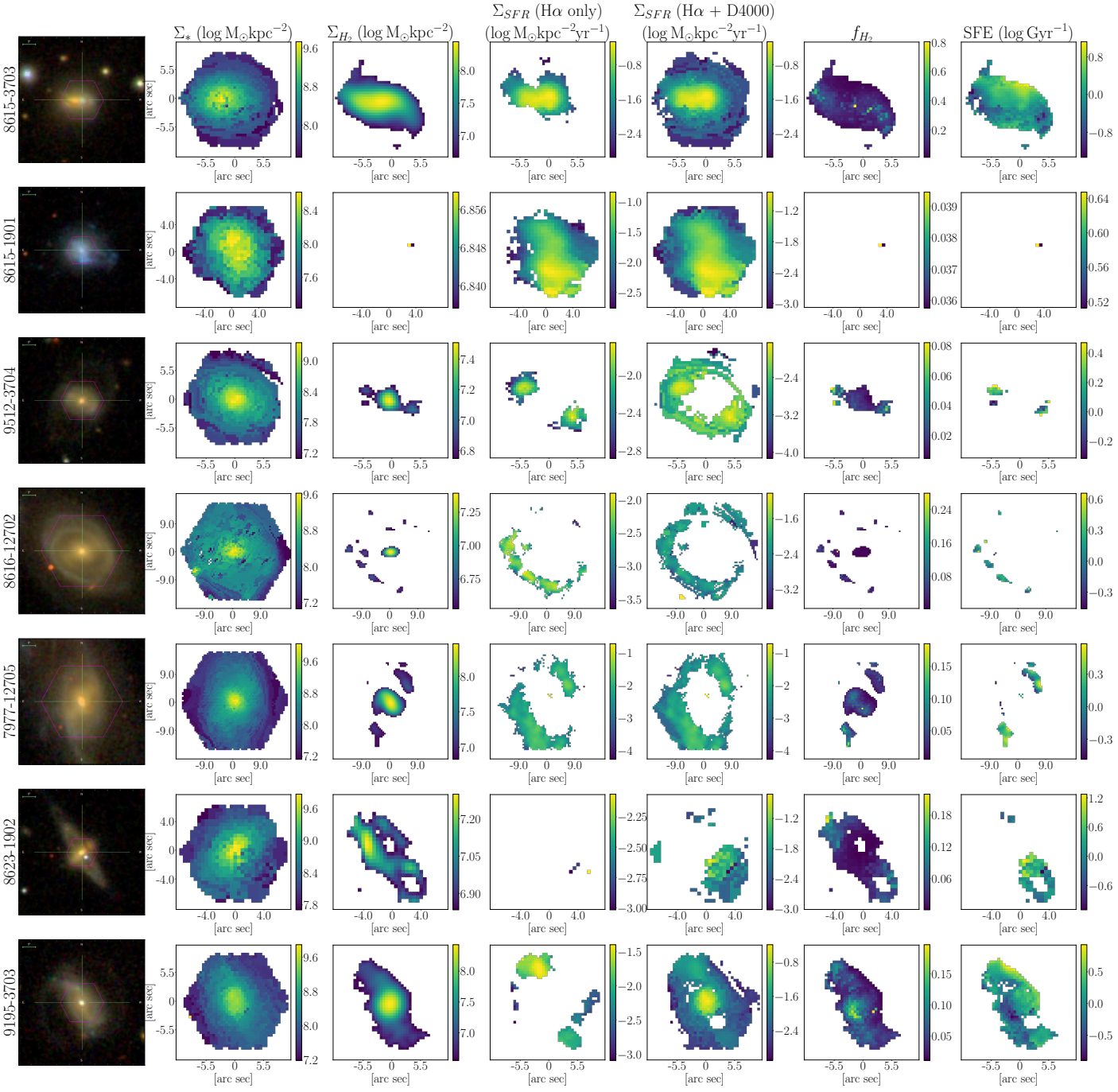
8615-3703
8615-1901
9512-3704
8616-12702
7977-12705
8623-1902
9195-3703
Σ_* (log M$_\odot$kpc^{-2})
Σ_{H_2} (log M$_\odot$kpc^{-2})
Σ_{SFR} (Hα only) (log M$_\odot$kpc^{-2}yr^{-1})
Σ_{SFR} (Hα + D4000) (log M$_\odot$kpc^{-2}yr^{-1})
f_{H_2}
SFE (log Gyr^{-1})
[arc sec]

Figure A.23

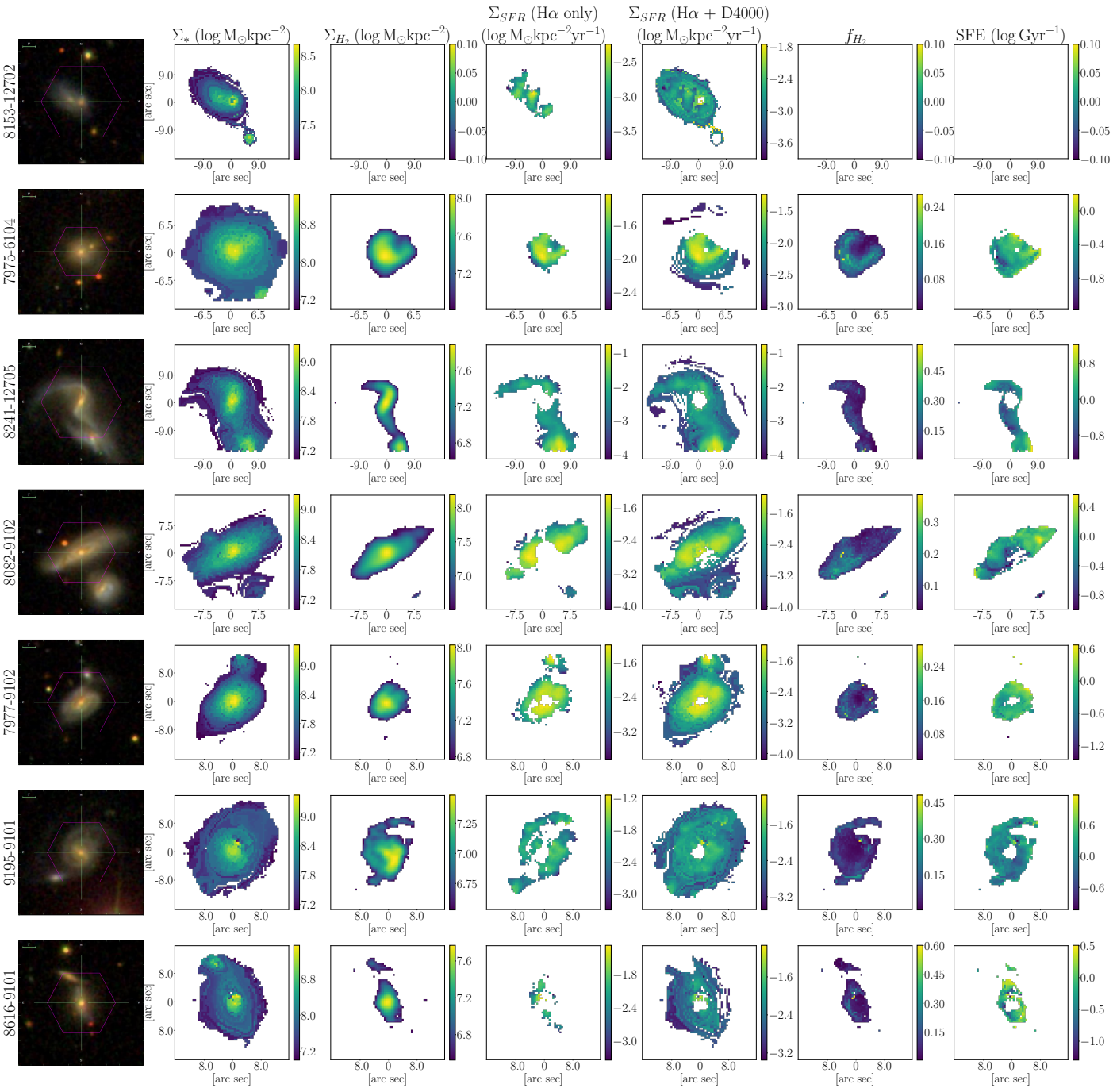
8153-12702
7975-6104
8241-12705
8082-9102
7977-9102
9195-9101
8616-9101
Σ_* (log M$_\odot$kpc^{-2})
Σ_{H_2} (log M$_\odot$kpc^{-2})
Σ_{SFR} (Hα only) (log M$_\odot$kpc^{-2}yr^{-1})
Σ_{SFR} (Hα + D4000) (log M$_\odot$kpc^{-2}yr^{-1})
f_{H_2}
SFE (log Gyr^{-1})
[arc sec]

Figure A.24

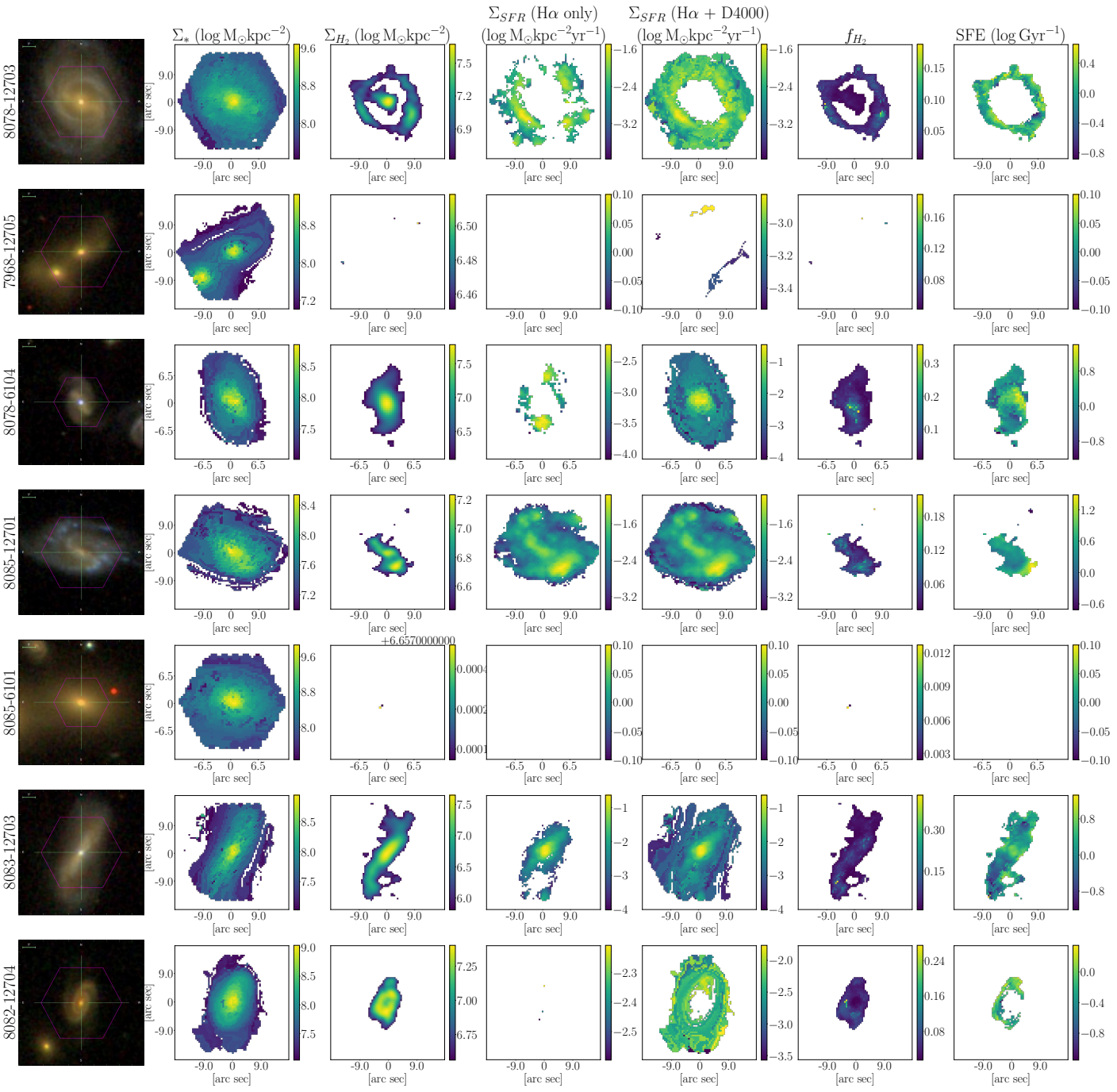
Σ_* (log M$_\odot$kpc^{-2})
Σ_{H_2} (log M$_\odot$kpc^{-2})
Σ_{SFR} (Hα only) (log M$_\odot$kpc^{-2}yr^{-1})
Σ_{SFR} (Hα + D4000) (log M$_\odot$kpc^{-2}yr^{-1})
f_{H_2}
SFE (log Gyr^{-1})
8078-12703
7968-12705
8078-6104
8085-12701
8085-6101
8083-12703
8082-12704
[arc sec]
+6.6570000000

Figure A.25

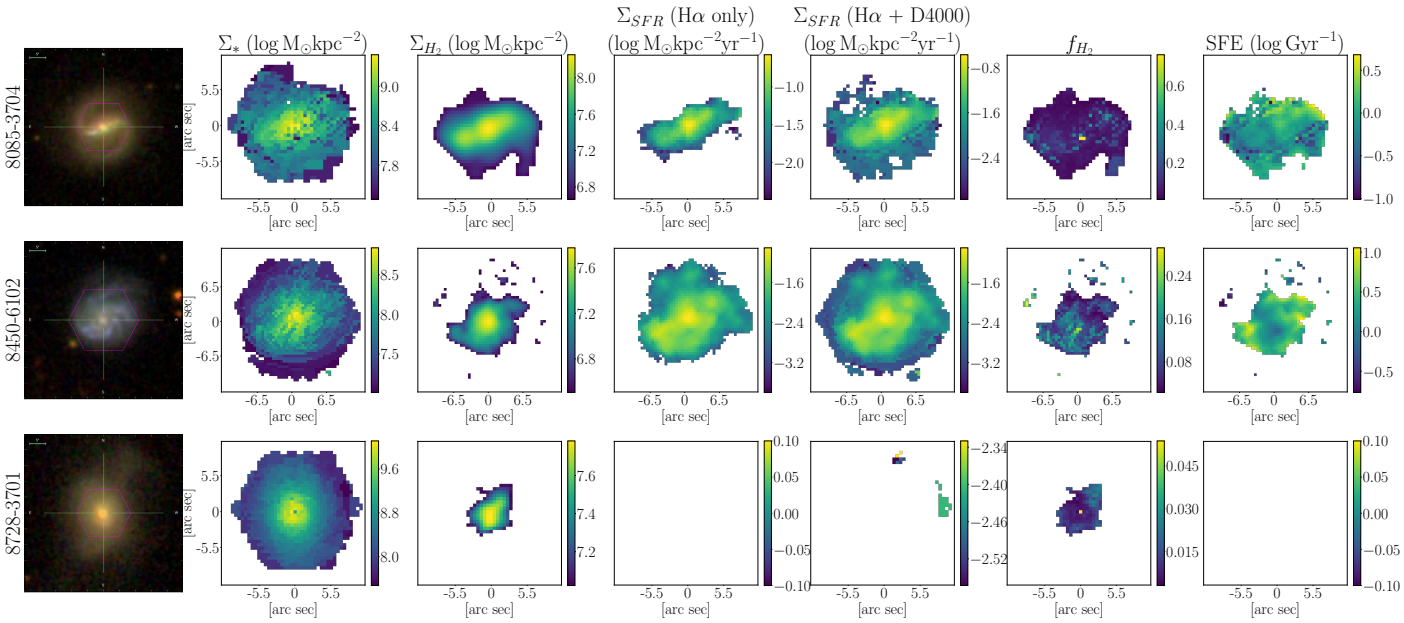
8085-3704
8450-6102
8728-3701
Σ_* (log M$_\odot$kpc^{-2})
Σ_{H_2} (log M$_\odot$kpc^{-2})
Σ_{SFR} (Hα only) (log M$_\odot$kpc^{-2}yr^{-1})
Σ_{SFR} (Hα + D4000) (log M$_\odot$kpc^{-2}yr^{-1})
f_{H_2}
SFE (log Gyr^{-1})
[arc sec]

Figure A.26

A.3 ALMaQUEST control spaxels - including D4000-$\Sigma_{\rm SFR}$

Throughout Chapter 4, control spaxels only use $\Sigma_{\rm SFR}$ derived from Hα luminosity. One hazard of this method is that we compare these control $\Sigma_{\rm SFR}$ values spaxels with D4000-$\Sigma_{\rm SFR}$. One reason a spaxel might use D4000-$\Sigma_{\rm SFR}$ instead of Hα-$\Sigma_{\rm SFR}$ is that they are classified as AGN by the BPT diagram (see Section 2.1.3), and the presence of an AGN can impact the local star formation. Thus it might be unfair to compare D4000-$\Sigma_{\rm SFR}$ to a control with no AGN contamination.

To check how including D4000-$\Sigma_{\rm SFR}$ in the control could impact final results from Chapter 4, I recompute $\Delta\Sigma_{\rm SFR}$ values from a new control spaxel set that includes D4000-$\Sigma_{\rm SFR}$. The control is limited to the rSFMS by making cuts in the old $\Delta\Sigma_{\rm SFR}$ value (-0.5 dex $< \Delta\Sigma_{\rm SFR}$ (old)$<$ 0.5 dex), providing a rough estimate of star-forming spaxels without having to exclude AGN or low S/N spaxels. The new control is made of 1542806 spaxels in ALMaQUEST: 0.2% of which are AGN, 4.0% of which are composite, 24% of which have too low S/N to classify, and the other 72% of which are appropriate to use Hα-$\Sigma_{\rm SFR}$. Overall, composite and AGN spaxels do not contribute much to the control sample, likely due to the fact that AGN spaxels are in the centre of the galaxy, where D4000$>$1.4 (and thus does not make our quality cuts for D4000-$\Sigma_{\rm SFR}$). This control is then used to determine $\Delta\Sigma_{\rm SFR}$ for the same spaxels as before.

Figure A.27 compares the old $\Delta\Sigma_{\rm SFR}$ computed from Hα-$\Sigma_{\rm SFR}$ controls to this new $\Delta\Sigma_{\rm SFR}$ measurement in the first panel. Despite scatter about the line of equality, the two values trace each other relatively well. The second panel plots the difference in these two measurements as a function of $\Delta\Sigma_{\rm SFR}$ (old). Although the difference in $\Delta\Sigma_{\rm SFR}$ can get as large as 0.5 dex, the majority of points lie about zero. The third panel better shows this by showing a histogram of the change in $\Delta\Sigma_{\rm SFR}$. The median difference is very small, 0.03 dex, but still biased to the new $\Delta\Sigma_{\rm SFR}$ values being slightly larger. Including D4000-$\Sigma_{\rm SFR}$ in the control should make $\Delta\Sigma_{\rm SFR}$ larger: by adding more spaxels with low S/N, the average $\Sigma_{\rm SFR}$ value of the control will be smaller.

To investigate how this new $\Delta\Sigma_{\rm SFR}$ would impact key results from Chapter 4, the fraction of fuel-driven spaxels is recomputed for each merger, and compared to the fuel fraction calculated with the old control. New ΔSFE are also computed using the updated control. A similar method was used to test the impact of a metallicity-dependent CO conversion factor in Section 4.4.1, Figure 4.17. The left panel of Figure

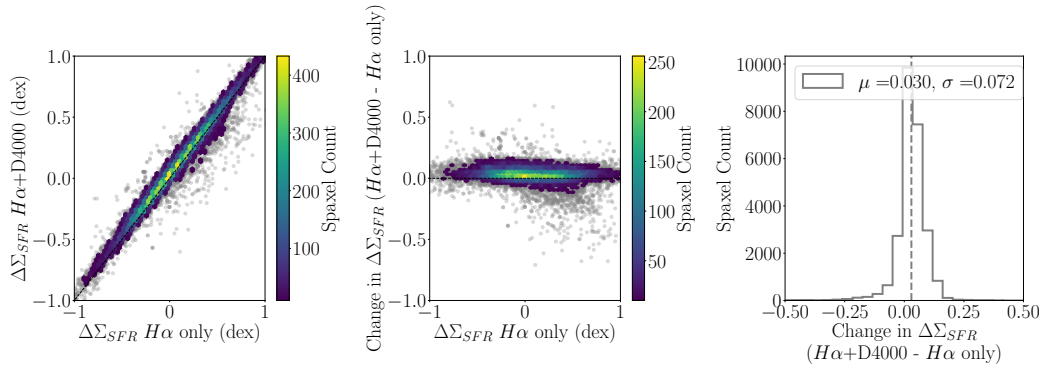

Figure A.27: *Left:* Comparison of $\Delta\Sigma_{\rm SFR}$ determined from a control that only contains Hα-$\Sigma_{\rm SFR}$ (x-axis) to $\Delta\Sigma_{\rm SFR}$ determined from a control with both Hα-$\Sigma_{\rm SFR}$ and D4000-$\Sigma_{\rm SFR}$ (y-axis). Data are shown as a density hexbin, with a scatter plot in the background as grey dots representing individual spaxels. The black dashed line represents where the new and old $\Delta\Sigma_{\rm SFR}$ are equal, demonstrating how closely the two values follow each other. *Middle:* The difference in $\Delta\Sigma_{\rm SFR}$ (Hα control spaxels only minus Hα and D4000 controls) plot against the original $\Delta\Sigma_{\rm SFR}$ measurement. Again, data are shown as a density hexbin with a grey scatter plot representing individual spaxels in the background There is a small bias for the new $\Delta\Sigma_{\rm SFR}$ value to be larger (difference is positive). *Right:* A histogram showing the range of change possible in $\Delta\Sigma_{\rm SFR}$. The median change is very small, shown as a dashed line at 0.03 dex. $\Delta\Sigma_{\rm SFR}$ computed from a Hα and D4000 controls are usually higher because the D4000-$\Sigma_{\rm SFR}$ values bring down the average $\Sigma_{\rm SFR}$ of the control.

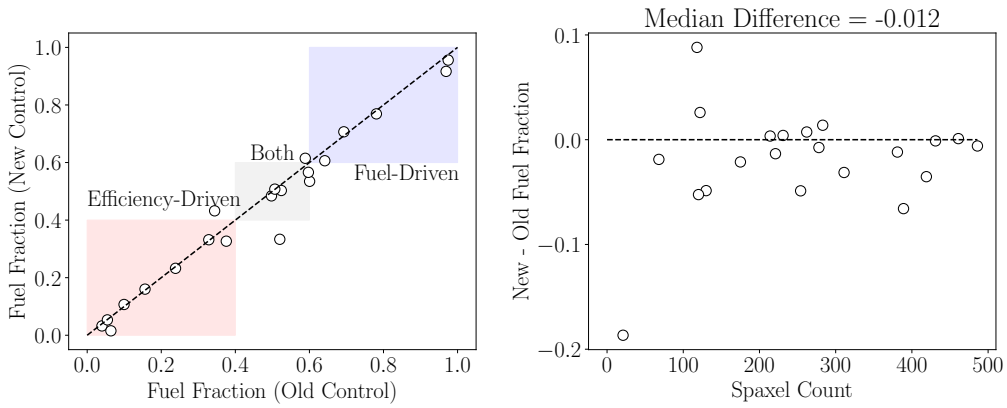

Figure A.28: *Left:* Comparing the original fuel fraction (x-axis) to the fuel fraction with $\Delta\Sigma_{\rm SFR}$ values using the new control (y-axis). Ideally the two fuel fractions would be equal, and thus lay on the dashed line. I have highlighted regions that indicate the dominant mechanism has not changed based on the criteria described in Chapter 4: where both fractions imply star formation is efficiency-driven (red), where both fractions imply star formation is fuel-driven (blue), and where both fractions imply star formation is driven by both (grey). Only 5 mergers change whether their dominant star-forming mechanisms, and these were already border cases (at the boundary for fuel-driven star formation). *Right:* The difference in fuel fraction (new - old) as a function of the number of spaxels used to determine fuel fraction. The galaxies with the most drastic change in fuel fraction are also those with the least spaxels, where only a handful of spaxels changing their $\Delta\Sigma_{\rm SFR}$ have a major impact on the final fuel fraction computed. There is also a small bias towards smaller fuel fractions, which is intuitive given when D4000-$\Sigma_{\rm SFR}$ are considered the average control $\Sigma_{\rm SFR}$ goes down, meaning both $\Delta\Sigma_{\rm SFR}$ and ΔSFE will be larger.

A.28 plots the new fuel fraction (computed with this new control) vs. the original fuel fraction. Again the red, grey, and blue boxes show space where points could move and not impact our final classification of fuel or efficiency-driven mergers. Of the sample of 21 mergers only 5 change whether they are fuel/efficiency-driven overall, and those are ones that were already at the border of these categories (changing from 0.6 to 0.53, for example).

The right panel shows the difference between these two fuel fractions, as a function of spaxel count. There appears to be a bias towards smaller fuel fractions with the new control - meaning efficiency is more important in driving star formation. Such an effect makes intuitive sense: if more low S/N regions are included, this should drive the control $\Sigma_{\rm SFR}$ down - meaning ΔSFE is larger despite the same amount of molecular gas. This difference is very small however, on the order of 0.01 (or 1%).

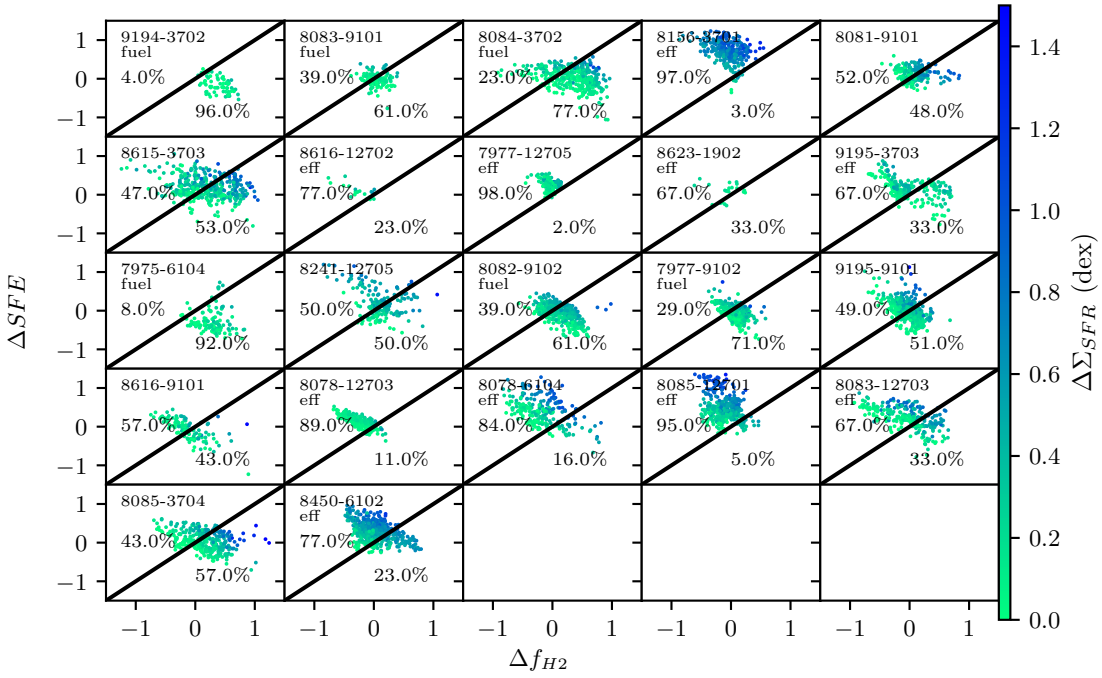

Figure A.29: A replication of Figure 4.11, where $\Delta\Sigma_{\rm SFR}$ and ΔSFE are based on a control which contains D4000-$\Sigma_{\rm SFR}$. Every panel shows ΔSFE versus $\Delta f_{\rm H_2}$ for all spaxels with $\Delta\Sigma_{\rm SFR}>0$ in each galaxy merger with more than 20 spaxels with $\Delta\Sigma_{\rm SFR}>0$, the plate-ifu number of each galaxy is provided in the left corner of every plot. Spaxels are colour-coded by $\Delta\Sigma_{\rm SFR}$. The percentage of spaxels above and below the line of equality are provided as well, which help discern whether the star formation in a galaxy is predominantly driven by enhanced SFE or enhanced $f_{\rm H_2}$. Galaxies that are predominantly efficiency-driven ($<$ 40% below the line) and fuel-driven ($>$ 60% above the line) are labelled for reference.

The galaxy that changes the most drastically from "Both" to "Efficiency" driven (8623-1902) also has the smallest spaxel count. This speaks more to the viability of these categories overall, rather than the validity of the fuel fraction. Chapter 4 already discusses in detail how the fuel fraction is a more robust term to analyze, rather than strictly delineated categories like "efficiency-driven".

The fuel fraction change in all but two galaxies is less than 0.05 (or 5%). The change in both fuel fraction and $\Delta\Sigma_{\rm SFR}$ when D4000-$\Sigma_{\rm SFR}$ are incorporated being so small confirms that results from Chapter 4 would not change if we adjusted the control calculation. For visual confirmation of this, Figure A.29 replicates Figure 4.11 from Chapter 4, but using the D4000+Hα control. From visual inspection alone one

can see how little the offset parameters change for each galaxy compared to Figure 4.11.

A.4 Offset maps for entire ALMaQUEST merger sample

Figures A.30-A.33 are a complete catalogue of the $\Delta\Sigma_{\rm SFR}$, ΔSFE, and $\Delta f_{\rm H_2}$ distributions for the galaxy merger sample examined in this work. Diverging colourbars are used such that blue spaxels represent enhancements in $\Sigma_{\rm SFR}$, SFE, or $f_{\rm H_2}$. Red spaxels represent a deficit in either variable. The SDSS *gri*-image is included as well, to provide context for the galaxy and the MaNGA IFU coverage. One will note that some galaxies have $\Delta f_{\rm H_2}$ measurements where no $\Delta\Sigma_{\rm SFR}$ or ΔSFE is measured. This results from the stricter cuts required to measure $\Sigma_{\rm SFR}$, a limitation not imposed on the calculation of $\Delta f_{\rm H_2}$. The fourth column provides a map of ΔSFE$-\Delta f_{\rm H_2}$ for all spaxels where $\Delta\Sigma_{\rm SFR}>0$, as described in Section 4.3.2.1. Note that most mergers have negative ΔSFE$-\Delta f_{\rm H_2}$ in the centre of the galaxy, implying gas fractions are more centrally enhanced than SFE.

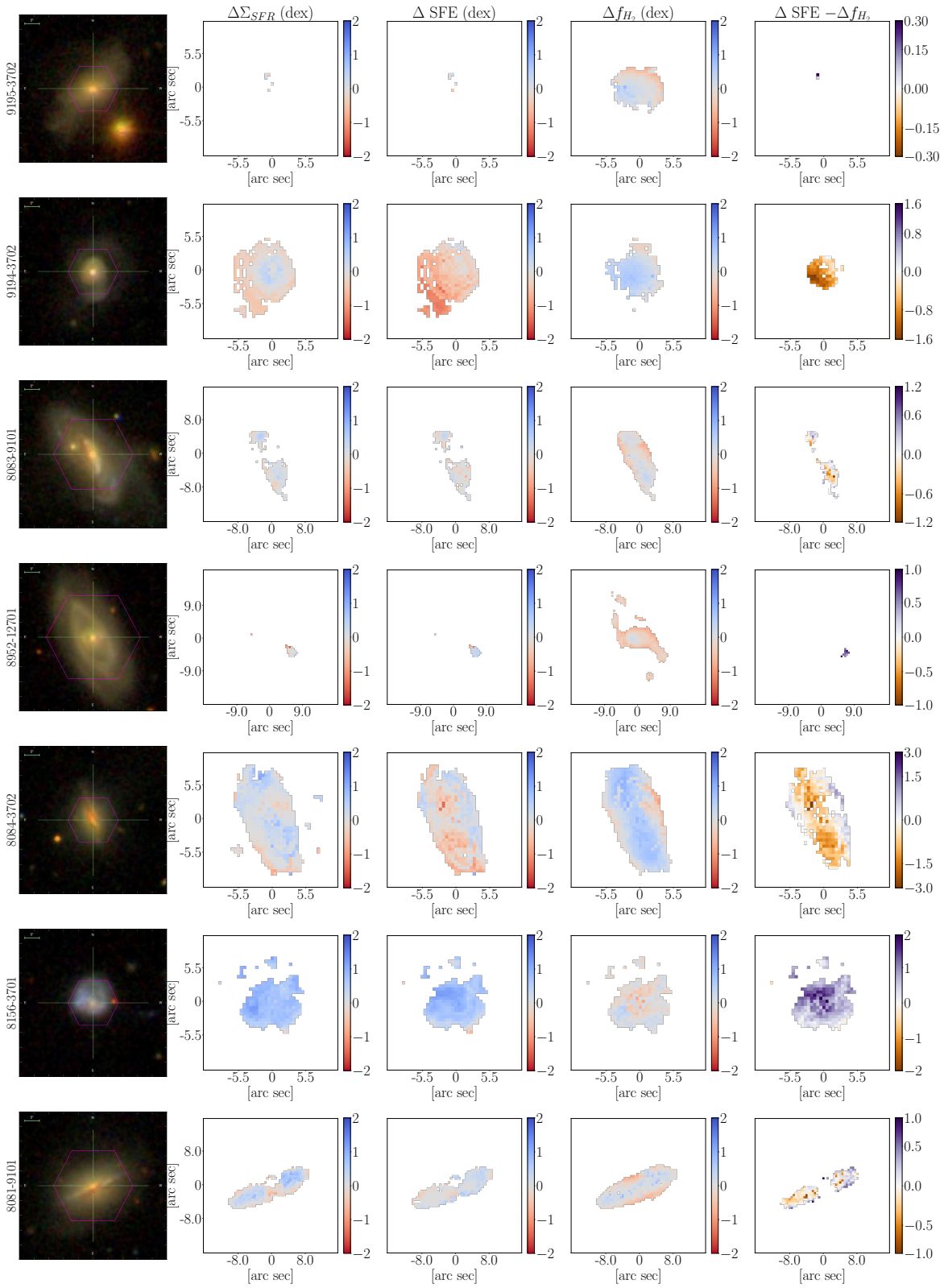
$\Delta\Sigma_{SFR}$ (dex)
Δ SFE (dex)
Δf_{H_2} (dex)
Δ SFE $-\Delta f_{H_2}$
9195-3702
9194-3702
8083-9101
8952-12701
8084-3702
8156-3701
8081-9101
[arc sec]

Figure A.30

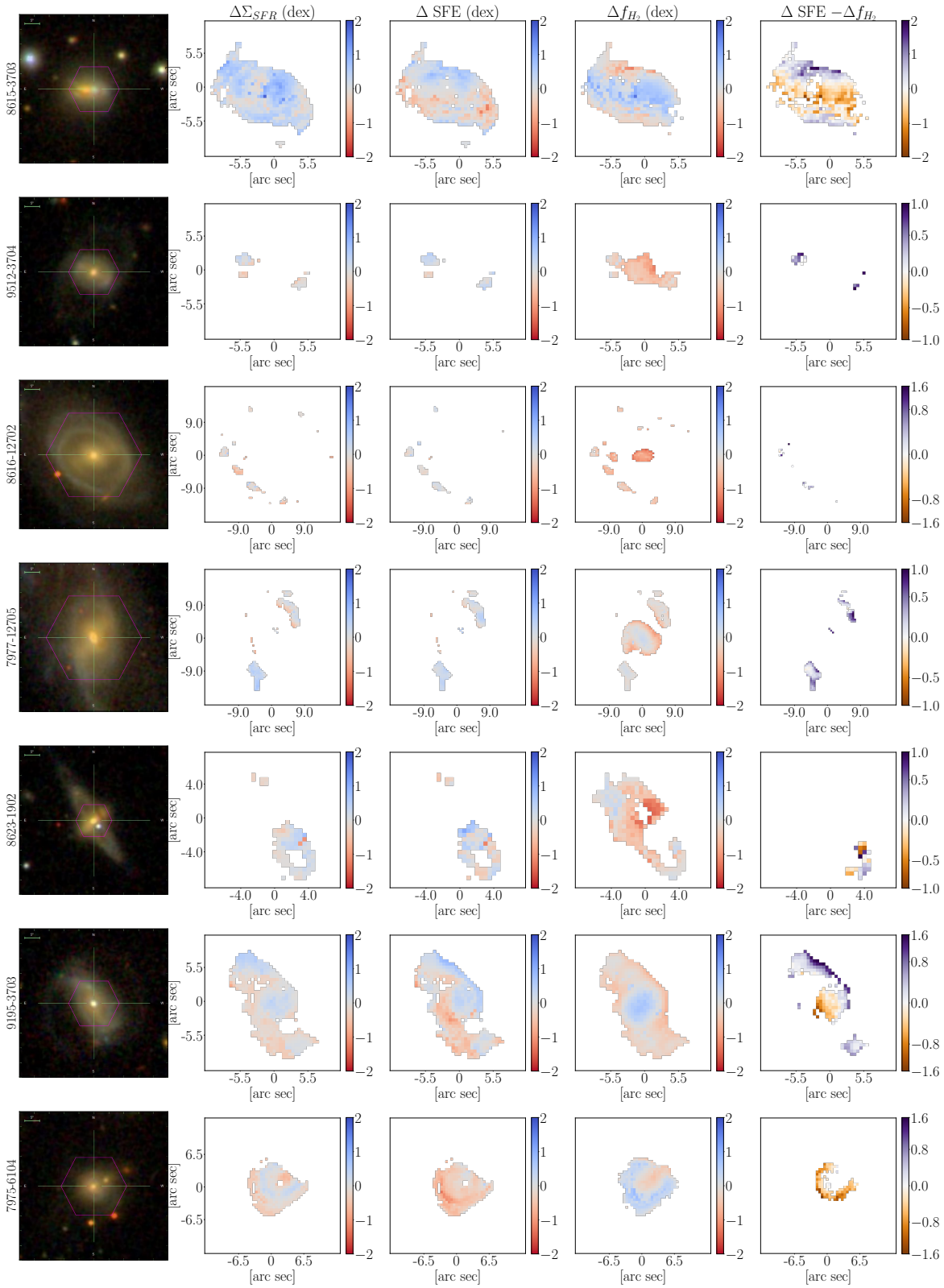
8615-3703
9512-3704
8616-12702
7977-12705
8623-1902
9195-3703
7975-6104
$\Delta\Sigma_{SFR}$ (dex)
Δ SFE (dex)
Δf_{H_2} (dex)
Δ SFE $-\Delta f_{H_2}$
[arc sec]

Figure A.31

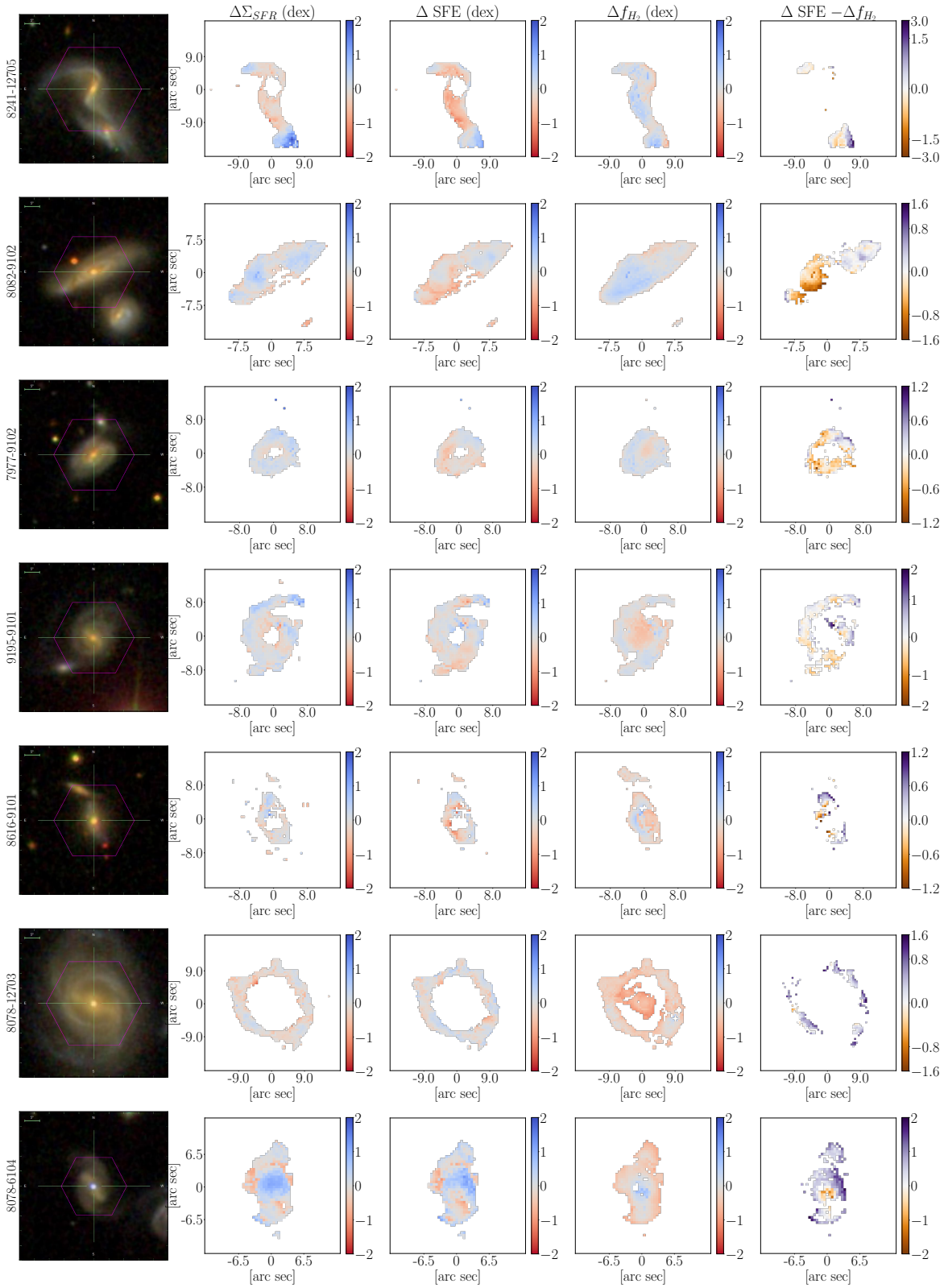
$\Delta\Sigma_{SFR}$ (dex)
Δ SFE (dex)
Δf_{H_2} (dex)
Δ SFE $-\Delta f_{H_2}$
8241-12705
8082-9102
7977-9102
9195-9101
8616-9101
8078-12703
8078-6104
[arc sec]

Figure A.32

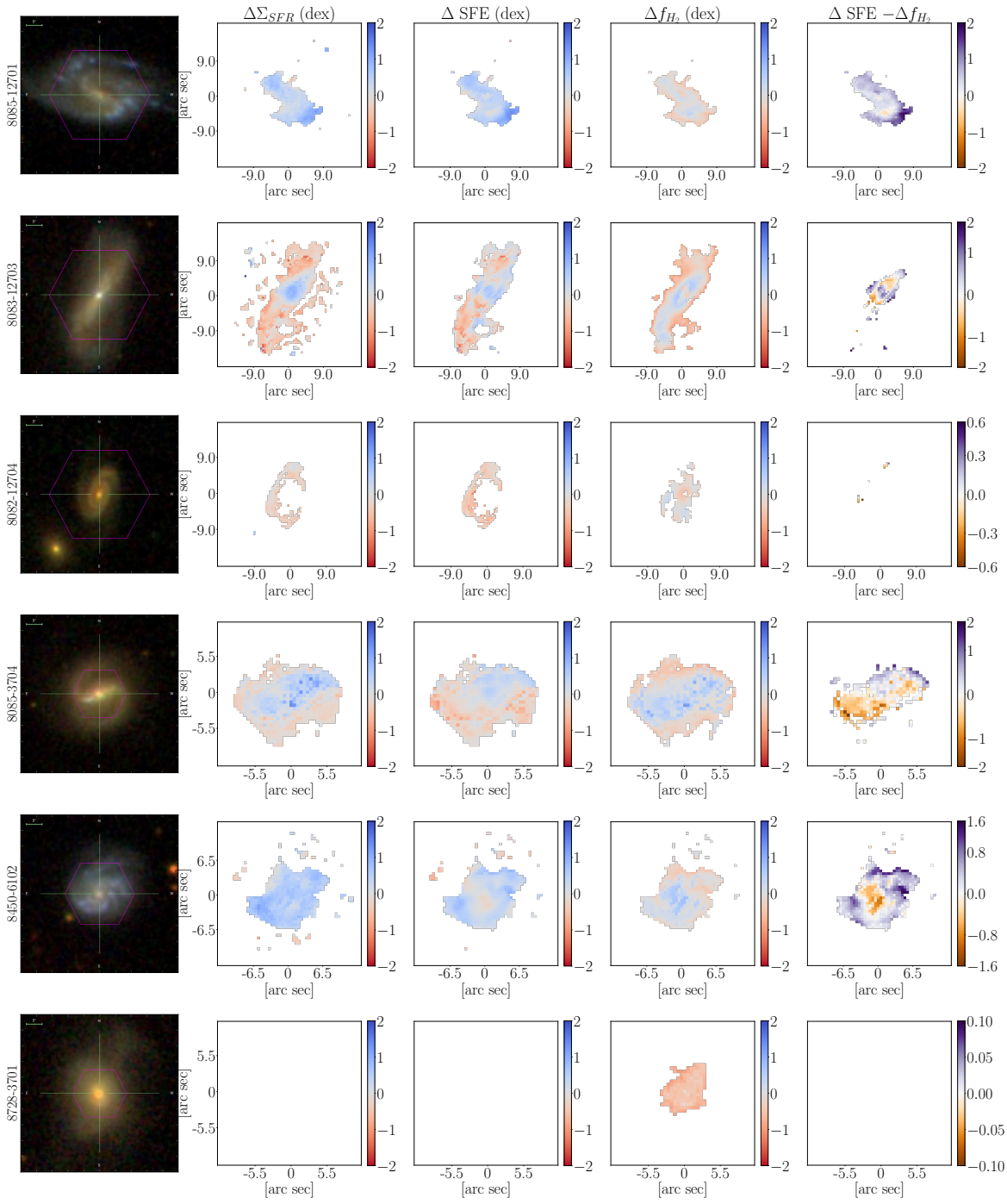
8085-12701
8083-12703
8082-12704
8085-3704
8450-6102
8728-3701
$\Delta\Sigma_{SFR}$ (dex)
Δ SFE (dex)
Δf_{H_2} (dex)
Δ SFE $-\Delta f_{H_2}$
[arc sec]

Figure A.33